

https://dspace.org/

Structural Characterization of Bimetal-Phosphate Based Solid-State Electrolytes: A PXRD, PDF and XAS Study

Nkala, Gugulethu Charmaine

2024

University of the Witwatersrand, Johannesburg

https://hdl.handle.net/10539/41801

Nkala, Gugulethu Charmaine. (2024). Structural Characterization of Bimetal-Phosphate Based Solid-State Electrolytes: A PXRD, PDF and XAS Study [PhD thesis, University of the Witwatersrand, Johannesburg]. WireDSpace.https://hdl.handle.net/10539/41801

Downloaded from a DSpace repository. https://dspace.org/

STRUCTURAL CHARACTERIZATION OF BIMETAL-PHOSPHATE BASED SOLID-STATE ELECTROLYTES: A PXRD, PDF AND XAS STUDY

Gugulethu Charmaine Nkala

Student Number: 721270

A thesis submitted to the Faculty of Science, University of the Witwatersrand, Johannesburg, in fulfilment of the requirements for the degree of

Doctor of Philosophy

Supervisors:

Prof. David G. Billing

Prof. Caren Billing

Dr Fernando D. Vila

Dr Roy P. Forbes

22 May 2024

DECLARATION

I declare that this thesis is, apart from the recognized assistance of my supervisors, my own unaided work. It is being submitted for the Degree of Doctor of Philosophy at the University of the Witwatersrand, Johannesburg School of Chemistry. It has not been submitted before for any degree or examination at any other University.



_____ on this 22nd day of May 2024

(Candidate)

_____ on this ____ day of _____

(Supervisor)

_____ on this ____ day of _____

(Co-Supervisor)

_____ on this ____ day of _____

(Co-Supervisor)

ABSTRACT

In this work, NASICON-type lithium titanium phosphate ($LiTi_2(PO_4)_3$, LTP) was synthesized following the conventional solid-state reaction methodology. Single and double-doped formulations of LTP were made, with the primary objective of improving the room-temperature ionic conductivity, for their application as potential solid-state electrolytes for all-solid-state Li ion batteries.

The primary characterization technique applied was ambient-temperature powder X-ray diffraction (PXRD) at both laboratory and synchrotron experimental conditions. The Rietveld refinement approach was used to determine the qualitative and quantitative phase compositions of each sample, revealing the rhombohedral (*R*-3*c*, space group #167) main phase, with phosphate-based secondary phases. Total scattering data, through the pair distribution function (PDF) was applied, revealing lattice site preference during the substitution of Ti with Al, Sn and Dy at the 12*c* site. Further analysis through small-box modelling indicated the local structure deviation below 10 Å, from rhombohedral (*R*-3*c*) to monoclinic ($P2_1/n$, space group #14). The application of experimental X-ray absorption spectroscopy (XAS) revealed a stable 4+ oxidation state for Ti regardless of doping. However, the extended X-ray absorption fine structure (EXAFS) data showed that the replacement of Ti with Sn results in heavy disorder and subsequent changes in the PO_4 tetrahedra, corroborating the findings from Raman spectroscopy. Theoretical XAS spectra were computed using FEFF, providing insights into the origins of experimentally observed XAS features from first-principles.

Applying electrochemical impedance spectroscopy (EIS) to assess the ambient-temperature ionic conductivity, co-doped systems showed an improvement in the conductivity. The application of characterization techniques at various length scales has been demonstrated to provide insights into the mechanisms governing the performance of the solid-state electrolytes.

DEDICATION

This is dedicated to the 6-year-old girl whose inquisitiveness was supported by parents who ignited a passion for science.

To the girl who dared to dream beyond her surroundings.

To the girl child whose great grandmother supported the education of a girl child.

Most importantly, to the (grand) child of domestic workers. We have done it!

Mama, for every risk, every first, every hug, ngibonge imisebenzi yakho, Ntombi.

This is dedicated to the matriarchs.

To the gents in the family, a great thank you for breaking the stereotype of not educating the girl children. To my dads, Jefrey and Mgcini Nkala, thank you for your dedication and support. For every ink and oil stain endured, this task is complete.

To my siblings, onwards and upwards <3

Nkala

Wena owesitsh'esihle esidlela amakhosi namakhosazana, bedlela amasi nenyama

Maphosa owaphos' umkhonto wangawulandeli

Vumisa

Wuyane

Konda

Konke kufezekile.

ACKNOWLEDGEMENTS

- The support of the DSI-NRF Centre of Excellence in Strong Materials towards this research is hereby acknowledged. Opinions expressed and conclusions arrived at, are those of the author and are not necessarily to be attributed to the CoE-SM.
- I would like to extend my thanks to the University of Witwatersrand's School of Chemistry and my colleagues and friends in the Energy Materials Research Group.
- I hereby express gratitude to my supervisors for their unwavering guidance, support and life-altering opportunities during the course of my studies.
- Part of this research used the Diamond Light Source at beamline B18 resources, and I would like to express my gratitude to the XAS team led by Prof. Allan Chadwick at Diamond Light Source for their assistance in sample preparation and data collection.
- Part of this research used the National Synchrotron Light Source-II at beamlines 28-ID-1 (PDF) and 6-BM (BMM) resources, a U.S. Department of Energy under Contract No. DE-SC0012704.
- Part of this research also used resources from the National Energy Research Scientific Computing Center, a DOE Office of Science User Facility supported by the Office of Science of the U.S. Department of Energy under Contract No. DE-AC02-05CH11231 using NERSC award project mp313.
- Some of this research was conducted as part of a research visit sponsored by the U.S.-Africa Initiative (supported by the Innovation Fund of the American Physical Society), in collaboration with the University of Washington, Columbia University and the East African Institute for Fundamental Research.
- I would like to acknowledge the contributions of Prof. John Rehr and Dr Joshua Kas from the Rehr Research Group at the University of Washington, to the computational XAS work presented herein.
- A thank you to Dr Rudolph Erasmus for his assistance with Raman spectroscopy data gathering and insightful discussions during my presentations.
- The researcher I am today would not have been possible without the contributions of Dr Paul Franklyn and Dr Shane Durbach in my undergrad and honours. I extend my gratitude to my colleagues in the CATOMAT group, especially Dr Tumelo Phaahlamohlaka, amongst others.

- Thank you to my friends, especially Ms. Lerato Mphahlele, Ms. Thandeka Kanyasa, Ms. Yongezile Mhlana and Ms. Lerato Moepye, for the coffee dates, the airport coffee and croissant allowances during travel, to the words of encouragement and comforting hugs. Dr Michelle Thiebaut, the cute notebooks recommendations and chats around XAS that further ignited our passion for the subject 😊.
- To Dr Mathias Kiefer, the journey has been wild and filled with laughter, joy, frustration, and insightful science. Dr Adam Shnier, thank you for offering a listening ear for science and beyond, and all the advice that carried me to the finish line. Most importantly, thank you to Dr Sikhumbuzo Masina for being the best friend and colleague one could ever ask for. His unwavering support in the darkest of moments, his cheers in moments of doubt and his claps in moments of accomplishment, and for being a sounding board and collaborator. Thank you, Buddy Wami <3.

To God, thank you for a life that continues to be the testament of Your presence and grace.

Be still and know that I am God – Psalms 46:10

CONFERENCES & WORKSHOPS

Nkala, G. C., Masina, S. M., Vila, F. D., Rehr, J. J., Erasmus, R., Forbes, R. P., Billing, C., Billing, D. G. **(Poster)**
"**On the average, local and electronic structure of $Li_{1.3}Al_{0.25}Dy_{0.05}Ti_{1.7}(PO_4)_3$ (LADTP)**,"
Proceedings of the U.S.-Africa Initiative in Electronic Structure & Recent Developments in Electronic Structure Workshop. May 25-Jun. 3, 2022, Columbia University, U.S.A.

Nkala, G. C., Masina, S. M., Billing, C., Forbes, R. P. and Billing, D. G. **(Oral)**
"**The Enhancement of the Ionic Conductivity of Sn-doped $LiTi_2(PO_4)_3$ by Formation of an Al, Sn co-doped System**,"
Proceedings of the African Synchrotron Network for Advanced Energy Materials (ASNAEM), Oct. 6, 2021, Johannesburg, South Africa. [Online Attendance]

Nkala, G. C., Masina, S. M., Billing, C., Forbes, R. P. and Billing, D. G. **(Poster)**
"**The Role of Al^{3+}, Dy^{3+} co-doping on the Structure-Property Correlations in NASICON-type $LiTi_2(PO_4)_3$ Solid-State Electrolytes**,"
Proceedings of the IUCr 2021- XXV General Assembly and Congress of the International Union of Crystallography, Aug. 14-22, 2021, Prague, Czech Republic. [Online Attendance]

Nkala, G. C., Billing, C., Forbes, R. P. and Billing, D. G. **(Poster)**
"**Exploring Structure-Property Relationships in NASICON-type Sn-doped $LiTi_2(PO_4)_3$**,"
Proceedings of the South Africa – European Synchrotron Radiation Facility (SA-ESRF) Light Source Conference & Workshop, Nov. 11-13, 2019, Johannesburg, South Africa.

Nkala, G. C., Billing, C., Billing, D. G. and Forbes, R. P. **(Poster)**
"**Studying the Effects of M^{4+}-Cationic Substitution (M = Ti, Sn, Hf) on the Ionic Conductivity of $LiTi_2^{(iv)}(PO_4)_3$**,"
Proceedings of the Annual CoE-SM / AMSEN Student Presentations, May 21, 2019, Johannesburg, South Africa

Workshops:

Recent Advance in Electronic Structure – Rehr Research Group

Department of Physics, University of Washington, Seattle, U.S.A, Jun. 4-13, 2022

Description: Determining the local and electronic structure of Al, Dy co-doped NASICON-type $LiTi_2(PO_4)_3$ through experimental and theoretical Dy L3-edge XAS analyses.

XAFS 2021 Short Course [Online]

Brookhaven National Laboratory, Nov. 17- 19, 2021

Description: Introduction to X-ray Absorption Fine Structure.

2021 APS/IIT XAFS Virtual Summer School [Online]

Advanced Photon Source/Illinois Institute of Technology, Aug. 1- 4, 2021

Description: Fundamental and practical aspects of X-ray Absorption Fine Structure Spectroscopy.

Pine Research EIS Webinar Series [Online]

Pine Research, Feb. 17- Mar. 17, Jun. 9, Sep. 15, 2021

Description: 5-part webinar series on Electrochemical Impedance Spectroscopy covering theory, data processing and advanced circuit fitting of EIS data.

X-ray Absorption Spectroscopy (XAS) 2020 Workshop

Diamond Light Source, Mar. 10 - 12, 2020

Description: Brief introduction to XANES spectroscopy, with a focus on the processing and analysis of EXAFS data, from a "starting from scratch" level.

African Neutron and Synchrotron Data Analysis Competency (ANSDAC) Workshop

University of Cape Town, Nov. 27 – Dec. 7, 2018

Description: Workshop aimed at developing expertise among emerging Africa-based researchers on theory and data analysis of synchrotron and neutron-based techniques, e.g., X-ray and neutron diffraction (XRD, ND), pair distribution function (PDF), and XAS.

Applications of Synchrotron and Electron-Based Techniques Course [Online]

Brookhaven National Laboratory, Jan. - May 2018

Description: 12-part lecture series on advanced synchrotron and electron-based techniques and their applications to materials studies in various scientific disciplines.

TABLE OF CONTENTS

DECLARATION ... ii

ABSTRACT ... iii

DEDICATION ... iv

ACKNOWLEDGEMENTS ... v

CONFERENCES & WORKSHOPS ... vii

LIST OF FIGURES ... xii

LIST OF TABLES ... xvi

LIST OF ABBREVIATIONS ... xix

LIST OF EQUATIONS ... xxi

Chapter 1: Introduction & Literature Review ... 1

1.1. The viability of renewable energies in South Africa ... 1

1.1.1. Waste-to-energy conversion ... 3

1.1.2. Solar energy ... 4

1.1.3. Wind energy ... 4

1.2. All-solid-state batteries in energy storage ... 5

1.2.1. An overview of ceramic solid-state electrolyte candidates ... 5

1.2.2. Determining cation migration mechanisms through structural characterization 11

1.3. Aims and Objectives ... 14

1.4. Thesis outline ... 15

1.5. References ... 16

Chapter 2: Experimental Synthesis and Characterisation Methods ... 24

2.1. Synthesis of NASICON-type $LiTi_2(PO_4)_3$-based systems ... 24

2.2. Materials characterization techniques ... 25

2.2.1. Powder X-ray diffraction (PXRD) ... 25

2.2.2. The Rietveld approach to structural analysis ... 29

2.2.3. Atomic Pair distribution function (PDF) ... 33

2.2.4. Raman spectroscopy (RS) ... 34

2.2.5. X-ray absorption spectroscopy (XAS) ... 35

2.2.6. Electrochemical impedance spectroscopy (EIS) ... 41

2.3. References ... 46

Chapter 3: Exploring the structure-property relationships in Sn-substituted $LiTi_2(PO_4)_3$ ... 51

3.1. Introduction ... 51

3.2. Experimental section ... 53

3.2.1. Synthesis ... 53

3.2.2. Characterization 53
3.3. Results and Discussion 55
3.3.1. Powder X-ray Diffraction (PXRD) 55
3.3.2. Room-temperature Raman spectroscopy (RS) 59
3.3.3. Probing the local and medium-range structure: Ti K-edge X-ray absorption spectroscopy (XAS) 61
3.3.4. Ambient-temperature conductivity studies 69
3.4. Conclusions 73
3.5. References 74
3.6. Supplementary information 79
Chapter 4: The enhancement of ionic conductivity of NASICON-type $LiTi_2(PO_4)_3$ by formation of Al, Sn and Al, Dy co-doped systems 90
4.1. Introduction 90
4.2. Experimental section 91
4.2.1. Synthesis 91
4.2.2. Characterization 92
4.3. Results & Discussion 93
4.3.1. Crystal structural analysis through synchrotron PXRD 93
4.3.2. Raman spectroscopy 95
4.3.3. Atomic pair distribution function: unravelling site preference in doped systems 97
4.3.4. Qualitative analysis of Ti K-edge XANES 100
4.3.5. Ionic conductivity enhancement induced by co-doping. 101
4.4. Conclusions & Recommendations 104
4.5. References 105
4.6. Supplementary Information 108
Chapter 5: On the average, local and electronic structure of NASICON-type $Li_{1.3}Al_{0.25}Dy_{0.05}Ti_{1.7}(PO_4)_3$ (LADTP) solid-state electrolyte 116
5.1. Introduction 117
5.2. Experimental Section 119
5.2.1. Synthesis 119
5.2.2. Characterization 119
Results & Discussion 122
5.3.1. Synchrotron powder X-ray diffraction (SXRD) 122
5.3.2. Raman spectroscopy 123
5.3.3. Small-box modelling of pair distribution function (PDF) 125
5.3.4. Analysing the local structure of LADTP using XANES 128
5.4. Conclusions 135

5.5. References 136
5.7. Supplementary Information 141
References 146
Chapter 6: General Conclusions & Recommendations 147
6.1. General Conclusions 147
6.2. Recommendations 149
6.3. References 151

LIST OF FIGURES

Figure 1.1. A schematic of an all-solid-state battery. Example compounds are given for each component; the negative anode is lithiated graphite (LiC_6), ref the electrolyte is the NASICON-type $LiTi_2(PO_4)_3$ (LTP), while the positive cathode is $LiFePO_4$. The **Li** atoms are **green**, **C** are **brown**, **Ti** are **blue**, **P** are **purple**, **Fe** are **yellow**, with **O** atoms being **red**.

Figure 2.1. Exemplary data of PXRD patterns of LTP were measured using a) lab-based and b) synchrotron-based instrumentation.

Figure 2.2. The Rietveld refinement result of the Si 640d CRM synchrotron PXRD pattern.

Figure 2.3. Energy level diagrams demonstrating the principles of a) Raleigh (elastic) scattering and b) Stokes Raman (inelastic) scattering.

Figure 2.4. An exemplary Ti K-edge XAS normalized XAS spectrum showing the pre-edge peaks (zoomed inset) and the dotted lines denoting the XANES and EXAFS regions.

Figure 2.5. The interference pattern generated by the interactions between the absorber and nearest neighboring scattering atoms, demonstrating the EXAFS phenomenon.

Figure 2.6. The Ti K-edge XAS data demonstrates the pre- and post-edge functions normalization procedure.

Figure 2.7. A Kramers-Kronig EIS data validity assessment for LTP synthesized via the solid-state reaction at 900 °C where (a) the full dataset was used and (b) the low-frequency data were excluded. The experimental data is shown as blue dots, while the fit is shown as a red line.

Figure 3.1. Unit cell depiction of the NASICON-type $LiTi_2(PO_4)_3$ belonging to the *R-3c* space group. It consists of Ti/SnO_6 octahedra corner-linked to PO_4 tetrahedra. Li^+ occupies M1.

Figure 3.2. A zoomed-in depiction of the lateral faces of LiO_6 octahedra. Highlighted in blue is the bottleneck formed by three O atoms (blue triangles), going into the M2 void.

Figure 3.3. XRD patterns of the NASICON-type Sn^{4+}-doped materials $LiTi_{2-x}Sn_x(PO_4)_3$ (for 0, 2, 4, 6, 8, 10 and 50 mole % Sn^{4+}).

Figure 3.4. The variation of cell volume with increasing Sn^{4+} content in NASICON-type $LiTi_{2-x}Sn_x(PO_4)_3$. A linear trend is observed for LTP to 6% Sn-LTP. The [Sn^{4+}] incorporated into LTP was determined to be 38.34% using the standardless Rietveld phase analysis methodology, with a corresponding cell volume of 1334.28 $Å^3$.

Figure 3.5. A Rietveld refinement result of 50% Sn-LTP and zoomed inset showing the presence of two isostructural phases, $LiTiSn(PO_4)_3$ (Sn-LTP) and $LiSn_2(PO_4)_3$ (LSP).

'Observed' = Experimental data; 'Calculate' = Theoretical data obtained from the input structures.

Figure 3.6. Raman spectra of Sn^{4+}-LTP electrolyte materials recorded at room temperature with an excitation wavelength of 514 nm.

Figure 3.7. Normalized Ti K-edge XANES spectra of Sn-LTP compositions synthesized at 900 °C. The zoomed inset shows the pre-edge features. The spectrum for TiO_2 (Degussa P-25; anatase: rutile = 87:13) is included for reference.

Figure 3.8. The splitting of atomic d-orbitals in the presence of a ligand field with different distortions.

Figure 3.9. A magnified view of the near-edge region of normalized XANES spectra of the Ti K-edge, for Sn-LTP formulations.

Figure 3.10. Ti K-edge: (a) Stacked $k^2\,\chi(k)$ data and (b) Fourier-transformed (FT) k^2 weighted EXAFS spectra for Sn-LTP compositions (no phase correction). Highlighted peaks correspond to the Ti-O single scattering, Ti-P single scattering and Ti-O-P multiple scattering shells.

Figure 3.11. Fitted Nyquist plots for Sn^{4+}-LTP phases (0-10, 50 mole % Sn^{4+}) and the EC model used in data fitting.

Figure S3.1. Rietveld refinement results for Sn-LTP compositions (a) LTP, (b) 2% Sn-LTP, (c) 4% Sn-LTP, (d) 6% Sn-LTP, (e) 8% Sn-LTP and (f) 10% Sn-LTP, showing the absence of the isostructural LSP phase. 'Observed' = Experimental data; 'Calculate' = Theoretical data obtained from the input structures.

Figure S3.2. Laboratory PXRD pattern of TiO2 Degussa P-25 standard, with Rietveld refinement as implemented on Topas ACADEMIC based on the tetragonal anatase (ICSD 9852) and rutile (ICSD 121630) structures, used in the Ti K-edge XAS analysis.

Figure S3.3. The k^2 weighted kR plots of the EXAFS fits for Sn-LTP formulations for (a) LTP, (b) 2% Sn-LTP (c) 4% Sn-LTP, (d) 6% Sn-LTP, (e) 8% Sn-LTP, (f) 10% Sn-LTP and (g) 50% Sn-LTP.

Figure 4.1. Synchrotron PXRD patterns for variously doped NASICON-type LTP systems.

Figure 4.2. Raman spectra of variously doped NASICON-type LTP systems. The spectra for LADTP and LATP were scaled by 0.5 and 5, respectively, for better visual comparison.

Figure 4.3. (a) Stacked X-ray atomic PDFs of variously doped NASICON-type LTP systems. The zoomed inserts represent the M-M interatomic distances at approximately (b) 5 Å and (c) 6 Å, showing lattice site preference.

Figure 4.4. A unit cell depiction of the lattice site preference because of Ti replacement with smaller Al^{3+} and larger Sn^{4+} and Dy^{3+}. The Al^{3+} occupies the 12*c* site at 5 Å, while the larger Sn and Dy cation occupy 12*c* sites further from the adjacent Ti at 6 Å.

Figure 4.5. Normalized Ti K-edge XANES spectra of variously doped NASICON-type systems. The respective spectra were shifted along the y-axis for clarity.

Figure 4.6. Experimental Nyquist impedance plots of NASICON-systems.

Figure S4.1. Rietveld refinement result of LTP.

Figure S4.2. Rietveld refinement result of LATP.

Figure S4.3. Rietveld refinement result of LATSP.

Figure S4.4. Rietveld refinement result of LADTP.

Figure S4.5. Simulated PDF of the ordered LTP (R-3c) structure, with accompanying atom-atom interaction partials.

Figure 5.1. The Rietveld refinement result of synchrotron XRD data of the Al, Dy co-doped LADTP system, indexed to the rhombohedral NASICON-type structure (space group *R*-3*c*) (blue circles = observed data, red line = calculated model, and grey line = difference).

Figure 5.2. The vibrational spectrum of LADTP, analogous to the rhombohedral *R*-3*c* space. group of NASICON-type LTP. The asterisk represents the PO_4 stretching mode of $DyPO_4$ in the $I4_1/amd$ space group setting.

Figure 5.3. Small-box modelling of LADTP G(r) in the range 0.75 – 50 Å, using the rhombohedral *R*-3*c* model obtained from XRD (Rw = 32.8%) (blue circles = observed data, red line = calculated model and green line = difference).

Figure 5.4. (a) Small-box modelling of LADTP using the β-$Fe_2(SO_4)_3$-type monoclinic (space group $P2_1/n$) model in the 0.75 to 10 Å range, Rw = 3.96%, (b) unit cell depiction of the NASICON-type LTP, based on the structure by Aatiq *et al.*,[22] and (c) unit cell depiction of the adapted β-$Fe_2(SO_4)_3$-type structure by Aono *et al.*[40] Both structures consist of TiO_6 octahedra (blue), corner-linked to PO_4 tetrahedra (purple).

Figure 5.5. Normalized experimental and computational Dy L_3-edge XANES spectra of Dy_2O_3 standard and LADTP. The computational spectrum of LADTP is made up of approximately 60% Dy_2O_3 (*Ia*-3), 35% $DyPO_4$ ($I4_1/amd$) and 5% $DyPO_4$ ($P2_1/n$).

Figure 5.6. Theoretical L_3-edge XANES spectra of Dy in a 12*c* site in the rhombohedral *R*-3*c* NASICON-type main phase, a 4*a* site in the tetragonal $I4_1/amd$ structure obtained from the PXRD-detected secondary phase, and the 4*e* site in the monoclinic $P2_1/n$ structure obtained from PDF.

Figure 5.7. Computational spectrum of cubic Dy_2O_3 (space group *Ia*-3) computed using two sites 8*b* and 24*d* with a 25:75 ratio to preserve stoichiometry. The localized Dy absorber *p*, *d* and *f*-DOS are also presented.

Figure 5.8. Dy-Dy interactions in (a) LADTP with an indirect line of site at 5.42 Å apart and (b) Dy_2O_3 with a direct line of site at 3.52 Å apart. The individual atoms are as follows: oxygen = red, lithium = turquoise, phosphorus = purple, dysprosium in LADTP = blue and dysprosium in Dy_2O_3 = green.

Figure 5.9. Comparison of computational Dy_2O_3 Dy L_3-edge XANES spectra, with that of an *Ia*-3 Dy-only system, showing (a) feature 'c' as Dy-Dy interactions and (b) feature 'd' as Dy-O interactions.

Figure 5.10. Comparison of experimental and computational Dy_2O_3 XANES spectra, showing the effect of Dy-O bond distance on the position of feature 'd' at ~7829 eV (marked).

Figure S5.1. Laboratory PXRD pattern of Dy_2O_3 standard, with Rietveld refinement as implemented on Topas ACADEMIC based on the cubic *Ia*-3 structure (ICSD 66736).[1]

Figure S5.2. Results from structure mining for G(r) for experimental LADTP refined against $LiTi_2(PO_4)_3$ (space group *R*-3*c*) (COD 722215/ ICSD 95979).[2] Experimental data = blue, calculated data = red, difference = black (Rw = 29.8%).

Figure S5.3. The small-box modelling of LADTP using the NASICON-type *R*-3*c*, $AlPO_4$ *C*2221 and $DyPO_4$ $I4_1/amd$ crystalline phases detected from PXRD (Rw = 28.053%).

Figure S5.4. Stacked LDOS of Dy_2O_3 in *Ia*-3 space group, showing the effect of increasing Dy-O bond distance in the first shell on the spread of *d*-DOS.

LIST OF TABLES

Table 1.1. Some classes of ceramic-based solid-state electrolyte materials and their respective conductivities.

Table 1.2. A non-exhaustive list of variously doped LTP systems and their respective ionic conductivities at room temperature.

Table 1.3. The respective chemical shifts of Li, Al and P in LATP NASICON-type rhombohedral (*R*-3*c*) pristine sample.[55, 76]

Table 2.1. A comprehensive list of all compositions synthesized in this work, showing the relevant chapters and the dopant %.

Table 2.2. Instrumental and data collection information of the laboratory-based Bruker D2 Phaser diffractometer.

Table 2.3. Instrumental and data collection information of the 28-ID-1 (Pair Distribution Function) beamline at National Synchrotron Light Source II (NSLS-II), Brookhaven National Laboratory, Upton, New York, USA. The reported values were those used in this work.

Table 2.4. Crystallographic data for the Si 640d CRM from Rietveld refinement of synchrotron XRD results (28-ID-1 at NSLS-II, 0.16635 Å).

Table 2.5. Figures of merit used in reporting and assessing the quality of Rietveld refinement fits.

Table 2.6. Parameters used in the measurement and analysis of EIS and their corresponding units of measurement.

Table 2.7. Kramers-Kronig fit results for LTP using the full data set and without the low-frequency region.

Table 3.1. The lattice parameters of undoped and Sn^{4+}-doped LTP phases, obtained from XRD, via Rietveld refinement (as implemented in TOPAS-Academic).

Table 3.2. EXAFS fit results for Sn-LTP compositions. The amplitude reduction factor S_0^2 was kept constant at 0.786. The coordination numbers (*N*) were also kept fixed as per the published structure of LTP. *R* the radial distance, σ^2 the Debye-Waller factor, and ΔE_0 is the shift in the edge energy. The R-factor determines the quality of the fit.

Table 3.3. The room temperature conductivity results for Sn^{4+}-substituted NASICON-type LTP formulations. The 8% Sn formulation showed the highest bulk and grain boundary conductivities, while 50% Sn-LTP showed the highest total conductivity (highlighted)

Table 3.4. The changes in Li-O2 bond lengths, M1 void volume, V_{M1}, and Ti/SnO_6 (V_{MO6}) octahedral volumes obtained from Rietveld refinement results for Sn-LTP compositions.

Table S3.1. Crystallographic data for Sn-LTP systems synthesized at 900 °C via the solid-state method.

Table S3.2 Raman band assignments for Sn-LTP systems synthesized at 900 °C via the solid-state method.

Table S3.3. Crystallographic data for TiO_2 Degussa P-25 from Rietveld refinement of laboratory PXRD results (D2 Phaser, Co Kα) in the range 10 to 90° 2θ.

Table 4.1. Structural information obtained from Rietveld refinements of synchrotron XRD data for various NASICON-type systems.

Table 4.2. Quantitative phase compositions of NASICON-based systems.

Table 4.3. The room-temperature conductivity values obtained from fitting the EIS experimental data for NASICON-type systems.

Table S4.1. Crystallographic data for LTP from Rietveld refinement of synchrotron XRD results (28-ID-1 at NSLS-II, 1.6635 Å).

Table S4.2. Crystallographic data for LATP from Rietveld refinement of synchrotron XRD results (28-ID-1 at NSLS-II, 1.6635 Å).

Table S4.3. Crystallographic data for LATSP from Rietveld refinement of synchrotron XRD results (28-ID-1 at NSLS-II, 1.6635 Å).

Table S4.4. Crystallographic data for LADTP from Rietveld refinement of synchrotron XRD results (28-ID-1 at NSLS-II, 1.6635 Å).

Table S4.5. Raman spectroscopy peak assignments for NASICON-type systems.

Table S4.6. The expected Raman spectroscopy peaks for the $AlPO_4$ cristobalite ($C222_1$)secondary phase observed in Al-bearing NASICON-type compositions. The last column presents whether the expected $AlPO_4$ phase peaks are observed in the measured NASICON spectra.

Table 5.1. Comparison of Rietveld refinement-obtained structural parameters for LADTP and literature-reported LTP and LATP systems both indexed to the rhombohedral NASICON structure (*R*-3*c*). The contraction and expansion % (shown in parentheses) correspond to the change from LTP.

Table 5.2. Quantitative results of WL peak fitting for experimental and computational spectra of Dy_2O_3 and LADTP.

Table S5.1. Crystallographic data for LADTP from Rietveld refinement of synchrotron XRD results (28-ID-1 at NSLS-II, 1.6635 Å).

Table S5.2. Structural parameters of LADTP deduced from Rietveld refinement of synchrotron XRD.

Table S5.3. Raman spectroscopy peak assignment for the NASICON-type rhombohedral LADTP system.

Table S5.4. Crystallographic data for Dy_2O_3 from Rietveld refinement from laboratory PXRD results (D2 Phaser, Co Kα) in the range 10 to 120° 2θ.

Table S5.5. The M-O distances in various Dy-bearing compositions obtained via Rietveld refinement of PXRD data, as implemented on TOPAS-Academic.

LIST OF ABBREVIATIONS

MW: mega Watt

GDP: gross domestic product

GHGs: greenhouse gases

GWh: giga Watt hour

RE: renewable energy

IRP: integrated resource plan

MWh: mega Watt hour

EPR: extended producer responsibility

GIS: geographical information systems

LIBs: Lithium-ion batteries

EVs: electric vehicles

LISICON: Lithium Super Ionic conductor

NASICON: Sodium Super Ionic conductor

LTP: Lithium titanium phosphate

LZP: Lithium zirconium phosphate

LSP: Lithium tin phosphate

LHP: Lithium hafnium phosphate

LATP: Lithium aluminium titanium phosphate

PXRD: Powder X-ray diffraction

NPD: Neutron powder diffraction

SS NMR: Solid-state nuclear magnetic resonance

PDF: Pair distribution function

AIMD: *ab initio* molecular dynamics

DFT: density functional theory

LGP: lithium germanium phosphate

XAS: X-ray absorption spectroscopy

PSD: position sensitive detector

NSLS-II: National Synchrotron Light Source II

ICSD: Inorganic crystallographic structure database

COD: crystallography open database

NIST: National Institute of Standards and Technology

CRM: certified reference materials

CIF: crystallographic information file

CCD: charge-coupled detector

XANES: X-ray absorption near-edge spectroscopy

EXAFS: extended X-ray absorption fine structure

EIS: electrochemical impedance spectroscopy

MPa: mega Pascals

mV: milli Volts

eV: electron Volts

MHz: mega Hertz

DC: direct current

LATSP: Lithium aluminium titanium tin phosphate

LADTP: Lithium aluminium dysprosium titanium phosphate

LIST OF EQUATIONS

Equation 1 33
Equation 2 33
Equation 3 33
Equation 4 36
Equation 5 38
Equation 6 39
Equation 7 39
Equation 8 42
Equation 9 42
Equation 10 42
Equation 11 42
Equation 12 42
Equation 13 42
Equation 14 42
Equation 15 43
Equation 16 43
Equation 17 44
Equation 18 44
Equation 19 69
Equation 20 69

Chapter 1: Introduction & Literature Review

1.1. The viability of renewable energies in South Africa

Coal supplies approximately 77% of South Africa's energy and more than 85% of its electricity.[1] Although coal is the primary source of energy, fossil fuel combustion continues to be detrimental to the environment. Coal and other fossil fuels produce carbon dioxide, amongst other gases, during energy production, which results in global warming, air pollution and acid rain.

Due to the growing economy and an increase in population in South Africa, the supply-demand balance has been offset. To handle the load on the national electrical grid, Eskom, the country's publicly-owned power utility generating approximately 95% of the country's electricity,[2] embarked on the construction of multi-billion-rand coal power plants. The construction of the 4767 and 4800 MW Medupi and Kusile coal-fired power stations would have been a milestone in the nation's energy sector as well as in presenting potential employment opportunities for the skilled youth as it would have been a source of more much-needed power to maintain homes and industries. Unfortunately, this venture resulted in cost overruns which resulted in delays of the entire project. One of the stated reasons behind the delay in project completion was as a result of the lack of adequate skills and their availability. The updated timeline for the operation of two power stations has now been revised to 2023 for Medupi and 2026 for Kusile.[3]

South Africa has an energy-intense economy, with the mining industry as one of the biggest contributors to the country's gross domestic product (GDP) at 21 % in the 1980s to a low 8 % in 2016.[4] The implemented power cuts in recent years have had adverse effects in the total mineral outputs, and by extension, the GDP contribution of the mining sector. Load shedding continued to plague the daily running of industries thus costing the country between R20 billion and R80 billion per month.[5, 6]

The effects of the delayed power plants have resulted in the country having to explore other means of generating electricity, such as renewable energy sources energies. The relatively lower prices for renewable power have probed an increasing interest in the subject hence an increased interest in investment, globally. The scientific community's interest in renewable energies puts South Africa at a point where the renewables are cheaper than the coal-based power. The new wind and solar power source initiatives have been estimated to be 20% cheaper than Eskom's coal-based 2016/17 electricity price.[7]

In a study conducted by Meridian Economics,[8] on Eskom's financial crisis and the viability of the new power plants, it was found that the use of alternative energy sources could meet Eskom's demand over the same period at a relatively cheaper cost than that of the energy that would be obtained from the new power plants through fossil fuel combustion.[9] The study concluded that it would, therefore, be more economically logical to consider other means of energy generation instead of continuing with the construction of power plants. This speaks to the importance of renewable energy and its potential economic impacts.[10-11]

The continued use of coal as a primary source of energy has rendered South Africa the 14th largest emitter of greenhouse gases (GHGs), accounting for 34% of Africa's emissions.[1]

The government's drive to introduce renewable energies was not only propelled by the need to decrease South Africa's carbon footprint but also favored by the constitution. Act No. 108 of 1996,[14] states that the government is to provide adequate and clean energy to all citizens regardless of their geographical location. Part of the Government's objectives to fulfil the Constitution was to address constraints on the development of renewable energy technologies in the industry, as well as ensure that there is liberalization of state-owned entities (Eskom) to encourage the energy mix.

The three energy policy documents that have shaped the energy sector are as follows:

- White Paper on Energy Policy (1998),[15]- this was solely based on satisfying the objectives of the constitution, wherein the Government had to provide safe, reliable and sustainable energy for all. This was after the 1996 shift towards democracy.
- Renewable Energy (RE) White Paper (2003),[15] – Although SA predominantly depended on coal as a source of energy due to its abundance (as well as its significant contribution to the nation's GDP), the rising concern towards the deteriorating health of the lower-class regions and the environmental effects of coal combustion further stimulated the need for alternative sources of energy. Target: 10 000 GWh by 2013
- National Climate Change Response Policy White Paper (2011),[15] – SA's energy-intensive economy resulted in SA having one of the largest CO_2 production per capita, resulting in the country having to commit to a much cleaner energy climate. The increase in the amount of RE integrated into the energy flow further increased the attention, hence further attracting investments both at a local and international level. Copenhagen Agreement: SA to reduce emissions by 34%.

The second level of implementation of the RE policy was based on the Integrated Energy Plan and Integrated Resource Plan (IRP).[16] The IRP was a 20-year plan that focused on the development of the correct energy mix as well as a delivery timeline. IRP 2010 was a 2010-2030 plan that aimed at increasing the energy mix to having 26% energy contribution coming from RE sources. To this end, three renewable energy sources are briefly discussed below, in the South African context.

1.1.1. Waste-to-energy conversion

The generation of approximately 122 million tons of waste per annum in South Africa has posed a significant threat to the environment and society.[17] The amount of generated waste in South Africa is projected to yield about 6.1 billion m^3 of methane (CH_4) gas under standard conditions of 273 K and 1 atmospheric pressure, which results in at least 528.7 MWh per annum of electricity.[18]

The decomposition of waste at landfills produces approximately 50-60% methane gas (CH_4), amongst others.[19] Also, leachates from waste degradation pollute the underground water systems, infringing on the constitutional rights to clean and safe water and the environment. South Africa's fast running out of landfill air space is attributed to population growth and urbanization, and existing landfills are regarded as non-compliant.

As such, the promulgation of the Extended Producer Responsibility (EPR) regulation,[22] as an extension to the National Waste Management Strategy,[21] has placed obligations on industries and consumers to find alternative beneficiation strategies to landfilling, for their waste in contribution to the circular economy. The EPR regulation places the responsibility of a product's end-of-life treatment on the producer who places the product on the market.[22] The circular economy encourages the minimal harvesting and use of raw materials by collecting and recycling certain waste streams (e.g., glass, plastics, electronic waste and paper and paper packaging) into the manufacturing of new products. This significantly decreases the contributions of yielding raw materials to the manufacturing process' environmental and economic costs. Proposed technologies for harnessing energy from waste are anaerobic digestion and microbial fuel cells. Microbial fuel cells have been reported to have higher energy recovery efficiency from waste, than anaerobic digestion.[23-24] Therefore, the large-scale applicability of these methods is a point for further research.

1.1.2. Solar energy

South Africa has an average daily direct normal radiation above 7 kWh/m^2, implying that solar energy is the most readily available source of renewable energy. Research has been conducted to determine the feasibility of solar power in South Africa. In one case study, Geographical Information System (GIS) was used as a tool to find the most viable provinces in which solar power plants could be built. Factors such as solar resources, proximity to transmission lines, land use profile and slope were taken into consideration. The study found that the Northern Cape was the most suitable province, with a potential output of 510.3 GW of power. Other provinces were identified as follows: Free State, Western Cape and Eastern Cape, each with potential outputs of 25.3, 10.5 and 1.6 GW, respectively. One needs to consider that the plants will not run at nominal capacity all year round, but instead, with a capacity factor of 40%.[25] One of the major drawbacks of solar power has been that of expensive energy storage systems because of their limited life span.[26] Also, thorough investigations need to be carried out to assess areas that would be best suitable for the construction of transmission lines from areas of energy generation to main electricity consumer centres.[11]

1.1.3. Wind energy

Wind energy has been shown to be one of the most viable sources of renewable energy. South Africa has average wind speeds of 7 m.s^{-1} in some coastal and escarpment regions. Wind energy would be applicable in South Africa due to the extensive coastlines and lowland escarpment. This has only been found to be practical in the Eastern and Western Cape provinces.[26] Two of the existing wind farms, Klipheuwel and Darling farms, each contribute 3.2 and 5.2 MW, respectively. The Klipheuwel farm served to demonstrate the possibility of harnessing wind for its inclusion in the energy mix. Although the Klipheuwel wind farm contributed to the energy capacity at Eskom, three wind turbines at this farm have since been decommissioned as of July 2016, owing to the completed construction of the Sere wind farm in the Western Cape (producing 100 MW of energy). The Darling Wind Farm Company, the first independent power producer, provides energy to the City of Cape Town, following a 20-year power purchase agreement.[27] Wind and solar power remain applicable in South Africa for integration into existing methods of generating energy. As it was alluded to earlier, investigating and improving means of renewable energy storage remains one of the core areas of interest in scientific research in South Africa.

1.2. All-solid-state batteries in energy storage

1.2.1. An overview of ceramic solid-state electrolyte candidates

Current research is based on finding materials that are capable of harnessing renewable energy, with the focus being the development of better energy storage materials and exploring ways in which lower-cost batteries can be synthesized. As some of the renewable energy sources have been discussed, it follows that if South Africa is to have a smooth transition towards higher inclusion of RE in the energy mix, efficient energy storage systems are required. It has been posited that for grid-level energy storage, redox flow batteries are a suitable candidate.[28] These are external energy storage devices have been reported to offer flexible and independent scalability in order to increase their capacity, better operational lifespan. Redox flow batteries involve the storage of liquid electrolytes in external tanks that are only pumped through the cell during the charge-discharge process. During charging, electrical energy is converted to chemical energy upon oxidation and reduction occurring at the anode and cathode, respectively. The discharge state involves the conversion of chemical energy to electrical energy, also facilitated by the oxidation-reduction processes occurring at the electrodes. The changes in oxidation states of the electrolytes are what facilitates the charge and discharge states. These energy storage devices therefore provide a relatively stable power supply to supplement the national grid.

The current challenges around redox flow batteries are the need for improved ionic conductivity and energy density. Increasing their energy density has a direct impact on the associated costs, while an improved ionic conductivity can only be achieved through increased concentrations of the electrolyte transition metal salts in water. This also leads to increased viscosity and thus, poor conductivity. Therefore, it is imperative that research endeavors also focus on finding the right balance to achieve a higher ionic conductivity. The other challenge of redox flow batteries is that they are more suitable for fixed installations, instead of flexible, mobile installations which would be more suitable to address energy poverty in remote areas, due to their low energy density.[29]

Although redox flow batteries have been studied and are currently being applied in other countries for grid energy storage, their limited energy efficiency affects their worldwide large-scale implementation. As such, lithium-ion batteries (LIBs) remain a worthy candidate.

The motivations for alternative energy storage systems are that the most widely used rechargeable batteries contain toxic electrolytes such as sulfuric acid in lead acid batteries and lithium perchlorate in LIBs.[30] More prevalent organic electrolytes are typically mixtures of ethylene carbonate and propylene carbonate, amongst others.[31-32] The presence of these organic electrolytes poses a safety threat, due to the formation of Li dendrites, that penetrate the electrodes, resulting in the leakage of electrolyte solution into the rest of the battery components.[33] The organic electrolytes exhibit low thermal stability and flame points, making them susceptible to flammability.[34] The drawbacks of current LIBs are, amongst others, their costs and reliability concerns. These are attributed to the deterioration of battery devices over a short period. The constant replacement of these materials has negative environmental effects, and as such, research into recycling technologies of spent battery materials seek to address this gap.[35]

Alternative electrolyte materials have received great attention, more specifically solid-state electrolytes, for their applications in all-solid-state batteries. All solid-state batteries refer to energy storage devices wherein all components, i.e., the cathode, anode and electrolyte are all in the solid state. **Figure 1.1** shows a general schematic of an all-solid-state Li ion battery. Lithium-ion batteries are widely used in portable devices such as phones, tablets, and smart watches, along with electric vehicles (EVs). The mechanism of operation is as follows: during the discharge process, a redox process occurs, allowing the flow of electrons across the external circuit from the anode to the cathode, with Li cations also moving from the anode to the cathode, through the electrolyte.

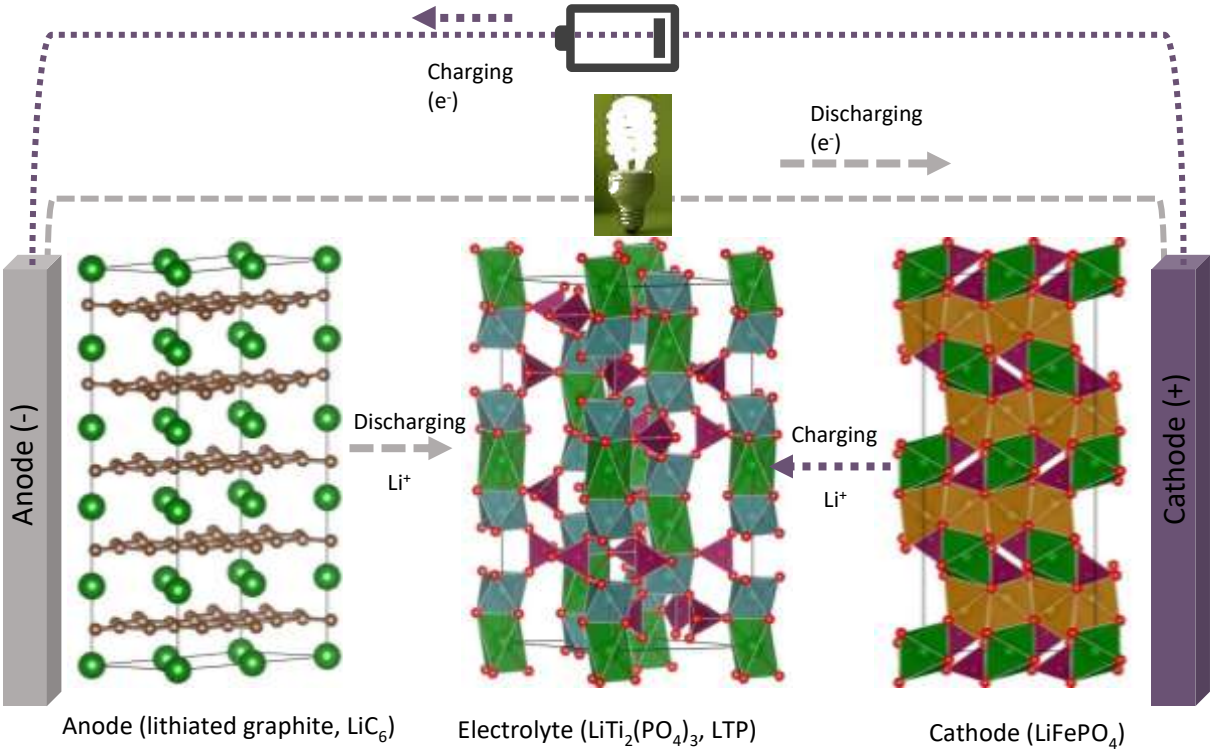


Figure 1.1. A schematic of an all-solid-state battery. Example compounds are given for each component; the negative anode is lithiated graphite (LiC_6), ref the electrolyte is the NASICON-type $LiTi_2(PO_4)_3$ (LTP), while the positive cathode is $LiFePO_4$. The **Li** atoms are **green**, **C** are **brown**, **Ti** are **blue**, **P** are **purple**, **Fe** are **yellow**, with **O** atoms being **red**.

Electrolytes determine the current (power) density, time stability and the safety of the battery as a whole.[36] The state-of-the-art liquid electrolytes are limited with regard to poor physical and chemical stability and their dependence on the formation of a solid electrolyte interface (SEI). The use of solid-state electrolytes would eliminate the need for a separator, avoid the use of organic electrolytes and therefore promote the use of safer batteries that do not pose any leakage risks.[37] An ideal solid-state electrolyte should possess properties such as chemical stability over the temperature range of operation for the battery, a transference number close to unity, wherein transference number is defined as the ratio of the Li^+ conductivity to the total conductivity in the electrolyte, it should be low cost and minimally toxic and exhibit electronic conductivity in the order of 10^{-10} S/cm, and an ionic conductivity that is greater than 10^{-4} S/cm. [32] The work by Sun,[38] delved into the challenges surrounding the application of all-solid-state batteries in EVs. In the work by Sun,[38] the challenges have been stated to be attributed to low ionic conductivity at operating temperatures, chemical and electrochemical stability, lack of understanding of interfacial mechano- and electrochemistry. Along with these challenges, the consistent call to action around existing research is in the development of novel systems (solid

electrolytes, cathode and anode materials) that can be applied to ASSBs in EVs, in alignment with other authors discussed in this study, in the field of ASSBs. Sun further highlights the need for structure-property analyses through a multiscale approach.

Extensive research has been conducted on ceramic materials meeting the above-stated criteria.[39] This work focuses on ceramic-type electrolytes. Li^+ ion conducting oxide electrolytes are further divided into:[40]

- Garnet-type
- Perovskite-type
- Anti-Perovskite-type
- Li superionic conductors (LISICON) type
- Na superionic conductors (NASICON) type
- Amorphous oxides

Table 1.1 provides a glimpse of the various oxide-based Li^+-ion conducting electrolytes that have been studied for their potential application as solid-state electrolytes. Their respective room temperature ionic conductivities are also given.

Table 1.1. Some classes of ceramic-based solid-state electrolyte materials and their respective conductivities.

Crystal structure	**Composition**	**Ionic Conductivity (S/cm)**
Garnet-type,[40-42]	$Li_7La_3Zr_2O_{12}$ (LLZO)	7.74×10^{-4}
Perovskite,[43]	$Li_{0.33}La_{0.56}TiO_3$	5.25×10^{-5}
Anti-Perovskites,[44]	Li_3OCl Li_3OBr	$> 10^{-3}$
LISICON,[45]	$Li_{3.55}(Ge_{0.45}Si_{0.10}V_{0.45})O_4$	5.8×10^{-5}
NASICON,[46]	$Li_{1.3}Al_{0.3}Ti_{1.7}(PO_4)_3$	7×10^{-4}

NASICON (Na Super Ionic Conductor) materials of formula $Na_{1+x}Zr_2P_{3-x}Si_xO_{12}$ ($AM_2(PO_4)_3$; A = Li, Cu, Ag; M = Ti, Ge, Hf, Zr and x = 0) have attracted great attention as solid-state electrolyte materials. These refer to a class of rigid structures that have the ability of 3D fast ionic transportation attributed to the mobility of A^+ cations through the interstitial sites of the crystal lattice. The crystal structure consists of chains of PO_4 tetrahedra that are corner-linked to MO_6 octahedra to form a helical structure extending along the z-axis.[30, 37] Li-based NASICON-type materials have been successfully synthesized and their electrical properties

established. The primary material LTP has been studied extensively in the past couple of years, and it has been found to have the ideal space group *R*-3*c*.[30, 47-49] One of the drawbacks of the analogous $LiZr_2(PO_4)_3$ (LZP), $LiSn_2(PO_4)_3$ (LSP) and $LiHf_2(PO_4)_3$ (LHP) materials is that they tend to exhibit a temperature-dependent polymorphism.

This change in the crystal structure with temperature results in varying voltage outputs and ionic conductivities, thus making the materials unsuitable for applications as solid-state electrolytes, if the temperature of the phase change is within the operating temperature range of the device. [30, 50-53]

Although the NASICON-type structure can readily be substituted at the A, M and P sites, the variation in ionic radii of the substituent cations alters the size of the migration channels for A-ion hopping, thus also affecting the ionic conductivity. Aono *et al.*,[54] found that the highest conductivity was displayed by LTP which showed the best size match between the Ti-bearing phosphate framework and the Li mobile cation. Although these 3D structures have the potential for fast ionic migration, they display ionic conductivities in the order of 10^{-7} S/cm, relatively poorer than what is desired (10^{-4} S/cm) for solid-state electrolytes. Therefore, various strategies have been employed to improve the ionic conductivity at room temperature, namely: improving the bottleneck size by replacing Ti^{4+} with ions of larger radii, and ii) increasing the amount of Li^+ migratory species through replacement of Ti^{4+} with aliovalent cations. As such, an extensive list of aliovalent and isovalent cations have been applied to try and improve the conductivity of Li^+ at room temperature, shown in **Table 1.2**, and subsequently briefly reviewed.[32, 36]

Table 1.2. A non-exhaustive list of variously doped LTP systems and their respective ionic conductivities at room temperature.

Doping strategy	**Dopants used**	**Ionic conductivity (S/cm)**
Singly doped	Al,[46]	7×10^{-4}
	Sc,[55] Fe, In,[56]	Sc (*R*-3*c*): 2.68×10^{-5} Fe (*Pbca*): 3.34×10^{-7}
	Mn,[57]	-
	Cr,[58]	4.41×10^{-7}
	In,[58]	8.30×10^{-6}
Doubly doped	Al, Nb,[59]	3.54×10^{-4}
	Al, Y,[60]	-
	Al, Sc,[61]	7×10^{-4}
	Al, Zr,[62]	7.9×10^{-4}
	Al, W,[63]	5.49×10^{-4}
	Al, Fe,[64]	1.1×10^{-3}
	Al, Cr,[64]	1.6×10^{-3}
	Ca, Fe,[65]	5.2×10^{-4}

Co-doping strategies, wherein Ti^{4+} is replaced with at least two other cations have also been applied at the Ti 12*c* site of the rhombohedral structure and have been reported to improve the conductivity of Li at room temperature. It has been reported that although LATP has been shown numerous times to be one of the most conductive NASICON systems, the reduction of Ti^{4+} to Ti^{3+} results in a redox reaction at 2.5 V against Li/Li. This leads to incompatibility with other low-potential anode material candidates attributed to increased resistance of the interface.[66-69] Systems doped with multiple cations (co-doped) such as $LiAl_xZr_yTi_{(2-x-y)}(PO_4)_3$ have also been reported to be a promising method of reducing the reduction of Ti^{4+} in LTP-type systems.[70]

1.2.2. Determining cation migration mechanisms through structural characterization

The mechanisms governing the improvement of ionic conductivity remain an active area of research. The application of various characterization techniques aids in this understanding, both from an experimental and first-principles perspective. The most widely used techniques in determining the average and local structure are powder diffraction methods based on both X-rays (powder X-ray diffraction, PXRD) and neutrons (neutron powder diffraction, NPD). Seeing how the ionic conductivity is largely dependent on the average structure and the percentage composition of secondary impurity phases, the analysis of diffraction data provides qualitative and quantitative insights into the phase compositions. The ionic conductivity at the grain boundaries is largely affected by the presence of secondary phases such as TiP_2O_7 and Al_2O_3. Therefore, determining the phase composition is of utmost importance.[71]

The application of neutron diffraction studies through difference Fourier maps has also been insightful in determining the average cationic distribution in solid ionic conductors.[72] In the case of NASICON-type LTP systems, the general proposed migration pathway for Li^+ in the rhombohedral NASICON structure is from the sites 6*b* to 18*e* and into the adjacent 6*b* sites (6b– 18*e* – 6*b*) along the *c*-axis. However, the migratory Li^+ cations were found to be distributed between the 6*b* and 36*f* sites in the rhombohedral structures (*R*-3*c*). The 36*f* sites were found to be more energetically favorable, resulting in faster cation movement (i.e., higher ionic conductivity). [73-75] This was the case in doped systems that have excess Li required for charge balance.

Solid-state nuclear magnetic resonance (SS NMR) around the Li (^{7}Li), Al (^{27}Al) and P (^{31}P) elements also provides information on the coordination environments that vary depending on the geometry around Li, Al and P, which can then be used to decipher the lattice sites occupied by these elements in the structure. The advantage of NMR is that the crystallinity (or lack thereof) of the sample is not a prerequisite, similar to PDF. SS NMR typically yields a single chemical shift for an element in a particular environment, as shown in **Table 1.3**. Different local order (geometry) around the nucleus of interest results in different chemical shifts, therefore this technique has been a useful complementary method for validating the occupied sites in NASICON-type solid-state electrolytes. The presence of Al in octahedral and tetrahedral environments results in the observation of peaks at -15 ppm and 40 ppm, respectively.

Since the replacement of Ti^{4+} by Al^{3+} happens at the 12*c* site (octahedral), the presence of a peak at 40 ppm is usually ascribed to the presence of the $AlPO_4$ secondary phase, typically obtained in LATP systems with more than 10% Al. For new sites of P, the peaks tend to move towards more positive chemical shifts, which may indicate the formation of a new, secondary phase.[55, 76] The presence of these secondary phases affects the cation migration, especially at the grain boundaries, resulting in the grain boundary conductivity being the rate-determining step.[77]

Table 1.3. The respective chemical shifts of Li, Al and P in LATP NASICON-type rhombohedral (*R*-3*c*) pristine sample.[55, 76]

Nucleus	**Wyckoff position in *R*-3*c***	**Approximate chemical shift (δ; ppm)**
^{7}Li	6*b* 36*f*	-1.2
^{27}Al	12*c*	-15 (octahedral) 40 (tetrahedral)
^{45}Sc	12*c*	17.5 (octahedral)
^{31}P	18*e*	-27.5

Raman spectroscopy provides a complementary analysis to that of diffraction and NMR methods in establishing the phase compositions, particularly the changes around the phosphate PO_4 and metal oxide MO_6 polyhedra. Computational and experimental vibrational spectra have been used successfully to assign the vibrational modes observed to the structure of materials that change depending on the chemical environments of atoms within the structure induced by various lattice site substitutions.[78] Infrared and Raman spectroscopy have been used to determine the presence of short-range static disorder, attributed to lattice site substitutions and the presence of Li in non-6*b* sites in rhombohedral NASICONs.[79-80] Since Li is typically found at the 6*b* site of the LTP rhombohedral structure, with a site symmetry of S_6, this atomic position is Raman-inactive.

Therefore, any changes in the site symmetry of Li to Raman-active sites due to distortions in the structure may be probed by Raman spectroscopy.

Although significant work has been done in the field of NASICON-type solid-state electrolytes in varying dopants to improve ionic conductivity, as well as characterization, the application

of techniques has been largely limited to those that have been briefly discussed in this section (i.e., PXRD, NPD, SS NMR, Raman and Infrared spectroscopy). The PDF remains an underutilized technique in the characterization of the local and medium-range structure of rhombohedral Li-NASICON systems. To our knowledge, only one study has been conducted that focused on the analysis of PDF data.[81] However, it is largely radial distribution functions stemming from *ab initio* molecular dynamics (AIMD) and density functional theory (DFT) that have been discussed.[82-83] In the work by Lang and colleagues,[84] the use of DFT determined the migration pathway of Li in doped NASICON-type LGP systems. The replacement of Ti by trivalent cations showed the occupation of the 36*f* site by Li in the *R*-3*c* structure, which was found to be more energetically favorable than the 18*e* site that had been previously proposed. This resulted in faster migration of Li^+ cations due to decreased activation energies, particularly around the dopant cations.

A more holistic approach to understanding the influence of structure on the properties of energy materials is obtained through the application of structural analysis probes at various length scales. To this effect, techniques such as the pair distribution function (PDF), both from X-rays and neutron large-scale facilities have been applied over a wide range of energy materials. Multiple studies have highlighted the limitations of conventional diffraction methods, which probe the long-range ordered structure, while the local structure is not confirmed. The application of PDF in unravelling the local structural phenomena has been used extensively in energy materials, showing the presence of distinct phases that are not detected through conventional diffraction methods and the deviation of a local structure from that detected from the average structure PXRD. In the perspective authored by Malavasi and references therein,[85] case studies relating to the application and importance of understanding the local structure, are given for oxide ion conductors and Li-ion battery materials. Sanchez *et al.*,[86] also applied PDF methods in detecting a glassy component in perovskite materials for photovoltaic applications and the presence of amorphous phases, which could not be detected from conventional diffraction methods such as PXRD. Proffen *et al.*,[87] studied the effects of Nb substitution in $SrTiO_3$ and $BaTiO_3$ compounds. The average structure of both systems at room temperature was found to be cubic *Pm*-3*m*, while the local structure investigations through PDF indicated a deviation of the Nb-doped $BaTiO_3$ system from *Pm*-3*m* to the rhombohedral *R*3*m* space group.

Another pertinent technique in the analysis of energy materials is X-ray absorption spectroscopy (XAS). XAS provides information on the local geometry and electronic structure around a specific element within a system. Similar to the PDF, XAS has no long-range order prerequisite, thus it can be used to probe the structure across crystalline, polycrystalline, nano and amorphous materials. XAS can also be applied in the structural determination of solids, liquids and gaseous state materials. This is particularly important in *in-situ* and *operando* studies of energy materials to track reaction mechanisms.[88] In our case, this thesis presents the analysis of NASICON-type structures from the perspective of Ti and Dy edges. In a recent review on XAS, Kerr *et al*., [89] highlights the application of XAS in determining the local structure of amorphous, crystalline, and mixed environment systems. It is imperative to establish oxidation states of solid-state systems, particularly in the case of Ti-bearing NASICONs, since the interaction between LTP and Li electrodes has been stated to induce a change in oxidation state for Ti (from Ti^{4+} to Ti^{3+}), which can affect the performance of the battery.[90] The K-edge spectra of transition metals, such as Ti, typically show pre-edge features attributed to the electronic transition from 1*s* to 3*d* states. The K-edge refers to the transition involving the excitation of innermost (1*s*) electrons surrounding the nucleus.[91] In-depth analysis of the pre-edge region provides systematic information on the effects of changes in the local environment and the degree of hybridization of the metal-oxygen moieties. These analyses are supported by computational XAS methods,[92] which provide assignments of spectral features from first principles.

Therefore, the primary focus of this thesis is on providing an in-depth analysis of the structure of various NASICON-type systems across various length scales, following techniques such as conventional X-ray diffraction (average), x-ray PDF with qualitative and small-box modelling methods (local atomic structure), and X-ray absorption spectroscopy (local geometry and electronic structure). These structural characterization methods provide insights into the factors that may govern changes in the observed room temperature Li^+ ionic conductivities. The background of these techniques is discussed in relatively more detail in **Chapter 2**, displaying how they have been applied to the characterization of LTP-based systems in the subsequent results chapters.

1.3. Aims and Objectives

Understanding the structure-property correlations in materials for potential use in solid-state batteries remains important in influencing the design of these materials. To this effect, variously doped LTP-based NASICON solid-state electrolytes have been synthesised

following the conventional solid-state reaction mechanism and the objectives of this work are as follows:

i) Proof of concept through synthesising Sn-doped LTP-based systems at 900 °C and characterization of the average and local structure, along with the thermal stability and ionic conductivity at ambient temperature.

ii) Preparation of novel Al, Sn ($Li_{1.2}Al_{0.2}Ti_{1.7}Sn_{0.1}(PO_4)_3$, LATSP) and Al, Dy ($Li_{1.3}Al_{0.25}Dy_{0.05}Ti_{1.7}(PO_4)_3$, LADTP) co-doped systems with improved ionic conductivity and uncovering the site occupancy preference through model independent PDF analysis, and the effect of doping on the degree of hybridization through experimental XAS.

iii) Using computational XAS to unravel the local structure of the Al, Dy co-doped system through Dy L_3-edge analysis.

1.4. Thesis outline

Chapter 1 provides the rationale and brief literature review of the study, focusing on the techniques applied in Energy Materials characterization and outlining the aims and objectives.
Chapter 2 gives insights into the synthesis procedure of various doped LTP systems, and the techniques used to probe the structure at multiple length scales.
Chapter 3 presents the Sn-doped $LiTi_{2-x}Sn_x(PO_4)_3$ systems and the effects of increased [Sn^{4+}] at the Ti^{4+} site, on the average and local structure of the NASICON-type systems through diffraction and spectroscopic techniques.
Chapter 4 probes the co-doped Al, Sn ($Li_{1.2}Al_{0.2}Ti_{1.7}Sn_{0.1}(PO_4)_3$, LATSP) and Al, Dy ($Li_{1.3}Al_{0.25}Dy_{0.05}Ti_{1.7}(PO_4)_3$, LADTP) systems showing an improved ionic conductivity, and the application of XAS in uncovering the site preference of dopant cations in the rhombohedral 12*c* metal sublattice.
Chapter 5 largely focuses on the description of the Dy environment in the Al, Dy co-doped system through the analysis of average, local and electronic structure through synchrotron-based PXRD, PDF and computational XANES techniques.
Chapter 6 provides the conclusions and recommendations for future structural analysis of NASICON-type systems in providing a unified structural description.

1.5. References

1. Akinbami, O.M., Oke, S.R. and Bodunrin, M.O., 2021. The state of renewable energy development in South Africa: An overview. *Alexandria Engineering Journal*, *60*(6), pp.5077-5093.
2. Dewa, M.T., Van Der Merwe, A.F. and Matope, S., 2020. Production scheduling heuristics for frequent load-shedding scenarios: a knowledge engineering approach. *South African Journal of Industrial Engineering*, *31*(3), pp.110-121.
3. https://businesstech.co.za/news/energy/635989/fresh-delays-at-medupi-and-kusile-amid-eye-watering-costs/; accessed 7 March 2023)
4. https://www.statssa.gov.za/?p=9720 (accessed 25 October 2023)
5. https://www.tralac.org/discussions/article/7000-the-economic-consequences-of-load-shedding-in-south-africa-and-the-state-of-the-electrical-grid.html (accessed 25 October 2023)
6. https://businesstech.co.za/news/trending/83429/eskom-blackouts-cost-south-africa-r80-billion-per-month/ (accessed 25 October 2023)
7. https://www.engineeringnews.co.za/article/south-africa-catching-up-with-global-energy-transition-sawea-2018-03-06
8. https://meridianeconomics.co.za/our-publications/meridian-economics-presentation-at-windaba-coalgen-eskoms-financial-crisis-and-the-future-of-coal-fired-power-in-south-africa-november-2017/ (accessed 25 October 2023)
9. http://meridianeconomics.co.za/wp-content/uploads/2017/11/Eskoms-financial-crisis-and-the-viability-of-coalfired-power-in-SA_ME_20171115.pdf (accessed 25 October 2023)
10. Banks, D. and Schäffler, J., 2005. *The potential contribution of renewable energy in South Africa*. Johannesburg, South Africa: Sustainable Energy & Climate Change Project (SECCP).
11. Pegels, A., 2010. Renewable energy in South Africa: Potentials, barriers and options for support. *Energy policy*, *38*(9), pp.4945-4954.
12. under this Act, R., CONSTITUTION OF THE REPUBLIC OF SOUTH AFRICA, ACT 108 OF 1996.
13. DME (Department of Minerals and Energy), 1998. White Paper on Energy Policy for South Africa. Pretoria, DME.
14. ENERGY, O.R., 2003. White Paper on Renewable Energy.

15. https://www.gov.za/sites/default/files/gcis_document/201409/nationalclimatechangeresponsewhitepaper0.pdf (accessed 25 October 2023)
16. Lyons, C. and Gross, C., 2015. Power Generation Technology Data for Integrated Resource Plan of South Africa.
17. https://infrastructurenews.co.za/2022/03/10/state-of-the-south-african-waste-industry/ (accessed 25 October 2023)
18. Yechiel, A. and Shevah, Y., 2016. Optimization of energy generation using landfill biogas. *Journal of Energy Storage*, *7*, pp.93-98.
19. Krause, M.J., W. Chickering, G., Townsend, T.G. and Reinhart, D.R., 2016. Critical review of the methane generation potential of municipal solid waste. *Critical Reviews in Environmental Science and Technology*, *46*(13), pp.1117-1182.
20. https://www.gov.za/sites/default/files/gcis_document/202105/44539gon400.pdf (accessed 25 October 2023)
21. https://www.dffe.gov.za/sites/default/files/docs/2020nationalwaste_managementstrategy1.pdf (accessed 25 October 2023)
22. https://www.packagingsa.co.za/wp-content/uploads/2019/11/Packaging-SA-EPR-Plan-Volume-1-1.pdf (accessed 7 March 2023)
23. Chiu, H.Y., Pai, T.Y., Liu, M.H., Chang, C.A., Lo, F.C., Chang, T.C., Lo, H.M., Chiang, C.F., Chao, K.P., Lo, W.Y. and Lo, S.W., 2016. Electricity production from municipal solid waste using microbial fuel cells. *Waste Management & Research*, *34*(7), pp.619-629.
24. Karluvalı, A., Köroğlu, E.O., Manav, N., Çetinkaya, A.Y. and Özkaya, B., 2015. Electricity generation from organic fraction of municipal solid wastes in tubular microbial fuel cell. *Separation and Purification Technology*, *156*, pp.502-511.
25. Fluri, T.P., 2009. The potential of concentrating solar power in South Africa. *Energy Policy*, *37*(12), pp.5075-5080.
26. Banks, D. and Schäffler, J., 2005. *The potential contribution of renewable energy in South Africa*. Johannesburg, South Africa: Sustainable Energy & Climate Change Project (SECCP).
27. Akom, K., Shongwe, T. and Joseph, M.K., 2021. South Africa's integrated energy planning framework, 2015-2050. *Journal of Energy in Southern Africa*, *32*(1), pp.68-82.

28. Girschik, J., Kopietz, L., Joemann, M., Grevé, A. and Doetsch, C., 2021. Redox flow batteries: stationary energy storages with potential. *Chemie Ingenieur Technik*, *93*(4), pp.523-533.
29. Emmett, R.K. and Roberts, M.E., 2021. Recent developments in alternative aqueous redox flow batteries for grid-scale energy storage. *Journal of Power Sources*, *506*, p.230087.
30. Anantharamulu, N.A., Koteswara Rao, K., Rambabu, G., Vijaya Kumar, B., Radha, V. and Vithal, M., 2011. A wide-ranging review on Nasicon type materials. *Journal of materials science*, *46*, pp.2821-2837.
31. Hou, J., Yang, M., Wang, D. and Zhang, J., 2020. Fundamentals and challenges of lithium ion batteries at temperatures between− 40 and 60° C. *Advanced Energy Materials*, *10*(18), p.1904152.
32. Goodenough, J.B. and Kim, Y., 2010. Challenges for rechargeable Li batteries. *Chemistry of materials*, *22*(3), pp.587-603.
33. Walter, M., Kovalenko, M.V. and Kravchyk, K.V., 2020. Challenges and benefits of post-lithium-ion batteries. *New Journal of Chemistry*, *44*(5), pp.1677-1683.
34. Zheng, F., Kotobuki, M., Song, S., Lai, M.O. and Lu, L., 2018. Review on solid electrolytes for all-solid-state lithium-ion batteries. *Journal of Power Sources*, *389*, pp.198-213.
35. Fan, E., Li, L., Wang, Z., Lin, J., Huang, Y., Yao, Y., Chen, R. and Wu, F., 2020. Sustainable recycling technology for Li-ion batteries and beyond: challenges and future prospects. *Chemical reviews*, *120*(14), pp.7020-7063.
36. Quartarone, E. and Mustarelli, P., 2011. Electrolytes for solid-state lithium rechargeable batteries: recent advances and perspectives. *Chemical Society Reviews*, *40*(5), pp.2525-2540.
37. Palomares, V., Serras, P., Villaluenga, I., Hueso, K.B., Carretero-González, J. and Rojo, T., 2012. Na-ion batteries, recent advances and present challenges to become low cost energy storage systems. *Energy & Environmental Science*, *5*(3), pp.5884-5901.
38. Sun, Y.K., 2020. Promising all-solid-state batteries for future electric vehicles. *ACS Energy Letters*, *5*(10), pp.3221-3223.
39. Wolfenstine, J., Allen, J.L., Sakamoto, J., Siegel, D.J. and Choe, H., 2018. Mechanical behavior of Li-ion-conducting crystalline oxide-based solid electrolytes: a brief review. *Ionics*, *24*, pp.1271-1276.

40. Kundu, S., Kraytsberg, A. and Ein-Eli, Y., 2022. Recent development in the field of ceramics solid-state electrolytes: I—oxide ceramic solid-state electrolytes. *Journal of solid state electrochemistry*, *26*(9), pp.1809-1838.
41. Murugan, R., Thangadurai, V. and Weppner, W., 2007. Fast lithium ion conduction in garnet-type $Li_7La_3Zr_2O_{12}$. *Angewandte Chemie International Edition*, *46*(41), pp.7778-7781.
42. Duan, H., Zheng, H., Zhou, Y., Xu, B. and Liu, H., 2018. Stability of garnet-type Li ion conductors: An overview. *Solid State Ionics*, *318*, pp.45-53.
43. Lu, J. and Li, Y., 2021. Perovskite-type Li-ion solid electrolytes: a review. *Journal of Materials Science: Materials in Electronics*, *32*, pp.9736-9754.
44. Dawson, J.A., Attari, T.S., Chen, H., Emge, S.P., Johnston, K.E. and Islam, M.S., 2018. Elucidating lithium-ion and proton dynamics in anti-perovskite solid electrolytes. *Energy & Environmental Science*, *11*(10), pp.2993-3002.
45. Zhao, G., Suzuki, K., Seki, T., Sun, X., Hirayama, M. and Kanno, R., 2020. High lithium ionic conductivity of γ-Li_3PO_4-type solid electrolytes in Li_4GeO_4− Li_4SiO_4–Li_3VO_4 quasi-ternary system. *Journal of Solid State Chemistry*, *292*, p.121651.
46. Nikodimos, Y., Tsai, M.C., Abrha, L.H., Weldeyohannis, H.H., Chiu, S.F., Bezabh, H.K., Shitaw, K.N., Fenta, F.W., Wu, S.H., Su, W.N. and Yang, C.C., 2020. Al–Sc dual-doped $LiGe_2(PO_4)_3$–a NASICON-type solid electrolyte with improved ionic conductivity. *Journal of Materials Chemistry A*, *8*(22), pp.11302-11313.
47. Aono, H., Sugimoto, E., Sadaoka, Y., Imanaka, N. and Adachi, G.Y., 1993. The electrical properties of ceramic electrolytes for $LiM_xTi_{2-x}(PO_4)_3$+ yLi_2O, M= Ge, Sn, Hf, and Zr systems. *Journal of The Electrochemical Society*, *140*(7), p.1827.
48. París, M.A., Martínez-Juárez, A., Iglesias, J.E., Rojo, J.M. and Sanz, J., 1997. Phase transition and ionic mobility in $LiHf_2(PO_4)_3$ with NASICON structure. *Chemistry of materials*, *9*(6), pp.1430-1436.
49. Kuwano, J., Sato, N., Kato, M. and Takano, K., 1994. Ionic conductivity of $LiM_2(PO_4)_3$ (M= Ti, Zr, Hf) and related compositions. *Solid State Ionics*, *70*, pp.332-336.
50. Ramar, V., Kumar, S., Sivakkumar, S.R. and Balaya, P., 2018. NASICON-type La^{3+} substituted $LiZr_2(PO_4)_3$ with improved ionic conductivity as solid electrolyte. *Electrochimica Acta*, *271*, pp.120-126.

51. Martinez-Juarez, A., Rojo, J.M., Iglesias, J.E. and Sanz, J., 1995. Reversible monoclinic-rhombohedral transformation in $LiSn_2(PO_4)_3$ with NASICON-type structure. *Chemistry of materials*, *7*(10), pp.1857-1862.
52. Kumar, P.P. and Yashonath, S., 2006. Ionic conduction in the solid state. *Journal of Chemical Sciences*, *118*(1), pp.135-154.
53. Xie, H., Goodenough, J.B. and Li, Y., 2011. $Li_{1.2}Zr_{1.9}Ca_{0.1}(PO_4)_3$, a room-temperature Li-ion solid electrolyte. *Journal of Power Sources*, *196*(18), pp.7760-7762.
54. Aono, H., Imanaka, N. and Adachi, G.Y., 1994. High Li+ conducting ceramics. *Accounts of chemical research*, *27*(9), pp.265-270.
55. Kahlaoui, R., Arbi, K., Sobrados, I., Jimenez, R., Sanz, J. and Ternane, R., 2017. Cation Miscibility and Lithium Mobility in NASICON $Li_{1+x}Ti_{2-x}Sc_x(PO_4)_3$ ($0 \leq x \leq 0.5$) Series: A Combined NMR and Impedance Study. *Inorganic Chemistry*, *56*(3), pp.1216-1224.
56. Catti, M., Comotti, A., Di Blas, S. and Ibberson, R.M., 2004. Extensive lithium disorder in $Li_{1.5}$ $Fe_{0.5}Ti_{1.5}(PO_4)_3$ Nasicon by neutron diffraction, and the $Li_{1+x}Fe_xTi_{2-x}(PO_4)_3$ phase diagram. *Journal of Materials Chemistry*, *14*(5), pp.835-839.
57. Sun, L., Hu, J., Bai, W., Mao, W. and Song, Z., 2023. Synthesis and electrochemical properties of Mn-doped $Li_2Mn_{0.1}Ti_{1.9}(PO_4)_3$ materials. *Frontiers in Chemistry*, *11*, p.1189866.
58. Sugantha, M. and Varadaraju, U.V., 1997. Ionic conductivity of Li^+ ion conductors $Li_2M^{3+}M^{4+}$ P_3O_{12}. *Solid State Ionics*, *95*(3-4), pp.201-205.
59. Cai, Z., Huang, Y., Zhu, W. and Xiao, R., 2020. Increase in ionic conductivity of NASICON-type solid electrolyte $Li_{1.5}Al_{0.5}Ti_{1.5}(PO_4)_3$ by Nb_2O_5 doping. *Solid State Ionics*, *354*, p.115399.
60. Kothari, D.H. and Kanchan, D.K., 2022. Inter-grain Li^+ conduction in Sc and Y doped LATP compounds. *Physica B: Condensed Matter*, *627*, p.413599.
61. Wang, S., Ben, L., Li, H. and Chen, L., 2014. Identifying Li^+ ion transport properties of aluminum doped lithium titanium phosphate solid electrolyte at wide temperature range. *Solid State Ionics*, *268*, pp.110-116.
62. Stenina, I., Pyrkova, A. and Yaroslavtsev, A., 2023. NASICON-Type $Li_{1+x}Al_xZr_yTi_{2-x-y}(PO_4)_3$ Solid Electrolytes: Effect of Al, Zr Co-Doping and Synthesis Method. *Batteries*, *9*(1), p.59.

63. Lu, X., Meng, F., Huang, S. and Zhao, D., 2018. Enhanced ionic conductivity and chemical stability of $Li_{1.3}Al_{0.3}Ti_{1.7}(PO_4)_3$ by doping of WO_3. *Materials Letters*, *230*, pp.177-179.
64. Zhang, P., Wang, H., Si, Q., Matsui, M., Takeda, Y., Yamamoto, O. and Imanishi, N., 2015. High lithium ion conductivity solid electrolyte of chromium and aluminum co-doped NASICON-type $LiTi_2(PO_4)_3$. *Solid State Ionics*, *272*, pp.101-106.
65. Ortiz, G.F., López, M.C., Lavela, P., Vidal-Abarca, C. and Tirado, J.L., 2014. Improved lithium-ion transport in NASICON-type lithium titanium phosphate by calcium and iron doping. *Solid State Ionics*, *262*, pp.573-577.
66. Ren, Y., Chen, K., Chen, R., Liu, T., Zhang, Y. and Nan, C.W., 2015. Oxide electrolytes for lithium batteries. *Journal of the American Ceramic Society*, *98*(12), pp.3603-3623.
67. Delmas, C., Nadiri, A. and Soubeyroux, J.L., 1988. The nasicon-type titanium phosphates $ATi_2(PO_4)_3$ (A= Li, Na) as electrode materials. *Solid State Ionics*, *28*, pp.419-423.
68. Aatiq, A., Ménétrier, M., Croguennec, L., Suard, E. and Delmas, C., 2002. On the structure of $Li_3Ti_2(PO_4)_3$. *Journal of Materials Chemistry*, *12*(10), pp.2971-2978.
69. Cao, W., Yang, Y., Deng, J., Li, Y., Cui, C. and Zhang, T., 2021. Localization of electrons within interlayer stabilizes NASICON-type solid-state electrolyte. *Materials Today Energy*, *22*, p.100875.
70. Mashekova, A., Baltash, Y., Yegamkulov, M., Trussov, I., Bakenov, Z. and Mukanova, A., 2022. Polycationic doping of the LATP ceramic electrolyte for Li-ion batteries. *RSC advances*, *12*(46), pp.29595-29601.
71. Aono, H., Sugimoto, E., Sadaoka, Y., Imanaka, N. and Adachi, G.Y., 1990. Ionic conductivity of solid electrolytes based on lithium titanium phosphate. *Journal of the electrochemical society*, *137*(4), pp.1023-1027.
72. Schlenker, R., Hansen, A.L., Senyshyn, A., Zinkevich, T., Knapp, M., Hupfer, T., Ehrenberg, H. and Indris, S., 2020. Structure and diffusion pathways in Li_6PS_5Cl argyrodite from neutron diffraction, pair-distribution function analysis, and NMR. *Chemistry of materials*, *32*(19), pp.8420-8430.
73. Weiss, M., Weber, D.A., Senyshyn, A., Janek, J. and Zeier, W.G., 2018. Correlating Transport and Structural Properties in $Li_{1+x}Al_xGe_{2-x}(PO_4)_3$ (LAGP) Prepared from Aqueous Solution. *ACS applied materials & interfaces*, *10*(13), pp.10935-10944.

74. Arbi, K., Hoelzel, M., Kuhn, A., García-Alvarado, F. and Sanz, J., 2013. Structural Factors That Enhance Lithium Mobility in Fast-Ion $Li_{1+x}Ti_{2-x}Al_x(PO_4)_3$ ($0 \leq x \leq 0.4$) Conductors Investigated by Neutron Diffraction in the Temperature Range 100–500 K. *Inorganic chemistry*, *52*(16), pp.9290-9296.
75. Monchak, M., Hupfer, T., Senyshyn, A., Boysen, H., Chernyshov, D., Hansen, T., Schell, K.G., Bucharsky, E.C., Hoffmann, M.J. and Ehrenberg, H., 2016. Lithium diffusion pathway in $Li_{1.3}Al_{0.3}Ti_{1.7}(PO_4)_3$ (LATP) superionic conductor. *Inorganic chemistry*, *55*(6), pp.2941-2945.
76. Arbi, K., Mandal, S., Rojo, J.M. and Sanz, J., 2002. Dependence of Ionic Conductivity on Composition of Fast Ionic Conductors $Li_{1+x}Ti_{2-x}Al_x(PO_4)_3$, $0 \leq x \leq 0.7$. A Parallel NMR and Electric Impedance Study. *Chemistry of materials*, *14*(3), pp.1091-1097.
77. Zhu, J., Zhao, J., Xiang, Y., Lin, M., Wang, H., Zheng, B., He, H., Wu, Q., Huang, J.Y. and Yang, Y., 2020. Chemomechanical failure mechanism study in NASICON-type $Li_{1.3}Al_{0.3}Ti_{1.7}(PO_4)_3$ solid-state lithium batteries. *Chemistry of Materials*, *32*(12), pp.4998-5008.
78. Pikl, R., De Waal, D., Aatiq, A. and El Jazouli, A., 1998. Vibrational Spectra and Factor Group Analysis of $Li_{2x}Mn_{0.5-x}Ti_2(PO_4)_3$ {x= 0, 0.25, 0.50}. *Materials research bulletin*, *33*(6), pp.955-961.
79. Barj, M., Lucazeau, G. and Delmas, C., 1992. Raman and infrared spectra of some chromium Nasicon-type materials: short-range disorder characterization. *Journal of Solid State Chemistry*, *100*(1), pp.141-150.
80. Dashjav, E., Ma, Q., Xu, Q., Tsai, C.L., Giarola, M., Mariotto, G. and Tietz, F., 2018. The influence of water on the electrical conductivity of aluminum-substituted lithium titanium phosphates. *Solid State Ionics*, *321*, pp.83-90.
81. Gammond, L.V., Auer, H., Mendes Da Silva, R., Zeidler, A., Ortiz-Mosquera, J.F., Nieto-Muñoz, A.M., Rodrigues, A.C.M., d'Anciães Almeida Silva, I., Eckert, H., Benmore, C.J. and Salmon, P.S., 2021. Structure of crystalline and amorphous materials in the NASICON system $Na_{1+x}Al_xGe_{2-x}(PO_4)_3$. *The Journal of Chemical Physics*, *155*(7), p.074501.
82. Noda, Y., Nakano, K., Otake, M., Kobayashi, R., Kotobuki, M., Lu, L. and Nakayama, M., 2018. Research update: Ca doping effect on the Li-ion conductivity in NASICON-type solid electrolyte $LiZr_2(PO_4)_3$: A first-principles molecular dynamics study. *APL Materials*, *6*(6).

83. Arjmandi, H.R. and Grieshammer, S., 2019. Defect formation and migration in Nasicon $Li_{1+x}Al_xTi_{2-x}(PO_4)_3$. *Physical Chemistry Chemical Physics*, *21*(43), pp.24232-24238.
84. Lang, B., Ziebarth, B. and Elsässer, C., 2015. Lithium ion conduction in $LiTi_2(PO_4)_3$ and related compounds based on the NASICON structure: a first-principles study. *Chemistry of Materials*, *27*(14), pp.5040-5048.
85. Malavasi, L., 2011. Total scattering investigation of materials for clean energy applications: The importance of the local structure. *Dalton Transactions*, *40*(15), pp.3777-3788.
86. Sanchez, S., Steiner, U. and Hua, X., 2019. Phase evolution during perovskite formation—insight from pair distribution function analysis. *Chemistry of Materials*, *31*(9), pp.3498-3506.
87. Proffen, T.E., Page, K.L., Kolodiazhnyi, T., Cheetham, A.K. and Seshadri, R., 2008. *Local structural origins of the distinct electronic properties of Nb-substituted $SrTiO_3$ and $BaTiO_3$* (No. LA-UR-08-04757; LA-UR-08-4757). Los Alamos National Lab.(LANL), Los Alamos, NM (United States).
88. Dong, C.L. and Vayssieres, L., 2018. In Situ/Operando X-ray Spectroscopies for Advanced Investigation of Energy Materials. *Chemistry–A European Journal*, *24*(69), pp.18356-18373.
89. Kerr, B.V., King, H.J., Garibello, C.F., Dissanayake, P.R., Simonov, A.N., Johannessen, B., Eldridge, D.S. and Hocking, R.K., 2022. Characterization of energy materials with X-ray absorption spectroscopy─ advantages, challenges, and opportunities. *Energy & Fuels*, *36*(5), pp.2369-2389.
90. Liu, J., Wang, T., Yu, J., Li, S., Ma, H. and Liu, X., 2023. Review of the Developments and Difficulties in Inorganic Solid-State Electrolytes. *Materials*, *16*(6), p.2510.
91. Rehr, J.J. and Albers, R.C., 2000. Theoretical approaches to x-ray absorption fine structure. *Reviews of modern physics*, *72*(3), p.621.
92. Cabaret, D., Joly, Y. and Renevier, H., 1999. Pre-edge structure analysis of Ti K-edge polarized X-ray absorption spectra in TiO_2 by full-potential XANES calculations. *Journal of Synchrotron Radiation*, *6*(3), pp.258-260.

Chapter 2: Experimental Synthesis and Characterisation Methods

2.1. Synthesis of NASICON-type $LiTi_2(PO_4)_3$-based systems

A series of NASICON-type $LiTi_2(PO_4)_3$ (LTP)-based materials have been synthesized via the conventional solid-state reaction method. The composition-specific synthetic procedures and characterization techniques are outlined in the respective **Results & Discussion** chapters. Across all chapters, all variously doped compositions are compared to the parent, undoped system, LTP. In this chapter, the background of characterization techniques used in the study is briefly explained. Here, we outline the instrumental setup, data collection and reduction, followed by the data analysis parameters used.

Table 2.1. A comprehensive list of all compositions synthesized in this work, showing the relevant chapters and the dopant %.

Chapter	Composition	Dopant %
3	$LiTi_2(PO_4)_3$	-
	$LiTi_{1.96}Sn_{0.02}(PO_4)_3$	2% Sn
	$LiTi_{1.92}Sn_{0.08}(PO_4)_3$	4% Sn
	$LiTi_{1.88}Sn_{0.12}(PO_4)_3$	6% Sn
	$LiTi_{1.84}Sn_{0.16}(PO_4)_3$	8% Sn
	$LiTi_{1.8}Sn_{0.2}(PO_4)_3$	10% Sn
	$LiTiSn(PO_4)_3$	50% Sn
4	$LiTi_2(PO_4)_3$	-
	$Li_{1.3}Al_{0.3}Ti_{1.7}(PO_4)_3$	15% Al (LATP)
	$Li_{1.2}Al_{0.2}Ti_{1.7}Sn_{0.1}(PO_4)_3$	10% Al, 5% Sn (LATSP)
	$Li_{1.3}Al_{0.25}Dy_{0.05}Ti_{1.7}(PO_4)_3$	12.5% Al, 2.5% Dy (LADTP)
5	$LiTi_2(PO_4)_3$	-
	$Li_{1.3}Al_{0.3}Ti_{1.7}(PO_4)_3$	15% Al (LATP)
	$Li_{1.3}Al_{0.25}Dy_{0.05}Ti_{1.7}(PO_4)_3$	12.5% Al, 2.5% Dy (LADTP)

2.2. Materials characterization techniques

The complex characterization of solid electrolytes exploring the average and local structures provides insights into the structural changes that occur as a result of synthesis conditions such as temperature,[1] lattice site substitution with various isovalent and aliovalent cations,[2-4] and their subsequent result on the ionic conductivity of the electrolytes. Employing multiple techniques for analysis allows for the application of different probes and operation methods to reveal different facets of the material's properties. Although extensive studies have been going on for decades on NASICON-type materials since their discovery by Goodenough *et al.*,[5] developments and improvements of synchrotron facilities and techniques have provided new insights that continue to inform further improvements on existing materials for their applicability in energy storage and transport.

The quality of structural information obtained in each technique is largely dependent on the method of sample preparation, the experimental set-up, and the correct data reduction and subsequent analysis. Each of the following setions will consist of a brief introduction to the technique and the importance of each technique in addressing the research questions stated in this work. Exemplary data sets are presented for each section, with the data analysis methodology.

2.2.1. Powder X-ray diffraction (PXRD)

PXRD is the preeminent analysis technique in this work, used as a method to establish the qualitative and quantitative phase compositions and crystallinity of the electrolyte materials. In PXRD using conventional diffractometers, a high-voltage field is used to accelerate electrons, which then collide with a metal target (the anode), thus generating X-rays. The interaction between an incident electron beam of sufficient energy and the anode results in the emission of bound electrons of the anode, generating a hole. An electron from a higher-energy shell fills the generated hole, and as the electron falls into the lower-energy vacancy, it releases energy by giving off characteristic X-rays of specific energy (or wavelength). If the 1s (*K* shell) core electron is ejected and the resulting hole is filled by an electron from the L shell, K_α radiation is given off; while the decay of an M-shell electron results in K_β X-rays being generated. The intensity of K_α radiation is significantly higher than that of K_β attributed to the relatively higher probability of an *L* shell electron filling a *K* shell hole, than that of an *M* shell electron filling a *K* shell hole.

The X-ray tube has both a filament as the source of electrons (usually W) and an anode as the source of X-rays, which can either be Ag, Mo, Cu, Co, Fe or Cr. The need for a monochromatic beam of X-rays is achieved using filters, that are strongly absorbing of X-rays up to a certain energy. Particularly, the respective K_β filters for the Ag, Mo, Cu, Co, Fe and Cr X-ray tubes are Ru, Zr, Ni, Fe, Mn, and V.

XRD operates on the phenomenon of the interference of scattered waves. Waves can interact with each other either constructively, or destructively depending on their phase. The interference of the scattered waves is governed by Bragg's Law, given by

$$n\lambda = 2d\ sin\ \theta$$

Where *n* is the multiplicity of wavelength, λ, θ is the angle of incidence of the incoming X-ray beam, and *d* is the interplanar spacing. Therefore, knowing the incident wavelength λ, we can determine the interplanar spacing as a function of θ, upon constructive interference. The changes in the atomic arrangements and periodicity thus yield different diffraction patterns, allowing the use of diffraction techniques as a means to establish the average structure of materials. Further background theory can be found elsewhere.[6-7]

In this work, the preliminary laboratory-based PXRD data were measured using the *Bruker D2 Phaser* diffractometer, equipped with a Co tube and a Lynxeye Position Sensitive Detector (PSD). The obtained data were analyzed using DIFFRAC. EVA V4,[8] to identify the phases in the materials under investigation. The instrument-specific details are shown in **Table 2.2**.

Table 2.2. Instrumental and data collection information of the laboratory-based Bruker D2 Phaser diffractometer.

X-ray source	Co Kα1/Kα2
Goniometer radius	141.0 mm
Primary radius	70.7 mm
Secondary radius	70.7 mm
Detector	Lynxeye 2Theta Angular
PSD opening	5.638°
2θ range	10° - 90°
Step size	0.026°
Steps	3030

Synchrotron PXRD

Although conventional laboratory-based PXRD provides information on the qualitative and quantitative aspects of polycrystalline materials, higher-resolution data yield more accurate structural information. **Figure 2.1** displays exemplary data for lab and synchrotron-based PXRD. The advantages of using synchrotron-based PXRD are as follows: [9-10]

- The wavelength can be tuned, allowing the determination of element-specific changes to the structure, through anomalous scattering techniques.
- The high intensity and brightness make the measurements of small samples, by volume, more feasible compared to laboratory-based measurements that require relatively larger volumes of samples to yield results that are representative of the sample space.
- The collimation of the beam allows for higher accuracy determination of structural parameters due to higher angular resolution.
- High photon energy allows for depth profiling (to the order of centimetres below the surface of the sample), attributed to the large penetration depth of the radiation.
- High photon energy also yields a large wave vector, allowing for the collection of more data in a smaller angular range.
- In-situ studies under various temperatures, pressures, and atmospheres are possible as a result of using an experimental set-up that consists of an area detector, which yields faster acquisition times.

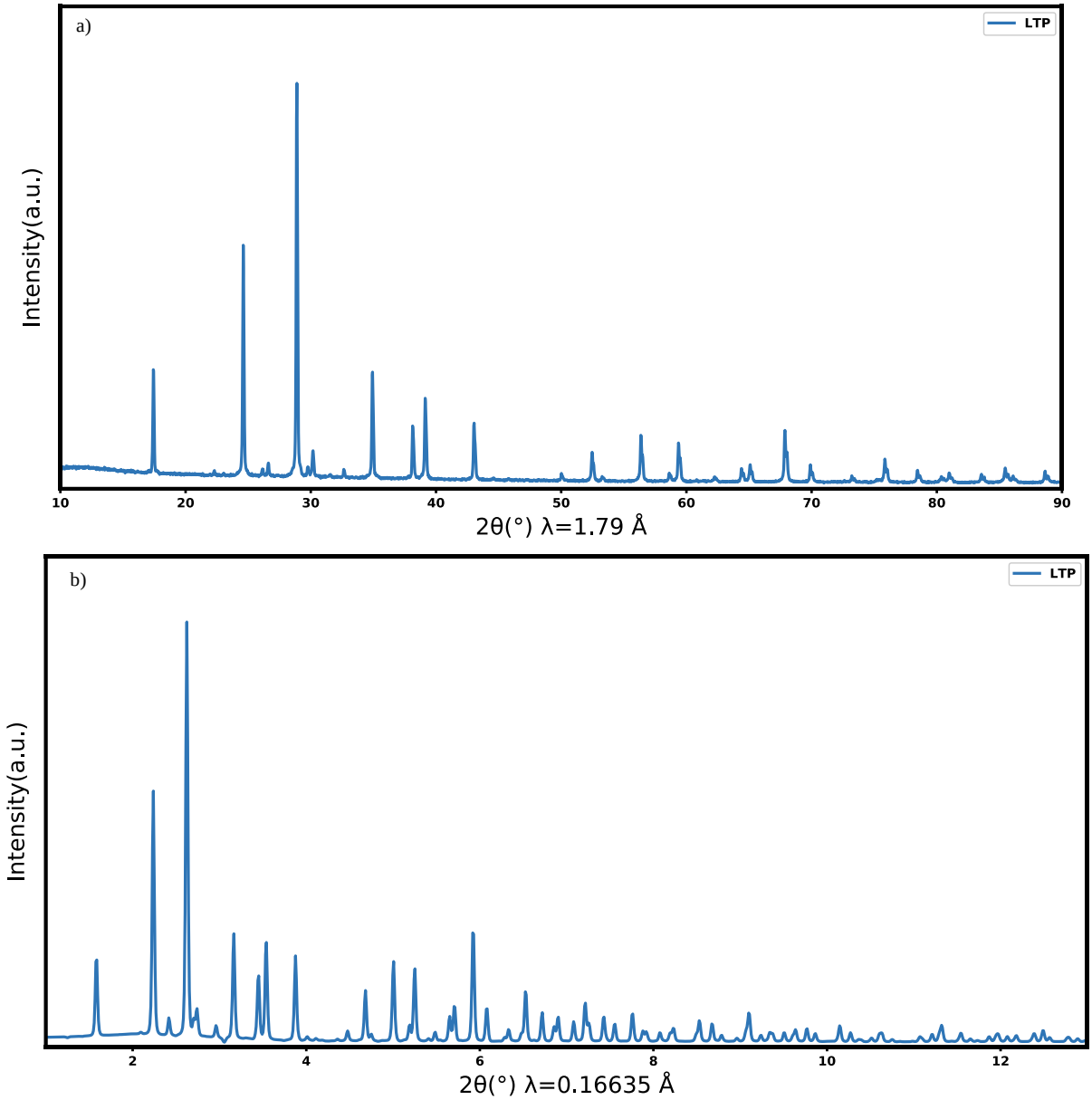


Figure 2.1. Exemplary data of PXRD patterns of LTP were measured using a) lab-based and b) synchrotron-based instrumentation.

The instrumental details for the synchrotron-based PXRD data presented in this work are provided in **Table 2.3**. More specific set-up details are presented in the Results sections of each chapters.

Table 2.3. Instrumental and data collection information of the 28-ID-1 (Pair Distribution Function) beamline at National Synchrotron Light Source II (NSLS-II), Brookhaven National Laboratory, Upton, New York, USA. The reported values were those used in this work.

Measurement mode	Transmission
Sample holder	Kapton capillary (OD = 0.9 mm)
Energy	75 keV
Sample-to-detector distance	200-1000 mm
2D area detector pixel size	200 μm × 200 μm

The MATCH! Software,[11] was used to confirm the phases present in the materials as it includes the option to input user-defined wavelengths, a very important feature when analyzing synchrotron data.

2.2.2. The Rietveld approach to structural analysis

The Rietveld refinement approach to structural analysis yields quantitative information of multiphase systems, on the structure of materials. The Rietveld refinement method is described as a non-linear least-squares structure-based fitting of experimental data to a structural model, which provides chemically reasonable starting parameters. The structural parameters, background coefficients and profile parameters are varied until the best fit is reached between the structural model and the whole experimental observed data.[11-13] It is imperative that a physically and structurally sound starting structural model is obtained. To this effect, programs such as DIFRRAC. EVA,[8] allow one to search for possible structures by specifying the elements present in the known compound and comparing these to literature powder patterns in crystal structure databases such as the Inorganic Crystal Structure Database (ICSD),[15-16] and Crystallography Open Database (COD). This allows one to determine the starting unit cell dimensions and space group of the sample.[17]

In this work, the PXRD data obtained from both conventional and synchrotron techniques were analyzed using TOPAS Academic, to establish the percentage phase composition and accompanying structural parameters of the systems explored.

The standard practice in analyzing PXRD data is to determine the instrument resolution function of the instrument through the measurement of a reference standard. In this case, the Si reference standard (NIST CRM 640d),[18] was used. The starting model for Si was the cubic *Fd*-3*m* structure (ICSD Collection Code 29287).[19] Under the structure (.str) component of the input file, the fractional coordinates (*x*, *y*, *z*) from the crystallographic information file (CIF) are replaced with the coordinates provided in the reference certificate, and the displacement parameter, *B*, is also refined. For all presented refinements, the B values were constrained between a minimum of 0.01 and a maximum of 5 $Å^2$ to ensure that the resulting fits produced crystallographically sound parameters and structures. Lattice parameters were kept fixed to check how well the diffractometers and wavelengths were calibrated. The displacement parameter accounts for the atomic vibrations about their equilibrium positions. Local static disorder may also contribute to the displacement parameter.[20]

The reference material provides information on the instrument resolution function. The peak and instrument profiles are subsequently kept constant for sample analyses, while the background function obtained from the standard was used as a starting point and varied for subsequent sample compositions. The Rietveld refinement result for Si is shown in **Figure 2.2**. The crystallographic information is given in **Table 2.4. Table 2.5.** gives the figures of merit used in assessing the quality of the fits. The figures of merit are explained in more details in the recommended literature.[20]

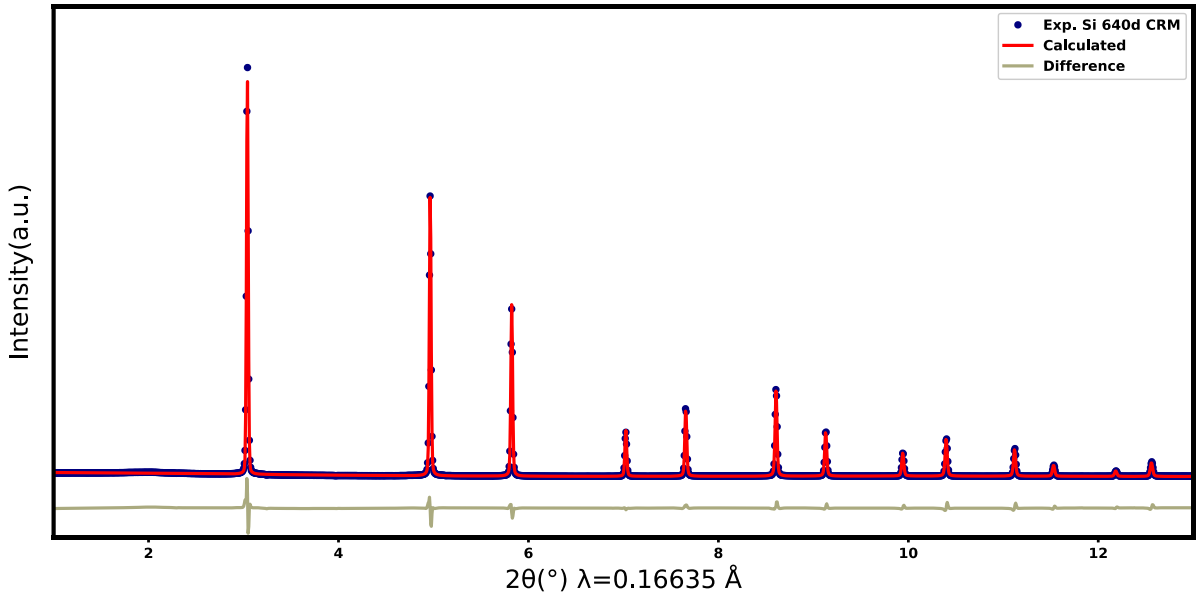


Figure 2.2. The Rietveld refinement result of the Si 640d CRM synchrotron PXRD pattern.

Table 2.4. Crystallographic data for the Si 640d CRM from Rietveld refinement of synchrotron XRD results (28-ID-1 at NSLS-II, 0.16635 Å).

	Si (ICSD 29287)
RBragg	2.13
Weight %	100
Space group	*Fd*-3*m*
a (Å)	5.432(2)
b (Å)	5.432(2)
c (Å)	5.432(2)
Volume (Å^3)	160.244
Phase density (g/cm^3)	2.328

Whole pattern refinement parameters: R_{exp} = 22.62%, R_{wp} = 9.24%, R_p = 6.59%, GOF = 0.41.

Table 2.5. Figures of merit used in reporting and assessing the quality of Rietveld refinement fits.

Figure of merit	**Formula**	**Explanation and expected value**
R_p, profile R-factor	$R_p = \frac{\sum_{i=1}^{N} \lvert y_{obs,i} - y_{calc,i}(\mathbf{p}) \rvert}{\sum_{i=1}^{N} y_{obs,i}}$	This is a measure of the difference between the observed and calculated profiles.
R_{wp}, weighted profile R-factor	$R_{wp} = \sqrt{\frac{\sum_{i=1}^{N} w_i \left(y_{obs,i} - y_{calc,i}(\mathbf{p}) \right)^2}{\sum_{i=1}^{N} w_i y_{obs,\ i^2}}}$	A weighting scheme is applied to R_p to overcome the overemphasis of strong reflections and previously excluded experimental uncertainties.

R_{exp}, expected R-factor	$R_{exp} = \sqrt{\frac{N-P}{\sum_{i=1}^{N} w_i y_{obs,\ i^2}}}$	This factor is mainly determined by counting statistics to give an estimate of the best possible fit, with *N* and *P* referring to the number of data points and number of parameters, respectively.
GOF, χ, goodness of fit	$\chi = \frac{R_{wp}}{R_{exp}} = \sqrt{\frac{\sum_{i=1}^{N} w_i \left(y_{obs,i} - y_{calc,i}(\mathbf{p})\right)^2}{N-P}}$	This is an absolute measure of the quality of Rietveld refinement fit. A good fit is obtained when χ is between 1 and 1.5. A smaller value (as observed in synchrotron PXRD patterns obtained in this work) is typically indicative of poor counting statistics.

2.2.3. Atomic Pair distribution function (PDF)

The atomic PDF method is used to gain insight into the local structure of materials. The advantage of this method is the lack of prerequisite for long-range order, unlike in conventional PXRD. Therefore, it allows for the determination of local structure across crystalline and non-crystalline materials. The PDF describes the distribution of distances between atomic pairs and its intensity corresponds to the probability of finding two atoms within a particular distance. While in PXRD, the structural information is obtained following Bragg's law, the PDF is derived from both Bragg and diffuse scattering, i.e., total scattering. This simply means that the total scattering data consists of structural information obtained from the periodic long-range order of atoms, as well as the information generated from a lack of periodicity in the long-range.

The advantage of high-energy X-ray in synchrotron facilities is in the measurement of total scattering data in a large reciprocal space range, attributed to the large wave vector, whose magnitude is given by Q, as defined in equation 1:

Equation 1

$$Q = \frac{4\pi \sin\theta}{\lambda}$$

where θ is half the scattering angle, 2θ, and λ is the wavelength of X-ray radiation.

The obtained signal is then corrected by removing contributions to the background such as air scattering, electronic noise, sample environment and Compton scattering, after which the reduced structure function F(Q) is given by: [21]

Equation 2

$$F(Q) = Q\big(S(Q)\big) - 1$$

Finally, to obtain the PDF a sine Fourier transform of the reduced structure function, $F(Q)$, is taken, yielding G(r): [10]

Equation 3

$$G(r) = {}^{2}/_{\pi} \int_{0}^{\infty} Q[S(Q) - 1] \sin Qr dQ$$

The reader is directed to literature for more detailed explanations of PDF.[22-25]

In this work, PDF data were collected simultaneously with synchrotron PXRD, with the sample-to-detector distance set to the 105 to 120 mm range.

The 2D data were converted to 1D data of intensity vs 2θ using the Fit2D software.[26] The contributions from the Kapton capillary were removed through background subtraction. More detailed experimental procedures and small-box modelling approaches are given in **Chapter 5**.

2.2.4. Raman spectroscopy (RS)

The Raman Effect results from the scattering of light with matter. Photon absorption occurs when the energy of the incident photon is equivalent to the energy change between the states of transition. This transition between the two states is accompanied by a change in the polarizability of the molecule. Elastic scattering occurs when scattering of the photon occurs without any net change in the energy of the molecule-photon system. This is referred to as Raleigh scattering. Inelastic scattering constitutes the Raman Effect. The molecule may either gain energy from or lose energy to the photon.

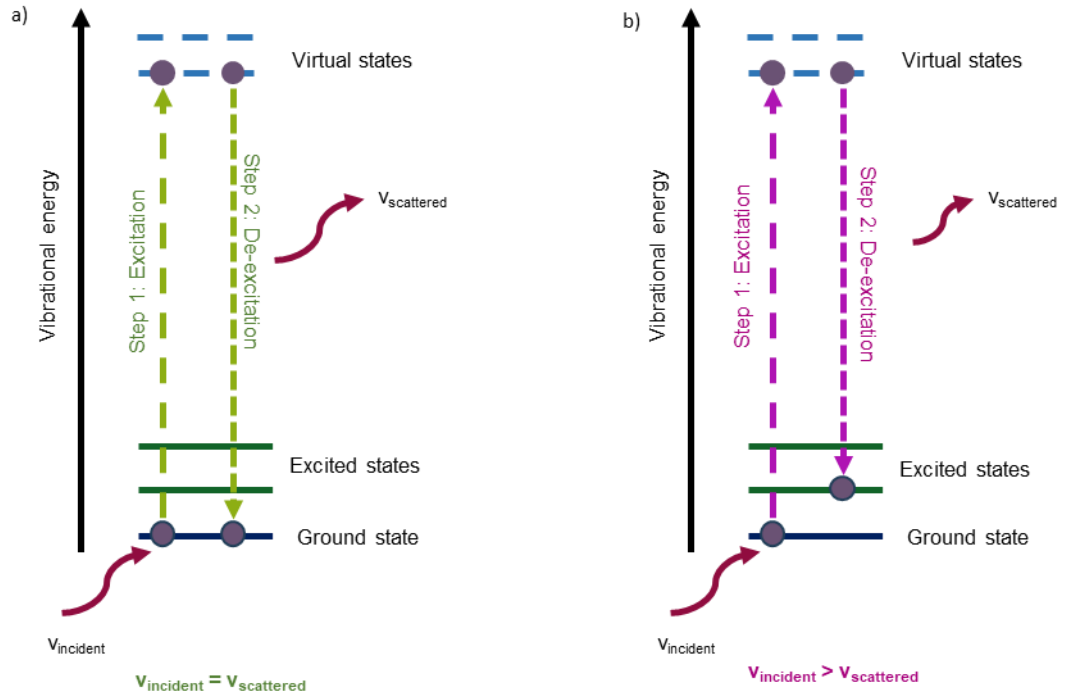


Figure 2.3. Energy level diagrams demonstrating the principles of a) Raleigh (elastic) scattering and b) Stokes Raman (inelastic) scattering.

There are two types of Raman scattering, namely i) Stokes scattering: wherein the scattered photon will be lower in energy than the incident photon if the transfer of energy in the virtual state is from the photon to the molecule (as demonstrated in **Figure 2.3(b)**); ii) anti-Stokes Raman scattering: if the transfer of energy in the virtual state is from the molecule to the photon, the scattered photon will be higher in energy than the incident photon.

Stokes lines tend to be more intense compared to anti-Stokes lines because the ground-state population is greater than that of the excited state, therefore in Raman spectroscopy, one would plot the intensity of the inelastically scattered light against the Stokes-shifted frequencies in wavenumbers.

The advantages of applying Raman spectroscopy to materials characterization is that the technique does not require large sample amounts for analysis, and samples can be probed under various conditions such as variable temperature and pressure that may result in phase changes. The technique is used as a fingerprinting technique, since each scattering molecule would have a particular point group symmetry. Therefore, the number of observed peaks would be determined by the number of symmetry-allowed modes that are Raman-active. However, it is not unusual that the resulting spectrum of a material shows fewer number of peaks than predicted by Group Theory. This is attributed to some of the modes being degenerate, while in some instances, the symmetry-allowed Raman-active modes may have intensities that are too low to be detected. For further information, the reader is directed to the references.[6, 27-29]

Laboratory-based Raman spectroscopy measurements were conducted at room temperature at a wavelength of 514.5 nm, using an Ar^{+} laser with a grating of 600 lines/mm and a 100× objective lens. The instrument employed a Symphony charge coupled device (CCD) detector, cooled with nitrogen. The instrument was calibrated with as Si single crystal standard, to an error of ± 0.4 cm^{-1}. The peak positions were obtained using the LabSpec software (V5.93.20, Evaluation Copy, HORIBA Jobin-Yvon).

2.2.5. X-ray absorption spectroscopy (XAS)

XAS, largely a synchrotron-based technique, provides insight into the electronic structure and local geometry of an X-ray absorbing atom in various materials, in gaseous, liquid and solid states (both amorphous and crystalline materials).[30] XAS measures the probability of X-ray absorption by an atom, depending on the atom's local geometry and electronic structures. The operating principle for XAS is that of the *Photoelectric Effect*.

In this phenomenon, a photon of energy, E, is bombarded onto a sample and is absorbed by a core-level electron with binding energy E_B , which results in the excitation of this core-level electron. This energy absorption results in the ejection of a photoelectron to an empty higher-energy state, leaving behind a hole, when the incident photon energy, E is greater than E_B. As the X-ray energy is increased above the absorption edge, the photoelectron is created and has some kinetic energy allowing it to propagate away from the absorbing atom. Therefore, XAS measures the probability of X-ray absorption as a function of energy, in accordance with Beer's law, when measured in transmission mode:

Equation 4

$$I = I_0 e^{-\mu(E)t}$$

I corresponds to the transmitted intensity through the sample, I_0 is the incident X-ray intensity, μ corresponds to the absorption coefficient as a function of energy, our parameter of interest, in a sample with thickness t. The absorption coefficient is traced as a function of energy, where a sharp rise in absorption is observed when the incident energy is equal or greater than the binding energy, E_B, of the core shell electron.

When the target element is available in low concentrations, the measurement is conducted in fluorescence mode. In this mode, the monitored intensity is that of a fluorescence line associated with the absorption process. The chemical specificity of XAS stems from the fact that every atom has well-defined binding energies for its core electrons, thus the incident X-ray energy can be tuned to that of the element of interest.

The XAS spectrum is divided into two sections, i.e., the X-ray absorption near-edge structure (XANES), and the extended X-ray absorption fine structure (EXAFS). The XANES is a portion of the XAS spectrum that consists of the pre-edge, rising edge, and approximately 30 eV above the rising edge, as shown in **Figure 2.4**.

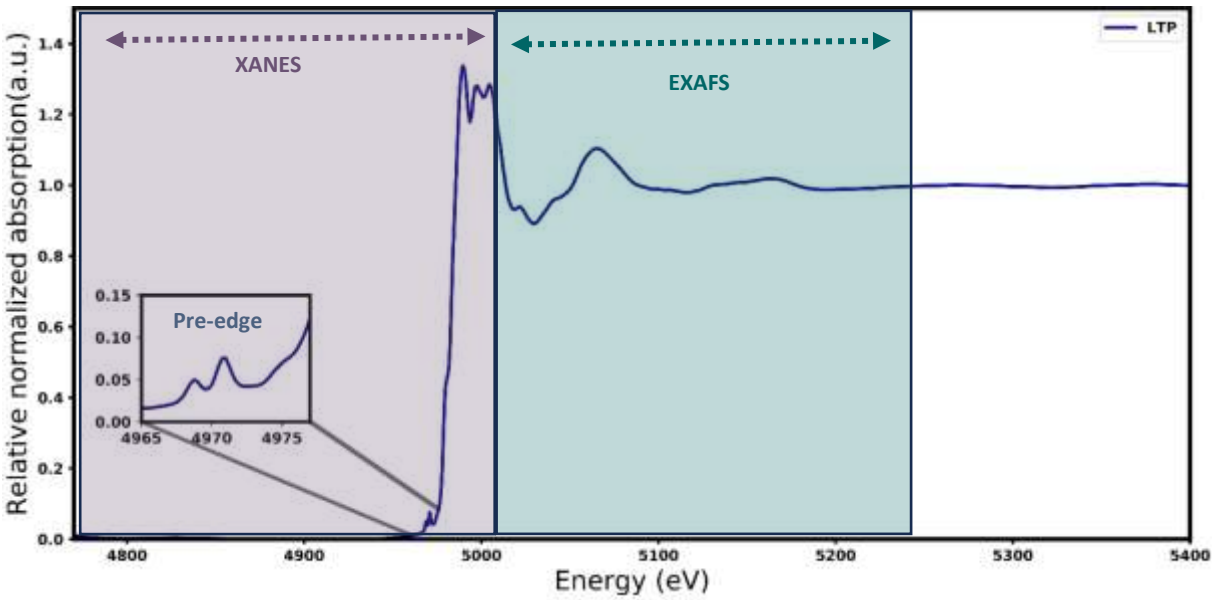


Figure 2.4. An exemplary Ti K-edge XAS normalized XAS spectrum showing the pre-edge peaks (zoomed inset) and the dotted lines denoting the XANES and EXAFS regions.

The XANES region is in the energy range within 30 to 50 eV of the absorption edge.[31] The typical structural analysis is done by fingerprinting, a method of direct comparison of spectral signatures from the compound and element of interest, to reference well-researched compounds.[32] In the fingerprinting method, the shape and energy position of the spectral signatures provide information into the local electronic structure of the absorbing atom, namely the formal oxidation state and coordination chemistry. The electronic transitions' names depend on the origin of the core orbital from which an electron is excited. The K-edge refers to the transition exciting the innermost 1*s* electron, while the L_3-edge refers to the excitation of the $2p^4{}_{3/2}$ electron to the free or unoccupied continuum states.[33] Taking Ti as an example, the pre-edge corresponds to the $1s \rightarrow 3d$ transition for the K-edge, and pre-edge peak fitting, particularly for the first-row transition metals, provides information pertaining to the degree of hybridization between the absorber and the near-neighbor atoms, and any changes in the centrosymmetry of the metal centre.[34] The rising edge corresponds to the $1s \rightarrow 4p$ and $1s \rightarrow continuum\ states$ transitions in the Ti K-edge. In the fingerprinting method, the energy position of the rising edge is used to determine the oxidation state of the element of interest, with a shift towards higher energy indicating an increase in the oxidation state. However, it is important to note that the shift in edge position is also affected by the identity of the ligands around the metal centre of interest.[35]

The application of XANES in the determination of local structure around lanthanide absorbers has been widely used across the energy materials field of research.[36-38] Through the analysis of the edge position and spectral features, the fingerprinting method is applied to establish the oxidation state, site symmetry and coordination around the element of interest. The analysis of the first- and second-derivative spectra of L_3-edge XANES remains informative in the changes around the absorber, possibly due to disorder,[39] and as a means of identifying the reaction mechanisms in catalysts.[40]

The region beyond the XANES is the EXAFS. The EXAFS is obtained when an X-ray ejects an electron from an atom (photoelectron). This photoelectron is described as a spherical wave and it scatters off neighbouring atoms, returning to the original absorber atom, as shown in **Figure 2.5**. The photoelectron wave can interact constructively or destructively with the neighboring atoms.

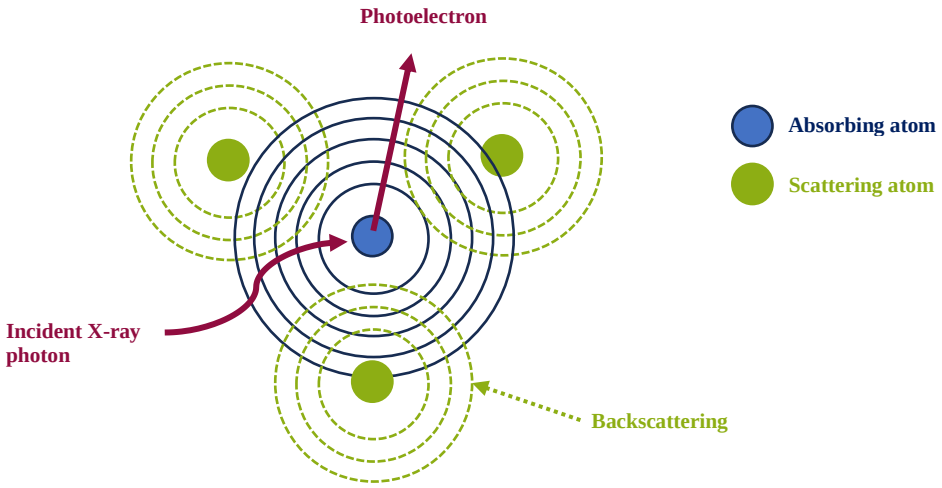


Figure 2.5. The interference pattern generated by the interactions between the absorber and nearest neighboring scattering atoms, demonstrating the EXAFS phenomenon.

The analysis of the EXAFS region provides details on the coordination number, degree of disorder and the interatomic distances between the absorber and the nearest-neighbor scatterers. The fine structure function, $\chi(E)$ above the absorption edge is given by

Equation 5

$$\chi(E) = \frac{\mu(E) - \mu_0(E)}{\Delta\mu_0(E)}$$

The $\mu(E)$ corresponds to the measured absorption coefficient as a function of energy, while $\mu_0(E)$ represents the smooth background function, describing the absorption of an isolated atom and $\Delta\mu_0(E)$ is the edge jump at the absorption energy, E_0.

The kinetic energy given to the photoelectron when the X-ray energy is above the edge energy, is described as

Equation 6

$$k = \sqrt{\frac{2m(E - E_0)}{\hbar^2}}$$

where k is the wave vector, m is the electron mass and E_0 is as described above. The EXAFS signal $\chi(k)$ is given by the EXAFS equation:

Equation 7

$$\chi(k) = \sum_j \frac{S_0^2 N_j f_j(k)}{kR_j^2} e^{-2k^2\sigma_j{}^2} e^{\frac{-2R_j}{\lambda_j}} sin\left[2kR + \delta_j(k)\right].$$

The equation describes the sum over all shells of equivalent atoms at the same radial distance. The parameters are as follows: S_0^2corresponds to the amplitude reduction factor that is determined from a standard. This factor is attributed to the relaxation of the electron in the absorbing atom to the hole in the core level; N_j corresponds to the number of nearest neighboring atoms to the j^{th} absorbing atom, R is the mean distance between the absorber and its neighboring scattering atoms, and $\sigma_j{}^2$ describe the disorder in the neighboring scatterer distance. The parameter λ_j is the mean free path of the photoelectron. It accounts for the decay in amplitude due to the decreasing coherence between the outgoing and backscattered waves. Given the scattering amplitude $f_j(k)$ and phase shift $\delta_j(k)$, we can determine *N*, *R* and $\sigma_j{}^2$. Since the scattering amplitude and phase shift are atom-dependent, we can evaluate the EXAFS equation for different neighboring atoms, giving insight into the local structure around the absorber.

Experimental XAS - In this work, the Ti K- and Dy L_3-edge data were measured and used to study the effects of doping on the *p-d* hybridization changes, and the local geometry around the absorbers. The data presented in this work have been collected at the Diamond Light Source, beamline B18, and at the National Synchrotron Light Source II (NSLS-II), at beamline 6-BM, at incident energies of 4996 and 7992 eV for Ti K- and Dy L_3-edges, respectively.

Samples were prepared by grinding a small amount of sample, determined using the ABSORBIX suite of the MAX software, V3.2.,[41] ABSORBIX allows the user to determine the appropriate sample mass depending on the chemical formula, absorber atom and the associated edge. In our case, the masses were determined for Ti K- and Dy L_3 absorption edges for the various compositions studied in this work. To ensure sample homogeneity, the samples were

ground along with 50 mg of cellulose for the Ti K and 100 mg of cellulose for the Dy L_3 edges, for 20 minutes per sample, using a pestle and mortar. The homogenous powders were cold-pressed in a Specac uniaxial hydraulic press. The applied pressure was approximately 40 MPa, for 15 minutes for each sample. The samples presented in this work were measured in both transmission and fluorescence modes. All Ti K-edges were measured in transmission, along with the Dy_2O_3 standard Dy L_3 edge. For the Al, Dy co-doped LADTP system, the Dy L_3 edge XAS were measured in fluorescence mode, since the target atom Dy was available in dilute concentrations (2.5%). Each presented spectrum is an average of 3 spectra.

Data reduction was carried out using ATHENA, a software in the DEMETER package.[42] A linear function is regressed in the pre-edge region, that is 150 eV to 30eV below the edge. By default, a quadratic is regressed in the post-edge region that follows the curvature of the exponential decay of the data, as demonstrated in **Figure 2.6**. The normalized data is obtained by subtracting the pre-edge line from the full spectrum and dividing the data by the edge step $\Delta\mu_0$. The $\Delta\mu_0$ is determined by the difference between the pre- and post-edge lines at the absorption edge energy, E_0.

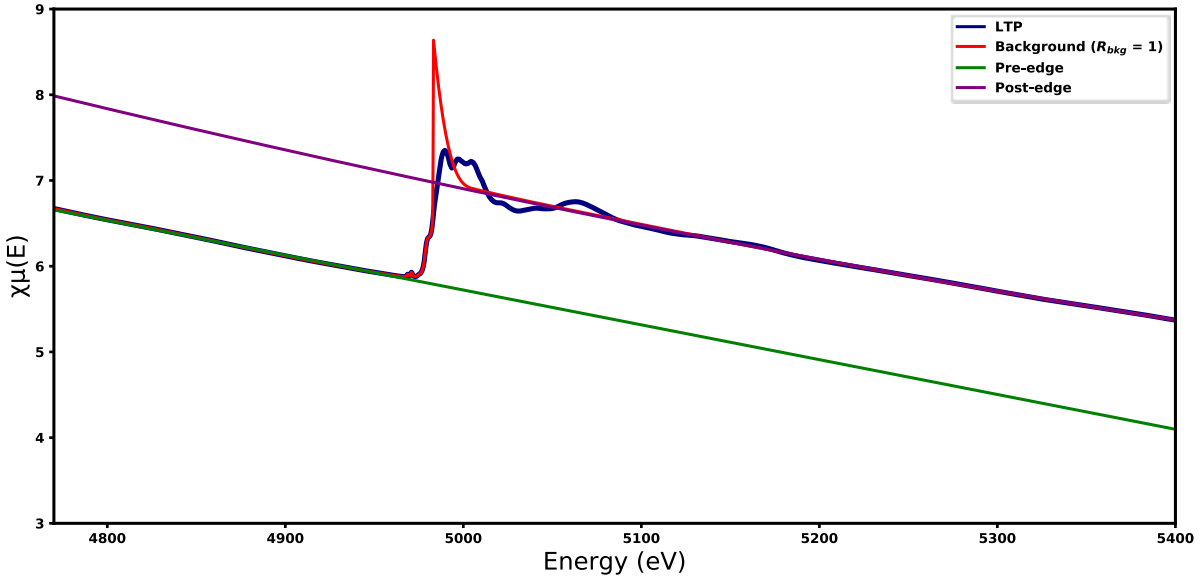


Figure 2.6. The Ti K-edge XAS data demonstrates the pre- and post-edge functions normalization procedure.

The normalized data is then used for further analysis via, for example, methods such as pre-edge fitting for the Ti K-edge data and linear combination fitting of the full spectra to determine the constituent spectra (i.e., materials of varying environments or oxidation states) of an "unknown" sample.

Normalization depends on the pre-edge and post-edge lines as shown in **Figure 2.6**. These are in Energy. The k-range is used for Fourier transformation from k-space to R-space. The R-range is used to define the part of the signal that will be modelled. The full description of pre-analysis data treatment is given in the manuals accompanying the DEMETER software package.[42]

Theoretical XAS – Although the analysis of experimental spectra through methods such as fingerprinting and linear combination fitting may provide both quantitative and qualitative information regarding the environment around the element of interest, it is equally important to determine the source of the observed spectral features through first-principles approaches. The initial important step is an understanding of the structure, typically obtained from other techniques such as PXRD, Raman and IR spectroscopy, and PDF. These "proposed" structures are then used to predict the XANES spectra. The mismatch in theoretical and experimental spectra is used as a method to disqualify a model that describes the local structure of the element of interest.[43] Similar to PDF, we can therefore use XANES to determine local atomic and electronic structure deviations. Extensive work has been done in computational XAS that sought to assign spectral features to experimental observations, particularly for transition metal K-edges.[32, 44-45] In this work, the theoretical XAS spectra were computed for Dy, to determine the local structure of Dy when placed in the 12*c* site of Ti^{4+} in rhombohedral NASICON-type systems. More details on the experimental approach are given in **Chapter 5**. More information on the background and developments and challenges on computational XANES can be found in the listed source.[46-47]

2.2.6. Electrochemical impedance spectroscopy (EIS)

One of the most important properties of solid-state electrolyte materials is the ionic conductivity. Electrochemical impedance spectroscopy is a useful technique in determining the ionic conductivity that can be linked to the average, local atomic and electronic structure of energy materials. EIS provides insights into the multiple interfaces present in the material.[48-50] In EIS, an electrochemical system such as a battery, electrolyte or electrode, is perturbed by an input sinusoidal wave which is potential (or current). An output sinusoidal signal is then measured as a current (or potential).

The input sinusoidal signal is given by:

Equation 8

$$E(t) = E_0 \sin(\omega t)$$

where E_0 is the amplitude of the potential sine wave, ω the angular frequency and t is time. The angular frequency, ω is given by:

Equation 9

$$\omega = 2\pi f$$

where f is the frequency.

The corresponding output current signal equation is similar to that of the input signal, except with a phase angle, ϕ that accounts for the shifts in frequency during system perturbation (equation 10):

Equation 10

$$i(t) = i_0 \sin(\omega t - \phi).$$

EIS is therefore measured across a range of frequencies applied with the same input potential amplitude, E_0, typically from high to low frequencies. The measurable quantities are the impedance, Z, the magnitude $|Z|$ and phase angle ϕ, for which the impedance amplitude is defined as

Equation 11

$$|Z| = \frac{E_0}{i_0}$$

Expressing the equation in terms of the previously stated definitions for the input potential and output current signals,

Equation 12

$$Z = \frac{E_0 \sin(\omega t)}{i_0 \sin(\omega t - \phi)}$$

Which simplifies to

Equation 13

$$Z = |Z|(cos\phi + jsin\phi)$$

where j is the imaginary unit of a complex number. This further simplifies to the complex expression:

Equation 14

$$Z = Z_r + jZ_i$$

After the completion of the measurement, the results are given as a set of five values (given in **Table 2.6**), namely the frequency (*f*), real component of the impedance (Z_r), imaginary component of the impedance ($-Z_i$), impedance magnitude ($|Z|$), and lastly the phase angle (ϕ). The imaginary component of impedance tends to be negative and is therefore given as negative again so that the data can be plotted in the first quadrant as a set of positive values. One can then express the data in the form of a Nyquist plot or a Bode plot.

Table 2.6. Parameters used in the measurement and analysis of EIS and their corresponding units of measurement.

Parameter	**Definition**	**Unit**
f	Frequency	Hertz (Hz)
Z_r	Real component of impedance	Ohms (Ω)
jZ_i	Imaginary component of impedance	Ohms (Ω)
$\|Z\|$	Magnitude of impedance	Ohms (Ω)
ϕ	Phase angle	Degrees (°)

The Nyquist impedance plots, that is plots of Z_r vs $-Z_i$, are used to determine the total resistance which is, in turn, used to determine the total conductivity. A Bode plot is a double-axis plot showing the variation of frequency (*f*) expressed in log scale, against impedance magnitude ($|Z|$), and phase angle (ϕ).

This work only focuses on quantifying the ionic conductivity determined from Nyquist impedance data. The total resistance is the sum of intragranular and intergranular (bulk and grain boundary) resistances, given by equation 15:

Equation 15

$$R_{total} = R_{bulk} + R_{grain\ boundary}$$

The total conductivity is then calculated using the total resistance using:

Equation 16

$$\sigma_{total} = \frac{1}{R_{total}} \times \frac{t}{A}$$

where σ_{total} is the total conductivity in S/cm^2. R_{total} is the total resistance in Ω (equation 15). t is the thickness of the solid electrolyte in cm, and A is the surface area of the solid electrolyte

in cm^2. The resistances are determined through circuit fitting using equivalent circuit models that can include a resistor (R), capacitors (C), inductors (L) and constant phase elements (Q), amongst others.

Determining the validity of EIS results prior to the analysis is essential. For EIS data to be valid, it must satisfy the following three conditions of the Kramers-Kronig relations:

1. Stability: the data must be free of potential decay with time
2. Causality: the input and output signals must only differ by the phase shift angle, with no contributions from noise that would affect the output signal.
3. Linearity: the output must scale with input; the magnitude of impedance must be independent of amplitude and data must follow the principle of superposition.

The Kramers-Kronig relations assist in evaluating the validity of EIS data, governed by the equations below, for real and imaginary impedance, respectively:[51-52]

Equation 17

$$Z_{R(\omega)} = R_{\infty} + \frac{2}{\pi}\int_0^{\infty} \frac{xZ_i(x) - \omega Z_R(\omega)}{x^2 - \omega^2} dx$$

Equation 18

$$Z_{i(\omega)} = \frac{2}{\pi}\int_0^{\infty} \frac{Z_R(x) - Z_R(\omega)}{x^2 - \omega^2} dx$$

To check the validity of EIS after the experiment, the Kramers-Kronig relations are evaluated through fitting a theoretical circuit consisting of any combination of resistors, capacitors and/or inductors. A test case of data validity evaluation for LTP is shown in **Figure 2.7**.

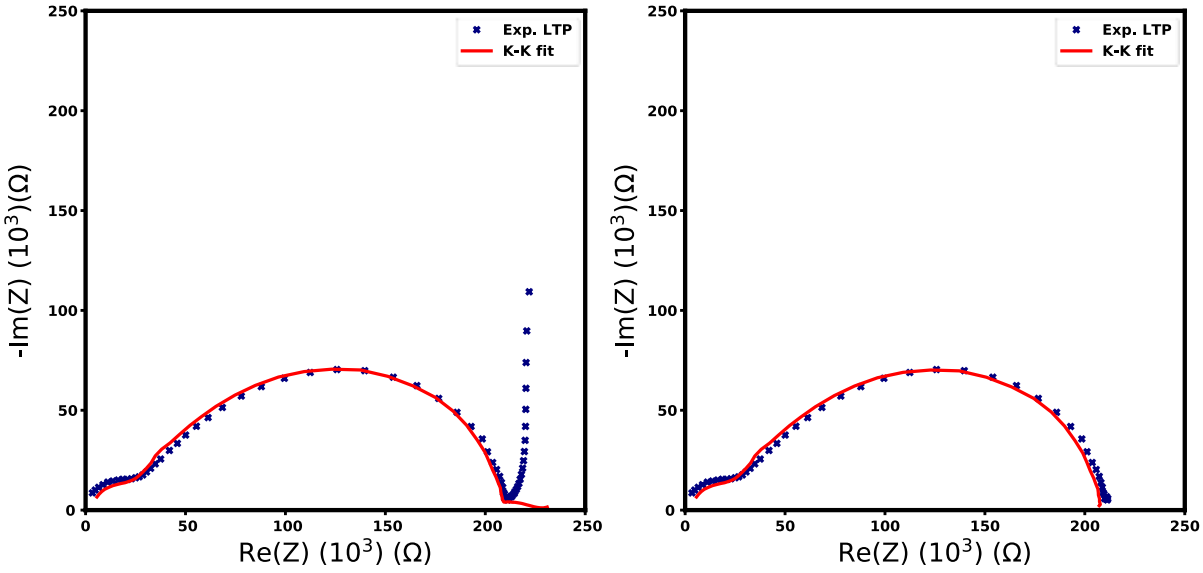


Figure 2.7. A Kramers-Kronig EIS data validity assessment for LTP synthesized via the solid-state reaction at 900 °C where (a) the full dataset was used and (b) the low-frequency data were excluded. The experimental data is shown as blue dots, while the fit is shown as a red line.

The test cases using LTP were evaluated using the full dataset (**Figure 2.7. (a)**) and one wherein the low-frequency region has been excluded (**Figure 2.7. (b)**). The fit results are presented in **Table 2.7.** There was a reasonable fit in the high and medium frequency ranges. However, the low frequency region was not included in the modelling, resulting in larger fit errors. This is largely due to drift shift in the real system data. At low frequencies, it has been stated that it takes longer to complete each sine wave. Furthermore, the qualitative analysis of the Nyquist data showed a suppressed semi-circle, indicative of the system's deviation from being ideal. Therefore, it is reasonable and recommended that the low-frequency data points are excluded from the validity assessment (b). [53] A reasonable fit is obtained upon this exclusion.

Table 2.7. Kramers-Kronig fit results for LTP using the full data set and without the low-frequency region.

Parameter	**Results**	
	Full data set (%)	**Without low-frequency region (%)**
$\Delta Re(Z)$	4.54	6.145
$\Delta Im(Z)$	26.94	8.998
$\Delta \lvert Z \rvert$	2.585	3.609
$\Delta Phase(Z)$	27.1	9.146

The results obtained from EIS experiments are shown as Nyquist plots, whose circuits are explained in more detail in subsequent results chapters. The reader is referred to the listed references for more detailed information.[54]

To determine the total conductivity, the powdered samples were ground in an agate pestle and mortar to ensure homogeneity and pelletized using an 8 mm die, to an approximate thickness in the range of 1 and 2 mm, using a Specac uniaxial hydraulic cold press. The applied pressure was approximately 40 MPa, for 15 minutes for each sample. The resulting pellets were then sintered at temperatures equivalent to the synthesis temperature, in air. The specific details on sintering are outlined in the Experimental section for each Results chapter (i.e., **Chapter 3** and **Chapter 4**).

2.3. References

1. Reddy, I.N., Akkinepally, B., Reddy, C.V., Sreedhar, A., Ko, T.J. and Shim, J., 2020. A systematic study of annealing environment and Al dopant effect on NASICON-type $LiZr_2$ $(PO_4)_3$ solid electrolyte. *Ionics*, *26*, pp.4287-4298.
2. Martínez-Juárez, A., Amarilla, J.M., Iglesias, J.E. and Rojo, J.M., 1997. Ionic conductivity of $LiHf_2(PO_4)_3$ with NASICON-type structure and its possible application as electrolyte in lithium batteries. *Journal of the Brazilian Chemical Society*, *8*, pp.261-264.
3. Mustafa, M., Rani, M.S.A., Adnan, S.B.R.S., Salleh, F.M. and Mohamed, N.S., 2020. Characteristics of new $Mg_{0.5}(Zr_{1-x}Sn_x)_2(PO_4)_3$ NASICON structured compound as solid electrolytes. *Ceramics International*, *46*(18), pp.28145-28155.
4. Xu, H., Wang, S., Wilson, H., Zhao, F. and Manthiram, A., 2017. Y-doped NASICON-type $LiZr_2(PO_4)_3$ solid electrolytes for lithium-metal batteries. *Chemistry of Materials*, *29*(17), pp.7206-7212.
5. Goodenough, J.B. and YP, H., 1976. Hong and JA Kafalas. *Mater. Res. Bull*, *11*, p.203.
6. Leng, Y., 2013. *Materials characterization: introduction to microscopic and spectroscopic methods*. John Wiley & Sons.
7. Pecharsky, V.K. and Zavalij, P.Y., 2003. *Fundamentals of diffraction* (pp. 99-260). Springer US.
8. *DIFFRAC.EVA: software to evaluate X-ray diffraction data*. Version 4.3. https://www.bruker.com/eva.
9. Fan, C. and Zhao, Z. eds., 2018. *Synchrotron Radiation in Materials Science: Light Sources, Techniques, and Applications*. John Wiley & Sons.
10. Billinge, S.J., 2004. The atomic pair distribution function: past and present. *Zeitschrift für Kristallographie-Crystalline Materials*, *219*(3), pp.117-121.
11. Putz, H. and Brandenburg, K., 1997. Match!–Phase Analysis Using Powder Diffraction, Crystal Impact. *GbR, Kreuzherrenstr. 102, 53227 Bonn, Germany*
12. Rietveld, H.M., 1969. A profile refinement method for nuclear and magnetic structures. *Journal of applied Crystallography*, *2*(2), pp.65-71.
13. Post, J.E. and Bish, D.L., 1989. Rietveld refinement of crystal structures using powder X-ray diffraction data. *Modern powder diffraction*, *20*, pp.277-308.

14. Young, R.A. and Wiles, D.B., 1980. Application of the Rietveld method for structure refinement with powder diffraction data. *Advances in X-ray Analysis*, *24*, pp.1-23.
15. Bergerhoff, G., Brown, I.D. and Allen, F., 1987. Crystallographic databases. *International Union of Crystallography, Chester*, *360*, pp.77-95.
16. Zagorac, D., Müller, H., Ruehl, S., Zagorac, J. and Rehme, S., 2019. Recent developments in the Inorganic Crystal Structure Database: theoretical crystal structure data and related features. *Journal of applied crystallography*, *52*(5), pp.918-925.
17. Vaitkus, A., Merkys, A. and Gražulis, S., 2021. Validation of the crystallography open database using the crystallographic information framework. *Journal of applied crystallography*, *54*(2), pp.661-672.
18. Black, D.R., Windover, D., Henins, A., Gil, D., Filliben, J. and Cline, J.P., 2010. Certification of NIST standard reference material 640d. *Powder Diffraction*, *25*(2), pp.187-190.
19. Bond, W.L. and Kaiser, W., 1960. Interstitial versus substitutional oxygen in silicon. *Journal of Physics and Chemistry of Solids*, *16*(1-2), pp.44-45. Billinge, S.J., 2019.
20. Dinnebier, R.E., Leineweber, A. and Evans, J.S., 2018. *Rietveld refinement: practical powder diffraction pattern analysis using TOPAS*. Walter de Gruyter GmbH & Co KG.
21. The rise of the X-ray atomic pair distribution function method: a series of fortunate events. *Philosophical Transactions of the Royal Society A*, *377*(2147), p.20180413.
22. Egami, T. and Billinge, S.J., 2003. *Underneath the Bragg peaks: structural analysis of complex materials*. Elsevier.
23. Fan, C. and Zhao, Z. eds., 2018. *Synchrotron Radiation in Materials Science: Light Sources, Techniques, and Applications*. John Wiley & Sons.
24. Dinnebier, R.E. and Billinge, S.J. eds., 2008. *Powder diffraction: theory and practice*. Royal society of chemistry.
25. Proffen, T., Billinge, S.J.L., Egami, T. and Louca, D., 2003. Structural analysis of complex materials using the atomic pair distribution function—A practical guide. *Zeitschrift für Kristallographie-Crystalline Materials*, *218*(2), pp.132-143.
26. Hammersley, A.P., 2016. FIT2D: a multi-purpose data reduction, analysis and visualization program. *Journal of Applied Crystallography*, *49*(2), pp.646-652.
27. Kaufmann, E.N., 2003. *Characterization of Materials, 2 Volume Set* (p. 1392).
28. Turrell, G. and Corset, J. eds., 1996. *Raman microscopy: developments and applications*. Academic Press.

29. Baddour-Hadjean, R. and Pereira-Ramos, J.P., 2010. Raman microspectrometry applied to the study of electrode materials for lithium batteries. *Chemical reviews*, *110*(3), pp.1278-1319.
30. Powers, L., 1982. X-ray absorption spectroscopy application to biological molecules. *Biochimica et Biophysica Acta (BBA)-Reviews on Bioenergetics*, *683*(1), pp.1-38.
31. Newville, M., 2014. Fundamentals of XAFS. *Reviews in Mineralogy and Geochemistry*, *78*(1), pp.33-74.
32. Cabaret, D., Bordage, A., Juhin, A., Arfaoui, M. and Gaudry, E., 2010. First-principles calculations of X-ray absorption spectra at the K-edge of 3d transition metals: an electronic structure analysis of the pre-edge. *Physical Chemistry Chemical Physics*, *12*(21), pp.5619-5633.
33. Rehr, J.J. and Albers, R.C., 2000. Theoretical approaches to x-ray absorption fine structure. *Reviews of modern physics*, *72*(3), p.621.
34. Frenkel, A.I., Pease, D.M., Giniewicz, J., Stern, E.A., Brewe, D.L., Daniel, M. and Budnick, J., 2004. Concentration-dependent short-range order in the relaxor ferroelectric (1− x) Pb (Sc, Ta) O_3− x $PbTiO_3$. *Physical Review B*, *70*(1), p.014106.
35. Kerr, B.V., King, H.J., Garibello, C.F., Dissanayake, P.R., Simonov, A.N., Johannessen, B., Eldridge, D.S. and Hocking, R.K., 2022. Characterization of energy materials with X-ray absorption spectroscopy─ advantages, challenges, and opportunities. *Energy & Fuels*, *36*(5), pp.2369-2389.
36. Komyoji, D., Yoshiasa, A., Moriga, T., Emura, S., Kanamaru, F. and Koto, K., 1992. EXAFS study of the fluorite-type compounds in the systems (1− x) $ZrO_{2-x}YbO_{1.5}$ (x= 0.18≦ x≦ 0.5) and $Zr_2Ln_2O_7$ (Ln= Tb, Dy, Ho, Er, and Yb). *Solid State Ionics*, *50*(3-4), pp.291-301.
37. Andreeva, A.Y., Pankin, I.A., Sukhikh, T.S., Kravtsova, A.N., Konchenko, S.N., Kozlova, S.G. and Soldatov, A.V., 2019. Application of X-ray absorption spectroscopy for L_3-edges of Dy and Yb in dibenzoylmethanide complexes: Experiment and theoretical interpretation. *Journal of Molecular Structure*, *1188*, pp.205-213.
38. Löble, M.W., Keith, J.M., Altman, A.B., Stieber, S.C.E., Batista, E.R., Boland, K.S., Conradson, S.D., Clark, D.L., Lezama Pacheco, J., Kozimor, S.A. and Martin, R.L., 2015. Covalency in lanthanides. An X-ray absorption spectroscopy and density functional theory study of $LnCl_6^{x-}$(x= 3, 2). *Journal of the American Chemical Society*, *137*(7), pp.2506-2523.

39. Piccinelli, F., Carrasco, I., Ma, C.G., Srivastava, A.M. and Bettinelli, M., 2018. Disorder-induced breaking of the local inversion symmetry in rhombohedral pyrochlores $M_2La_3Sb_3O_{14}$ (M= Mg or Ca): a structural and spectroscopic investigation. *Inorganic Chemistry*, *57*(15), pp.9241-9250.
40. Willinger, E., Massué, C., Schlögl, R. and Willinger, M.G., 2017. Identifying key structural features of IrO_x water splitting catalysts. *Journal of the American Chemical Society*, *139*(34), pp.12093-12101.
41. Alain, M., Jacques, M., Diane, M.B. and Karine, P., 2009, November. MAX: multiplatform applications for XAFS. In *Journal of Physics: conference series* (Vol. 190, No. 1, p. 012034). Iop Publishing
42. Ravel, B and Newville, M., 2005. ATHENA, ARTEMIS, HEPHAESTUS: data analysis for X-ray absorption spectroscopy using IFEFFIT. Journal of synchrotron radiation, 12(4), pp.537-541.
43. Calvin, S., 2013. *XAFS for Everyone*. CRC press.
44. Bohr, F., Ruiz-López, M.F. and Muñoz-Páez, A., 1993. A multiple-scattering approach to the study of X-ray absorption spectra of anatase and rutile. *Catalysis letters*, *20*, pp.59-71.
45. Uozumi, T., Okada, K., Kotani, A., Durmeyer, O., Kappler, J.P., Beaurepaire, E. and Parlebas, J.C., 1992. Experimental and theoretical investigation of the pre-peaks at the Ti K-edge absorption spectra in TiO_2. *Europhysics Letters*, *18*(1), p.85.
46. Rehr, J.J. and Ankudinov, A.L., 2001. Progress and challenges in the theory and interpretation of X-ray spectra. *Journal of Synchrotron Radiation*, *8*(2), pp.61-65.
47. Nesvizhskii, A.I., 2001. *Theory and Interpretation of L-shell X-ray Absorption Spectra*. University of Washington.
48. Bredar, A.R., Chown, A.L., Burton, A.R. and Farnum, B.H., 2020. Electrochemical impedance spectroscopy of metal oxide electrodes for energy applications. *ACS Applied Energy Materials*, *3*(1), pp.66-98.
49. Vadhva, P., Hu, J., Johnson, M.J., Stocker, R., Braglia, M., Brett, D.J. and Rettie, A.J., 2021. Electrochemical impedance spectroscopy for all-solid-state batteries: Theory, methods and future outlook. *ChemElectroChem*, *8*(11), pp.1930-1947.
50. Chen, S., Zhao, Y., Yang, J., Yao, L. and Xu, X., 2017. Hybrid solid electrolytes with excellent electrochemical properties and their applications in all-solid-state cells. *Ionics*, *23*, pp.2603-2611.

51. Agarwal, P., Orazem, M.E. and Garcia-Rubio, L.H., 1993. Application of the Kramers-Kronig relations in electrochemical impedance spectroscopy. *ASTM Special Technical Publication*, *1188*, pp.115-115.
52. Esteban, J.M. and Orazem, M.E., 1991. On the application of the kramers-kronig relations to evaluate the consistency of electrochemical impedance data. *Journal of the Electrochemical Society*, *138*(1), p.67.
53. https://pineresearch.com/shop/kb/knowledge-category/eis-theory/ (accessed 23 October 2023, 23:46)
54. Macdonald, D.D., 1990. Review of mechanistic analysis by electrochemical impedance spectroscopy. *Electrochimica Acta*, *35*(10), pp.1509-1525.

Chapter 3: Exploring the structure-property relationships in Sn-substituted $LiTi_2(PO_4)_3$

3.1. Introduction

The need for better energy storage devices such as batteries has been one of the driving forces behind the research on Li^+-ion batteries (LIBs). To this extent, $LiTi_2(PO_4)_3$ (LTP) and its solid solutions have been researched for their potential application as solid-state electrolytes in LIBs.[1] LTP belongs to the Na Super Ionic Conductors (NASICONs) family, a structure-type to which $NaZr_2(PO_4)_3$ belongs, with *R-3c* space group. The structure of LTP consists of TiO_6 octahedra corner-linked to PO_4 tetrahedra, bonded helically to form a three-dimensional network as depicted in **Figure 3.1**. The conducting ion, Li^+, tunnels through this rigid framework, resulting in ionic conductivity. Li^+ can occupy two sites in the structure: the more energetically favored M1 site at *6b* Wyckoff position (6-fold O coordination) and the M2 site, which consists of an eight to ten-fold oxygen environment.[1-4] The currently accepted overall migration path of Li^+ is M1-M2-M1 along the c-axis.

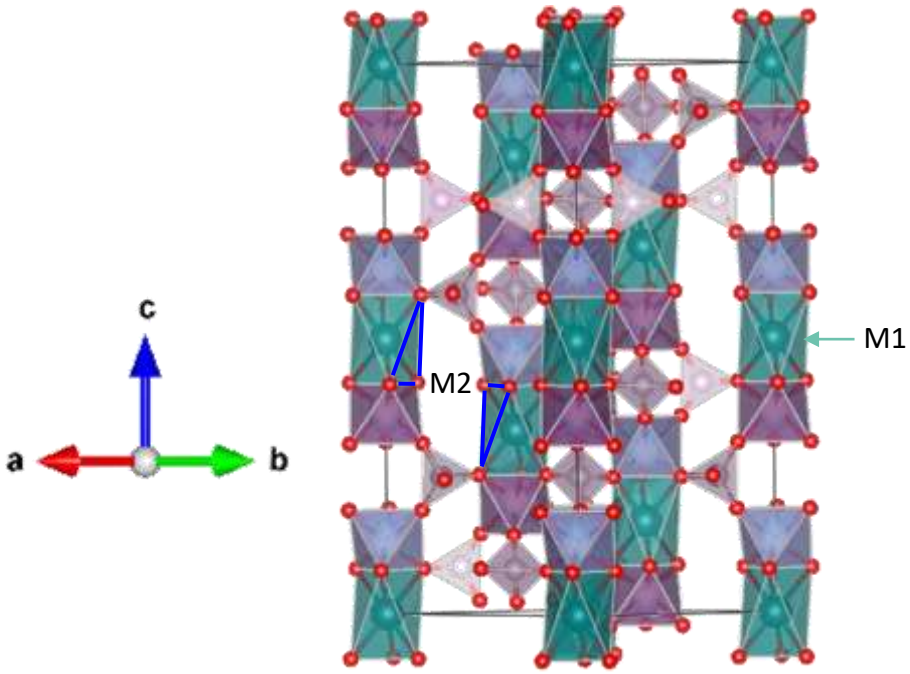


Figure 3.1. Unit cell depiction of the NASICON-type $LiTi_2(PO_4)_3$ belonging to the *R-3c* space group. It consists of Ti/SnO_6 octahedra corner-linked to PO_4 tetrahedra. Li^+ occupies M1.

The currently reported ambient temperature conductivity of LTP is too low for applications as a solid-state electrolyte, in the order of 10^{-7} S/cm.[3, 5-8] The highest known conductivity in NASICONs is for the Al^{3+}-doped $Li_{1.3}Al_{0.3}Ti_{1.7}(PO_4)_3$ (LATP), in the order of 10^{-3} S/cm.[8] To improve the ionic conductivity, a bottleneck which is formed by the two oxygens in TiO_6 and one oxygen in PO_4, forming a lateral face of a triangle going into the M2 site (**Figure 3.2.**) must be increased/optimized.

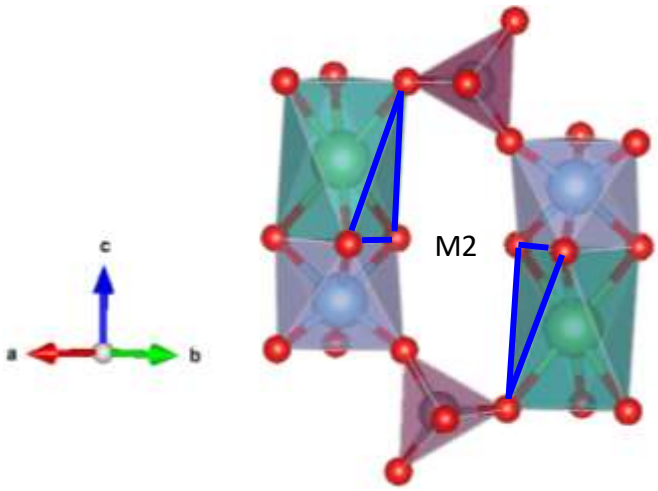


Figure 3.2. A zoomed-in depiction of the lateral faces of LiO_6 octahedra. Highlighted in blue is the bottleneck formed by three O atoms (blue triangles), going into the M2 void.

This can be done via lattice site substitution of Ti^{4+} by isovalent (M^{4+}) and aliovalent (M^{3+}; M= Sc, Ga, Al) cations. Studies on the substitution of Ti^{4+} with isovalent cations such as Hf^{4+}, Zr^{4+} and Sn^{4+} have been done; the addition of a cation with a larger ionic radius improves the conductivity by forming larger bottlenecks. Larger bottleneck size results in easier Li^+ migration within the structure.[9, 10] In a review article, Bachman *et al.*[5] state that doping with M^{4+} cations resulted in an increase in ionic conductivity by up to four orders of magnitude. First-principles studies on the migration mechanism of Li^+ ions within the NASICON framework have been done, with varying substituents. Since there are two possible sites wherein Li^+ can sit, the six-fold M1 site exhibited lower activation energy compared to the M2 site, which is ten-fold oxygen-coordinated in geometry. Doping with isovalent cations such as Sn^{4+} allows for alteration of these energy barriers. However, the local structural distortions caused by the larger Sn^{4+} cation need to be understood, as well as their effects on conductivity.[4] Previous studies where Sn^{4+} was used as a substituent have been done. However, in the work done by Bounar and colleagues,[1] larger substitution increments were considered (10%

increments of Sn^{4+}). This did not provide sufficient information on the effects of incorporating Sn^{4+} in smaller amounts on the structure of LTP and its properties. Another study by Rao *et al.*,[11] explored the structural and conductivity effects of Sn-doping at 5, 10 and 25% Sn. In this work, we seek to explore the effect of lower dopant content on the structure of LTP and its effect on enhancing the ionic conductivity.

3.2. Experimental section

3.2.1. Synthesis

$LiTi_2(PO_4)_3$, as well as the Sn^{4+}-doped formulations, were synthesized following the conventional solid-state mechanism.[1] Stoichiometric amounts of Li_2CO_3, $(NH_4)_2HPO_4$, TiO_2 and SnO_2 were ground into a fine powder in an agate pestle and mortar for twenty minutes. The ground precursors were placed into an alumina crucible and heated at 450 °C for one hour under air. Upon cooling, the decomposed samples were ground for one hour before being annealed at 900 °C for eight hours under the constant flow of nitrogen gas. The obtained products were then stored for characterization.

3.2.2. Characterization

Powder X-ray diffraction (PXRD)

PXRD was employed as the primary characterization technique in this work to establish the phase compositions and XRD phase purities of the products. The room temperature XRD data were collected in-house, using the *Bruker D2 Phaser* diffractometer, equipped with a Co tube and a Lynxeye PSD detector. The obtained data were analyzed using DIFFRAC. EVA V4 to identify the phases in the materials under investigation. TOPAS-Academic V6 and 7 were used to carry out the non-linear least squares Rietveld refinements.[12] This gave insights into the phase compositions as well as information on the structure of the materials in question.

Room temperature Raman spectroscopy (RS)

Vibrational modes of the materials under study were investigated via Raman spectroscopy (RS) at an excitation wavelength of 514 nm. The spectra were recorded in the range of 100-1200 cm^{-1} calibrated using a Si standard with an error of ± 0.4 cm^{-1}. The instrument is fitted with a Symphony CCD detector, cooled with nitrogen.

X-ray absorption spectroscopy

XAS of Ti K-edges (4966 eV) were recorded at the Core-XAS beamline B18 at Diamond Light Source, for Sn-LTP compositions, under ambient conditions. XANES measurements were also done on TiO_2 Degussa P-25 for reference. Data were recorded in transmission mode using a Si (111) double-crystal monochromator, with the storage ring running at 3.0 GeV and approximately 300 mA ring current. The samples were ground into fine powders, along with 50 mg of cellulose (AVICEL PH-101, ~50 μm cellulose, Sigma-Aldrich) as the diluent. The homogeneous powder + diluent mixtures were pressed into 13 mm diameter pellets using a Specac uniaxial hydraulic cold press. Three nitrogen-filled ionization chamber detectors set up in series to measure the incident intensity (I_0), the transmitted intensity through the sample (I_t), as well as the transmitted intensity by the reference metal foil (I_{ref}).[13] XANES evaluation was carried out on an average of three independent scans for every sample. Each scan was imported along with the reference channel data for energy calibration. The calibrated scans were then merged to produce a single scan per sample composition. The edge energy, E_0 was determined as the maximum of the first derivative. The background removal was conducted with an Rbkg of 1 and a k-weight of 2.0 $Å^{-1}$ in the range 0 to 14.8 $Å^{-1}$. No spline clamps were used at low energy ranges, while strong spline clamps were applied at high energy. The Fourier transform was performed on the k-space data weighted with k-weight of 2.0 $Å^{-1}$, using the range from 3.00 to 12.8 $Å^{-1}$. EXAFS fitting was performed with ARTEMIS software of the DEMETER package.

Electrochemical impedance spectroscopy (EIS)

The obtained powders were pressed into pellets using an 8 mm die and an average thickness of 1.35 mm using a Specac uniaxial hydraulic cold press. The pellet thicknesses were measured after sintering using a Vernier scale. The applied pressure was approximately 40 MPa. These pellets were sintered in air for 8 hours at 900 °C. Two layers of Au/Pd electrodes of approximately 5 nm thickness each were sputter-coated onto either side of the pellets. Room temperature impedance measurements were done using a BioLogic VMP300 potentiostat, using a four-probe, two-electrode system. The frequency range was 10^{-1}-10^{-6} MHz with a sinus amplitude of 100 mV and no DC bias. The BioLogic EC-Lab V11.27 (demonstration version) software was employed in the data analysis.

3.3. Results and Discussion

3.3.1. Powder X-ray Diffraction (PXRD)

X-ray diffraction data showed that the products consisted of two phases: the major NASICON-type phase, belonging to the *R-3c* space group (LTP, ICSD collection code 95979) as well as an impurity phase of TiP_2O_7 (ICSD 83831) in all samples under investigation, shown in **Figure 3.3**. Lattice constants for undoped LTP were obtained from Rietveld refinement, and they were found to be 8.511 and 20.864 Å for the '*a'* and '*c'* constants, respectively. The literature values were reported to be 8.512 and 20.858 Å for '*a'* and '*c'*, respectively in samples that were considered phase-pure.[2 - 3]

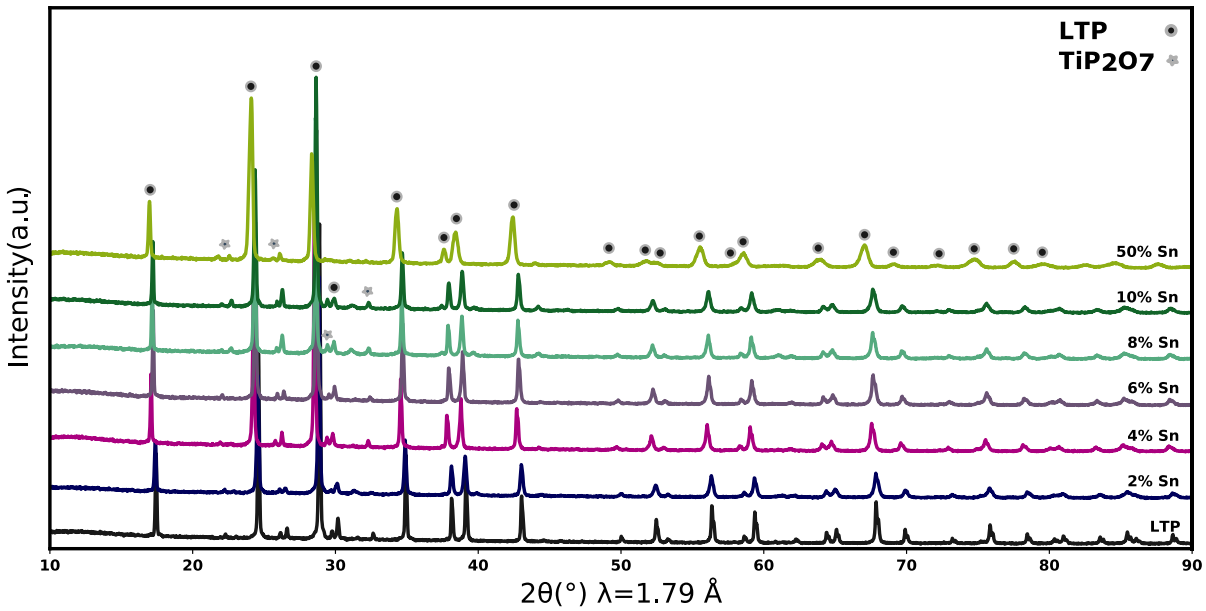


Figure 3.3. XRD patterns of the NASICON-type Sn^{4+}-doped materials $LiTi_{2-x}Sn_x(PO_4)_3$ (for 0, 2, 4, 6, 8, 10 and 50 mole % Sn^{4+}).

Table 3.1. shows the structural parameters that were obtained from Rietveld refinement for all compositions. Based on the reported errors, the Sn^{4+}-substituted LTP phases showed lattice constants along the *a* (=*b*) axis to be within standard error for LTP and 4 up to 10% Sn compositions, indicating that there was no significant contraction or expansion along the *a*-axis. However. 2% Sn exhibited a lower value along the *a*-axis, relative to LTP. As can be observed across the various compositions, the variation in the *a* lattice constant showed a relatively non-systematic change, compared to that of the *c*-axis.

The addition of Sn results in the preferential expansion of the *c*-axis, attributed to the slight displacement of Li atoms at 6*b* to more stables positions within the structure.[4] At 50% Sn, we saw significant unit cell expansion along the *a*-axis, indicating the successful replacement of Ti by Sn at the 12*c* site.

Table 3.1. The lattice parameters of undoped and Sn^{4+}-doped LTP phases, obtained from XRD, via Rietveld refinement (as implemented in TOPAS-Academic).

Composition	**Lattice parameters**		**Cell volume**	**XRD phase purity**
	a (Å)	**c (Å)**	**($Å^3$)**	**% (Sn)LTP**
$LiTi_2(PO_4)_3$	8.511(1)	20.864(4)	1308.731(5)	98.17
2% Sn-LTP	8.505(2)	20.899(9)	1309.171(1)	98.78
4% Sn-LTP	8.511(2)	20.903(8)	1311.331(9)	97.45
6% Sn-LTP	8.514(2)	20.914(7)	1313.047(8)	98.39
8% Sn-LTP	8.511(2)	20.910(1)	1311.656(1)	96.39
10% Sn-LTP	8.513(2)	20.929(1)	1313.530(1)	96.66
50% Sn-LTP	8.5700(3)	21.152(1)	1345.352(1)	83.54

As NASICON-type LTP systems have been previously reported to show preferential unit cell expansion along the *c*-axis, significant changes are noted along the *c*-axis. The 2 up to 8% Sn compositions showed statistically similar values along the c-axis, relative to the undoped LTP system. A notable increase along the *c*-axis was observed for 10 and 50% Sn, regardless of the noticeable phase separation at 50% Sn.

Figure 3.4 shows the variation in cell volume with increasing lattice site substitution, showing that a maximum is reached at 6% Sn content. A significant deviation from linearity for 8 and 10% Sn was observed, showing that these two compositions are outliers (closer to LTP volume) in the series. This may be due to less Sn^{4+} being incorporated into the structure, shown by the higher impurity content. However, the missing Sn content could have formed an amorphous phase which could not be detected from traditional PXRD methods. The linear regression line equation was determined to be $y = 0.6906x + 1307.8$. For 50%, the PXRD quantitative phase analysis showed a Sn-bearing impurity content of approximately 15% (14.67%). Using the standardless Rietveld quantitative phase analysis methodology, the amount of Sn that was incorporated into the NASICON-type main phase was approximately 38.34%.

As such, using the best fit line through the data, the expected cell volume at this concentration determined using linear extrapolation is 1334.28 Å^3. Furthermore, the y-intercept from the linear regression line yielded an LTP cell volume of 1307.8 Å^3, which compared well to what was obtained experimentally.

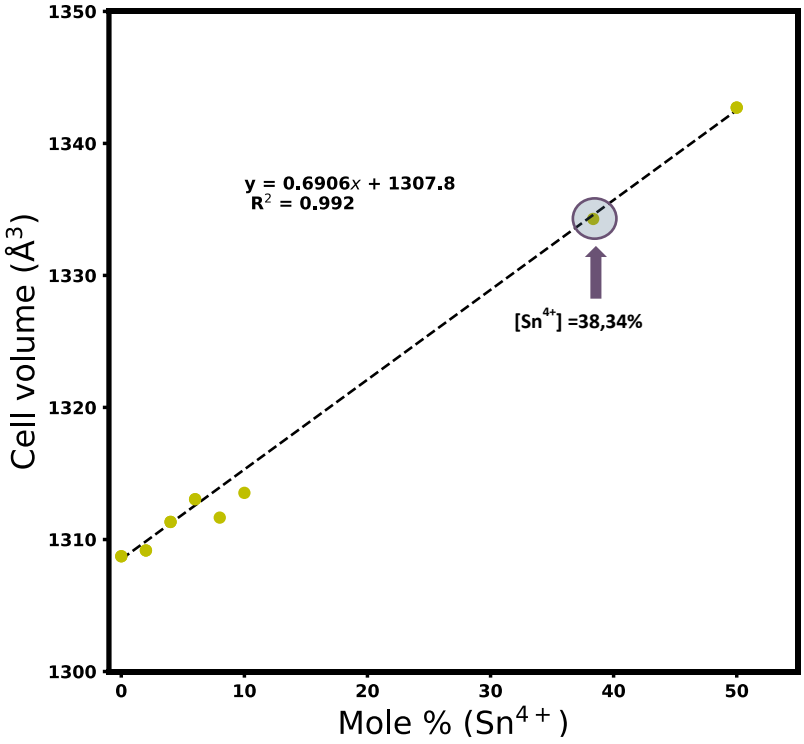


Figure 3.4. The variation of cell volume with increasing Sn^{4+} content in NASICON-type $LiTi_{2-x}Sn_x(PO_4)_3$. A linear trend is observed for LTP to 6% Sn-LTP. The [Sn^{4+}] incorporated into LTP was determined to be 38.34% using the standardless Rietveld phase analysis methodology, with a corresponding cell volume of 1334.28 Å^3.

It is expected that for materials with a larger cell volume relative to LTP, the total corresponding room-temperature conductivity would be higher. This is attributed to the larger tunnel size as a function of increasing Ti^{4+} lattice site substitution with Sn^{4+} (which has a larger cationic radius, r = 0.69 Å in an octahedral environment relative to Ti^{4+}, (r = 0.605 Å according to Shannon[14])) resulting in increased migration of Li^+ ions in the NASICON structure. This effect occurs because the larger Sn^{4+} ion causes an enlargement of the MO_6 octahedra, thus increasing the bottleneck size for ion transport.[10] However, it is worth noting that some of the samples contained a higher impurity phase than others. The presence of TiP_2O_7 has been reported to decrease the grain boundary conductivity in NASICON-type electrolyte materials.[3] Therefore, one would expect slightly lower grain-boundary conductivities in the lower XRD phase-pure compositions.

Peak broadening, which was more apparent at 50% substitution, was also observed as the lattice site substitution increased. Microstructural effects such as smaller crystallite size for doped formulations and relatively poorly crystalline Sn^{4+}-LTP might not be the only cause of this peak broadening. It may also be attributed to peak overlap because of the presence of $LiSn_2(PO_4)_3$ (LSP, ICSD 83831), another phase that has a NASICON-type structure, with the lattice parameters being slightly higher (a = 8.586 Å, c = 21.266 Å). The noted peak asymmetry served as evidence to this possibility, as shown in **Figure 3.5**.

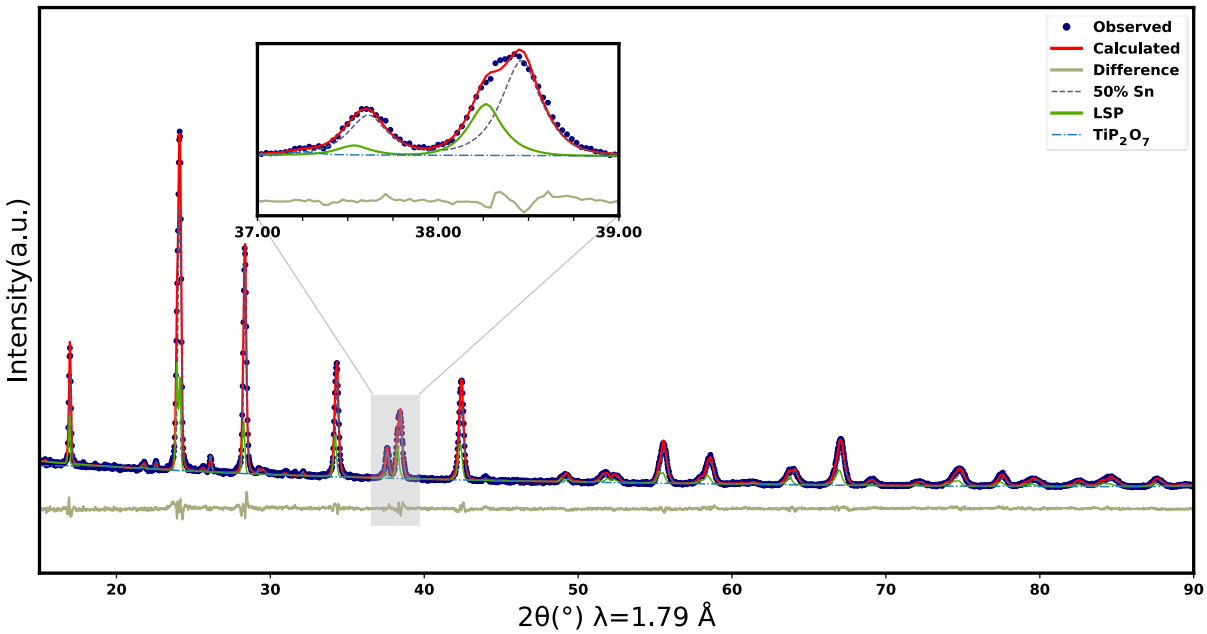


Figure 3.5. A Rietveld refinement result of 50% Sn-LTP and zoomed inset showing the presence of two isostructural phases, $LiTiSn(PO_4)_3$ (Sn-LTP) and $LiSn_2(PO_4)_3$ (LSP). 'Observed' = Experimental data; 'Calculate' = Theoretical data obtained from the input structures.

A similar study by Francisco *et al.*,[15] where the Ge^{4+} site in $LiGe_2(PO_4)_3$ (r = 0.53 Å) was substituted by Sn^{4+} (LGSP), found that the Sn^{4+}-containing formulation showed broad peaks, indicative of overlap of LGSP and $LiSn_2(PO_4)_3$ phases, similar to our study.[15, 16] Rietveld refinement results of LTP and the lower Sn-LTP compositions did not show any significant mismatches between the observed data and the calculated model. The crystallographic information for all compositions is provided in the **Supplementary Information**.

3.3.2. Room-temperature Raman spectroscopy (RS)

Raman spectroscopy was used to confirm the phase compositions of the materials under study, and to further probe the effects of doping on the local structure of LTP. As already mentioned, lattice site substitution of Ti^{4+} by larger cations such as Sn^{4+} causes local structural distortions. The Raman spectra (**Figure 3.6**) confirmed that there were only two phases present, namely the NASICON-type LTP phase and the TiP_2O_7 impurity phase (denoted by an asterisk). However, this technique did not provide much insight into the presence of the isostructural $LiSn_2(PO_4)_3$ phase. It is expected that the vibrational modes of this structure overlapped with those of the main phase structure, Sn^{4+}-LTP, as seen in XRD.

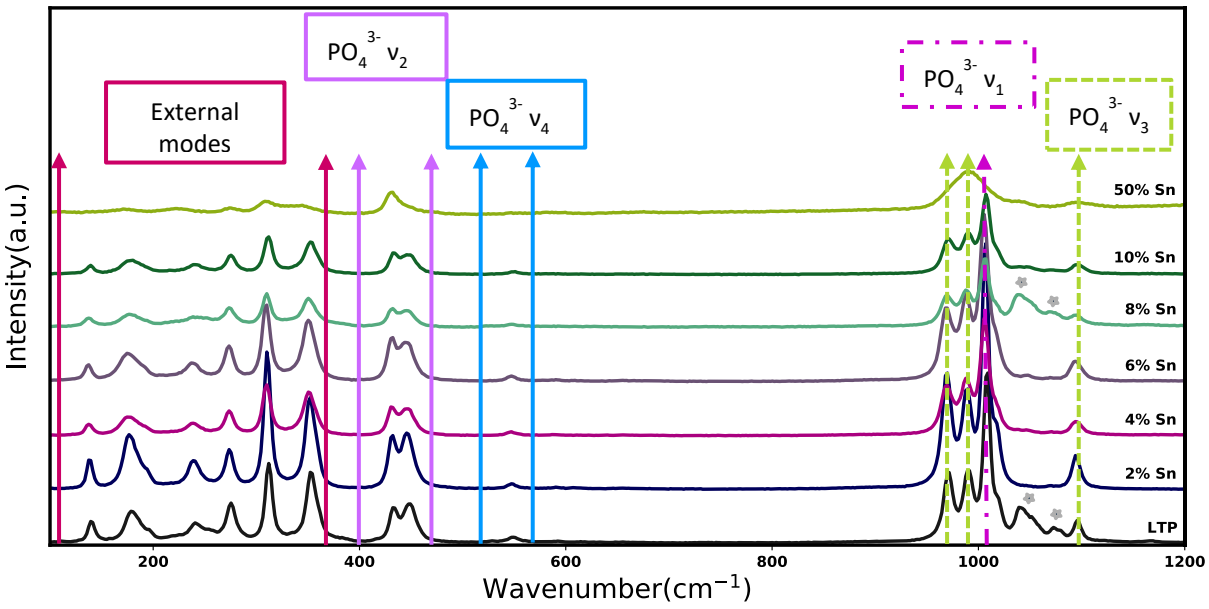


Figure 3.6. Raman spectra of Sn^{4+}-LTP electrolyte materials recorded at room temperature with an excitation wavelength of 514 nm.

The observed Raman bands are separated into external modes that occur in the region below 350 cm^{-1} and internal vibrations that consist of symmetric and antisymmetric stretching and bending modes occurring above approximately 350 cm^{-1}.[11] External vibrations (lattice phonon modes) correspond to the translational vibrations of Li^+, Ti^{4+}/Sn^{4+} and pseudo-rotations of the PO_4^{3-} anion groups. Internal modes largely consist of intramolecular stretching and bending movements of the PO_4^{3-} anion groups. Further discussions of the NASICON compositions' spectra follow.

External modes

The vibrational modes below 350 cm^{-1} consist of Li^{+} translations, M^{4+} translations as well as PO_4^{3-} translations and pseudo rotations. In the NASICON structure, Li^{+} occupies a site with an *S6* symmetry thus making the ion's translation Raman-inactive.[21] The peaks are therefore modes for M^{4+} and PO_4^{3-} anions.

Raman bands of M^{4+} cations are susceptible to mass effects and their shifts give insight into local structural changes. The peak at 139.5 cm^{-1} in LTP shifted to 137.5 cm^{-1} regardless of Sn^{4+} concentration. The A_{1g} band at 178.5 cm^{-1} also shifted towards lower wavenumbers (176.6 cm^{-1}) for 2% Sn-LTP and moved even further at higher concentrations to 174.6 cm^{-1}.

At 238.8 and 273.6 cm^{-1}, there was almost no peak shift observed and the peaks were ascribed to PO_4^{3-} pseudo rotations and/or translations. Significant lattice site substitution by Sn^{4+} at 50% led to a further shift from 238.8 to 221.3 cm^{-1}. This significant shift is rationalized by understanding that the surrounding, corner-sharing PO_4^{3-} anions were significantly distorted by the expansion of MO_6 octahedra caused by Sn^{4+}. Giarola *et al.*,[21] attributed the band at 273.6 cm^{-1} strictly to a PO_4^{3-} translation since it was not affected by mass effects.

PO_4^{3-} bending modes

The region between 380 and 600 cm^{-1} corresponds to the symmetric (ν_2) and antisymmetric (ν_4) bending modes of the PO_4^{3-} anions. Symmetric modes generally occur at lower wavenumbers relative to antisymmetric modes.[22] The symmetric bending mode occurring at 432.4 cm^{-1} did not show any shifts, while the band at 447.5 cm^{-1} shifted only slightly as Sn^{4+} content increased. Since the PO_4 tetrahedra are corner-linked to MO_6 octahedra, the exchange of Ti^{4+} for Sn^{4+} causes an increase in the volume of the MO_6 octahedron by a change in the M^{4+}-O bond length, from considering average Ti-O against Sn-O bond lengths. To accommodate the local structural change, the adjacent polyhedra become distorted and/or rotated, thus affecting the vibrational motion of PO_4^{3-}.[21, 23] This distortion of PO_4^{3-} tetrahedra is evident from the peaks merging into one, thus becoming broader, especially at 50% Sn-LTP.

PO_4^{3-} stretching modes

Symmetric (ν_1) and antisymmetric (ν_3) stretching modes of the PO_4^{3-} tetrahedra are observed at higher wavenumbers: 800 to 1100 cm^{-1}. LTP is characterized by the presence of three peaks of increasing intensity occurring at 969.8, 989.5 and 1007.3 cm^{-1}, respectively.

The symmetric stretch appears as the peak with the highest intensity, at 1007.3 cm^{-1}. This is because symmetric stretches have high Raman scattering cross-sections.[22]

The peaks at 969.8, 989.5 and 1094 cm^{-1} belong to the antisymmetric stretching of PO_4^{3-} polyhedra. This assignment is due to the lower intensities of these peaks, relative to the symmetric mode.

The peak broadening observed for 50% Sn-LTP specifically at the 900 to 1007 cm^{-1} region may be indicative of the poor long-range order in this specific composition, further agreeing with results from XRD. In this study, we speculate that broadening is due to the shared peaks by the NASICON phases Sn-LTP and LSP.

Although Li^+ occupies the M1 site in both these structures, its interaction with differently distorted environments might have caused the observed peak broadening. However, this remains unclear and could not hold for $LiSn_2(PO_4)_3$ since, in single M^{4+} NASICON materials, PO_4^{3-} distortions are insignificant. Therefore, the broadening is attributed largely to the distortions of MO_6 octahedra in the main phase, Sn-LTP.[15] The decrease in intensity of the symmetric stretch at 1007 cm^{-1} for 50% Sn-LTP is also indicative of a change in symmetry of the PO_4^{3-} polyhedra because of high Sn^{4+} content. Similarly, the antisymmetric stretches also showed a significant decrease in intensity at 50% Sn-LTP. These changes in symmetry are therefore attributed to polymorphism at the local level in these NASICON-type Sn-LTP structures. The peak assignments and positions are given in **Supplementary Information**.

3.3.3. Probing the local and medium-range structure: Ti K-edge X-ray absorption spectroscopy (XAS)

It is important to understand the effects of changes of local and average structure of the materials in this study, to better understand how these changes influence the properties. In probing the materials further, X-ray absorption spectroscopy (XAS) was employed. The analyses of the X-ray absorption near-edge structure (XANES) and the extended x-ray absorption fine structure (EXAFS) provided insights into the electronic structure of the absorbing atom, Ti, and the local-range order, respectively, in NASICON-type compounds.

An extensive amount of literature is based on the study of Ti in compounds such as the anatase and rutile phases of TiO_2,[24-28] ilmenite-type compounds $FeTiO_3$,[28] and perovskites such as $CaTiO_3$.[30] In most cases, these studies have entailed both experimental work, and theoretical computational analyses exploring the effects of multiple scattering events. Exploring both experimental and computational approaches of studying these materials leads to a better understanding of their structures.

In the available literature for NASICON-type materials, the study by Wang *et al.*,[31] evaluated the sodium storage mechanism in Sodium vanadium titanium phosphate. However, they did not discuss the observed features in their Ti K-edge XANES in depth, nor did they study the changes in local structure by EXAFS. Therefore, the observations made in this study were done by considering different spectra of Ti-containing materials, TiO_2, $FeTiO_3$ and $CaTiO_3$ that have been reported in literature, bearing in mind that the surrounding atoms differ for a qualitative analysis based on the fingerprinting approach, as discussed in **Chapter 2**. It is also important to note that the TiO_6 clusters in each of these compounds possess varying distortions despite all of the clusters being octahedral. XANES is important to understanding the coordination number, spin states and oxidation state of Ti.

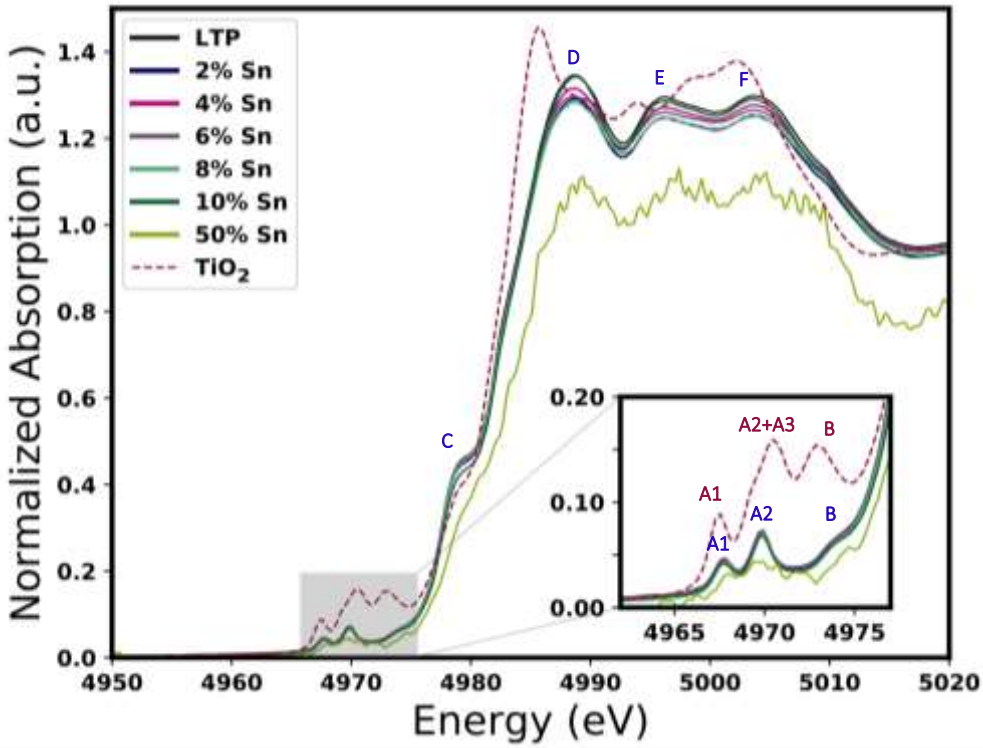


Figure 3.7. Normalized Ti K-edge XANES spectra of Sn-LTP compositions synthesized at 900 °C. The zoomed inset shows the pre-edge features. The spectrum for TiO_2 (Degussa P-25; anatase: rutile = 87:13) is included for reference.

The Ti K-edge XANES spectrum, at 4+ oxidation state is characterized by the presence of 3 pre-edge features (labelled A1, A2 and B in **Figure 3.8** inset). The first feature, A1, is assigned to the core-hole effect on the Ti absorbing atom that is coupled with quadrupolar transitions.[25, 27, 31] The next two features, A2 and B, correspond to the hybridization-induced dipolar transitions from the 1*s* to the empty 3*d*-t_{2g} and 3*d*-e_g empty states, respectively.

In first-principles calculations by Cabaret *et al.*,[32] simulations of the Ti K pre-edge region showed that the presence of a core-hole in the absorbing Ti especially affected the energy positions of the two local transitions 1*s* to 3*d*-t_{2g}, and 1*s* to 3*d*-e_g by shifting them to lower energies. The A1 feature was absent in the simulation that excluded the core-hole contribution. The non-centrosymmetric nature of the C_3 symmetry of Ti in TiO_6 octahedra of LTP allowed for the mixing of *p*-*d* orbitals, where the empty *p*-states of the absorbing Ti atom, hybridized with the empty 3*d* states of the absorbing Ti atom, hence relaxing the dipole selection rule of ***ΔL=1***, allowing for *s* to *d* transitions.

The splitting of the 3*d* orbitals is attributed to the removal of the degeneracy because of the metal-ligand interactions, thus it is imperative to understand the crystallographic structure and how the metal-ligand bonding affects *d*-orbital splitting. Since the peaks were assigned via the fingerprinting method by comparing to the TiO_2 spectrum, it is important to understand the average structure of the standard. The structure of the TiO_2 reference sample was determined from PXRD analysis with Rietveld refinement. The results are presented in the Supplementary Information (**Figure S3.2** and **Table S3.3**), showing the presence of both anatase and rutile (~ 87% : 13% anatase to rutile). Therefore, the standard's XAS spectrum is largely that of anatase. The geometry of the TiO_6 cluster in TiO_2 shows a [4+2] distortion of the Ti-O bonds, which is a classic tetragonal distortion of an octahedral environment.

This is different to NASICON-type formulations, showing a trigonal distortion of [3+3] nature.[18] The implication of the difference in the *d*-orbital splitting is in the intensities and energies of the pre-edge features. **Figure 3.8** shows a representation of *d*-orbital splitting across various environments. Niltharach and colleagues,[27] observed that the difference in relative peak intensities were attributed to the differences in the crystal structure and the detailed octahedron shapes of TiO_6 clusters.

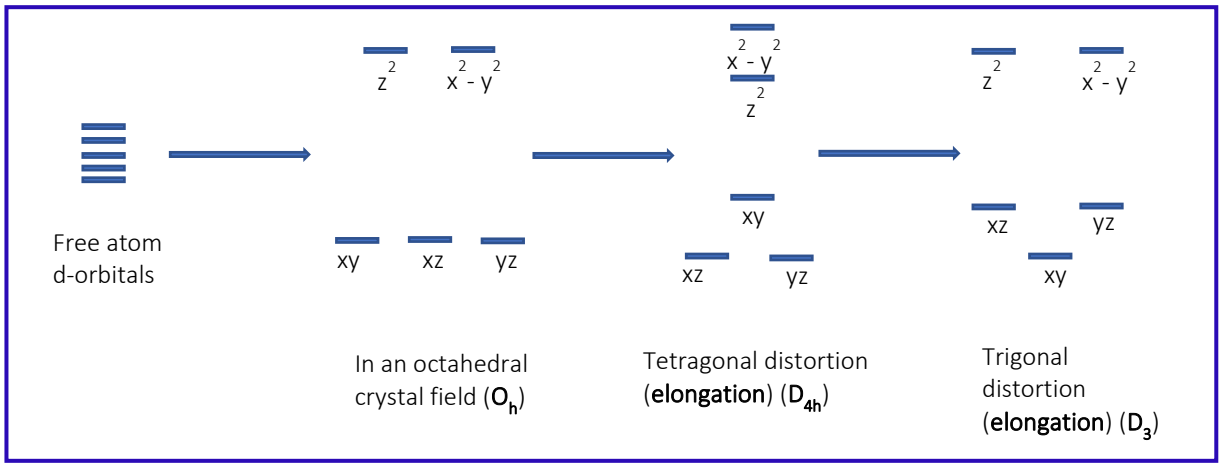


Figure 3.8. The splitting of atomic d-orbitals in the presence of a ligand field with different distortions.

The A1 and A2 features in Sn-LTP compositions are symmetrical, unlike those in TiO_2. Phoohinkong *et al.*,[29] deconvoluted the A2 feature in TiO_2 to 'A2+A3', showing that the local symmetry around the Ti absorbing atom had a distorted octahedron to tetragonal, with Jahn-Teller distortion. In our study, the distortion is an elongation trigonal distortion of the TiO_6 octahedron.

The reported energies of pre-edge features in rutile are 4968.7, 4971.0 and 4972.1 eV (A1 to A3, respectively),[24] and for Sn-LTP, these appeared at slightly lower energies of 4967.7 and 4969.8 eV for features A1 and A2. The difference in the order of orbitals (tetragonal Ti environment in TiO_2 vs trigonal Ti environment in Sn-LTP) may be the reason behind the absence of the A3 feature and the shifts in energy between rutile and Sn-LTP compositions.

Feature A3 in TiO_2 was attributed to the non-local, electric quadrupolar transition from 1*s* to 4*p*, where the empty *p*-states of the absorbing atom are hybridized with empty 3*d* states of the Ti second neighbors.[32]

In this work, the lower Sn-doped compositions (0 to 10%) showed no significant difference in peak intensity, however at 50% Sn, although present, the pre-edge features were quite low in intensity. Lower pre-edge peak intensity could be indicative of the poor crystallinity at this high dopant content. This may also suggest that there was a change in the symmetry, from a trigonally distorted octahedral Ti system to a more symmetric, near-perfect octahedral Ti environment. However, the noise in the 50% Sn-LTP data is too high to indicate any local changes in symmetry. Although the shown spectrum is an average of 3 spectra and the data was deglitched, the noise was not sufficiently removed to make any notable conclusions based on the pre-edge peak analysis.

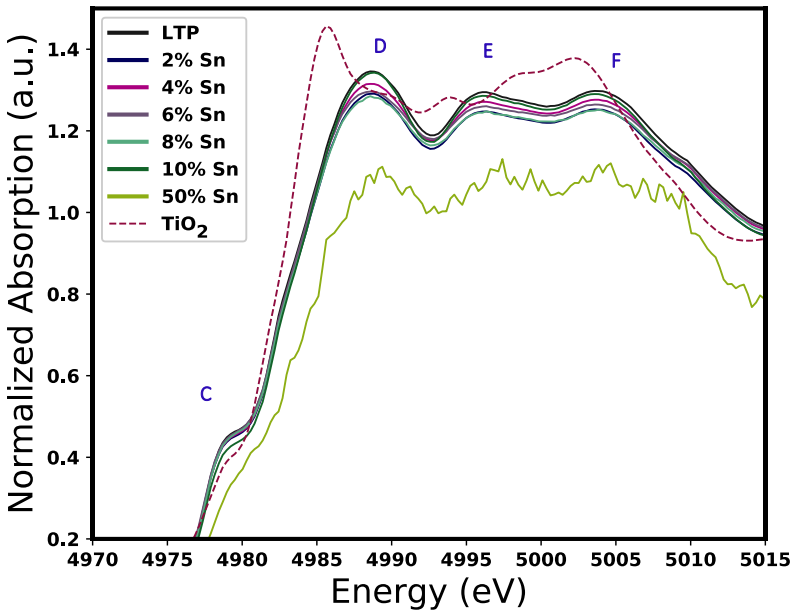


Figure 3.9. A magnified view of the near-edge region of normalized XANES spectra of the Ti K-edge, for Sn-LTP formulations.

Figure 3.9 shows the rising edge and post-edge features. The shoulder (feature C) corresponds to the 1*s* to 4*p* transition. Although there was no clear trend observed for the lower dopant concentrations of 2 to 8% Sn, at 10% Sn, there was a decrease in the observed normalized intensity. Increasing Sn^{4+} content to 50% Sn produced an even greater decrease. This may be indicative of the poor crystallinity and phase mixture observed at 50% Sn.

The three post-edge features labelled D, E and F were said to be due to electronic transitions from 1*s* to the 4*p* orbitals in the continuum states that have b_{1u}, b_{2u} and b_{3u} character, respectively, hybridized with neighboring O 2*p* states of the same symmetry, attributing these features to the multiple scattering of the ejected photoelectron wave from the central absorbing atom to the nearest neighbors.[24-26]

In TiO_2, these bands appear at 4984, 4992 and 5004 eV, respectively; however, in NASICON-type Sn-LTP, they correspond to 4988.6, 4996.2 and 5003.9 eV, respectively. Unsubstituted LTP had the highest normalized intensity across all three post-edge features, suggesting a relatively ordered structure. As the lattice site substitution of Ti^{4+} by Sn^{4+} increased from 2 to 8%, a non-systematic decrease in intensity was noted. However, at 10% Sn^{4+}, the comparable intensity to that of LTP could suggest that although the presence of Sn^{4+} caused local-range distortions, the structure was still reasonably ordered. The decreased intensity in 50% Sn-LTP suggested that the high Sn^{4+} content may have caused significant changes in the local-medium range order, resulting in significantly poor crystallinity of the NASICON-type structure.

These results were consistent with Raman spectroscopy results, which suggested a similar conclusion: a large amount of Sn^{4+} in the structure led to the poor crystallinity of the resultant structure.

To further study the effects of lattice site substitution of Ti^{4+} by Sn^{4+} on the local structure of Sn-LTP compositions, extended X-ray absorption fine structure (EXAFS) data were considered (**Figure 3.10**). The k^2-weighted EXAFS spectra were fitted using the NASICON-type LTP structure model (ICSD collection code 95979) in the Artemis software,[33] to generate scattering paths. The built LTP model was obtained using a cluster size of 8.0 Å, with longest path being 5 Å.

The *k*-space stacked plot of Sn-LTP and TiO_2 compositions are presented in **Figure 3.10 (a)**. The oscillations are similar for the NASICON-type systems for 0 to 10% Sn, while at 50% Sn, the oscillations are noisy. The Sn-LTP systems data look similar up to ~ 12 $Å^{-1}$, after which the noise supersedes the available usable data. The k-space data for the TiO_2 standard has similar spectral signatures to the Sn-LTP compositions, indicating that the compositions have similar oxidation states and nearest neighbour interactions.

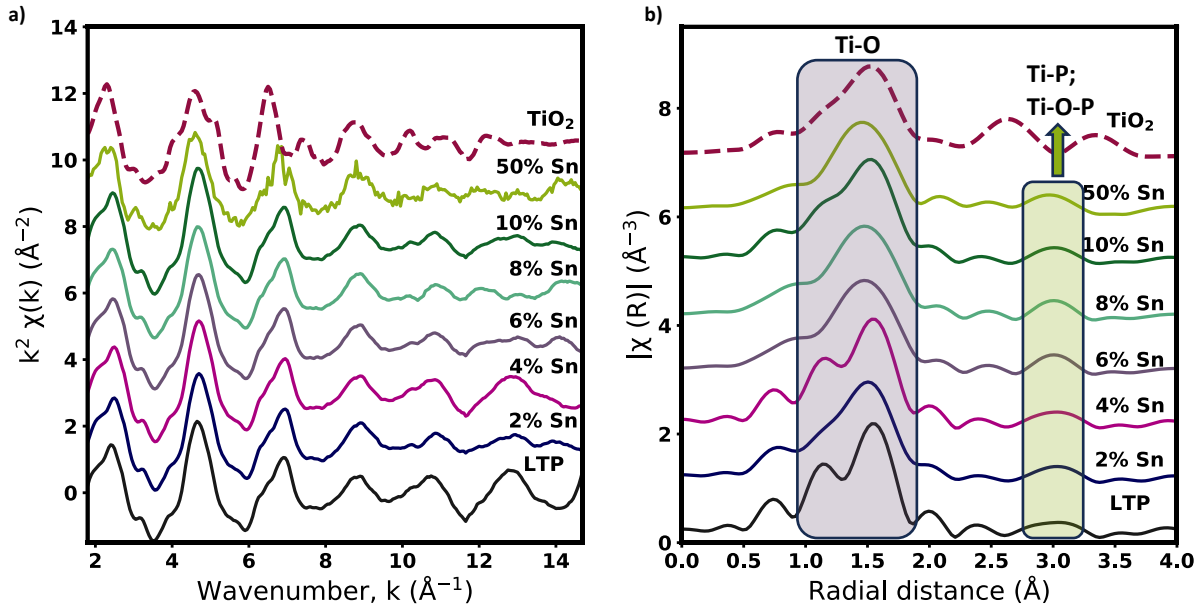


Figure 3.10. Ti K-edge: (a) Stacked k^2 χ(k) data and (b) Fourier-transformed (FT) k^2 weighted EXAFS spectra for Sn-LTP compositions (no phase correction). Highlighted peaks correspond to the Ti-O single scattering, Ti-P single scattering and Ti-O-P multiple scattering shells.

At high *k* (> 12 $Å^{-1}$), the oscillations are relatively poor for Sn-LTP systems in comparison to the TiO_2 standard, possibly indicating a lower degree of symmetry in NASICON-type systems than in TiO_2 as seen in the XANES spectra. It can be noted that the *R*-space data (**Figure 3.10 (b)**) show a low r shoulder across all compositions including the standard. The shoulder is attributable to slightly inaccurate background removal (at R_{bkg} of 1 Å). However, increasing the R_{bkg} to 1.2 Å resulted in an *R*-range that is not enough to cover the entire first peak of the FT-EXAFS spectra.

The EXAFS fits were performed by varying the Debye-Waller factor (σ^2), shift in edge energy (ΔE_0), and the change in radial distance (ΔR) across all three paths. In total, 7 fitted parameters were evaluated ($1 \times \Delta E_0$; $3 \times \sigma^2$; $3 \times \Delta R$). The fitting ranges were 1 to 3.4 Å and 3 to 12.8 $Å^{-1}$ for R and k, respectively. The coordination numbers (N) were kept constant as per the crystal structures for TiO_2 and LTP. The starting values for the refined parameters were as follows: $\Delta E_0 = 0$; $\sigma^2 = 0.003$; $\Delta R = 0$). The amplitude reduction factor, S_0^2 was obtained from the refinement of the TiO_2 standard and the value of 0.786 was kept constant across the EXAFS fits of the NASICON-type systems.

Carrying out the fit with two separate O paths (to account for the [3+3] distortion in NASICON) resulted in strong correlations, such that the Debye-Waller (σ^2) factor became negative for the second Ti-O path, suggesting that the fitting model was incorrect. Therefore, N for the Ti-O shells were set to 6 regardless of the structures showing [4+2] and [3+3] distortions for the TiO_6 octahedra for TiO_2 and LTP, respectively. An average Ti-O bond distance of 1.928 and 1.95 Å for LTP and TiO_2, respectively, were then used as starting values. The assumption of a perfect octahedral system resulted in a stable σ^2 to account for the distortion. The EXAFS fit results are presented in **Table 3.2**. The accompanying fits are presented in the Supplementary Information (**Figure S3.4**).

Table 3.2. EXAFS fit results for Sn-LTP compositions. The amplitude reduction factor S_0^2 was kept constant at 0.786. The coordination numbers (*N*) were also kept fixed as per the published structure of LTP. *R* the radial distance, σ^2 the Debye-Waller factor, and ΔE_0 is the shift in the edge energy. The R-factor determines the quality of the fit.

Composition	Shell	N	R (Å)	σ^2 (Å^2)	ΔE_0 (eV)	R-factor (%)
LTP	Ti-O	6	1.94(6)	0.003(2)	3.034 ± 2.209	6.68
	Ti-P	3	3.26(1)	0.003(2)		
	Ti-O-P	6	3.369(4)	0.004(4)		
2% Sn-LTP	Ti-O	6	1.93(5)	0.0040(7)	2.571 ± 1.706	2.48
	Ti-P	3	3.23(3)	0.001(3)		
	Ti-O-P	6	3.35(2)	0.004(2)		
4% Sn-LTP	Ti-O	6	1.95(6)	0.0033(8)	4.048 ± 2.119	5.33
	Ti-P	3	3.26(1)	0.002(5)		
	Ti-O-P	6	3.36(1)	0.004(4)		
6% Sn-LTP	Ti-O	6	1.94(6)	0.0040(7)	3.247 ± 1.737	2.56
	Ti-P	3	3.25(2)	0.001(2)		
	Ti-O-P	6	3.36(1)	0.003(2)		
8% Sn-LTP	Ti-O	6	1.94(5)	0.0045(7)	2.581± 1.813	3.11
	Ti-P	3	3.24(3)	0.000(2)		
	Ti-O-P	6	3.35(2)	0.003(2)		
10% Sn-LTP	Ti-O	6	1.94(6)	0.0033(8)	3.274 ± 1.987	3.59
	Ti-P	3	3.26(1)	0.001(4)		
	Ti-O-P	6	3.36(1)	0.003(3)		
50% Sn-LTP	Ti-O	6	1.93(5)	0.0050(7)	-0.463 ± 1.861	3.00
	Ti-P	3	3.25(2)	0.001(2)		
	Ti-O-P	6	3.36(1)	0.033(2)		

The first peak at ~1.95 Å is attributed to the Ti-O single scattering shell. The distance was noted to be quite similar, within the error margins, across all the Sn-LTP compositions. Similarly, the second peak corresponding to the Ti-P single scattering path, and the Ti-O-P multiple scattering path showed little to no variation across the various compositions. This suggests that the local geometry around, particularly, the TiO_6 motif does not show significant distortions as a result of doping.

No significant changes in polyhedral distortions were noted from the EXAFS analysis of the Ti-P interactions, to corroborate the findings from Raman spectroscopy.

The shift in energy from the absorption edge was also noted to not change significantly with changing compositions. At 50% Sn, the fitted energy shift was negative, largely attributable to the high noise level in the data, regardless of the deglitching procedures and averaging 3 scans during the data normalization process. No deductions were made about the presence of the isostructural LSP phase, from the perspective of Ti XAS. Although XAS is an insightful, element-specific technique, the EXAFS analysis has not shown any significant changes in the polyhedral distortion.

3.3.4. Ambient-temperature conductivity studies

Impedance measurements conducted at ambient temperature sought to understand the structure-property correlations in Sn-doped LTP NASICON materials. The data shown in **Figure 3.11** were fitted using the Randomise + Simplex minimization method, as described in the EC-Lab software manual. Since starting values of the fits are unknown, the Randomise method allows the software to establish starting values of the model that are then used as starting values for further minimization using the Simplex minimization algorithm (formally known as the Downhill Simplex algorithm,[33] or the Nelder and Mead algorithm,[34]) least-squares fitting of the data, to the equivalent circuit (EC) model.

The model is made up of two semicircles, one consists of a resistor (R) and constant phase element (Q) arranged in parallel; the second semicircle was modelled with a resistor in series with a finite Warburg element (Mg), both in parallel with a constant phase element to model the low frequency region corresponding to the electrode response of the Li^+ ion blocking process at the Au/Pd electrodes.[10-28] Estimates were derived via the maximum conditions of relaxation frequency (ω), given by the equation 19, where *R* is the resistance estimated from the x-intercepts of the semi-circles and *C* corresponds to the capacitance:

Equation 19

$$\omega(Hz) = \frac{1}{R(\Omega) \times C(F)}$$

Conductivity (σ) is given by equation 20, where L is the thickness of the pelletized material, R being the resistance and S as the surface area of the sample pellet:

Equation 20

$$\sigma\ (S/cm) = \frac{L\ (cm)}{R\ (\Omega) \times S(cm^2)}$$

Capacitances indicate the respective regions that influence the ion migration in the material. At high frequency, the semi-circle modelled gave information about the bulk (intragranular) conductivity (≈10^{-11} F) and intermediate frequency corresponded to grain boundary (intergranular) conductivity (≈10^{-9} F). Lastly, the Li-ion blocking at the electrodes (sample-electrode interfaces) occurred in the low-frequency region. These regions were assigned according to their respective capacitances.[10, 15, 35-36] An α value of 1 indicates an ideal capacitor, and as such, since a constant phase element, Q, is not an ideal capacitor, the value for α will deviate from 1.

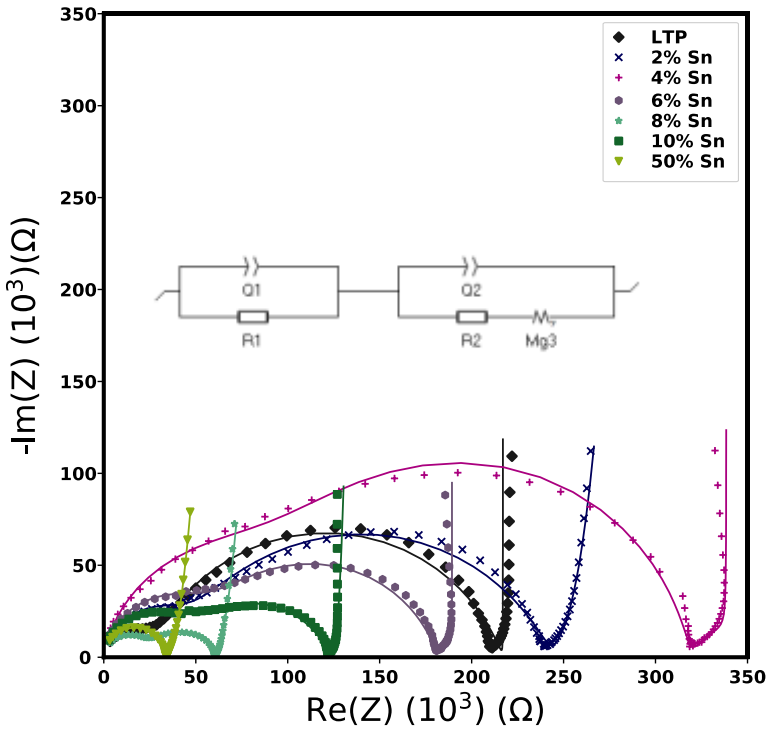


Figure 3.11. Fitted Nyquist plots for Sn^{4+}-LTP phases (0-10, 50 mole % Sn^{4+}) and the EC model used in data fitting.

These results showed that LTP in this work has a comparable conductivity relative to literature-reported values that are in the order of 10^{-6} to 10^{-7} S/cm.[2, 5-8] Desirable solid-state electrolytes should have significantly higher conductivities, ranging at 10^{-3} to 10^{-4} S/cm, such as those observed in $L_{1.3}Al_{0.3}Ti_{1.7}(PO_4)_3$, the most conductive NASICON-type compound. [2-3, 5-6, 8, 35]

Table 3.3. The room temperature conductivity results for Sn^{4+}-substituted NASICON-type LTP formulations. The 8% Sn formulation showed the highest bulk and grain boundary conductivities, while 50% Sn-LTP showed the highest total conductivity (highlighted)

Composition	**σ_{bulk} (S/cm)**	**σ_{gb} (S/cm)**	**σ_{total} (S/cm)**
LTP	9.54×10^{-6}	1.27×10^{-6}	1.12×10^{-6}
2% Sn-LTP	6.21×10^{-6}	1.25×10^{-6}	1.04×10^{-6}
4% Sn-LTP	2.85×10^{-6}	1.19×10^{-6}	8.40×10^{-7}
6% Sn-LTP	4.87×10^{-6}	1.99×10^{-6}	1.41×10^{-6}
8% Sn-LTP	1.05×10^{-5}	6.54×10^{-6}	4.03×10^{-6}
10% Sn-LTP	5.61×10^{-6}	3.10×10^{-6}	2.00×10^{-6}
50% Sn-LTP	7.10×10^{-6}	-	7.10×10^{-6}

The presence of a secondary phase, TiP_2O_7, at the grain boundaries significantly decreases grain boundary conductivity, since grain boundary conductivity is the rate-determining step in ionic conduction, the total conductivity also decreased.[2] The Sn^{4+}-substituted formulations had variable amounts of TiP_2O_7, with a maximum of approximately 3.61% for 8% Sn-LTP.

The 50% Sn^{4+}-LTP composition showed the highest bulk conductivity. This observation supported the predictions from structural analysis. Rietveld refinement results suggested that at this composition, the cell volume was the highest, at 1342.714 $Å^3$ for all doped formulations. Since the addition of Sn^{4+} was hypothesized to result in lattice expansion, and by extension, increased bottleneck size, it follows that 50% Sn-LTP would exhibit the highest bulk conductivity of all the Sn-LTP compositions, as seen in **Table 3.3**.

Although the 8 and 10% were the outliers regarding their comparable phase purities (96.39 and 96.66%, respectively), the bulk conductivity of 8% Sn-LTP was higher than that of 10% Sn-LTP, supporting that phase purity is not the only factor playing a role in the observed conductivity results. Also, the grain boundary conductivity at 8% Sn^{4+} was higher than for all other compositions, except for 50% Sn-LTP. The 8% Sn-LTP was an outlier because its cell volume (1311.656 $Å^3$) was smaller than that of 10% Sn-LTP (1313.530 $Å^3$), while they have comparable phase purities.

Table 3.4. The changes in Li-O2 bond lengths, M1 void volume, V_{M1}, and Ti/SnO_6 (V_{MO6}) octahedral volumes obtained from Rietveld refinement results for Sn-LTP compositions.

Composition	Li-O2 bond length (Å)	V_{M1} (Å^3)	V_{MO6} (Å^3)
LTP	2.232(6)	12.687(6)	8.927(9)
2% Sn-LTP	2.229(6)	12.611(3)	9.044(4)
4% Sn-LTP	2.214(6)	12.372(0)	9.048(8)
6% Sn-LTP	2.229(6)	12.556(0)	9.027(4)
8% Sn-LTP	2.244(8)	12.839(1)	9.320(9)
10% Sn-LTP	2.250(7)	12.926(1)	9.350(9)
50% Sn-LTP	2.284(1)	13.666(6)	10.348(6)

The PXRD analysis showing the Li-O2 bond length, M1 (6*b*) void volume and MO_6 (12*c*) void volume is shown in **Table 3.4**. The 2% Sn-LTP system showed a contraction in M1 void volume, contrary to what is expected with partial replacement of Ti with larger Sn. However, other compositions from 4 to 50% showed a systematic increase in the size of the M1 void occupied by Li. This is indicative of successful partial replacement of Ti with Sn, as expected. The 12*c* MO6 octahedra showed an increase in volume upon doping with 2% Sn, while an overlap was noted in the volume of 2 to 4%. At 6% Sn, a unexpected decrease in the void volume was observed, attributed to the possibility of secondary TiP_2O_7 phase's effect on the real stoichiometry of the system. Also, as previously noted, some Sn^{4+} may have formed amorphous phases that are undetectable from PXRD. An increase in the12*c* void volume was also observed for compositions 8 to 50%. These void volumes overlapped.

The data showed that the longest Li-O2 bond was obtained for 50% Sn-LTP. This explains the high total conductivity. Longer Li-O2 bond distances suggest larger M1 voids.

The first-principles study by Lang and colleagues found that doped LTP compositions with larger M1 voids have lower activation energy for Li^+ migration at this site, hence the higher intragranular conductivity.[4] Also, at 50% Sn-LTP, the MO_6 octahedra were the largest. There was no plausible explanation for the high bulk conductivity observed at 8% Sn-LTP. Understanding the effects of lattice site substitution on the M1 void volumes would explain the changes in the bottleneck sizes, hence the conductivity in the structure.[38] The high M1 volume exhibited by 50% Sn composition further supports the high total conductivity obtained for the composition.

Studying local structural disorders through Raman spectroscopy showed that 8% of Sn^{4+}-LTP exhibited distortions of PO_4 polyhedra to a lesser extent than 50% Sn-LTP. As discussed earlier, lattice site substitution causes local triclinic disorders. Therefore, at 50% Sn^{4+}, the distortions are well distributed within the structure, resulting in trapped Li^+ ions in M1 voids and higher activation energies.[14]

Li^+-ion trapping occurs because the MO_6 octahedra counteract the said local distortions by rotating about the c-axis resulting in a narrowing of the bottleneck. This means that although ideally one would expect a higher substituent content to result in higher conductivity, the experimental results support the observations made by Lang *et al.*,[4] that there can only be an optimum allowed substituent percentage before Li-ion trapping comes into play. Through our study, the optimum allowed substituent concentration would be in the range of 8 to 10% Sn^{4+}.

3.4. Conclusions

In this work, we sought to understand structure-property correlations in Sn^{4+}-substituted $LiTi_2(PO_4)_3$ formulations. The XRD results confirmed the average structure, showing that Sn^{4+}-LTP phases belong to the NASICON-type, rhombohedral structure, with the *R-3c* space group (#167). A persistent impurity phase of TiP_2O_7 was found in all compositions. The qualitative phase analyses were further confirmed by Raman spectroscopy, which confirmed the presence of NASICON-type LTP structure and a TiP_2O_7 impurity phase. Raman spectroscopy also gave insight into the effects of doping on the local order of the structure, showing that the lattice site substitution of Ti^{4+} by the isovalent Sn^{4+} cation led to some local distortions around the PO_4^{3-} anion groups.

XANES gave further insight into the local environment around the Ti absorbing atom, showing that all compositions maintained the Ti^{4+} state and no significant changes in the crystallinity of doped compositions were observed in Sn-LTP compositions. An undistorted octahedral symmetry was applied in the EXAFS fitting of Sn-LTP systems, regardless of the crystal structure obtained from PXRD indicating a [3+3] TiO_6 motif. EXAFS was limited in providing further insight on any changes around the framework polyhedra due to doping, as observed in Raman spectroscopy.

Conductivity studies showed that although lattice site substitution enhanced the total conductivity for some compositions, 50% Sn^{4+} showed the highest value, attributed to larger M1 void and MO_6 octahedral volumes due to the presence of the larger Sn^{4+} cation in the structure. Therefore, substitution by M^{4+} cations of a larger ionic radius relative to Ti^{4+} increases the observed room temperature conductivity, but only to a certain degree of structural tolerance, before changes in the local Ti/SnO_6 symmetry that may result in Li-ion trapping starts coming into play. Finally, although the phase purity of the materials is important in grain boundary conductivity, it is not the only factor that plays a role in the total conductivity of these materials. The amount and ionic radius of the dopant must be considered, as it is imperative in establishing the extent of local distortions that result in Li^+ ion trapping, which, in turn, increases the activation barrier.

In conclusion, future work focused on studying the local order around the framework through techniques such as the pair distribution function with small-box modelling. The PDF will also provide possible clarity on accounting for the less than expected cell volume expansion for 8 and 10% Sn. Also, Sn and P XAS would provide more conclusive information on the effects of Sn on the TiO_6 and PO_4 polyhedra, and how these possible distortions contribute to the changes in conductivity.

3.5. References

1. Bounar, N., Benabbas, A., Bouremmad, F., Ropa, P. and Carru, J.C., 2012. Structure, microstructure and ionic conductivity of the solid solution $LiTi_{2-x}Sn_x(PO_4)_3$. *Physica B: Condensed Matter*, *407*(3), pp.403-407.
2. Aono, H., Sugimoto, E., Sadaoka, Y., Imanaka, N. and Adachi, G.Y., 1990. Ionic conductivity of solid electrolytes based on lithium titanium phosphate. *Journal of the electrochemical society*, *137*(4), pp.1023-1027.
3. Best, A.S., Forsyth, M. and Macfarlane, D.R., 2000. Stoichiometric changes in lithium conducting materials based on $Li_{1+x}Al_xTi_{2-x}(PO_4)_3$: impedance, X-ray and NMR studies. *Solid State Ionics*, *136*, pp.339-344.
4. Lang, B., Ziebarth, B. and Elsässer, C., 2015. Lithium ion conduction in $LiTi_2(PO_4)_3$ and related compounds based on the NASICON structure: a first-principles study. *Chemistry of Materials*, *27*(14), pp.5040-5048.

5. Bachman, J.C., Muy, S., Grimaud, A., Chang, H.H., Pour, N., Lux, S.F., Paschos, O., Maglia, F., Lupart, S., Lamp, P. and Giordano, L., 2015. Inorganic solid-state electrolytes for lithium batteries: mechanisms and properties governing ion conduction. *Chemical Reviews*, *116*(1), pp.140-162.

6. Xu, X., Wen, Z., Wu, J. and Yang, X., 2007. Preparation and electrical properties of NASICON-type structured $Li_{1.4}Al_{0.4}Ti_{1.6}(PO_4)_3$ glass-ceramics by the citric acid-assisted sol-gel method. *Solid State Ionics*, *178*(1-2), pp.29-34.

7. Kuwano, J., Sato, N., Kato, M. and Takano, K., 1994. Ionic conductivity of $LiM_2(PO_4)_3$ (M= Ti, Zr, Hf) and related compositions. *Solid State Ionics*, *70*, pp.332-336.

8. Wang, S., Ben, L., Li, H. and Chen, L., 2014. Identifying Li^+ ion transport properties of aluminum doped lithium titanium phosphate solid electrolyte at wide temperature range. *Solid State Ionics*, *268*, pp.110-116.

9. Martinez-Juarez, A., Pecharromán, C., Iglesias, J.E. and Rojo, J.M., 1998. Relationship between activation energy and bottleneck size for Li^+ ion conduction in NASICON materials of composition $LiMM'(PO_4)_3$; M, M '= Ge, Ti, Sn, Hf. *The Journal of Physical Chemistry B*, *102*(2), pp.372-375.

10. Ramar, V., Kumar, S., Sivakkumar, S.R. and Balaya, P., 2018. NASICON-type La^{3+} substituted $LiZr_2(PO_4)_3$ with improved ionic conductivity as solid electrolyte. *Electrochimica Acta*, *271*, pp.120-126.

11. Rao, A.V., Veeraiah, V., Rao, A.P., Babu, B.K. and Brahmayya, M., 2015. Spectroscopic characterization and conductivity of Sn-substituted $LiTi_2(PO_4)_3$. *Research on Chemical Intermediates*, *41*(7), pp.4327-4337.

12. Coelho, A.A., 2018. TOPAS and TOPAS-Academic: an optimization program integrating computer algebra and crystallographic objects written in C++. *Journal of Applied Crystallography*, *51*(1), pp.210-218.

13. https://www.diamond.ac.uk/Instruments/Spectroscopy/B18/Station.html (accessed 6 May 2024, 23:21)

14. Shannon, R.D., 1976. Revised effective ionic radii and systematic studies of interatomic distances in halides and chalcogenides. *Acta crystallographica section A: crystal physics, diffraction, theoretical and general crystallography*, *32*(5), pp.751-767.

15. Francisco, B.E., Stoldt, C.R. and M'Peko, J.C., 2014. Lithium-ion trapping from local structural distortions in sodium super ionic conductor (NASICON) electrolytes. *Chemistry of Materials*, *26*(16), pp.4741-4749.

16. Winand, J.M., Rulmont, A. and Tarte, P., 1991. Nouvelles solutions solides $Li(M^{IV})_{2-x}(N^{IV})_x(PO_4)_3$ (L= Li, Na M, N= Ge, Sn, Ti, Zr, Hf) synthèse et étude par diffraction x et conductivité ionique. *Journal of Solid State Chemistry*, *93*(2), pp.341-349.

17. Forbes, R.P., Barrett, D.H., Rodella, C.B. and Billing, D.G., 2019. The thermoresponsive behavior of Nasicon-like $CuTi_2(PO_4)_3$. *Materials Characterization*, *155*, p.109795.

18. Burba, C.M. and Frech, R., 2006. Vibrational spectroscopic study of lithium intercalation into $LiTi_2(PO_4)_3$. *Solid State Ionics*, *177*(17-18), pp.1489-1494.

19. Aatiq, A., Ménétrier, M., Croguennec, L., Suard, E. and Delmas, C., 2002. On the structure of $Li_3Ti_2(PO_4)_3$. *Journal of Materials Chemistry*, *12*(10), pp.2971-2978.

20. Arbi, K., Hoelzel, M., Kuhn, A., García-Alvarado, F. and Sanz, J., 2013. Structural Factors That Enhance Lithium Mobility in Fast-Ion $Li_{1+x}Ti_{2-x}Al_x(PO_4)_3$ ($0 \leq x \leq 0.4$) Conductors Investigated by Neutron Diffraction in the Temperature Range 100–500 K. *Inorganic chemistry*, *52*(16), pp.9290-9296.

21. Giarola, M., Sanson, A., Tietz, F., Pristat, S., Dashjav, E., Rettenwander, D., Redhammer, G.J. and Mariotto, G., 2017. Structure and vibrational dynamics of NASICON-type $LiTi_2(PO_4)_3$. *The Journal of Physical Chemistry C*, *121*(7), pp.3697-3706.

22. Ramaraghavulu, R. and Buddhudu, S., 2011. Analysis of structural, thermal and dielectric properties of $LiTi_2(PO_4)_3$ ceramic powders. *Ceramics International*, *37*(8), pp.3651-3656.

23. Tarte, P., Rulmont, A. and Merckaert-Ansay, C., 1986. Vibrational spectrum of nasicon-like, rhombohedral orthophosphates $M^IM^{IV}_2(PO_4)_3$. *Spectrochimica Acta Part A: Molecular Spectroscopy*, *42*(9), pp.1009-1016.

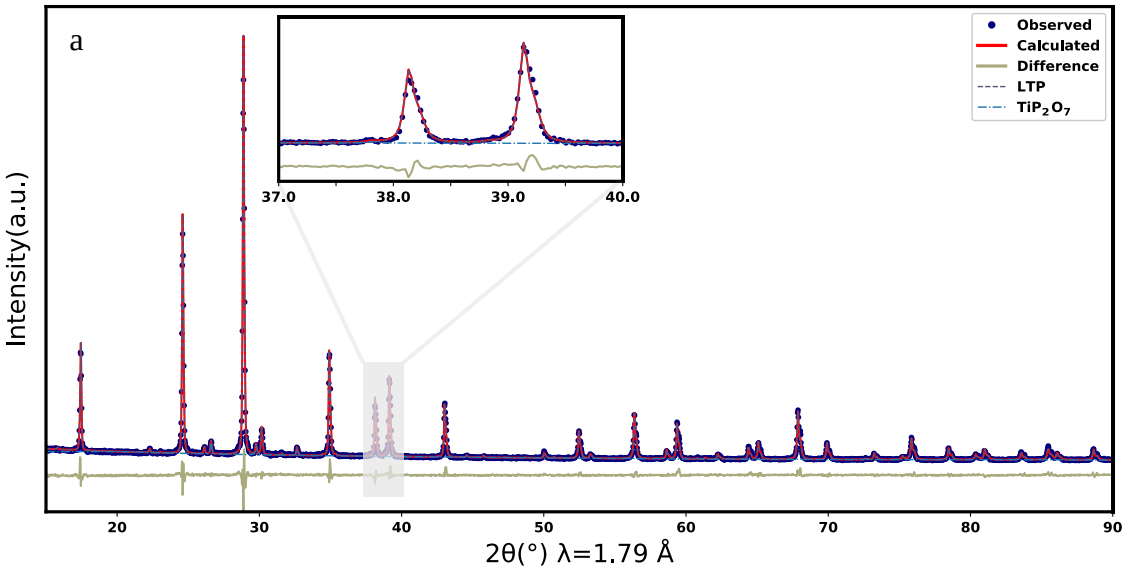
24. Wu, Z.Y., Ouvrard, G., Gressier, P. and Natoli, C.R., 1997. Ti and O K edges for titanium oxides by multiple scattering calculations: Comparison to XAS and EELS spectra. *Physical Review B*, *55*(16), p.10382.

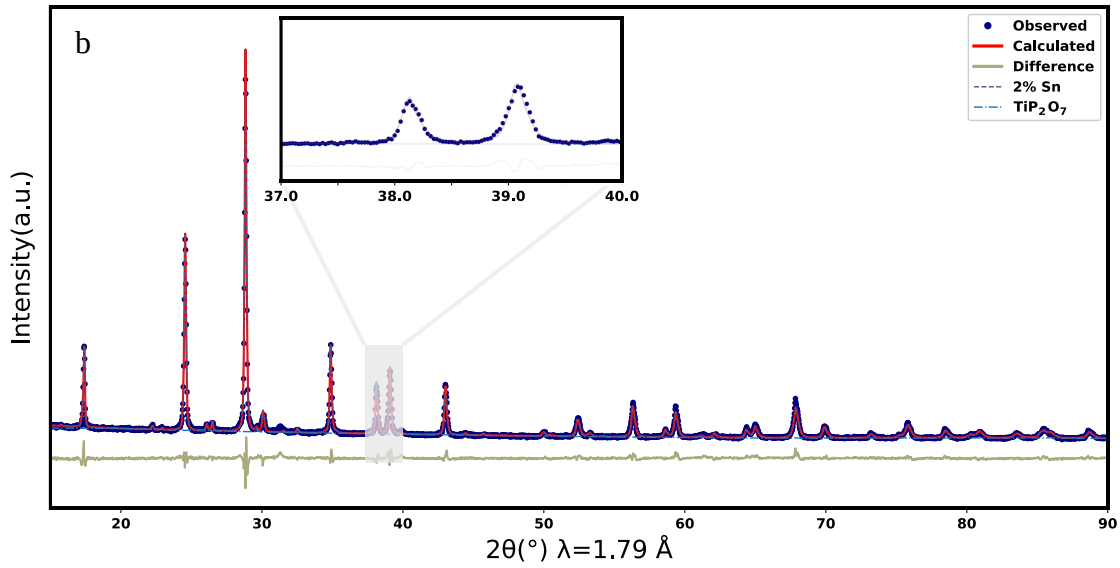
25. Farges, F., Brown, G.E. and Rehr, J.J., 1997. Ti K-edge XANES studies of Ti coordination and disorder in oxide compounds: Comparison between theory and experiment. *Physical Review B*, *56*(4), p.1809.
26. Jiang, N., Su, D. and Spence, J.C.H., 2007. Determination of Ti coordination from pre-edge peaks in Ti K-edge XANES. *Physical Review B*, *76*(21), p.214117.
27. Niltharach, A., Kityakarn, S., Worayingyong, A., Klysubun, W., Songsiriritthigul, P. and Limpijumnong, S., 2012. Structural characterizations of sol–gel synthesized TiO_2 and Ce/TiO_2 nanostructures. *Physica B: Condensed Matter*, *407*(15), pp.2915-2918.
28. Chen, L.X., Rajh, T., Wang, Z. and Thurnauer, M.C., 1997. XAFS studies of surface structures of TiO_2 nanoparticles and photocatalytic reduction of metal ions. *The Journal of Physical Chemistry B*, *101*(50), pp.10688-10697.
29. Phoohinkong, W., Pavasupree, S., Wannagon, A., Sanguanpak, S., Boonyarattanakalin, K., Mekprasart, W. and Pecharapa, W., 2017. Characterization and x-ray absorption spectroscopy of ilmenite nanoparticles derived from natural ilmenite ore via acid-assisted mechanical ball-milling process. *Advances in Natural Sciences: Nanoscience and Nanotechnology*, *8*(3), p.035012.
30. Yoon, S., Otal, E.H., Maegli, A.E., Karvonen, L., Matam, S.K., Riegg, S., Ebbinghaus, S.G., Fallas, J.C., Hagemann, H., Walfort, B. and Pokrant, S., 2013. Improved photoluminescence and afterglow of $CaTiO_3$: Pr^{3+} by ammonia treatment. *Optical Materials Express*, *3*(2), pp.248-259.
31. Wang, D., Bie, X., Fu, Q., Dixon, D., Bramnik, N., Hu, Y.S., Fauth, F., Wei, Y., Ehrenberg, H., Chen, G. and Du, F., 2017. Sodium vanadium titanium phosphate electrode for symmetric sodium-ion batteries with high power and long lifespan. *Nature communications*, *8*(1), pp.1-7.
32. Cabaret, D., Bordage, A., Juhin, A., Arfaoui, M. and Gaudry, E., 2010. First-principles calculations of X-ray absorption spectra at the K-edge of 3d transition metals: an electronic structure analysis of the pre-edge. *Physical Chemistry Chemical Physics*, *12*(21), pp.5619-5633.
33. Ravel, B and Newville, M., 2005. ATHENA, ARTEMIS, HEPHAESTUS: data analysis for X-ray absorption spectroscopy using IFEFFIT. Journal of synchrotron radiation, 12(4), pp.537-541.

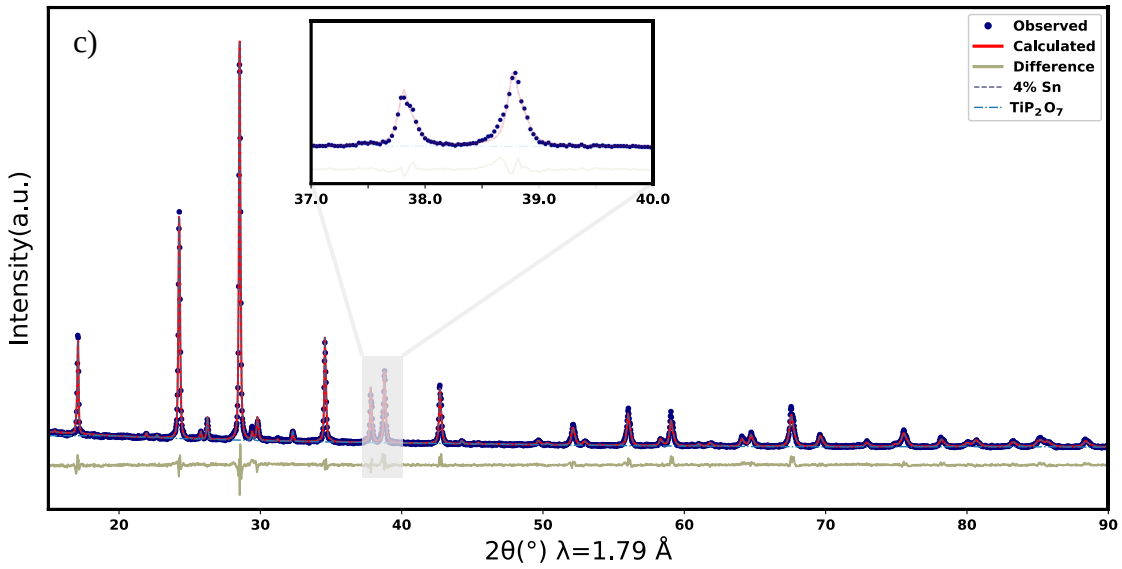
34. Press, W.H., Teukolsky, S.A., Flannery, B.P. and Vetterling, W.T., 1992. *Numerical recipes in Fortran 77: volume 1, volume 1 of Fortran numerical recipes: the art of scientific computing*. Cambridge university press.
35. Dellis, J.L. and Carpentier, J.L., 1993. Nelder and Mead algorithm in impedance spectra fitting. *Solid state ionics*, *62*(1-2), pp.119-123.
36. Thangadurai, V., Huggins, R.A. and Weppner, W., 2002. Use of simple ac technique to determine the ionic and electronic conductivities in pure and Fe-substituted $SrSnO_3$ perovskites. *Journal of power sources*, *108*(1-2), pp.64-69.
37. Irvine, J.T., Sinclair, D.C. and West, A.R., 1990. Electroceramics: characterization by impedance spectroscopy. *Advanced Materials*, *2*(3), pp.132-138.
38. Kumar, P.P. and Yashonath, S., 2006. Ionic conduction in the solid state. *Journal of Chemical Sciences*, *118*(1), pp.135-154.

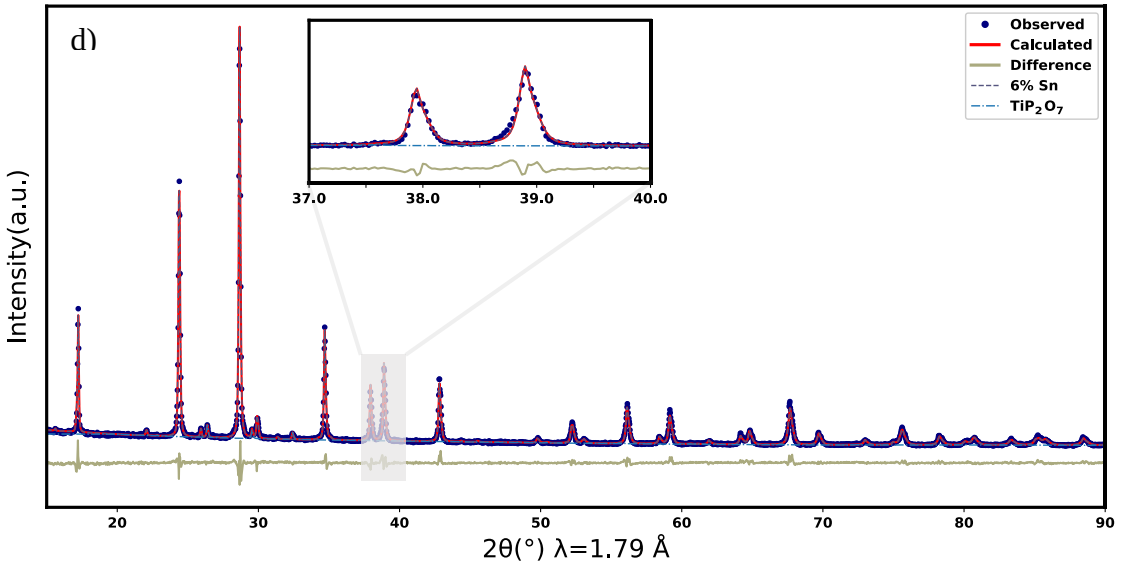
3.6. Supplementary information

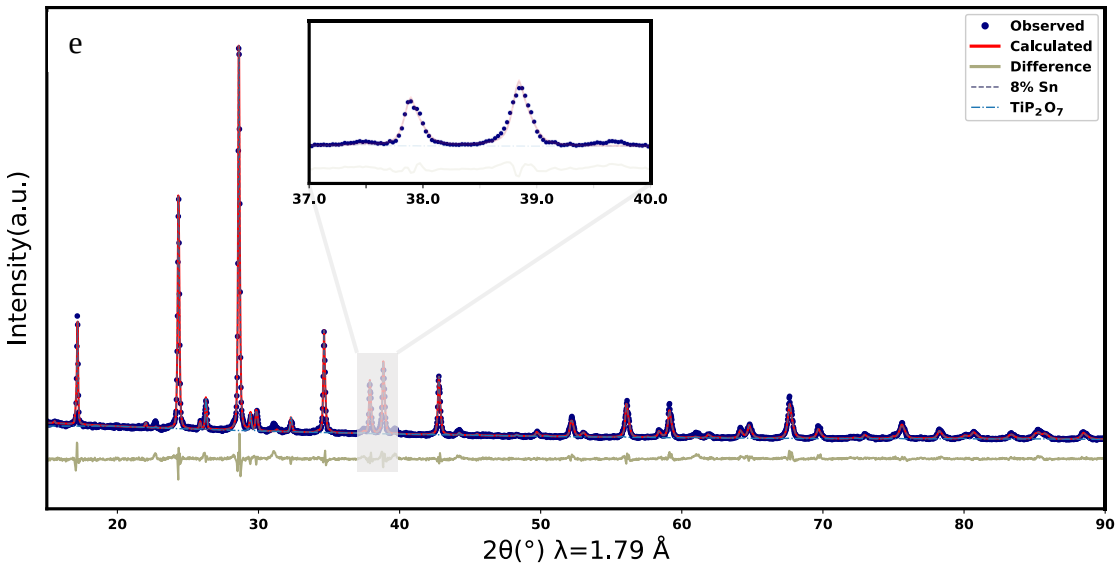
Figure S3.1. Rietveld refinement results for Sn-LTP compositions (a) LTP, (b) 2% Sn-LTP, (c) 4% Sn-LTP, (d) 6% Sn-LTP, (e) 8% Sn-LTP and (f) 10% Sn-LTP, showing the absence of the isostructural LSP phase. 'Observed' = Experimental data; 'Calculate' = Theoretical data obtained from the input structures.






c)
Observed
Calculated
Difference
4% Sn
TiP_2O_7
Intensity(a.u.)
37.0
38.0
39.0
40.0
20
30
40
50
60
70
80
90
2θ(°) λ=1.79 Å


d)
Observed
Calculated
Difference
6% Sn
TiP_2O_7
Intensity(a.u.)
37.0
38.0
39.0
40.0
20
30
40
50
60
70
80
90
2θ(°) λ=1.79 Å


e
Observed
Calculated
Difference
8% Sn
TiP2O7
Intensity(a.u.)
2θ(°) λ=1.79 Å

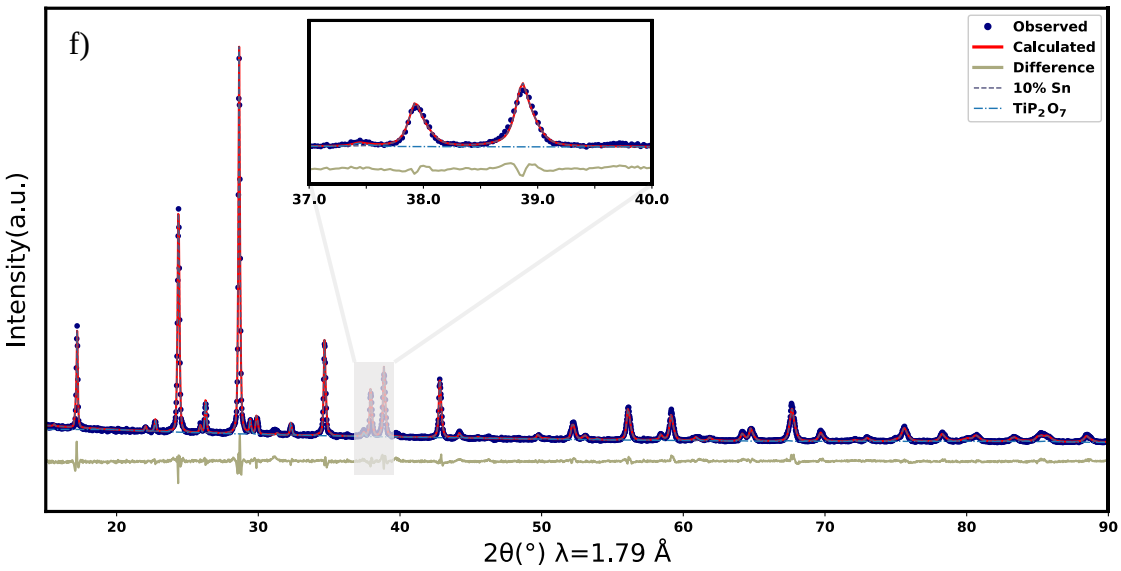

f)
Observed
Calculated
Difference
10% Sn
TiP2O7
Intensity(a.u.)
2θ(°) λ=1.79 Å

Table S3.1. Crystallographic data for Sn-LTP systems synthesized at 900 °C via the solid-state method.

Whole pattern	**LTP**	**2% Sn**	**4% Sn**	**6% Sn**	**8% Sn**	**10% Sn**	**50% Sn**
Rexp (%)	3.79	4.06	3.88	3.87	3.93	3.98	4.00
Rwp (%)	6.56	7.09	6.82	6.67	7.62	7.34	5.90
Rp	5.17	2.39	5.29	5.15	5.72	5.54	4.62
GOF	1.73	1.74	1.76	1.72	1.94	1.84	1.47
$LiTi_2(PO_4)_3$							
R Bragg	2.57	2.35	2.62	2.41	1.60	1.65	1.43
Weight %	98.17	98.78	97.45	98.39	96.39	96.66	69.74
Space group	*R*-3*c*	*R*-3*c*	*R*-3*c*	*R*-3*c*	*R*-3*c*	*R*-3*c*	*R*-3*c*
a (Å)	8.511(1)	8.505(2)	8.511(2)	8.514(2)	8.511(2)	8.513(2)	8.567(5)
c (Å)	20.864(4)	20.899(9)	20.903(8)	20.914(7)	20.910(1)	20.929(1)	21.125(1)
Volume ($Å^3$)	1308.731(5)	1309.171(1)	1311.331(9)	1313.047(8)	1311.656(1)	1313.530(1)	1342.714(1)
Phase density (g/cm^3)	2.951(1)	2.971(2)	2.988(2)	3.005(1)	3.030(2)	3.047(2)	3.402(4)
TiP_2O_7							
R Bragg	2.46	2.66	2.33	2.12	3.64	3.90	2.50
Weight %	1.83	1.22	2.55	1.61	3.61	3.34	1.46
Space group	*Pa*-3	*Pa*-3	*Pa*-3	*Pa*-3	*Pa*-3	*Pa*-3	*Pa*-3

a (Å)	7.876(6)	7.898(1)	7.882(6)	7.885(1)	7.899(7)	7.912(6)	7.937(1)
Volume (Å^3)	488.643(1)	492.611(3)	489.720(1)	490.241(2)	492.901(1)	495.204(1)	500.001(2)
Phase density (g/cm^3)	4.699(1)	4.661(3)	4.689(1)	4.684(1)	4.659(1)	4.637(1)	4.592(1)

$LiSn_2(PO_4)_3$	
R Bragg	1.28
Weight %	28.49
Space group	*R*-3*c*
a (Å)	8.586(7)
c (Å)	21.266(2)
Volume (Å^3)	1357.647(2)
Phase density (g/cm^3)	3.884(7)

Table S3.2 Raman band assignments for Sn-LTP systems synthesized at 900 °C via the solid-state method.

	External Modes						**PO_4 bending modes**			**PO_4 stretching modes**				**TiP_2O_7 sec. phase (*Pa*-3)**	
Peak Assignment	E_g (2)	A_{1g} (1)	E_g (5)	E_g (6)	A_{1g} (3)	E_g (7)	A_{1g} (4)	A_{1g} (5)	E_g (11)	E_g (14)	E_g (15)	E_g (16)	A_{1g} (8)		
Composition															
LTP	139.9	178.5	238.8	273.6	312.1	352.4	432.4	447.5	547.3	969.8	989.5	1007.3	1094	1037.5	1074.1
2% Sn	138.7	179.0	239.8	274.3	310.9	352.6	431.6	446.5	548.6	969.9	989.0	1007.3	1095	-	-
4% Sn	137.5	177.7	240.0	273.6	309.7	351.2	431.0	445.8	549.2	976.6	990.5	1006.2	1094.5	1031.0	1062.9
6% Sn	137.5	174.6	236.8	273.6	310.2	350.4	432.4	443.7	547.3	968.1	987.7	1005.5	1094	1048.1	1069.3
8% Sn	137.5	176.6	238.8	273.6	310.2	350.4	432.4	445.6	547.3	969.8	987.7	1007.3	1095.8	1039.2	1069.3
10% Sn	139.5	180.5	238.8	275.5	312.1	352.4	432.4	445.6	551.1	971.6	989.5	1007.3	1097.5	1039.2	1069.3
50% Sn		170.7	221.3	273.6	308.2	344.7	432.4	468.3			991.3		1094.0	1039.2	

Figure S3.3. Laboratory PXRD pattern of TiO2 Degussa P-25 standard, with Rietveld refinement as implemented on Topas ACADEMIC based on the tetragonal anatase (ICSD 9852) and rutile (ICSD 121630) structures, used in the Ti K-edge XAS analysis.

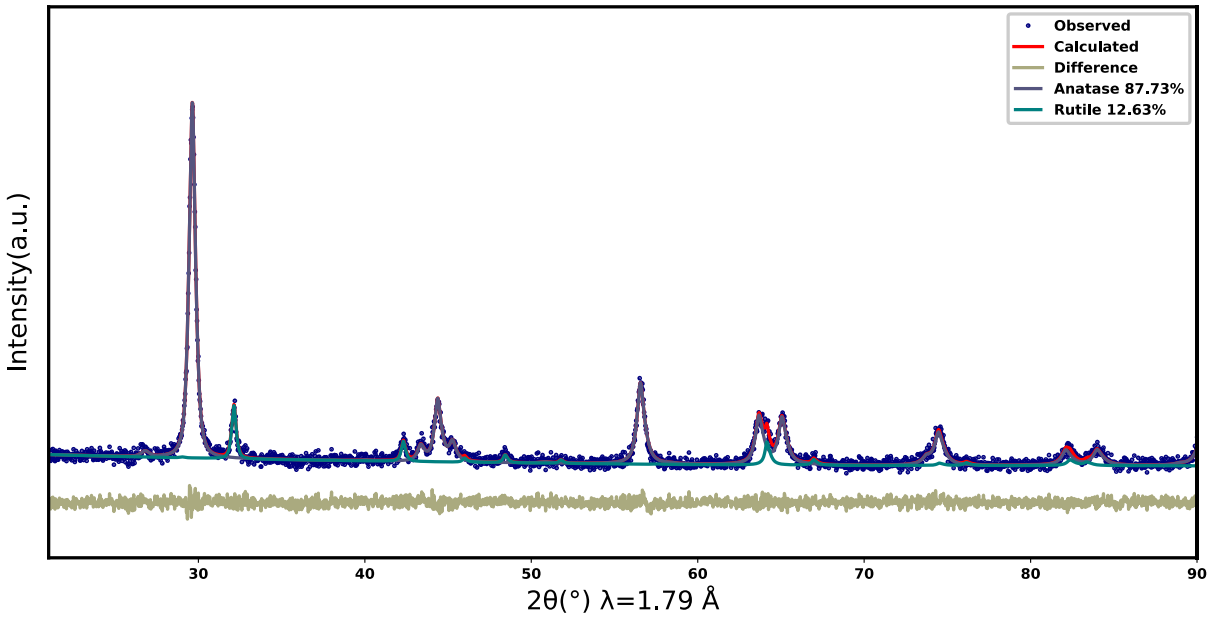
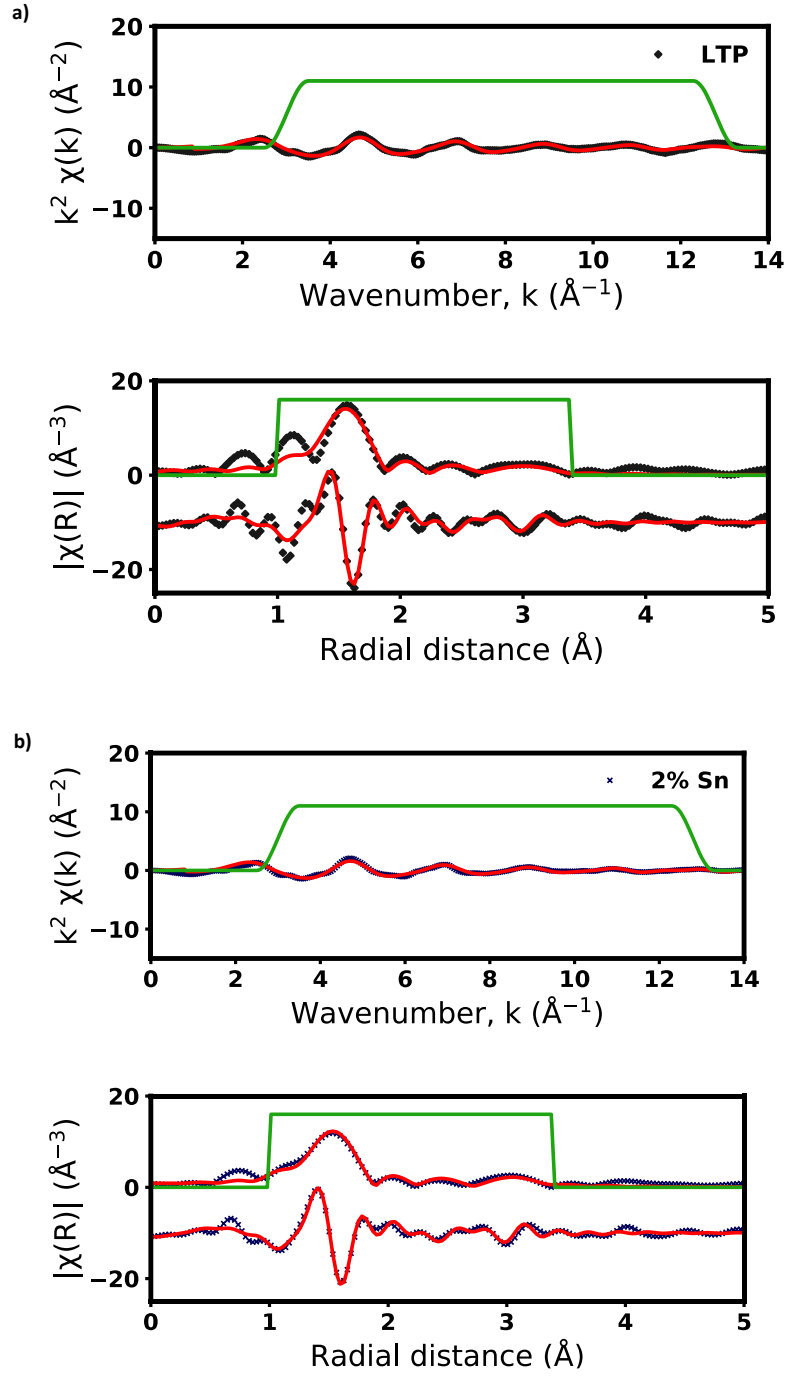


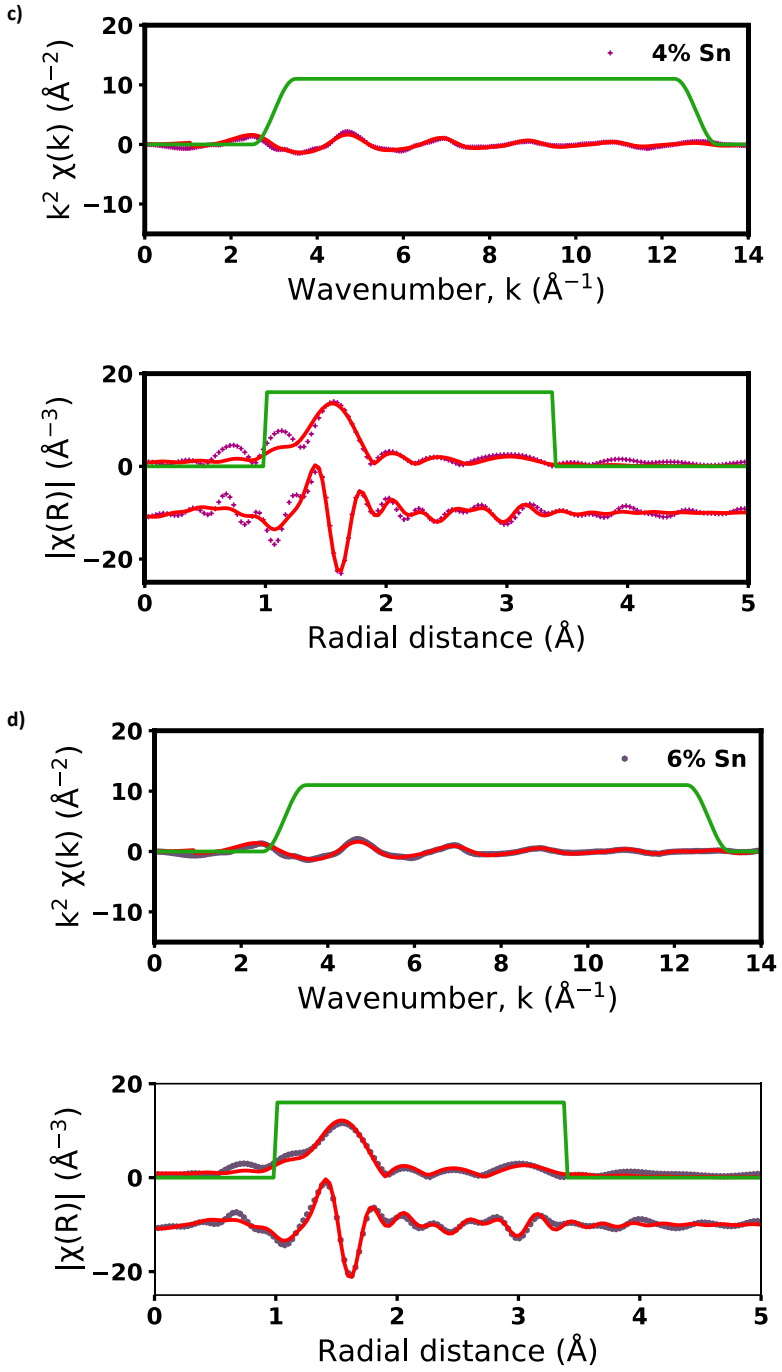
Table S3.3. Crystallographic data for TiO_2 Degussa P-25 from Rietveld refinement of laboratory PXRD results (D2 Phaser, Co Kα) in the range 10 to 90° 2θ.

	Anatase TiO_2 (ICSD 9852)	**Rutile TiO_2 (ICSD 121630)**
RBragg	0.61	1.32
Weight %	87.73	12.63
Space group	$I4_1/amd$	$P4_2/mnm$
a (Å)	3.7900(5)	4.600(1)
b (Å)	3.7900(5)	4.600(1)
c (Å)	9.518(1)	2.963(1)
Volume ($Å^3$)	136.71(4)	62.68(3)
Phase density (g/cm^3)	3.880(1)	4.232(2)

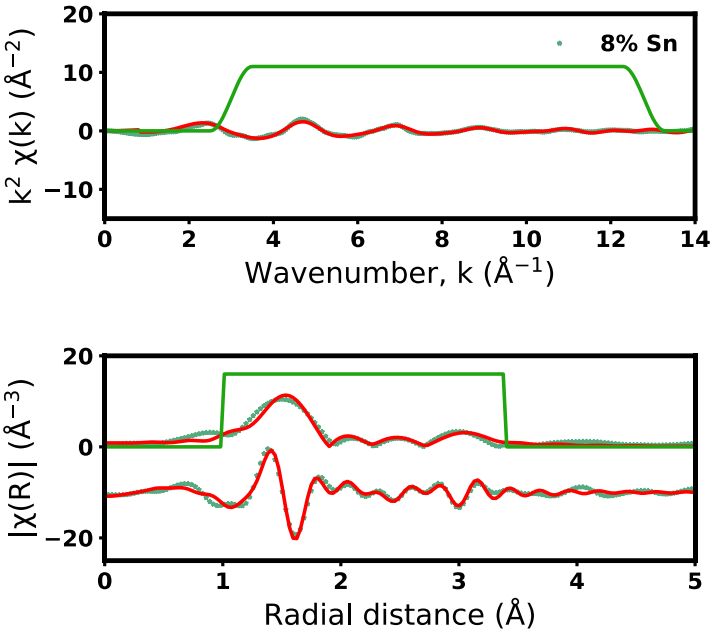
Whole pattern refinement parameters: R_{exp} = 7.45 %, R_{wp} = 7.58, R_p = 5.98, GOF = 1.02.

Figure S3.4. The k^2 weighted kR plots of the EXAFS fits for Sn-LTP formulations for (a) LTP, (b) 2% Sn-LTP (c) 4% Sn-LTP, (d) 6% Sn-LTP, (e) 8% Sn-LTP, (f) 10% Sn-LTP and (g) 50% Sn-LTP.

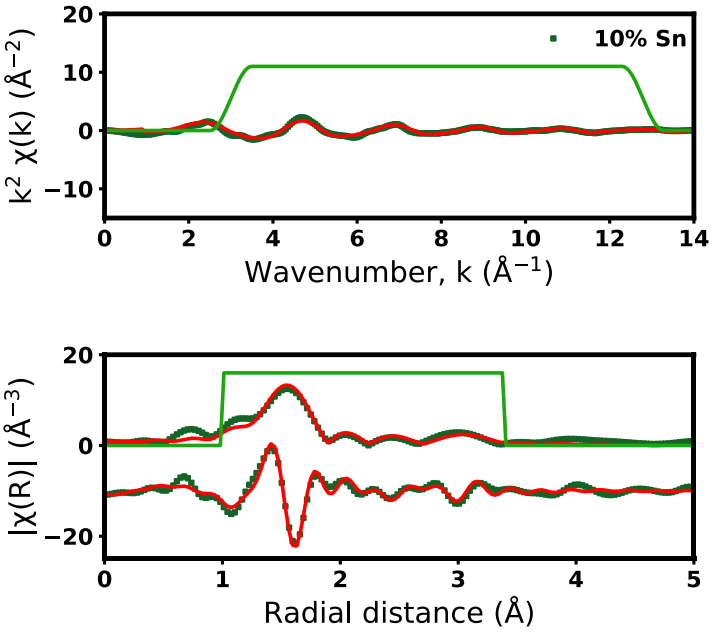



c)
4% Sn
$k^2\ \chi(k)\ (Å^{-2})$
Wavenumber, k ($Å^{-1}$)
$|\chi(R)|\ (Å^{-3})$
Radial distance (Å)
d)
6% Sn
$k^2\ \chi(k)\ (Å^{-2})$
Wavenumber, k ($Å^{-1}$)
$|\chi(R)|\ (Å^{-3})$
Radial distance (Å)

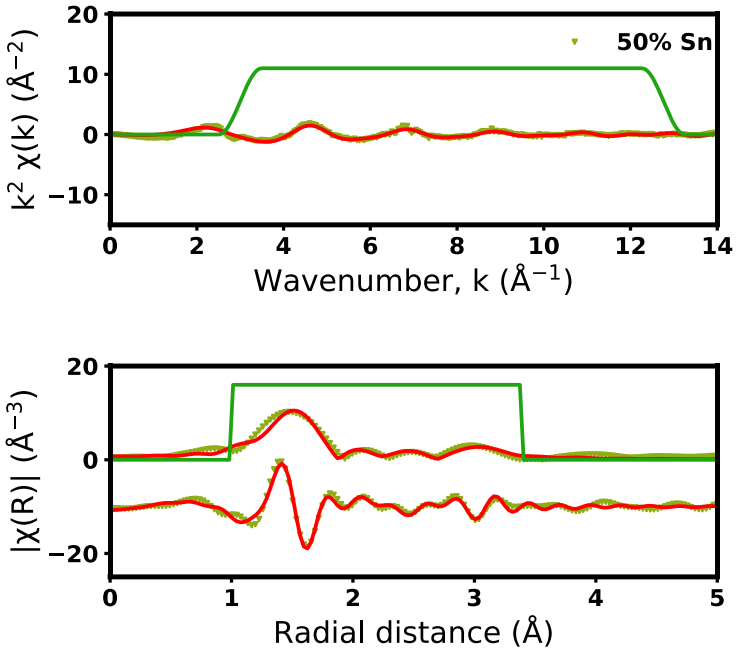
e)


8% Sn
k² χ(k) (Å⁻²)
Wavenumber, k (Å⁻¹)
|χ(R)| (Å⁻³)
Radial distance (Å)

f)


10% Sn
k² χ(k) (Å⁻²)
Wavenumber, k (Å⁻¹)
|χ(R)| (Å⁻³)
Radial distance (Å)

g)



Chapter 4: The enhancement of ionic conductivity of NASICON-type $LiTi_2(PO_4)_3$ by formation of Al, Sn and Al, Dy co-doped systems

4.1. Introduction

Understanding the influence of structure on the properties of materials of technological importance is imperative in influencing material design. Two strategies for ionic conductivity enhancement in the NASICON-type $LiTi_2(PO_4)_3$ have been proposed: i) increasing the number of charge carriers by aliovalent doping with M^{3+} cations (e.g., Al, Sc, Ga, In, etc.) [3, 4, 5] and, ii) enlarging the LiO_6 octahedra to improve the bottleneck size for easier Li migration, by doping with optimum amount of larger M^{4+} cations (e.g., Sn, Hf),[4, 6] as we have explored in the **previous chapter**. The presence of cations larger than Ti^{4+} such as Sn^{4+}, Hf^{4+} and Zn^{4+} has been reported to cause local triclinic distortions which may lead to the phenomenon of Li^+ ion trapping.[7, 8] Nikodimos *et al.*[9] studied the effect of Sc^{3+} doping and found that although the presence of the relatively larger Sc^{3+} cation enlarged the tunnelling size, there was a limit to the amount of Sc^{3+} that could be added prior to the structure exhibiting distortions, and the formation of secondary phases. [9]

Co-doping strategies have been proposed to enhance the total ionic conductivities of NASICON-type formulations. Nikodimos *et al.*,[9] also studied the Al, Sc co-doped $LiGe_2(PO_4)_3$ (LGP) system. The best bulk ionic conductivity of 5.826×10^{-3} S/cm was found when a small amount (8.5%) of Sc^{3+} was incorporated into the LAGP system compared to 2.989×10^{-3} S/cm for the singly-doped LAGP system. However, at higher Sc^{3+} dopant contents, they observed lower Li^+ diffusion, attributing it to the larger radius of Sc^{3+} (r = 0.745 Å), which affects the solubility of Sc into the NASICON-type structure at the 12*c* site. The inclusion of larger radii cations only improves ionic conductivity up to a point, after which other effects like triclinic and/or monoclinic distortions, and Li ion trapping take over.

Sugantha *et al.*,[4] conducted a study on $Li_2M^{3+}M^{4+}(PO_4)_3$ systems. They state that the amount and the cationic radius of the tri/tetravalent cations in the octahedral site of the framework determine whether the resulting solid solution was rhombohedral (*R*-3*c*) or orthorhombic (*Pbca*). They explored only the orthorhombic phases, with the highest conductivity found to be 8.30×10^{-6} S/cm for $Li_2InTi(PO_4)_3$ at room temperature.

In this work, two double-doped systems of $Li_{1.2}Al_{0.2}Ti_{1.7}Sn_{0.1}(PO_4)_3$ (LATSP; 10% Al, 5% Sn) and $Li_{1.3}Al_{0.25}Dy_{0.05}Ti_{1.7}(PO_4)_3$ (LADTP; 12.5% Al, 2.5% Dy) were studied, with $Li_{1.3}Al_{0.3}Ti_{1.7}(PO_4)_3$ (LATP) used as a reference material. The addition of small amounts of larger cations Sn^{4+} (r = 0.69 Å) and Dy^{3+} (r = 0.913 Å) was expected to enlarge the LiO_6 octahedra without causing significant structural distortions, while the addition of Al^{3+} and Li^{+} increased the number of charge carriers within the structure. Employing the strategy of co-doping allowed for the exploitation of both factors of improving the total ionic conductivity of NASICON-type systems.

4.2. Experimental section

4.2.1. Synthesis

LATSP: stoichiometric amounts of Li_2CO_3, $(NH_4)_2HPO_4$, TiO_2, SnO_2 and Al_2O_3 were manually ground into a fine powder in an agate pestle and mortar for twenty minutes. The ground powder was placed into an alumina crucible and heated to 450 °C at 10 °C/min for one hour. Upon cooling, the precursors were manually ground for an hour and heated in a tube furnace to 900 °C at 10°C/min and held at this temperature for 8 hours under the constant flow of nitrogen gas. The resulting white powders were ground for twenty minutes upon cooling and stored in sample vials for characterization.

LADTP: The Al^{3+}, Dy^{3+} co-doped $LiTi_2(PO_4)_3$ was synthesized following the conventional solid-state method. Dy_2O_3 was obtained via the thermal decomposition of $Dy(NO_3)_3{\cdot}6H_2O$ (Sigma-Aldrich, 99.999%) at 700 °C in air, for 2 hours. Stoichiometric amounts of Li_2CO_3, TiO_2 (Degussa P25), Al_2O_3 (99.99% purity), $(NH_4)_2HPO_4$ and Dy_2O_3 were ground in an agate pestle and mortar for 1 hour. The fine powder was decanted into an alumina crucible and heated at 450 °C in air, at a heating rate of 10 °C for 1 hour to decompose the phosphate. Upon cooling to room temperature, the intermediate was removed by scraping, ground for 1 hour in an agate pestle and mortar and transferred into a boat. The boat was placed into a horizontal tube furnace and heated to 900 °C in nitrogen at a heating rate of 10 °C/min and soaked at 900 °C for 9 hours. The final product was a white powder that was finely ground for 20 minutes and stored for further characterization.

4.2.2. Characterization

The average and local structure of NASICON-type systems were investigated with synchrotron based PXRD and PDF following the outlined methodologies in **Chapter 2**. The crystallographic data and structural parameters obtained from Rietveld refinements are reported in **Table S1** and **S2**. The $LiTi_2(PO_4)_3$ and $Li_{1.3}Al_{0.3}Ti_{1.7}(PO_4)_3$ NASICON-type rhombohedral structure models were used in the Rietveld refinements using the Thompson-Cox-Hastings pseudo-Voigt peak profile, where the lattice parameters, fractional coordinates, atomic displacement parameters and site occupancies were refined. The 12*c* site for Ti, Al, Sn and Dy was set to the nominal compositions for both systems, similarly for Li^+ at 6*b* and 36*f* sites. The crystallite size and strain were also refined. The resultant crystallographic structures were visualized in the VESTA software. The program xPDFsuite was used to extract the experimental PDF. The r-poly was set to 0.98 Å and an upper Q-range cutoff of 25.4 $Å^{-1}$ was used. The real-space structure fits were carried out in TOPAS-Academic (Version 7.12).

Laboratory-based Raman spectroscopy measurements were conducted at room temperature at a wavelength of 514.5 nm, using an Ar^+ laser with a grating of 600 lines/mm and a 100× objective lens. The instrument employed a Symphony CCD detector, cooled with nitrogen. The instrument was calibrated with as Si single crystal standard, to an error of ±0.4 cm^{-1}. The peak positions were obtained using the LabSpec software (V5.93.20). The tabulated peak assignments are given in Table S3.

The XAS experimental spectra were collected at the National Synchrotron Light Source at beamline 6-BM at Brookhaven National Laboratory. All samples were measured in transmission mode at the Ti K-edge (4966.0 eV). The presented XAS spectra are an average of three scans per sample to ensure reproducibility. The background subtraction and normalization procedures were done as described in **Chapter 2**.

4.3. Results & Discussion

4.3.1. Crystal structural analysis through synchrotron PXRD

The PXRD patterns of the parent and co-doped LTP-based compositions are shown in **Figure 4.1**. The highest intensity peaks correspond to the NASICON-type rhombohedral structure (space group *R*-3*c*).

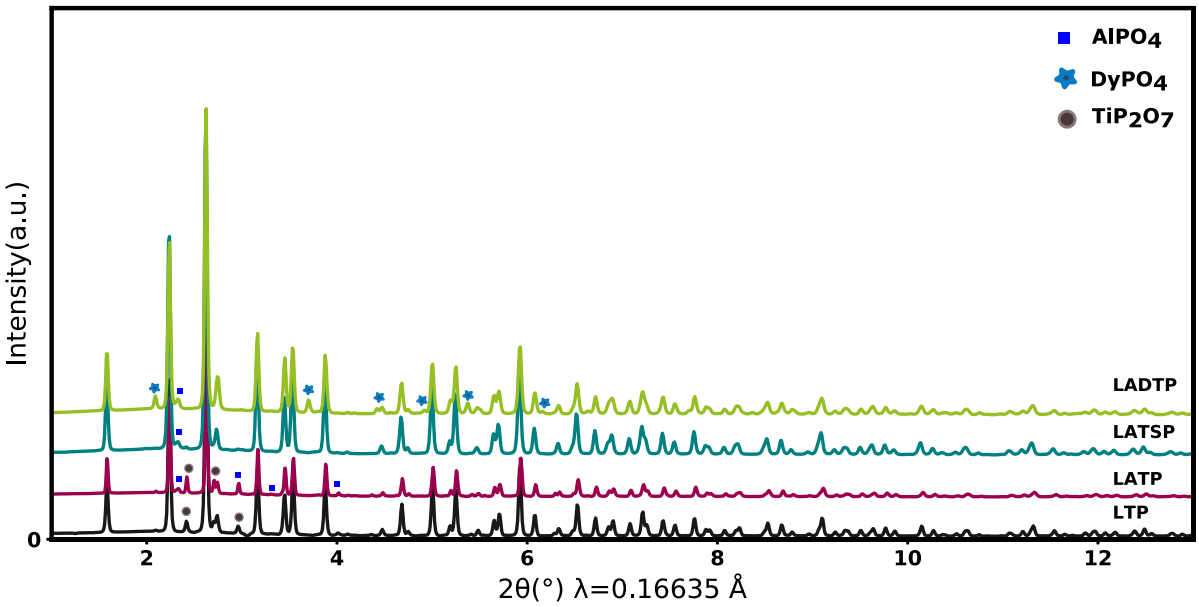


Figure 4.1. Synchrotron PXRD patterns for variously doped NASICON-type LTP systems.

At 15% Al (LATP), the diffraction peaks shifted towards higher 2θ, indicating unit cell contraction that is consistent with the replacement of Ti^{4+} (r = 0.605 Å) with a smaller cation, Al^{3+} (r = 0.535 Å). The radii under comparison are those of Ti^{4+} and Al^{3+} cations. The partial replacement of Ti^{4+} with Al, Sn and Al, Dy in the co-doped systems resulted in unit cell expansion, observed as a shift towards lower 2θ, as expected upon substitution with cations of larger ionic radii (r_{Dy}^{3+} = 0.912 Å; r_{Sn}^{4+} = 0.69 Å). These observations suggest successful addition of dopant cations into the Ti 12*c* site in the rhombohedral NASICON-type phase. The quantitative structural information obtained through Rietveld refinement is presented in **Table 4.1**.

Table 4.1. Structural information obtained from Rietveld refinements of synchrotron XRD data for various NASICON-type systems.

Composition	a (Å)	c (Å)	Volume (Å^3)
LTP	8.520(2)	20.87(1)	1312.0(9)
LATP	8.505(2)	20.864(9)	1306.9(8)
LATSP	8.525(2)	20.929(9)	1317.4(8)
LADTP	8.515(2)	20.910(1)	1313.2(1)

It can be expected that the replacement of Ti with Al, Dy in the LADTP system, the unit cell expansion would be larger than in the LATSP system, owing to the difference in the cationic radii for Dy vs Sn. However, the results in **Table 4.1** show a larger expansion for the LATSP system, which is attributed to the presence of higher Sn (nominal composition 5% of Sn), than in LADTP (nominal composition 2.5% of Dy^{3+}). It is also important to note that the LADTP composition has more Al^{3+} (12.5 mol %) than LATSP (10 mol%), therefore it follows that LADTP would exhibit a relatively smaller unit cell than LATSP.

Upon doping, the systems exhibit TiP_2O_7 (*Pa*-3), $AlPO_4$ ($C222_1$) and $DyPO_4$ ($I4_1/amd$) secondary phases. The respective quantitative phase compositions of each system are provided in **Table 4.2**. In LATSP, only the $AlPO_4$ impurity was present, suggesting that the addition of Al^{3+} to Sn-doped LTP (see Chapter 3) may have hindered the formation of the TiP_2O_7 phase. Also, since the total Al^{3+} present in the structure was approximately $x = 0.2$ and 0.3 for the Al-bearing systems LATSP and LATP, respectively, the resulting $AlPO_4$ phase was relatively smaller, than that observed in the higher Al-containing LATP.[13] In the work by Arbi and colleagues,[13] they suggested that the addition of Sc^{3+} or In^{3+} delayed the formation of secondary phases, such as $AlPO_4$. Kahlaoui *et al.*,[7] found that the addition of Sc^{3+} in amounts $x \geq 0.3$, in Sc-doped LTP resulted in the formation of $LiSc(P_2O_7)$, $LiScO_2$ and TiO_2 impurity phases. The presence of secondary phases has been said to affect the real stoichiometry of the main NASICON phases, indicating that not all the dopants were successfully incorporated into the structure.[14] Furthermore, these secondary phases are known to occupy the grain boundaries, which may decrease the grain boundary conductivities in ceramics.[3]

Table 4.2. Quantitative phase compositions of NASICON-based systems.

Composition	NASICON-type "LTP" (*R*-3*c*) (%)	TiP_2O_7 (*Pa*-3) (%)	$AlPO_4$ ($C222_1$) (%)	$DyPO_4$ ($I4_1/amd$) (%)
LTP	96.6(2)	3.4(2)		
LATP	90.6(3)	3.5(1)	5.9(3)	
LATSP	90.0(9)		10.1(9)	
LADTP	94.5(2)		3.3(2)	2.1(7)

In NASICON-type structures, there are two possible sites for Li^+. In the undoped LTP, Li^+ occupies the 6*b* (M1) site, whilst in the M^{3+}-doped structure, Li occupies both the 6*b* (M1) and 36*f* (M1/2) sites. In the present study, the excess Li^+ required for charge balance were placed at the 36*f* site.[16] The structure-based Rietveld refinements yielded less than 5% per secondary phases across all systems, except for LATSP with ~10% $AlPO_4$.

4.3.2. Raman spectroscopy

The solid electrolyte materials were further studied with Raman spectroscopy to understand the effects of doping on their local structures. The Raman spectra of LTP and its doped compositions are presented in **Figure 4.2**. The spectrum of LADTP was scaled by a factor of 0.5 while that of LATP was multiplied by a factor of 5 to enhance the visibility of the peaks and enable better visual comparison in the plot.

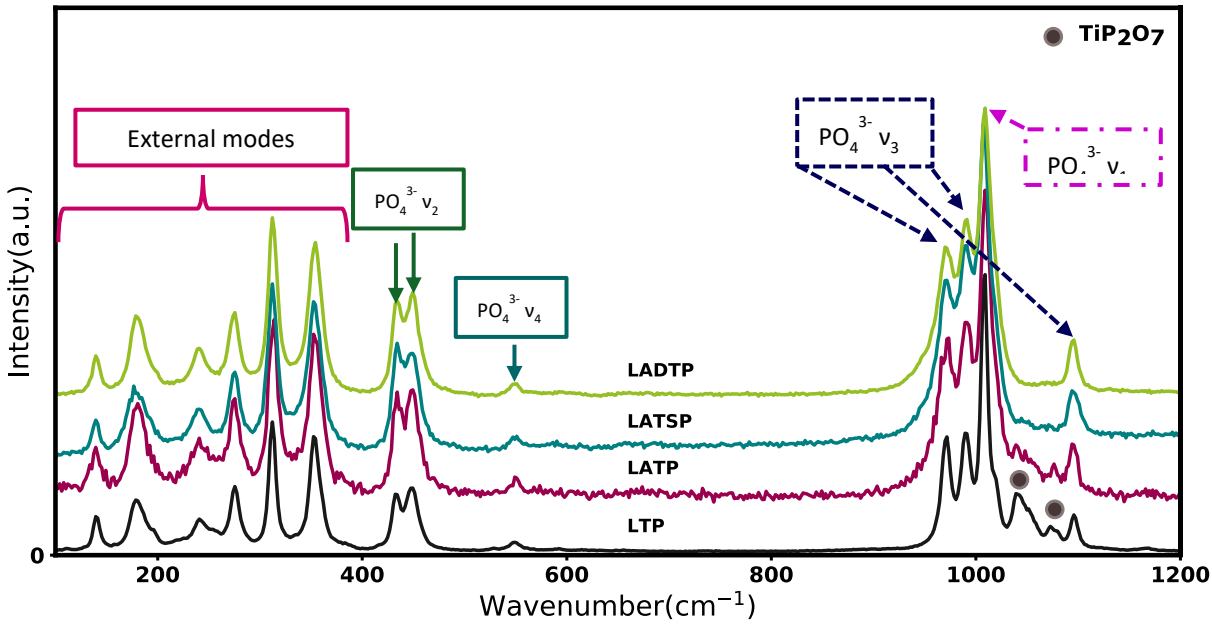


Figure 4.2. Raman spectra of variously doped NASICON-type LTP systems. The spectra for LADTP and LATP were scaled by 0.5 and 5, respectively, for better visual comparison.

The dominant spectral features in the range between 800 to 1100 cm^{-1} correspond to the symmetric (ν_1) and antisymmetric (ν_3) stretching vibrations of PO_4^{3-} tetrahedra.[18-19] There were no notable peak shifts for the lower dopant containing LATP, LATSP and LADTP compositions. Since these characteristic peaks were maintained for LATSP, the co-doping did not induce any significant structural disorder of the NASICON framework.[18]

The peaks at approximately 1039 and 1074 cm^{-1} were attributed to phosphate-bearing impurity TiP_2O_7.[21] However, the peaks for $AlPO_4$ could not be assigned and/or detected in the Al-bearing compositions, as **Figure 4.2** shows, regardless of evidence of phosphate-containing impurity phases seen in PXRD (**Figure 4.1**). The peaks corresponding to the cristobalite $C222_1$ phase of $AlPO_4$ are expected to appear in the regions given in the Supplementary Information **Table S4.6**, obtained from literature.[22-24] The peaks for $AlPO_4$ have not been observed in our work due to significant overlap with those of the main phase Al-bearing NASICON-type systems. The highest intensity peak for $AlPO_4$ is expected to be observed at ~ 1119 cm^{-1} corresponding to the 1D symmetric stretching mode of PO_4^{3-} groups.[22]

In the work by Dashav *et al.*,[25] for Al^{3+} = *0.2* mol%, the substitution of Ti^{4+} with Al^{3+} and Li^{+} induced the presence of some peaks in the 550 to 800 cm^{-1} range. They attributed these peaks to the breaking of symmetry rules, allowing for the observation of infrared and silent modes, resulting from increased substitution.

These results were contrary to what was observed in our study. In our work and for the compositions LATP (Al^{3+} = *0.3* mol%) , LATSP (Al^{3+} = *0.2* mol%) and LADTP (Al^{3+} = *0.25* mol%), no discernible peaks consistent with symmetry breaking were observed in the 550 to 800 cm^{-1} range. However, the peak at 551 cm^{-1} corresponds to the anti-symmetric bending of the PO_4^{3-} groups, consistent with the observations in **Chapter 3** (Sn-doped compositions). We posit that although the substitution of Ti^{4+} with Al^{3+} and Li^+ induces some disorder, as seen in the peak broadening of Al-containing compositions, there was no significant changes in symmetry that may have led to the presence of peaks in the 550 to 800 cm^{-1} region. The occupation of excess Li^+ of the *36f* site would have been expected to induce Raman-active Li^+ vibrational modes due to the symmetry of this site, however, this was not observed in a manner similar to literature. In the work by Burba *et al.*,[20] the addition of excess Li^+ to form $Li_3Ti_2(PO_4)_3$ also did not show any peaks in the 550 to 800 cm^{-1} region similar to our study. This was attributed to the negligible polarizability derivatives of Li^+ ion cage modes, hence no measurable Raman intensities. The symmetric (ν_2) and antisymmetric (ν_4) bending modes were similar across all compositions.

4.3.3. Atomic pair distribution function: unravelling site preference in doped systems

Average bond distances between atoms obtained from total scattering data are, in general, more accurate than those obtained from Bragg data.[26, 27] The differences are even more pronounced in structures that exhibit rigid body motion due to correlated motion of atoms in these types of structures. In this work, the pair distribution function technique was used to probe the effect of substituting Ti with Al, Sn and Al, Dy on the local structure of the $[M_2(PO_4)_3]^-$ framework. The distribution of the average M–M distances from total scattering data (**Figure 4.3**) revealed a shift for some peaks in real space distance (*r*) for the substituted analogues compared to the

parent, while others had no significant shift. This indicated a preference for some sites for the M substituent.

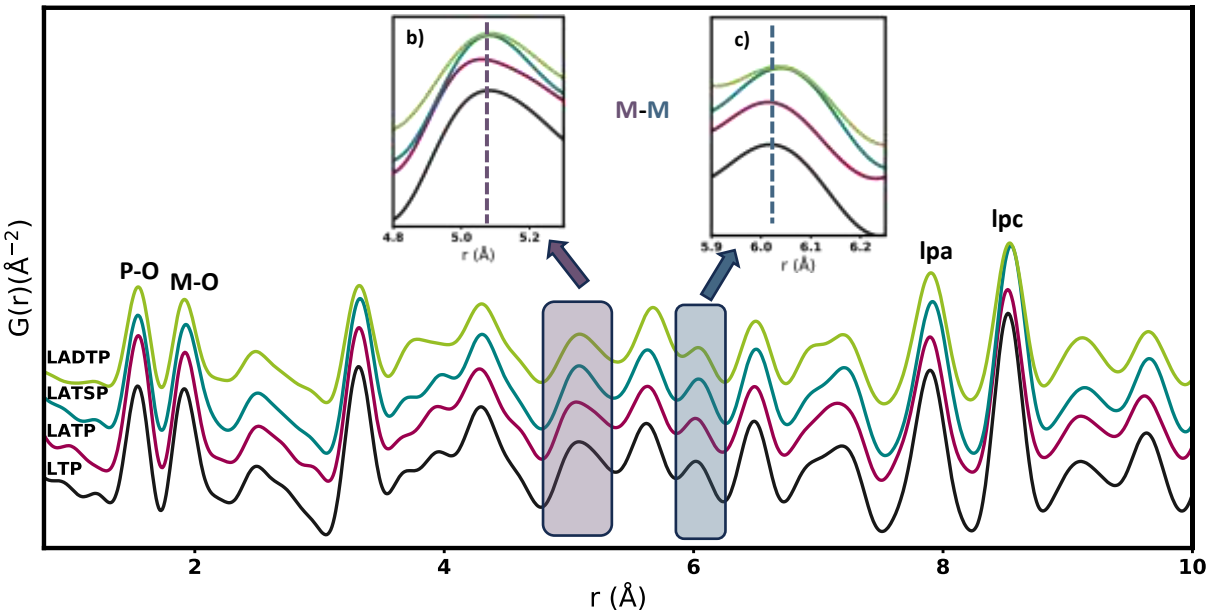


Figure 4.3. (a) Stacked X-ray atomic PDFs of variously doped NASICON-type LTP systems. The zoomed inserts represent the M-M interatomic distances at approximately (b) 5 Å and (c) 6 Å, showing lattice site preference.

For instance, when some of the Ti atoms were replaced with only Al to form LATP, the M–M peak at around 5 Å was shifted to lower *r* values compared to the Ti–Ti distances from the parent material for all the strictly M–M distances inside one unit cell (**Figure 4.3 insert (b)).** This suggested that Al prefers to occupy those positions in the structure, within 5 Å, and this is more energetically favourable due to reduced M–M octahedra repulsions. When Ti was substituted with both Al and Sn in the LATSP sample, there was no significant shift in the M–M peak at around 5 Å ((**Figure 4.3 insert (b)),** suggesting that the Ti in this position was not significantly substituted by Al and/or Sn/Dy in the co-doped analogues.

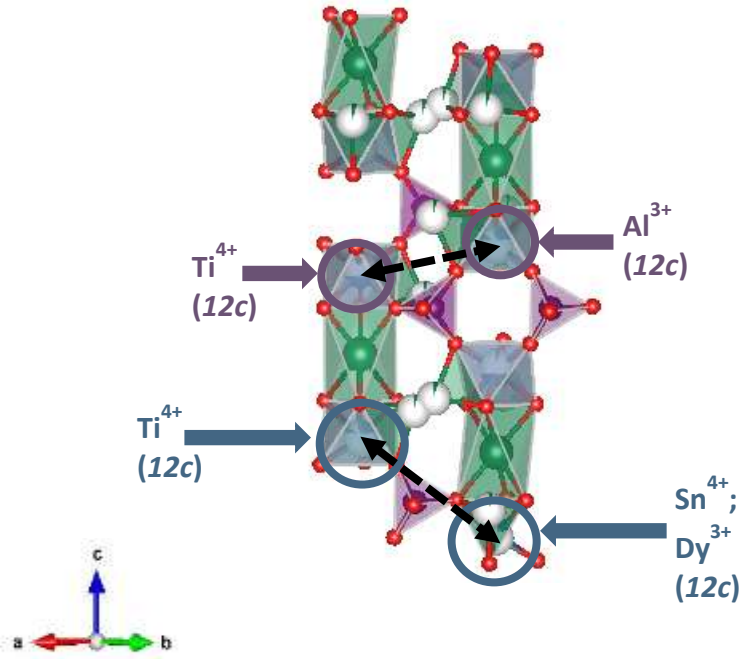


Figure 4.4. A unit cell depiction of the lattice site preference because of Ti replacement with smaller Al^{3+} and larger Sn^{4+} and Dy^{3+}. The Al^{3+} occupies the 12*c* site at 5 Å, while the larger Sn and Dy cation occupy 12*c* sites further from the adjacent Ti at 6 Å.

Looking farther in *r* space in **Figure 4.3 (insert (c))**, the M–M peak at around 6 Å revealed no significant peak shift for the LATP analogue. However, at this same distance the M–M peaks for the LATSP and LADTP analogues exhibited shifts to higher *r* values ((**Figure 4.3 insert (c))** indicating that the larger Sn and Dy cations with larger ionic radii than Ti^{4+}, might prefer to be further apart from adjacent metals to minimise strain in the unit cell and reduce electrostatic repulsions between the M–M octahedra. **Figure 4.4** provides a clearer picture of the phenomenon described as observed from the PDF.

A simulated PDF of the ordered LTP structure, along with selected atom-atom pair partials are presented in **Figure S4.5** in the Supplementary Information. As can be noted in **Figure 4.3.**, other regions in the PDF show slight changes as the doping changes, particularly the peaks at approximately 3.9 and 7 Å, respectively. Both peaks are attributed to the superposition of Ti-O and P-O atom pair interactions as evidenced by the partial PDFs. By virtue of the slight changes noted, it follows that the presence dopant cations in the 12*c* site may have led to local lattice distortions in the MO_6 octahedra and PO_4 tetrahedra.

4.3.4. Qualitative analysis of Ti K-edge XANES

X-ray absorption spectroscopy as a local structure probe was applied to determine the effects of doping on the observed spectral features, which relate to geometry and electronic structure. The normalized Ti K-edge XAS spectra of variously doped NASICON-type systems are presented in **Figure 4.5** relative to the undoped LTP sample.

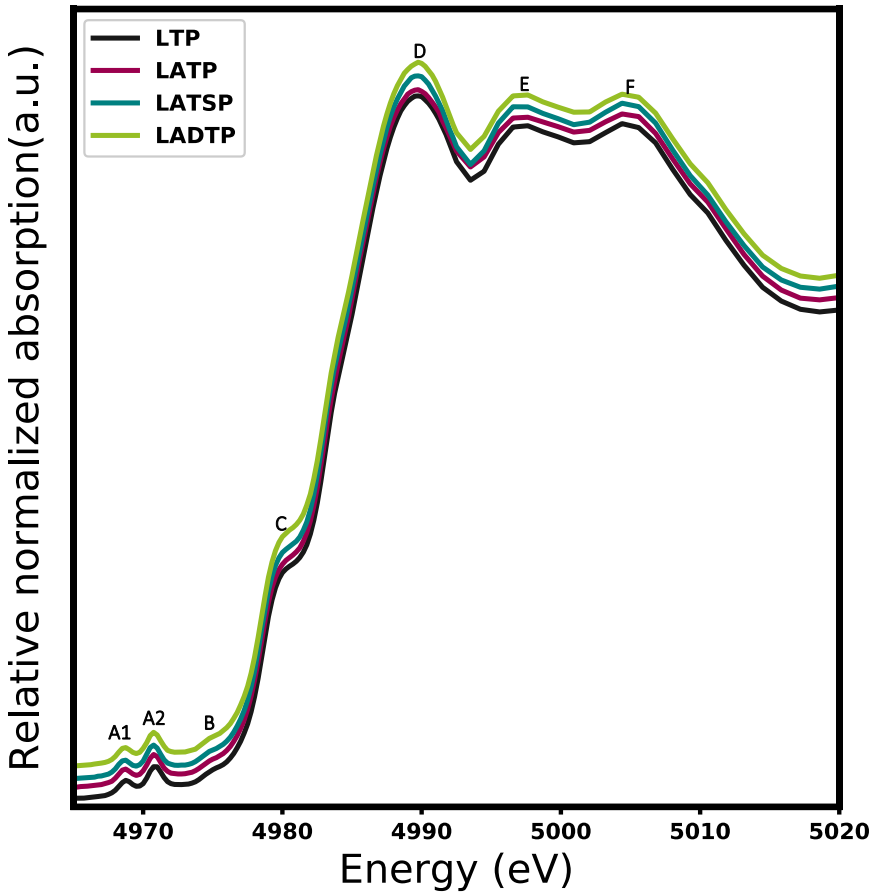


Figure 4.5. Normalized Ti K-edge XANES spectra of variously doped NASICON-type systems. The respective spectra were shifted along the y-axis for clarity.

The qualitative analysis of the Ti K-edge XANES regions of all spectra shows that the spectral features observed were similar to what has been reported in literature for LATP, whose average structure is that of the presented composition; the rhombohedral *R*-3*c* structure.[28] The pre-edge region is characterized by three peaks at approximately 4968 (A1), 4970 (A2) and 4974 (B) eV. The pre-edge features, which are dipole-forbidden according to the Laporte selection rules, become allowed due to orbital mixing between the metal's 3*d* and 4*p* orbitals.[29] An in-depth analysis was provided in **Chapter 3**.

The various compositions did not show significant edge energy shifts, which would imply a change in oxidation states, therefore the Ti species remained at the 4+ oxidation state across all compositions. Qualitatively, the compositions did not exhibit any apparent relative disorder regardless of doping with different elements, as evidenced by the well-defined spectral features across all systems. Further qualitative inspection of the pre-edge peaks indicates that the Ti environment maintained the non-centrosymmetric site occupancy regardless of doping.
Although the regions at approximately 3.9 and 7 Å in the PDF (highlighted in **Figure S4.5**) showed some variations in the peaks attributed to Ti-O and P-O atom pair correlations, the qualitative analysis from the pre-edge XAS has shown no significant changes in the TiO6 octahedra, regardless of doping. However, a quantitative understanding of the peaks' origins is not prevalent for NASICON-type LTP-based systems. Therefore, analysis will provide more insights on the degree of hybridization induced by co-doping, which has rarely been done in NASICON-type LTP-based systems.

4.3.5. Ionic conductivity enhancement induced by co-doping.

EIS was employed in order to investigate the resulting ionic conductivities. The Nyquist impedance plots for LTP, LATP, LATSP and LADTP are shown in **Figure 4.6**. The observed data for the (co)-doped systems LATP, LATSP and LADTP were largely governed by the bulk/intragrain contributions, shown as one semi-circle in the spectra. Also, since only one semi-circle was observed for these three compositions, only the total ionic conductivities could be reported. However, for LTP, the bulk/intragrain and grain boundary contributions were well-resolved through two semi-circles at relatively high and low frequency regions, respectively, giving the individual contributions of intragranular and grain boundary conductivities.

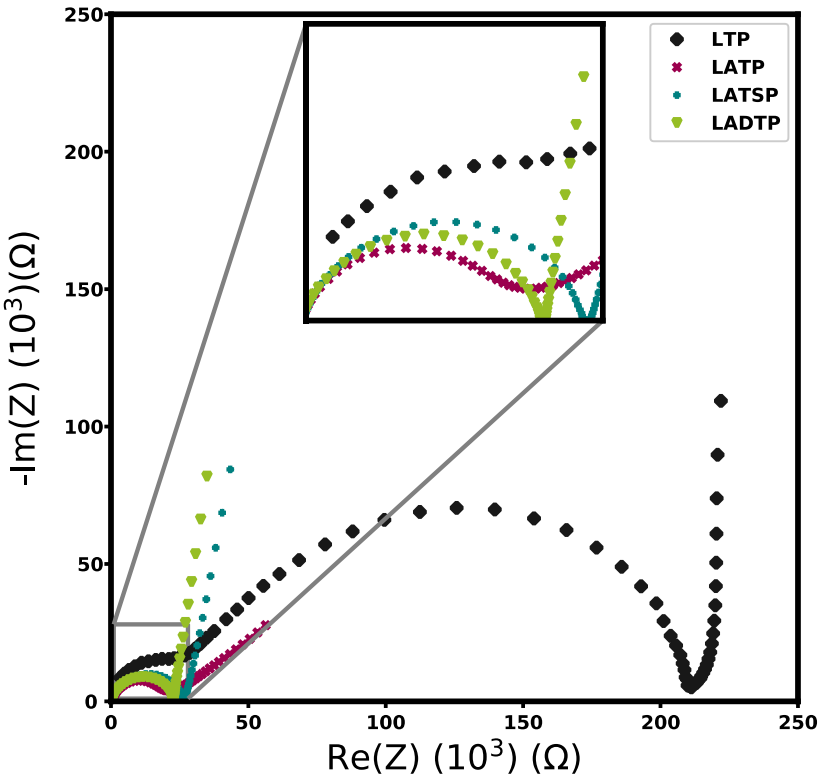


Figure 4.6. Experimental Nyquist impedance plots of NASICON-systems.

The fitted experimental data gave the conductivity values shown in **Table 4.3**. The undoped LTP exhibited the lowest total ionic conductivity of 1.12×10^{-6} S/cm in the series. This was comparable to the conductivity of 1.6×10^{-6} S/cm, found in the study by Arbi and colleagues.[13] LATP showed the second highest total conductivity in the series (8.39×10^{-6} S/cm). However, the result was significantly lower than the expected value in the range of 10^{-3} to 10^{-4} S/cm obtained by Aono *et al.*,[3] for Al^{3+} or Sc^{3+}-doped systems.[28] Arbi *et al.*,[13] obtained a total ionic conductivity of 5.2×10^{-6} S/cm for the 10% Al^{3+}-doped LTP composition. In the present study, LATSP, also containing 10% Al^{3+}, showed a total conductivity that was higher than that in the work by Arbi and colleagues, in the 10^{-6} S/cm range, and approximately 7 times higher than that for LTP. The slightly higher ionic conductivity in LATSP relative to 10% LATP by Arbi *et al.*,[13] could be attributed to the partial replacement of Ti and Al by Sn, of larger ionic radius, thus improving the tunnelling size for Li cations through the structure.

Table 4.3. The room-temperature conductivity values obtained from fitting the EIS experimental data for NASICON-type systems.

	σ_{bulk} (S/cm)	$\sigma_{grain\ boundary}$ (S/cm)	σ_{total} (S/cm)
LTP	9.54×10^{-6}	1.27×10^{-6}	1.12×10^{-6}
LATP	-	-	8.39×10^{-6}
LATSP	-	-	8.04×10^{-6}
LADTP	-	-	1.28×10^{-5}

The presence of impurity phases, although minor, across all doped compositions were the largest contributing factor to the lower conductivities observed. These secondary phases decrease the intergranular/grain boundary Li^+ ionic conduction since they have been reported to occupy the grain boundaries in the pelletized materials. Since the grain boundary conduction is the rate-determining step, the presence of less conducting phases such as TiP_2O_7 and $AlPO_4$ would therefore hinder the fast ionic migration across the solid electrolyte.[3]

Although SXRD (**Table 4.1**) results showed that LATSP has the largest unit cell, the highest conductivity was obtained for LADTP, suggesting that the unit cell expansion, and by extension, the expansion of the LiO_6 polyhedra only influence the total conductivity up to a certain degree, prior to severe structural distortion and stagnant ionic conductivity.[9] The presence of Al^{3+}, and additional Li^+ improves the rate of cation migration by generating additional migration pathways of lower activation energies, thus facilitating improved conductivity by increasing the unit cell volume and the amount of charge carriers.[9] The addition of Dy^{3+}, although small, contributes to the overall improvement of the ionic conductivity possibly mostly due to the higher concentration of charge carriers and easier densification since the addition of Li^+ decreases the melting point of the material. [25]

4.4. Conclusions & Recommendations

This chapter presents two new NASICON-type compositions of Al, Sn and Al, Dy NASICON-type LTP systems. The solid electrolytes were synthesized following the solid-state method. Synchrotron-based PXRD, through Rietveld refinement showed the formation of a rhombohedral major phase, with minor TiP_2O_7, $AlPO_4$ and $DyPO_4$ secondary phases. Raman spectroscopy corroborated the qualitative results from PXRD, confirming the *R*-3*c* main phase of the electrolytes. The effects of doping on the framework were determined using PDF. The qualitative analysis considering the M-M interatomic distances showed that the dopant atoms exhibit lattice site preference relative to adjacent Ti atoms. The replacement of Ti with the smaller Al atoms resulted in the occupation of the adjacent 12*c* site at 5 Å, while the replacement of Ti with larger Sn and Dy cations resulted in the occupancy of 12*c* sites in an adjacent ribbon at approximately 6 Å. To further establish the effects of lattice site substitution on the Ti groups, Ti K-edge XAS indicated that the partial replacement of Ti with iso and/or aliovalent cations did not alter the oxidation state of Ti, attributed to the minimal shifts in edge energy across the various compositions. The co-doping approach resulted in improved ionic conductivity relative to the undoped LTP NASICON-type system, highlighting the importance of simultaneous increase in the tunnelling size for Li migration, and in the concentration of Li charge carriers. Most significantly, the doped systems had negligible grain boundary resistance compared to the parent, resulting in higher total conductivity. DFT studies will aid in resolving the cation migration mechanism as a result of co-doping.

4.5. References

1. Meesala, Y., Jena, A., Chang, H. and Liu, R.S., 2017. Recent advancements in Li-ion conductors for all-solid-state Li-ion batteries. *ACS Energy Letters*, *2*(12), pp.2734-2751.
2. Bachman, J.C., Muy, S., Grimaud, A., Chang, H.H., Pour, N., Lux, S.F., Paschos, O., Maglia, F., Lupart, S., Lamp, P. and Giordano, L., 2015. Inorganic solid-state electrolytes for lithium batteries: mechanisms and properties governing ion conduction. *Chemical reviews*, *116*(1), pp.140-162.
3. Aono, H., Sugimoto, E., Sadaoka, Y., Imanaka, N. and Adachi, G.Y., 1990. Ionic conductivity of solid electrolytes based on lithium titanium phosphate. *Journal of the electrochemical society*, *137*(4), pp.1023-1027.
4. Sugantha, M. and Varadaraju, U.V., 1997. Ionic conductivity of Li^+ ion conductors $Li_2M^{3+}M^{4+}P_3O_{12}$. *Solid State Ionics*, *95*(3-4), pp.201-205.
5. Francisco, B.E., Stoldt, C.R. and M'Peko, J.C., 2015. Energetics of ion transport in NASICON-type electrolytes. *The Journal of Physical Chemistry C*, *119*(29), pp.16432-16442.
6. Lang, B., Ziebarth, B. and Elsässer, C., 2015. Lithium ion conduction in $LiTi_2(PO_4)_3$ and related compounds based on the NASICON structure: a first-principles study. *Chemistry of Materials*, *27*(14), pp.5040-5048.
7. Kahlaoui, R., Arbi, K., Sobrados, I., Jimenez, R., Sanz, J. and Ternane, R., 2017. Cation Miscibility and Lithium Mobility in NASICON $Li_{1+x}Ti_{2-x}Sc_x(PO_4)_3$ ($0 \leq x \leq 0.5$) Series: A Combined NMR and Impedance Study. *Inorganic chemistry*, *56*(3), pp.1216-1224.
8. Rao, A.V., Veeraiah, V., Rao, A.P., Babu, B.K. and Brahmayya, M., 2015. Spectroscopic characterization and conductivity of Sn-substituted $LiTi_2(PO_4)_3$. *Research on Chemical Intermediates*, *41*(7), pp.4327-4337.
9. Nikodimos, Y., Tsai, M.C., Abrha, L.H., Weldeyohannis, H.H., Chiu, S.F., Bezabh, H.K., Shitaw, K.N., Fenta, F.W., Wu, S.H., Su, W.N. and Yang, C.C., 2020. Al–Sc dual-doped $LiGe_2(PO_4)_3$–a NASICON-type solid electrolyte with improved ionic conductivity. *Journal of Materials Chemistry A*, *8*(22), pp.11302-11313.

10. Yang, X., Juhas, P., Farrow, C.L. and Billinge, S.J., 2014. xPDFsuite: an end-to-end software solution for high throughput pair distribution function transformation, visualization and analysis. *arXiv preprint arXiv:1402.3163*.
11. Coelho, A.A., 2018. TOPAS and TOPAS-Academic: an optimization program integrating computer algebra and crystallographic objects written in C++. *Journal of Applied Crystallography*, *51*(1), pp.210-218.
12. Momma, K. and Izumi, F., 2011. VESTA 3 for three-dimensional visualization of crystal, volumetric and morphology data. *Journal of applied crystallography*, *44*(6), pp.1272-1276.
13. Arbi, K., Mandal, S., Rojo, J.M. and Sanz, J., 2002. Dependence of Ionic Conductivity on Composition of Fast Ionic Conductors $Li_{1+x}Ti_{2-x}Al_x(PO_4)_3$, $0 \leq x \leq 0.7$. A Parallel NMR and Electric Impedance Study. *Chemistry of materials*, *14*(3), pp.1091-1097.
14. Best, A.S., Forsyth, M. and Macfarlane, D.R., 2000. Stoichiometric changes in lithium conducting materials based on $Li_{1+x}Al_xTi_{2-x}(PO_4)_3$: impedance, X-ray and NMR studies. *Solid State Ionics*, *136*, pp.339-344.
15. Aatiq, A., Ménétrier, M., Croguennec, L., Suard, E. and Delmas, C., 2002. On the structure of $Li_3Ti_2(PO_4)_3$. *Journal of Materials Chemistry*, *12*(10), pp.2971-2978.
16. Emery, J., Šalkus, T., Abramova, A., Barré, M. and Orliukas, A.F., 2016. NMR investigations in $Li_{1.3}Al_{0.3}Ti_{1.7}(PO_4)_3$ ceramics. Part I: structural aspect. *The Journal of Physical Chemistry C*, *120*(46), pp.26173-26186.
17. Morin, E., Angenault, J., Couturier, J.C., Quarton, M. and He, H., 1997. Phase transition and crystal structures of $LiSn_2(PO_4)_3$. *European journal of solid state and inorganic chemistry*, *34*(9), pp.947-958.
18. Li, L., Zhang, Z., Luo, L., You, R., Jiao, J., Huang, W., Wang, J., Li, C., Han, X. and Chen, S., 2020. Enhancing the interface stability of $Li_{1.3}Al_{0.3}Ti_{1.7}(PO_4)_3$ and lithium metal by amorphous $Li_{1.5}Al_{0.5}Ge_{1.5}(PO_4)_3$ modification. *Ionics*, *26*, pp.3815-3821.
19. Giarola, M., Sanson, A., Tietz, F., Pristat, S., Dashjav, E., Rettenwander, D., Redhammer, G.J. and Mariotto, G., 2017. Structure and vibrational dynamics of NASICON-type $LiTi_2(PO_4)_3$. *The Journal of Physical Chemistry C*, *121*(7), pp.3697-3706.
20. Burba, C.M. and Frech, R., 2006. Vibrational spectroscopic study of lithium intercalation into $LiTi_2(PO_4)_3$. *Solid State Ionics*, *177*(17-18), pp.1489-1494.

21. Bamberger, C.E. and Begun, G.M., 1987. Synthesis and characterization of titanium phosphates, TiP_2O_7 and $(TiO)_2P_2O_7$. *Journal of the Less Common Metals*, *134*(2), pp.201-206.
22. Poswal, H.K., Garg, N., Somayazulu, M. and Sharma, S.M., 2013. Pressure-induced structural transformations in the low-cristobalite form of $AlPO_4$. *American Mineralogist*, *98*(2-3), pp.285-291.
23. Zhang, M. and Scott, J.F., 2007. Raman studies of oxide minerals: a retrospective on cristobalite phases. *Journal of Physics: Condensed Matter*, *19*(27), p.275201.
24. Angot, E., Le Parc, R., Levelut, C., Beaurain, M., Armand, P., Cambon, O. and Haines, J., 2006. A high-temperature Raman scattering study of the phase transitions in $GaPO_4$ and in the $AlPO_4$–$GaPO_4$ system. *Journal of Physics: Condensed Matter*, *18*(17), p.4315.
25. Dashjav, E., Ma, Q., Xu, Q., Tsai, C.L., Giarola, M., Mariotto, G. and Tietz, F., 2018. The influence of water on the electrical conductivity of aluminum-substituted lithium titanium phosphates. *Solid State Ionics*, *321*, pp.83-90.
26. Egami, T. and Billinge, S.J., 2003. *Underneath the Bragg peaks: structural analysis of complex materials*. Elsevier.
27. Tucker, M.G., Dove, M.T. and Keen, D.A., 2000. Direct measurement of the thermal expansion of the Si-O bond by neutron total scattering. *Journal of Physics: Condensed Matter*, *12*(26), p.L425.
28. Ichihara, F., Miyoshi, S. and Masuda, T., 2022. Co-sintering process of $LiCoO_2$ cathodes and NASICON-type LATP solid electrolytes studied by X-ray diffraction and X-ray absorption near edge structure. *Physical Chemistry Chemical Physics*, *24*(42), pp.25878-25884.
29. DeBeer George, S., Brant, P. and Solomon, E.I., 2005. Metal and ligand K-Edge XAS of organotitanium complexes: Metal 4p and 3d contributions to pre-edge intensity and their contributions to bonding. *Journal of the American Chemical Society*, *127*(2), pp.667-674.

4.6. Supplementary Information

Figure S4.1. Rietveld refinement result of LTP.

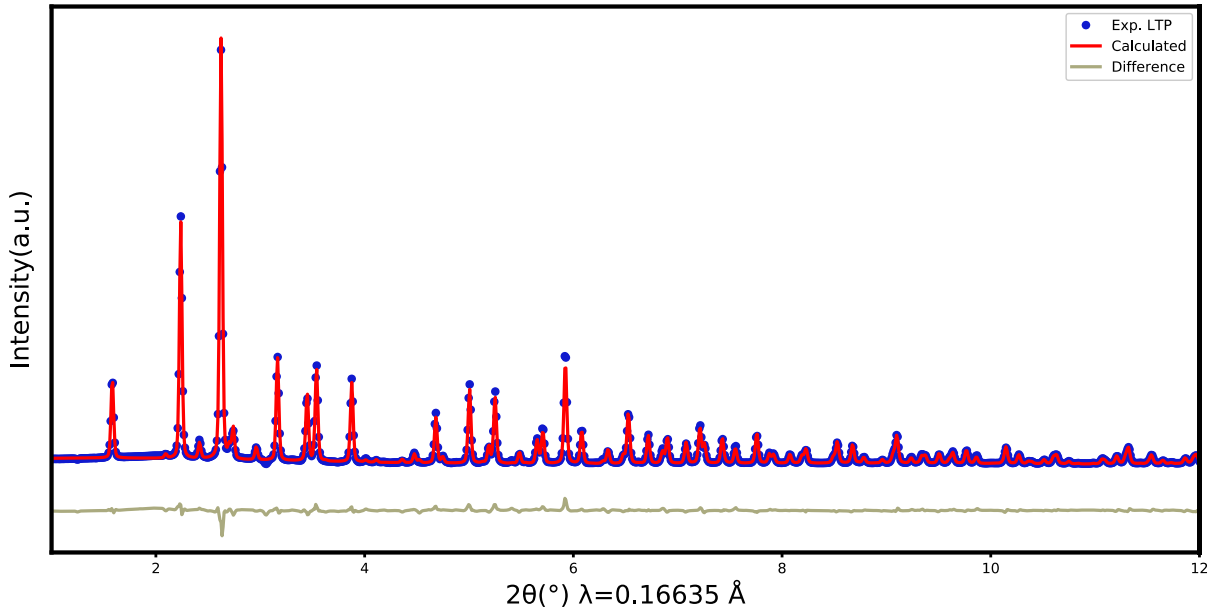


Table S4.1. Crystallographic data for LTP from Rietveld refinement of synchrotron XRD results (28-ID-1 at NSLS-II, 1.6635 Å).

	LTP (ICSD 95979)	**TiP_2O_7 (ICSD 189807)**
RBragg	3.51	5.20
Weight %	96.6(2)	3.4(2)
Space group	*R*-3*c*	*Pa-3*
a (Å)	8.520(2)	7.89(1)
b (Å)	8. 520(2)	7.89(1)
c (Å)	20.87(1)	7.89(1)
Volume ($Å^3$)	1312.0(9)	490.(3)
Phase density (g/cm^3)	2.943(2)	4.68(2)

Whole pattern refinement parameters: R_{exp} = 17.21%, R_{wp} = 6.95, R_p = 5.19, GOF = 0.40.

Figure S4.2. Rietveld refinement result of LATP.

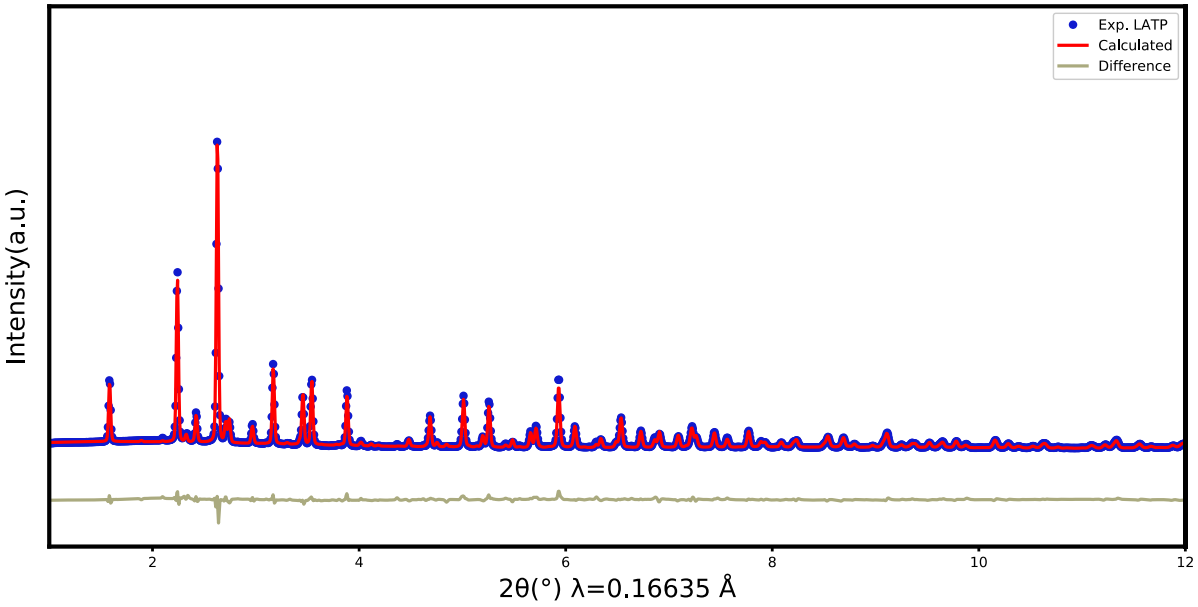


Table S4.2. Crystallographic data for LATP from Rietveld refinement of synchrotron XRD results (28-ID-1 at NSLS-II, 1.6635 Å).

	LATP (ICSD 95979)	**TiP_2O_7 (ICSD 189807)**	**$AlPO_4$ (ICSD 98382)**
RBragg	3.71	4.47	3.70
Weight %	90.6(3)	3.5(1)	5.9(3)
Space group	*R*-3*c*	*Pa-3*	$C222_1$
a (Å)	8.505(2)	7.871(9)	7.22(2)
b (Å)	8. 505(2)	7.871(9)	7.04(3)
c (Å)	20.864(9)	7.871(9)	7.04(6)
Volume ($Å^3$)	1306.9(8)	488.(1)	358.(4)
Phase density (g/cm^3)	2.923(1)	3.02(1)	2.26(2)

Whole pattern refinement parameters: R_{exp} = 20.64%, R_{wp} = 6.82, R_p = 5.33, GOF = 0.33.

Figure S4.3. Rietveld refinement result of LATSP.

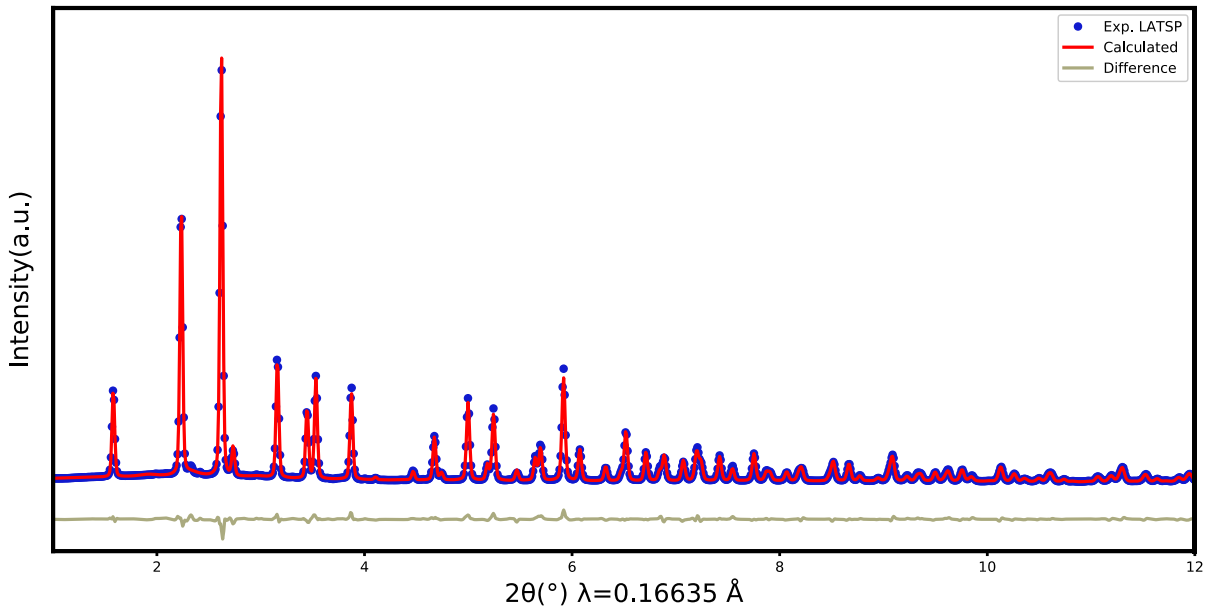


Table S4.3. Crystallographic data for LATSP from Rietveld refinement of synchrotron XRD results (28-ID-1 at NSLS-II, 1.6635 Å).

	LATSP (ICSD 95979)	**$AlPO_4$ (ICSD 98382)**
RBragg	3.02	3.70
Weight %	90.0(9)	10.1(9)
Space group	*R*-3*c*	$C222_1$
a (Å)	8.525(2)	7.2(8)
b (Å)	8. 525(2)	7.2(10)
c (Å)	20.930(9)	7.4
Volume ($Å^3$)	1317.4(8)	380.(5)
Phase density (g/cm^3)	2.963(1)	2.1(4)

Whole pattern refinement parameters: R_{exp} = 20.64%, R_{wp} = 6.82, R_p = 5.33, GOF = 0.33.

Figure S4.4. Rietveld refinement result of LADTP.

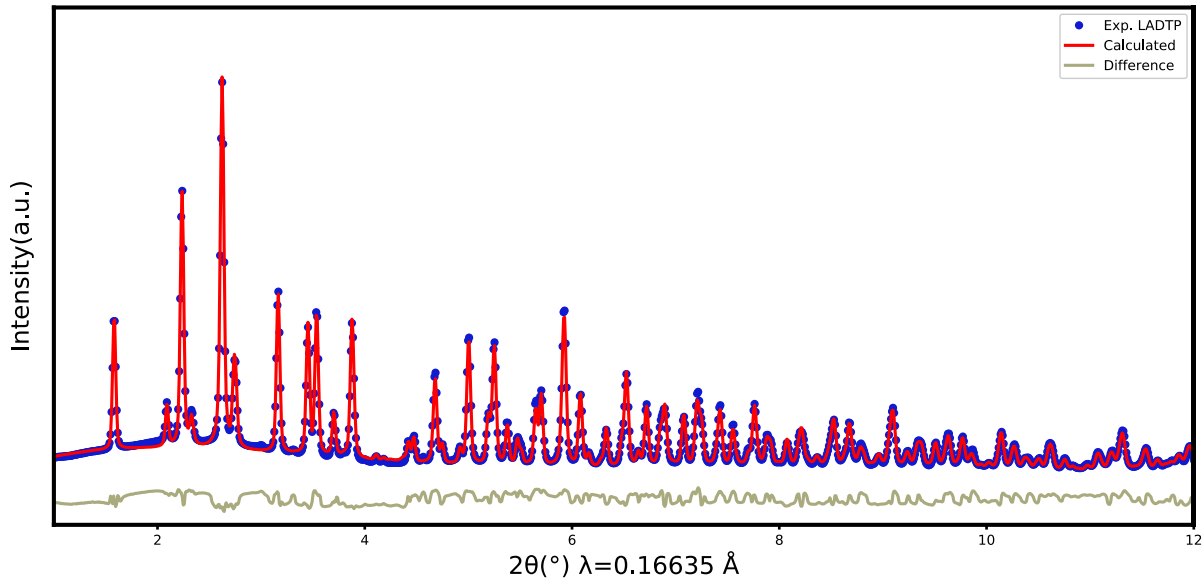


Table S4.4. Crystallographic data for LADTP from Rietveld refinement of synchrotron XRD results (28-ID-1 at NSLS-II, 1.6635 Å).

	LADTP (ICSD 95979)	**$AlPO_4$ (ICSD 98382)**	**$DyPO_4$ (ICSD 35705)**
RBragg	3.25	4.07	3.49
Weight %	94.3(2)	3.5(2)	2.2(7)
Space group	*R*-3*c*	$C222_1$	$I4_1/amd$
a (Å)	8.515(2)	7.07(2)	6.921(9)
b (Å)	8.515(2)	7.286(7)	6.921(9)
c (Å)	20.910(1)	6.93(2)	6.06(1)
Volume ($Å^3$)	1313.2(1)	357(1)	290.3(1)
Phase density (g/cm^3)	2.96	2.27	5.89

Whole pattern refinement parameters: R_{exp} = 14.43%, R_{wp} = 5.30, R_p = 4.32, GOF = 0.37.

Table S4.5. Raman spectroscopy peak assignments for NASICON-type systems.

	External Modes (cm^{-1})						**PO_4 bending modes (cm^{-1})**			**PO_4 stretching modes (cm^{-1})**				**Secondary phase peaks (cm^{-1})**	
Peak Assignment	E_g (2)	A_{1g} (1)	E_g (5)	E_g (6)	A_{1g} (3)	E_g (7)	A_{1g} (4)	A_{1g} (5)	E_g (11)	E_g (14)	E_g (15)	E_g (16)	A_{1g} (8)		
Composition															
LTP	139.9	178.5	238.8	273.6	312.1	352.4	432.4	447.5	547.3	969.8	989.5	1007.3	1094	1037.5	1074.1
LATP	141.4	178.5	238.8	275.5	312.1	354.3	434.3	451.3	551.1	969.8	991.3	1009.1	1095.8	1051.6	1072.9
LATSP	139.5	176.6	240.7	275.5	312.1	352.4	443.3	449.4	551.1	971.6	991.3	1007.3	1094.0	1051.6	1071.1
LADTP	139.5	178.5	240.7	275.5	312.1	354.3	434.3	449.4	551.1	969.8	991.3	1009.1	1095.8		1076.4

Figure S4.5. Simulated PDF of the ordered LTP (R-3c) structure, with accompanying atom-atom interaction partials.

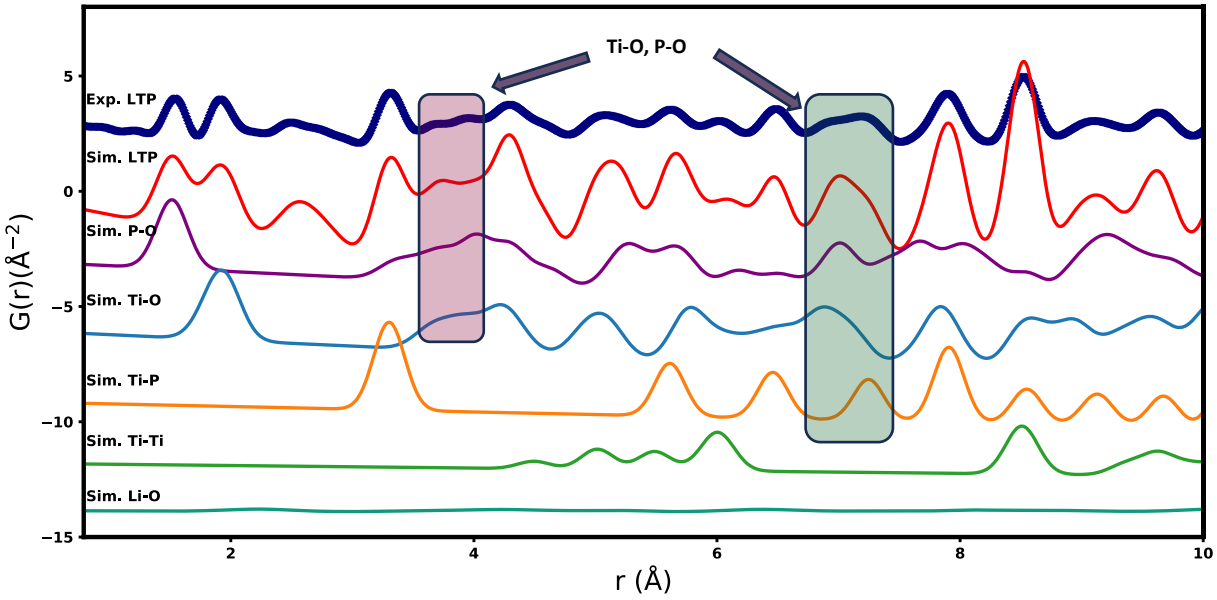


Table S4.6. The expected Raman spectroscopy peaks for the $AlPO_4$ cristobalite ($C222_1$)secondary phase observed in Al-bearing NASICON-type compositions. The last column presents whether the expected $AlPO_4$ phase peaks are observed in the measured NASICON spectra.

	Compositions				**$AlPO_4$ Peak Observation in NASICON spectra**
	LATP	**$AlPO_4$,[22]**	**$AlPO_4$,[23]**	**$AlPO_4$,[24]**	
Peak positions (cm^{-1})		99			
	141.4			145	
	178.5				
			188	188	Possible overlap with NASICON peaks.
	238.8	240.7	240.7	240.7	
	275.5	278		279	Possible overlap with NASICON peaks.
	312.1				
	354.3	352.4	352.4	352.4	
		380-390	388	388	Not observed.
	434.3				
	451.3	449.4	449.4	449.4	
		482		482	Not observed.
	551.1				
				713	Not observed.
				924	Not observed.
	969.8				
	991.3		996	996	Possible overlap with NASICON peaks.
	1009.1			1013	
	1095.8				

		1109		1113	Not observed.
		1119		1124	

Chapter 5: On the average, local and electronic structure of NASICON-type $Li_{1.3}Al_{0.25}Dy_{0.05}Ti_{1.7}(PO_4)_3$ (LADTP) solid-state electrolyte

Gugulethu C. Nkala[1,2], Sikhumbuzo M. Masina[1], Fernando D. Vila[3], John J. Rehr[3], Rudolph Erasmus[4], Roy P. Forbes[1], Caren Billing[1], David G. Billing[1,2]

[1] Molecular Sciences Institute, School of Chemistry, University of the Witwatersrand, Private Bag X3, Johannesburg, 2050, South Africa

[2] DSI-NRF Centre of Excellence in Strong Materials

[3] Department of Physics, University of Washington, Seattle, WA, 98195, United States

[4] Materials Physics Research Institute, University of the Witwatersrand, Private Bag X3, Johannesburg, 2050, South Africa

KEYWORDS: NASICON solid electrolytes, synchrotron PXRD, pair distribution function, XANES, FEFF

This chapter has been prepared for submission, in fulfillment of the degree requirements, and has been formatted accordingly. Part of the work presented herein was accomplished in collaboration with the University of Washington, Seattle in the Rehr Research Group as part of a research visit.

ABSTRACT: We report a rhombohedral (*R*-3*c*) Al, Dy co-doped $LiTi_2(PO_4)_3$ NASICON-type (LADTP) solid-state electrolyte for potential applications in all-solid-state batteries. Co-doping strategies have been proposed as a method for improving the room-temperature ionic conductivity in NASICON-type solid-state electrolytes. However, it is important to establish the substituents' influence on the local, average, and electronic structure of the electrolytes to gain a better understanding of the factors that may influence ionic conductivity. To this effect, this work has employed a combination of techniques to explore the average, local and electronic structure of NASICON-type systems. Synchrotron-based PXRD was used to determine the qualitative and quantitative phase composition of the LADTP system, through Rietveld analysis, showing a rhombohedral *R*-3*c* average structure. Raman spectroscopy confirmed the presence of the rhombohedral major phase, with minimal insights into the degree of local structural disorder induced by cationic replacement of Ti^{4+} with Dy^{3+}.

Local atomic structural insights were gained through the small-box modelling of the X-ray pair distribution function, showing a local monoclinic $P2_1/n$ description at the region below 10 Å, a local structure deviation from the rhombohedral structure observed in PXRD. X-ray absorption spectroscopy provided insights into the Dy environment in the LADTP system. Using both experimental and theoretical XANES, the Dy local environment in LADTP was predominantly found to be similar to that of Dy in Dy_2O_3 (*Ia*-3). This work highlights the importance of using structural probes that study the material across various length scales to improve the design of future energy materials.

5.1. Introduction

The increasing need for better energy storage devices has been the driving force in researching solid electrolytes that can be used in all-solid-state batteries. These batteries offer better alternatives to their organic electrolyte-bearing counterparts due to their thermal and chemical stability in air and moisture, as well as their high energy, and power density.[1-5] NASICON-type based compounds, with the chemical formula $LiM_2(PO_4)_3$ have a rhombohedral structure, belonging to the space group *R*-3*c* for M = Ti and Ge. The rigid framework consists of MO_6 octahedra that are corner-linked to PO_4 tetrahedra, forming a helical structure about the c-axis. The mobile cations, in this case Li^+, occupy two possible interstitial sites; i) the 6-fold O-coordinated 6*b*, or ii) the 8-fold O-coordinated 18*e*. The 6*b* site has been shown to be the more thermodynamically stable, and thus more favorable than the 18*e* site in $LiTi_2(PO_4)_3$ (LTP). LTP exhibits a 3D network that, in principle, should allow for fast migration of Li^+ species, and this class of materials has been proposed and studied as possible solid-state electrolytes for Li-ion batteries (LIBs).[1-4] Although these materials should allow for good ionic conduction due to the presence of such a 3D structure, their room-temperature ionic conductivity in the order of 10^{-7} S/cm is insufficient for solid-state batteries.

Various sites, i.e., the Li^+ 6*b* and especially the M 12*c* sites within the NASICON framework can be substituted with a wide range of aliovalent and isovalent cations, allowing for tuning the structure and, in turn, the physical properties of the materials. Upon substituting the M 12*c* site with aliovalent +3 cations, the chemical formula becomes $Li_{1+x}Ti_{2-x}M^{3+}{}_x(PO_4)_3$. The highest conductivity for NASICON-based systems has been reported for 15% Al-doped LTP ($Li_{1.3}Al_{0.3}Ti_{1.7}(PO_4)_3$, LATP), to the order of 10^{-4} S/cm.[2] The ionic conductivity can be improved by tuning the size of the tunnel for the Li cations.

This tunnel is formed by three O atoms at the vertices of the face of the 6b site via lattice site substitution with ions of larger radii at the neighboring 12*c* site (Ti^{4+}). Another strategy is to increase the concentration of charge carriers, i.e., Li^+ ions, by replacing Ti with trivalent cations such as Al, In, Fe, Sc and rare-earth elements such as Eu.[5 - 6] The charge deficit created by the +3 species is neutralized by additional Li^+. The changes in chemical composition and synthetic conditions of the NASICON-related compounds alter the average structure from the typical NASICON-type rhombohedral, to monoclinic, orthorhombic, and triclinic structures, related through the slight distortions of the hexagonal lattice.[7] The complex polymorphism in the average structure leads to changes in the ionic conductivity of these materials.[6, 8-11]

First-principles studies have provided information on the effect of doping on the conductivity properties of NASICONs. Lang *et al.*,[4] showed that the additional Li^+ cations in M^{3+}-doped compositions occupy the 36*f* site, a 4-fold O-coordinated site on either side of the 18*e* site, near the +3 dopant at the 12*c* site. This occupation by Li^+ ions is attributed to the dopant cations altering the activation energy for Li^+ migration in the bulk. These observations were supported by multiple studies based on neutron powder diffraction (NPD) since Li can be readily probed through NPD due to its negative coherence length, in relation to the framework elements.[12-13] The Fourier difference maps allow for the determination of the location of Li^+ cations within the structure. Typically, the average structure and phase compositions of various conductive compounds have been extensively studied using powder X-ray diffraction (PXRD). Solid-state Nuclear Magnetic Resonance (NMR) has also been extensively used in elucidating the coordination environment around the dopants at the 12*c* site, such as Al, and any changes on the PO_4^{-3} polyhedra.[3, 14] The position of Li ions within the structure can also be obtained from NMR. Raman and infrared spectroscopy provide insight into the changes in the framework and around Li. However, since in the rhombohedral LTP system Li occupies a site with S_6 symmetry, this renders the site Raman-inactive, but the structural insights around Li can be well established from IR spectroscopy.[15]

Synchrotron-based probes such as the atomic pair distribution function (PDF) have rarely been applied in the study of the rhombohedral LTP. An LTP-analogous $Na_{1+x}Al_xGe_{2-x}(PO_4)_3$ system was studied using NMR and PDF.[16] Although the PDF analysis provided an understanding of the coordination numbers around Ge, Al and P, no structure-based, Rietveld-like modelling was applied.

In the present study, an Al, Dy co-doped system with a nominal composition $Li_{1.3}Al_{0.25}Dy_{0.05}Ti_{1.7}(PO_4)_3$ (LADTP), with 12.5% Al and 2.5 % Dy has been designed. The simultaneous use of Al^{3+} (r = 0.535 Å) and Dy^{3+} (r = 0.912 Å) in this composition yielded the best possible combination of cations such that the resultant radii were comparable to that of Ti^{4+} (r = 0.74 Å).[17] This strategy allows for the simultaneous increase in the tunnel size for Li^+, and the enhancement of the concentration of charge carriers. We investigate the effects of co-doping on the average structure and phase composition via synchrotron-based PXRD and in-house Raman spectroscopy. The atomic PDF is employed to determine the structure across multiple length scales through small-box modeling to potentially elucidate any deviation from the Bragg-detected average structure, and XANES gives insight into the changes around the Dy dopant. Finally, the experimental XANES features are assigned from first principles using FEFF.

5.2. Experimental Section

5.2.1. Synthesis

The Al^{3+}, Dy^{3+} co-doped $LiTi_2(PO_4)_3$ was synthesized following the conventional solid-state method. Dy_2O_3 was obtained via the thermal decomposition of $Dy(NO_3)_3•6H_2O$ (Sigma-Aldrich, 99.999%) at 700 °C in air, for 2 hours. Stoichiometric amounts of Li_2CO_3, $(NH_4)_2HPO_4$, TiO_2 (Degussa P25), Al_2O_3 (99.99% purity), and Dy_2O_3 were ground in an agate pestle and mortar for 1 hour. The fine powder was decanted into an alumina crucible and heated to 450 °C in air, at a heating rate of 10 °C/min and soaked at 450 °C for 1 hour to decompose the phosphate. Upon cooling to room temperature, the intermediate was removed by scraping, ground for 1 hour in an agate pestle and mortar and transferred into a boat. The boat was placed into a horizontal tube furnace and heated to 900 °C in nitrogen at a heating rate of 10 °C/min and soaked at 900 °C for 9 hours. The final product was a white powder that was finely ground for 20 minutes and stored for further characterization.

5.2.2. Characterization

The average structure of LADTP was investigated with synchrotron based PXRD (PXRD) and PDF. The data were collected at the National Synchrotron Light Source-II (NSLS-II) at the 28-ID-1 (PDF) beamline at room temperature.

The powder sample was loaded into a Kapton capillary and measured in transmission geometry. The direct sample to detector distances were 819.16 mm and 241.78 mm for PXRD and PDF, respectively. The wavelength of the radiation was 0.1663 Å. A 2D PerkinElmer area detector with a 200 × 200 μm pixel size was employed. The Si (NIST SRM 640d) standard was also measured to determine the instrumental profile. An empty Kapton capillary was measured to obtain the background function. Rietveld analyses of the PXRD results were implemented on TOPAS-Academic (Version 7.12).[18] The crystallographic data and structural parameters are reported in **Table S1** and **S2**. The $LiTi_2(PO_4)_3$ and $Li_{1.3}Al_{0.3}Ti_{1.7}(PO_4)_3$ NASICON-type rhombohedral structure models were used in the Rietveld refinements using the Thompson-Cox-Hastings pseudo-Voigt peak profile, where the lattice parameters, fractional coordinates, atomic displacement parameters and site occupancies were fined. The 12*c* site for Ti, Al and Dy was set to the nominal composition, similarly for Li^+ at 6*b* and 36*f* sites. The crystallite size and strain were also refined. The resultant crystallographic structures were visualized in the VESTA software. The program xPDFsuite was used to extract the experimental PDF. The r-poly was set to 0.98 Å and an upper Q-range cutoff of 25.4 $Å^{-1}$ was used. The real-space structure fits were carried out in TOPAS-Academic (Version 7.12).

Raman spectroscopy measurements were conducted at room temperature at a wavelength of 514.5 nm, using an Ar+ laser with a grating of 600 lines/mm and a 100× objective lens. The instrument employed a Symphony CCD detector, cooled with nitrogen. The instrument was calibrated with as Si single crystal standard, to an error of ±0.4 cm^{-1}. The peak positions were obtained using the LabSpec software (V5.93.20). The tabulated peak assignments are given in **Table S3**.

Experimental XAS data for LADTP and a Dy_2O_3 standard were collected at the 6-BM beamline at NSLS-II.[19] The powdered LADTP and Dy_2O_3 samples with approximate particle sizes of 41(1) nm and 27(4) nm, respectively, were individually ground with cellulose filler (Avicel PH-101, ~50 μm cellulose, Sigma-Aldrich,) in an agate pestle and mortar until they were homogeneous. The mixtures were pressed into pellets of 13 mm diameter at 40 MPa pressure, using a uniaxial hydraulic press at room temperature. The pellets were loaded onto sample holders and held with Kapton tape. The measurements for LADTP and Dy_2O_3 were done in fluorescence and transmission modes, respectively, using a Si (111) double monochromator. The typical edge steps for Dy_2O_3 measured in transmission mode were set to 10 eV before the edge, 2 eV at the edge and 0.03 eV after the edge. The steps were 0.05k for the EXAFS region. The nominal composition for LADTP had a maximum of 2.5% Dy, therefore no self-absorption correction was applied for the fluorescence data as the sample was sufficiently dilute and thin.

Typical data reduction (i.e., background subtraction, energy calibration and alignment) were carried out in the ATHENA software of the DEMETER package.[20] The evaluation of the results was done on an average of three scans for each system. The edge energies were determined as the maxima of the first-derivative spectra.

Computational details for theoretical XANES

Computational details for theoretical XANES. The Dy L_3-edge XANES spectra were calculated for both LADTP and Dy_2O_3 using the FEFF10 software.[21] The starting models for both systems were generated from PXRD. The average structure of Dy_2O_3 was indexed to the cubic system (space group *Ia*-3) (see **Figure S1** and **Table S4**) The structure of Dy_2O_3 consists of two inequivalent sites, 8*b* at (0.25, 0.25, 0.25) and 24*d* at (x, 0, 0.25), therefore, calculations were done for both, and the resultant theoretical spectrum was a weighted average according to the stoichiometry of the system. The optimum parameters obtained from calculations for Dy_2O_3 standard were used in subsequent calculations for LADTP. An 8 Å cluster was constructed around the Dy absorbers. Both the electric dipole and quadrupole transitions were accounted for. The Hedin-Lundqvist self-energy and a ground-state background function were used, with self-consistent field (SCF) radii of 5 Å and full multiple scattering (FMS) radii of approximately 7.96, 7.87 and 7.98 Å for Dy_2O_3, $DyPO_4$ ($I4_1/amd$) and $DyPO_4$ ($P2_1/n$), respectively. The amplitude reduction factor was set to 1.0. In order to obtain better resolution for the low energy peaks, the energy grid was customized to minimum and maximum values of -26 eV and 10 eV, respectively, at 0.03 eV steps, while the *k*-grid was customized to a maximum value of 6.0 $Å^{-1}$ at 0.03 $Å^{-1}$ steps. The local l-projected density of states (LDOS) calculations was conducted in the energy range -30 eV to 20 eV, with the Lorentzian broadening set to 0.01 eV. Finally, the theoretical spectra were shifted by 4.86 eV to align the high-energy (EXAFS) regions to that observed in experiment. This shift was applied to all theoretical spectra to preserve the relative behavior.

5.3.1. Synchrotron powder X-ray diffraction (SXRD)

The room-temperature diffraction pattern of LADTP is shown in **Figure 5.1**. The most intense peaks were indexed to the NASICON-type rhombohedral structure of LTP at 94.3(2) weight% (space group *R*-3*c*) (ICSD 95979).[22] Minor secondary phases of $AlPO_4$ (space group $C222_1$, ICSD 257190) and $DyPO_4$ (space group *I*41/*amd*, ICSD 35705) were also detected at 3.5(2) and 2.2(2) weight %, respectively.[23, 24]

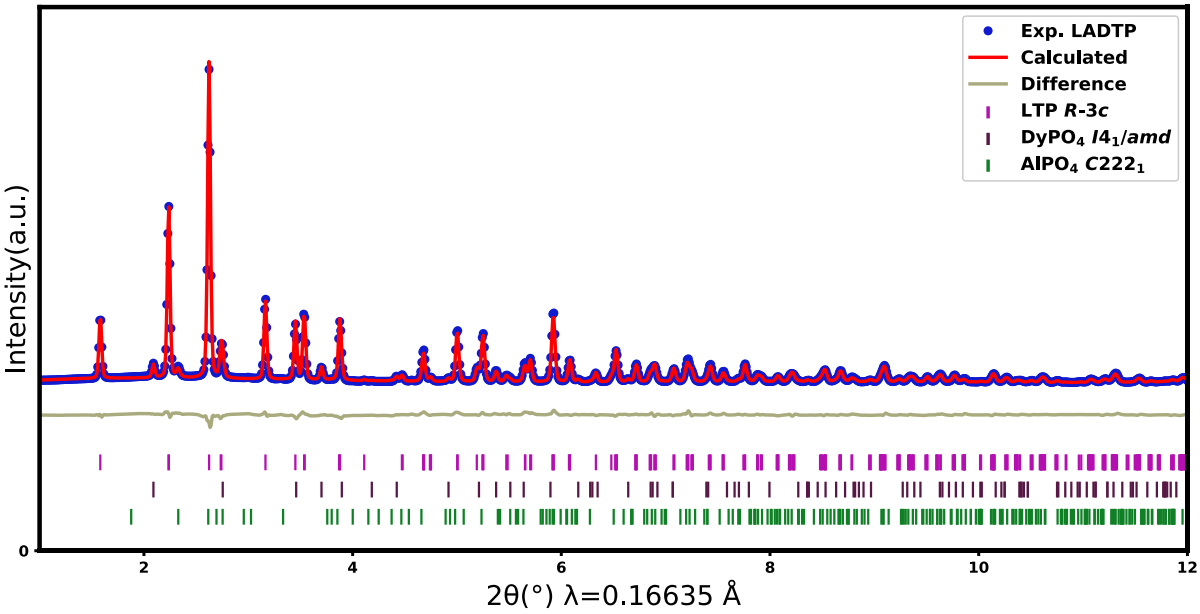


Figure 5.1. The Rietveld refinement result of synchrotron XRD data of the Al, Dy co-doped LADTP system, indexed to the rhombohedral NASICON-type structure (space group *R*-3*c*) (blue circles = observed data, red line = calculated model, and grey line = difference).

The Rietveld refinement analysis for LADTP was carried out using the NASICON-type rhombohedral model, with i) Li occupying the 6*b* and 36*f* sites, ii) Ti, Al, Dy at 12*c*, iii) P at 18*e* and iv) O1 and O2 at 36*f* sites. The resulting structural parameters presented in **Table 5.1** showed unit cell expansion more notably along the c-axis (~0.32% expansion) relative to the starting model of LTP, similar to the findings of Lang *et al.*,[4] The unit cell expansion is suggestive of the successful partial replacement of Ti^{4+} with Dy^{3+} attributed to the larger ionic radius of Dy^{3+} (r_{Dy3+}, six-fold coordination = 0.912 Å), than Ti^{4+} in the same environment (r_{Ti4+} = 0.605 Å)

Table 5.1. Comparison of Rietveld refinement-obtained structural parameters for LADTP and literature-reported LTP and LATP systems both indexed to the rhombohedral NASICON structure (*R*-3*c*). The contraction and expansion % (shown in parentheses) correspond to the change from LTP.

Cell parameters	**[a] LTP**	**[b] LATP**	**LADTP**
a (Å)	8.5110(1)	8.5098(1) (-0.02%)	8.515 (+0.05%)
c (Å)	20.843(4)	20.8305(4) (-0.06%)	20.909(+0.32%)
Volume ($Å^3$)	1307.53	1306.38 (-0.09%)	1313.21 (+0.43%)

[a, b] Literature values from ICSD 95979 for $LiTi_2(PO_4)_3$ (LTP) and ICSD 257190 for $Li_{1.3}Al_{0.3}Ti_{1.7}(PO_4)_3$ (LATP) reference compositions, respectively.

The formation of $AlPO_4$ has previously been reported for Al-doped LTP at Al contents higher than 15%.[25] In the present study, 12.5% Al^{3+} nominal concentration was used, and the secondary phase still formed. The formation of $DyPO_4$ was attributed to the size disparity between Ti^{4+} (r = 0.605 Å) and Dy^{3+} (r = 0.912 Å) in a six-fold coordination geometry. In previous works wherein lanthanides were substituted into the NASICON-type structure at the Ti 12*c* site, an ideal solid solution was formed when the ionic radius of Ln^{3+} was approximately 0.9 Å.[5] The amount of Dy^{3+} incorporated into the structure was determined following the standard-less Rietveld quantitative phase analysis methodology,[26] and found to be 96.6%, and it was also suggested by the unit cell expansion.

5.3.2. Raman spectroscopy

The NASICON-type framework consists of MO_6 and PO_4 polyhedra that can be readily probed with Raman spectroscopy to further establish the phase compositions and the effects of doping on the structure of LADTP. **Figure 5.2** shows the Raman spectrum of LADTP. The deconvoluted peak positions and assignments are given in **Table S3**.

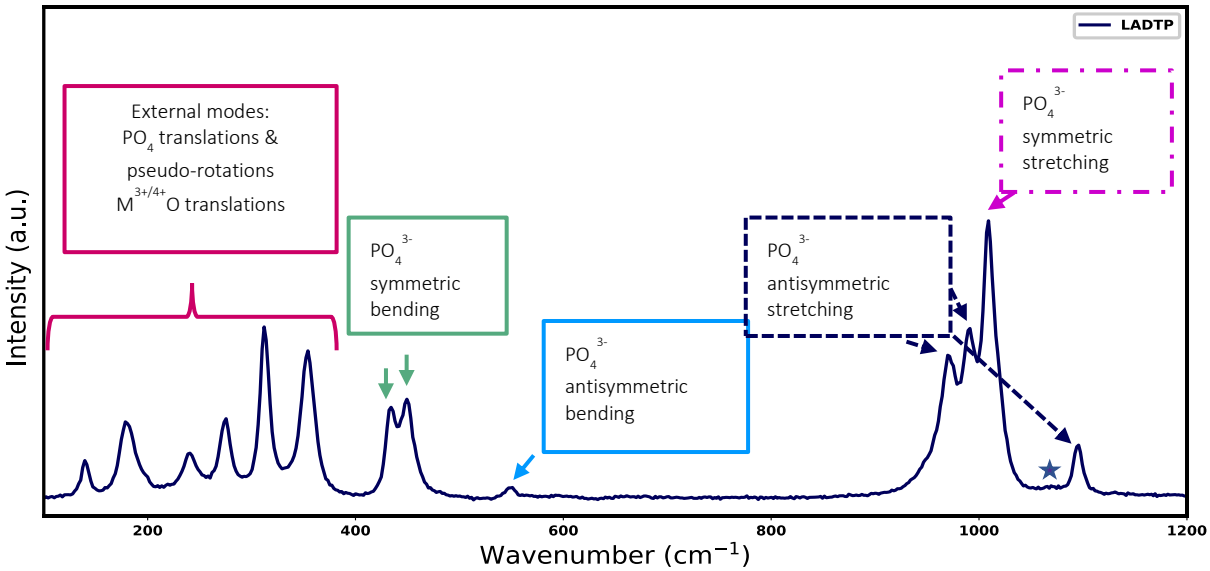


Figure 5.2. The vibrational spectrum of LADTP, analogous to the rhombohedral *R*-3*c* space. group of NASICON-type LTP. The asterisk represents the PO_4 stretching mode of $DyPO_4$ in the $I4_1/amd$ space group setting.

The observed vibrational spectrum for LADTP is consistent with NASICON-type LTP and LATP systems reported in literature.[27] The region below 350 cm^{-1} corresponds to the external modes, made up of the M^{3+} and M^{4+} translational modes and PO_4^{3-} translations and/or pseudo-rotations. External modes refer to the movement of molecules making up the crystal through partial rotations and translations.[28, 29] The peaks at 434 and 449 cm^{-1} correspond to the symmetric bending modes of PO_4^{3-}, while the asymmetric bending modes occurred at 549.2 cm^{-1}. The migratory cations, Li^+, occupy both the 6*b* and 36*f* sites, as found in Rietveld refinement of XRD data. However, the dominant 6*b* Li^+ cations have an S_6 site symmetry, resulting in their cage modes being Raman-inactive. Although the excess Li^+ at 36*f* occupies a site that renders them Raman-active, their contributions are significantly small. In the work by Dashav *et al.*,[30] for Al^{3+} = 0.2 mol%, the substitution of Ti^{4+} with Al^{3+} and Li^+ induced the presence of some peaks in the 550 to 800 cm^{-1} range. They attributed these peaks to the breaking of symmetry rules, allowing for the observation of infrared and silent modes, resulting from increased substitution.

The region between 900 and 1030 cm^{-1} consists of three peaks of increasing intensity, and a small feature. These peaks correspond to the symmetric and asymmetric stretching modes of the PO_4^{3-} groups.[31] The asterisk at 1069.3 cm^{-1} is attributed to the PO_4 stretching mode of $DyPO_4$ in the $I4_1/amd$ space group setting that was detected in XRD.

The computational work by Giarola *et al.*,[15] showed the presence of an Eg feature at 1065.0 cm^{-1}, while their corresponding experimental work showed this feature at 1071 cm^{-1}, comparable to what we observed in this work. This feature could be attributed to both the rhombohedral main phase of LADTP, and the tetragonal $DyPO_4$, indicating an overlap of vibrational modes of the secondary phase with those of the main phase. The $AlPO_4$ and $DyPO_4$ secondary phases observed in XRD could not be easily detected from Raman spectroscopy, possibly due to overlap of vibrational modes with those of the main phase, or the phase contents being too low, at less than 4 weight %.

5.3.3. Small-box modelling of pair distribution function (PDF)

The X-ray PDF was used to probe the effect of lattice site substitution at the 12*c* site, replacing Ti^{4+} with larger Dy^{3+} cations, on the $[Ti_{2-x-y}Al_xDy_y(PO_4)^3]^-$ framework. Structure mining,[32] a methodology that allows a user to search through a repository of data to find the best possible structural match to experimental data, revealed the best agreement to the rhombohedral NASICON-type model (*R*-3*c*) in the intermediate to long range (r > 10 Å), in agreement with average structure from XRD (see **Figure S5.2**), thus providing a starting model for small-box modelling.

The small-box modelling approach has been used extensively in studying various energy materials.[33-35] This has provided information on the changes in local and average structure due to distortions, the formation of an amorphous phase and the detection of minor crystalline phases. Small-box modelling using the *R*-3*c* model showed a reasonable agreement in the region 8 Å < *r* < 50 Å (**Figure 5.3**, Rw = 32.8%). However, the residual curve in the low-*r* region showed a discrepancy between the experimental G(r) and the applied average structure, especially around the first two peaks at 1.5 Å and 1.9 Å corresponding to the P-O and Ti/Al/Dy-O peaks, respectively. The deviation of the local structure from average structure could be due to i) a secondary phase with short-range structural coherence,[36] or ii) a distortion of the structure at a local level.[37]

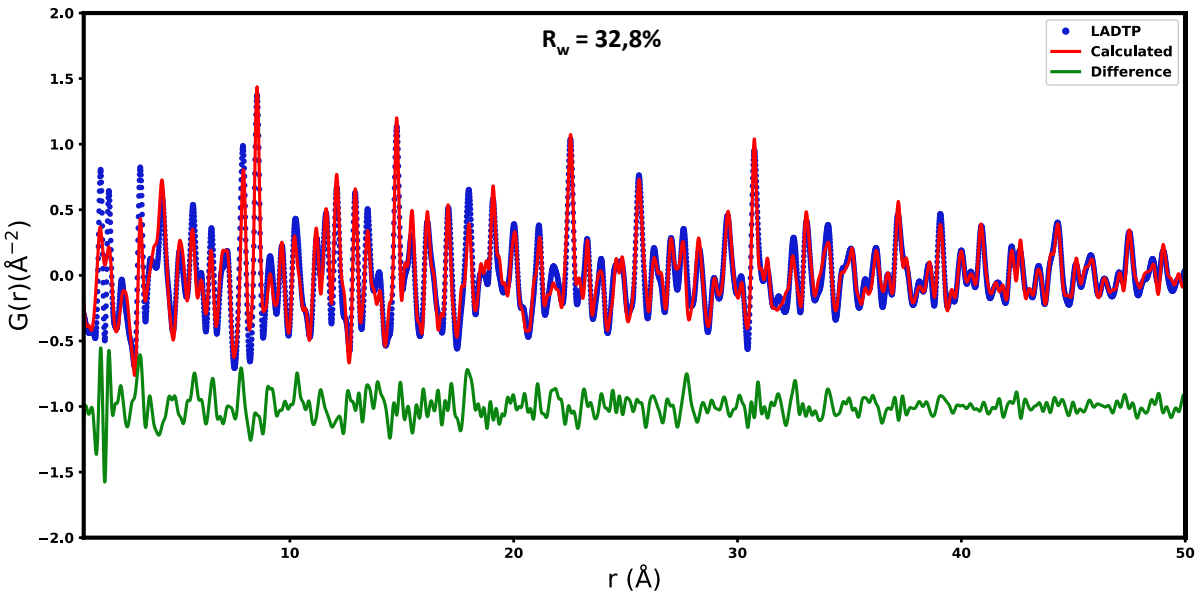


Figure 5.3. Small-box modelling of LADTP G(r) in the range 0.75 – 50 Å, using the rhombohedral *R*-3*c* model obtained from XRD (Rw = 32.8%) (blue circles = observed data, red line = calculated model and green line = difference).

The presence of minor crystalline phases has also been previously shown to account for the structure deviation at low-*r*.[38] The qualitative analysis of PXRD data showed the presence of Al- and Dy-bearing phosphate secondary phases. Applying the LTP (*R*-3*c*), $AlPO_4$ ($C222_1$) and DyPO4 ($I4_1/amd$) three-phase model only gave a slight improvement in the fit (Rw = 28.1%), but the misfits at low-r were still unaccounted for (see **Figure S3**). The secondary phases did not show any considerable contributions to the fit, thus suggesting that structural distortions are more likely the cause of the disagreement at low-r.

The deviation of the local structure from the average due to local distortions has been extensively studied by means of PDF. Christensen *et al.*,[39] studied nano-rutile TiO_2 anodes and found that the local structure was better described as a monoclinic distortion ($P2/m$), than the typical $P4_2/mnm$ structure of rutile. Other NASICON-type systems containing Hf^{4+}, Sn^{4+} or Zr^{4+} have been shown to possess monoclinic or triclinic crystal structures. First-principles DFT studies found that the substitution of Ti^{4+} with larger cations such as Dy^{3+} results in distortions around the metal's 12*c* site due to size difference.[4] Aono *et al.*,[40] reported the existence of a β-$Fe_2(SO_4)_3$-type structure upon replacement of Ti^{4+} to form an analogous Hf-bearing compound. The β-$Fe_2(SO_4)_3$-type monoclinic structure (space group $P2_1/n$) was then tested in the region below 10 Å, and this model showed the best agreement with the experimental data (Rw = 3.96%), as shown in **Figure 5.4 (a)**. Both the rhombohedral NASICON-type and monoclinic β-$Fe_2(SO_4)_3$-type structures have similar framework arrangements (**Figure 5.4(b)** and **(c)**, respectively), wherein the MO_6 polyhedra are linked to

PO_4 polyhedra, with a difference in the angles. This suggests that the local distorted monoclinic arrangement may have to undergo rototranslation to yield the rhombohedral geometry in the average structure, suggesting that the two phases show a group-subgroup relationship.

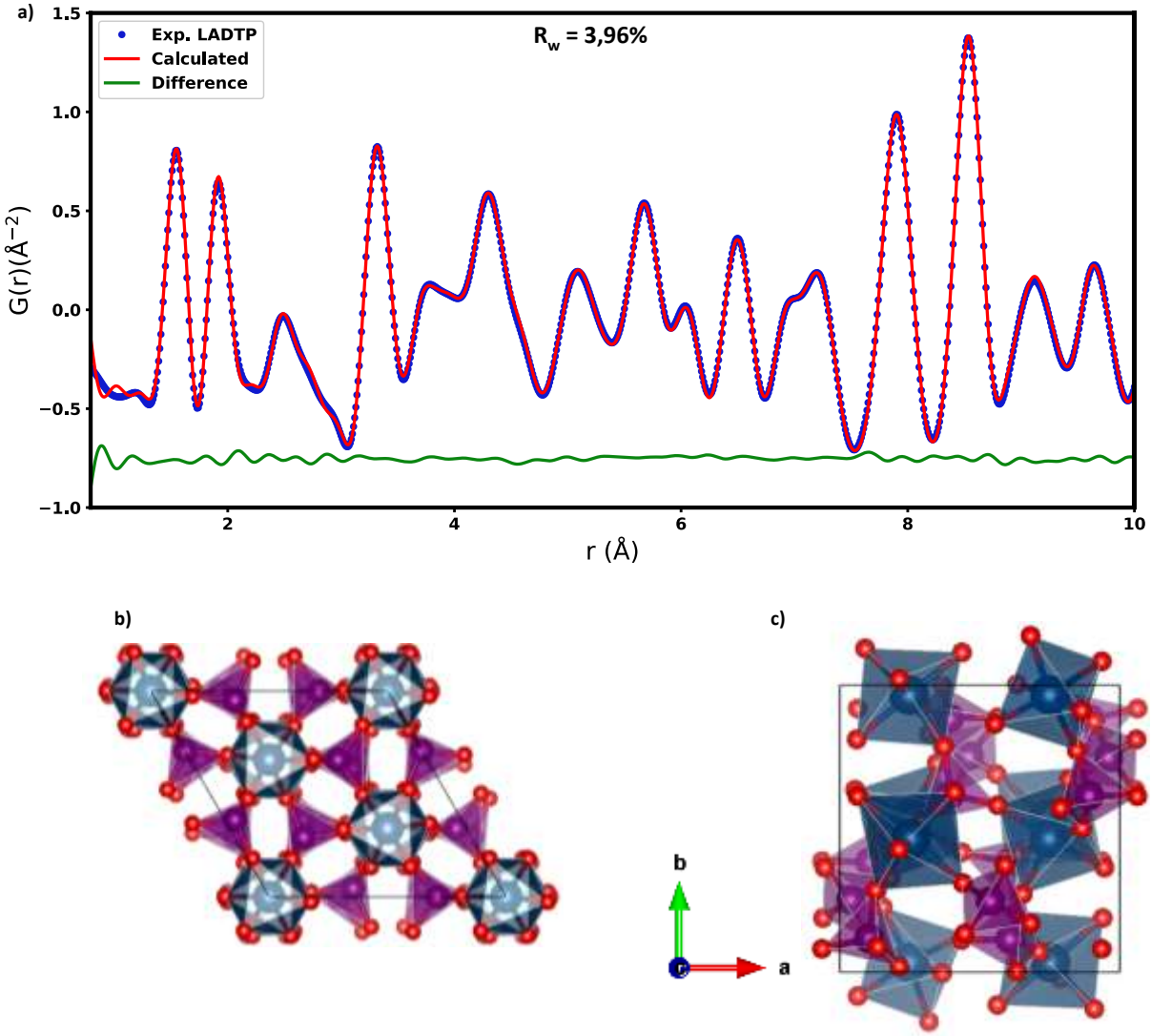


Figure 5.4. (a) Small-box modelling of LADTP using the β-$Fe_2(SO_4)_3$-type monoclinic (space group $P2_1/n$) model in the 0.75 to 10 Å range, Rw = 3.96%, (b) unit cell depiction of the NASICON-type LTP, based on the structure by Aatiq *et al.*,[22] and (c) unit cell depiction of the adapted β-$Fe_2(SO_4)_3$-type structure by Aono *et al.*[40] Both structures consist of TiO_6 octahedra (blue), corner-linked to PO_4 tetrahedra (purple).

5.3.4. Analysing the local structure of LADTP using XANES

In this section we first discuss the overall agreement between LADTP and the Dy_2O_3 standard, for both the experimental and theoretical results. We then explore, in detail, the origin of each feature in the spectra.

Comparison of experimental and theoretical LADTP and Dy_2O_3 XANES spectra - The elemental specificity of XAS is useful for probing the local atomic and electronic structure around an X-ray absorbing atom. **Figure 5.5** shows the stacked Dy L_3-edge experimental and theoretical spectra of LADTP and Dy_2O_3. The experimental spectra of these systems have similar spectral signatures, with just a few small differences particularly a small increase in the white line intensity and a peak shift in the 7820-7840 eV region. The theoretical results reproduce these differences semi-quantitatively across the full spectrum. As discussed in detail below, this agreement is achieved by using a mix of 60% Dy_2O_3 (*Ia*-3), 35% $DyPO_4$ ($I4_1/amd$) and 5% $DyPO_4$ ($P2_1/n$) to represent LADTP theoretically.

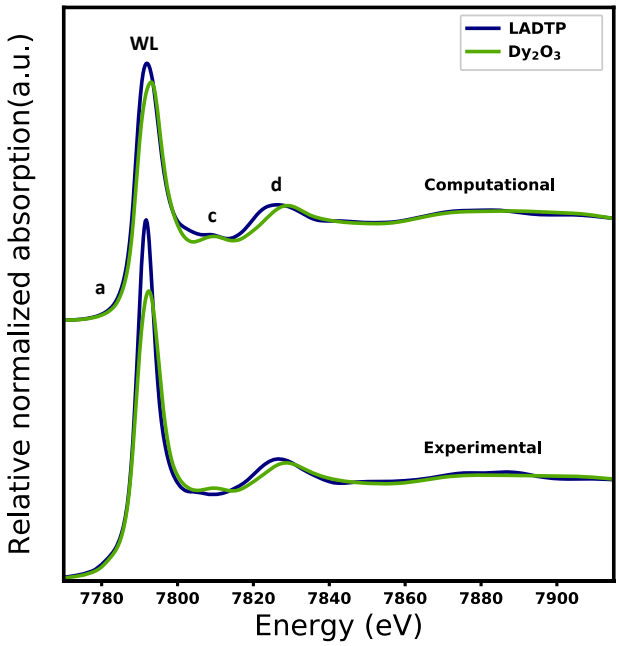


Figure 5.5. Normalized experimental and computational Dy L_3-edge XANES spectra of Dy_2O_3 standard and LADTP. The computational spectrum of LADTP is made up of approximately 60% Dy_2O_3 (*Ia*-3), 35% $DyPO_4$ ($I4_1/amd$) and 5% $DyPO_4$ ($P2_1/n$).

To gain a clear understanding of the local environment around Dy in LADTP, it was imperative to compute theoretical spectra of Dy in different compounds with various crystallographic orientations around Dy. To this end, the structures from phases obtained via PXRD and PDF were used as starting models, and the results are shown in **Figure 5.6**.

The main phase with a rhombohedral structure assumes the statistical distribution of Dy at the 12*c* site of the *R*-3*c* space group. The white line (WL) of Dy in rhombohedral *R*-3*c* structure (site 12*c*) split into two states, indicating a relatively large crystal field splitting, hence a different electronic structure than observed in the experiment. It is also worth noting that PXRD is a long-range probe, while XANES is a local structure probe, therefore it is not unexpected that the PXRD model is inadequate in describing the local structure that is observed through XANES.

The tetragonal $I4_1/amd$ structure for the secondary $DyPO_4$ phase detected from PXRD was also calculated, similar to the monoclinic $P2_1/n$ local structure determined from small-box modelling of the PDF. The WL obtained from the tetragonal and monoclinic models of $DyPO_4$ resembled that of the experiment, unlike the 12*c* site in *R*-3*c*, pointing to Dy possibly being absent in 12*c*-like environments. This was suggestive of these models providing a better local structural description of Dy in LADTP, than what was observed from the average structure model.

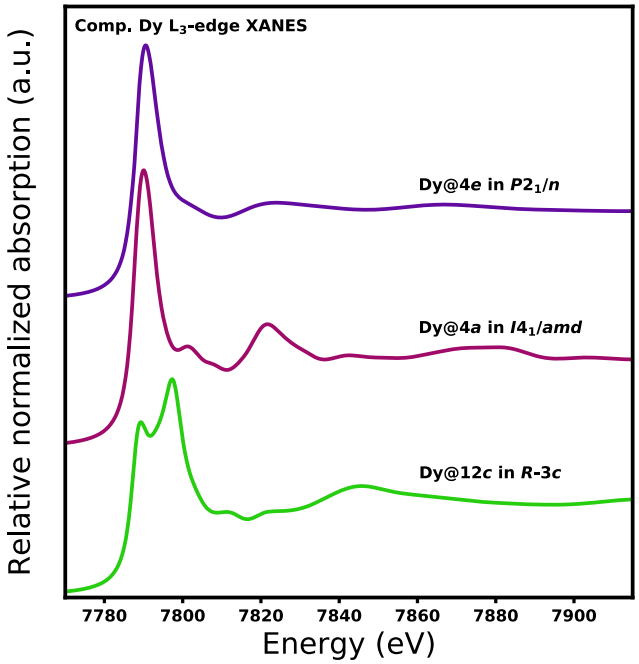


Figure 5.6. Theoretical L_3-edge XANES spectra of Dy in a 12*c* site in the rhombohedral *R*-3*c* NASICON-type main phase, a 4*a* site in the tetragonal $I4_1/amd$ structure obtained from the PXRD-detected secondary phase, and the 4*e* site in the monoclinic $P2_1/n$ structure obtained from PDF.

It should be noted that the structures used in the XANES simulations do not imply that phases with similar structures are present in LADTP, but rather that the local environment in these structures is representative of that in LADTP. This highlights the importance of using structural probes that study the material across various length scales.

It is important to note that these structure proportions are only estimates; however, all known Dy environments have been accounted for.

Assignment of spectral features in LADTP and Dy_2O_3 - The origin of features in the XAS spectra is best understood by analyzing the LDOS associated with the spectra of the Dy L_3-edge. **Figure 5.7** shows the computational XAS Dy_2O_3 spectrum together with the *p*-, *d*- and *f*- DOS of the Dy absorber to elucidate the origin of the spectral features.

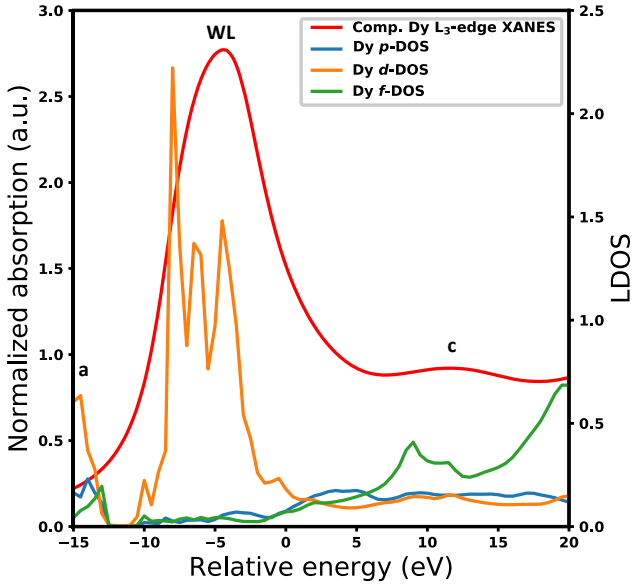


Figure 5.7. Computational spectrum of cubic Dy_2O_3 (space group *Ia*-3) computed using two sites 8*b* and 24*d* with a 25:75 ratio to preserve stoichiometry. The localized Dy absorber *p*, *d* and *f*-DOS are also presented.

Pre-edge features - The pre-edge feature 'a' in **Figure 5.5** is poorly resolved in our experimental spectra, which were measured in conventional transmission (Dy_2O_3) and fluorescence (LADTP) modes, with the need for high-resolution measurements to resolve the pre-edge features of Ln L_3-edge XANES spectra having been demonstrated by Vitova *et al.*[41] This feature has been attributed previously mainly to the quadrupolar $2p_{3/2} \rightarrow 4f$ electronic transition.[42, 43] In contrast, the LDOS calculated in this work (**Figure 5.7**) show that this feature (appearing at a relative energy of approximately -10 eV) is largely attributed to the dipolar $2p_{3/2} \rightarrow 5d$ transition, with a smaller contribution from the quadrupolar $2p_{3/2} \rightarrow 4f$ transition.

White line - As expected from the selection rules, the white line (WL) transition corresponds to $2p_{3/2} \rightarrow$ 5d dipole transitions (*d*-DOS in **Figure 5.7**). The experimental edge energies of LADTP and Dy_2O_3 were found to be 7791.81 eV and 7792.39 eV, respectively.

Given that changes in oxidation state from +2 to +3 in Ln ions show an energy shift between 7 to 10 eV,[44] the observed small energy difference of 0.58 eV (very accurately reproduced by the theoretical results) suggests an oxidation state of +3 in both compounds. Moreover, since the oxidation state of the oxide standard is known, the close match between LADTP and Dy_2O_3 suggests the same oxidation state for LADTP. The integrated peak centroids from computational spectra (shown in **Table 5.2**) showed a similar energy difference of -0.58 eV. The LADTP system showed a slightly narrower and higher WL relative to the oxide standard in the experimental data. The integration of the WL is instrumental in deducing the reason behind experimental observations possibly linked to changes in local structure. The results from peak integration, showing the intensity of the WL, peak centroids and peak width are given in **Table 5.2**.

Table 5.2. Quantitative results of WL peak fitting for experimental and computational spectra of Dy_2O_3 and LADTP.

	WL integrated intensity (a. u.)	**Peak centroid (eV)**	**Peak width (eV)**
Exp. Dy_2O_3	18.0	7792.44	3.2
Exp. LADTP	17.6	7791.81	2.5
	Ratio: 0.98	Difference: -0.58	Ratio: 0.79
Comp. Dy_2O_3	16.4	7791.55	3.3
Comp. LADTP	16.2	7790.97	3.1
	Ratio: 0.99	Difference: -0.58	Ratio: 0.93

The narrow WL in LADTP could be attributed to a higher coordination number than 6, expected from the undoped NASICON-type LTP.[45] Aliovalent M^{3+}-doped systems have been studied both experimentally with techniques such as NPD, and from first principles using DFT.[4, 12] Both these methodologies showed that the additional Li^+ cations required for charge balance upon M^{3+} doping tend to occupy the 36*f* sites located close to the M^{3+} dopants. In this case, Dy cations are, therefore, surrounded by 6 O atoms, and at least one additional Li^+, resulting in a coordination number of at least 7. This phenomenon has been observed in Ho and La compounds, showing a decrease in the WL peak width with increasing number of ligands around the Ho absorber.[45, 46]

A similar deduction was made by Asakura et al.,[46] for Eu and Dy amongst other Ln elements, where they found that increasing the coordination number from 6 to 12 for Eu and Dy complexes led to a decrease in the splitting of the *d*-states, thus a narrower WL.

The quantitative results from WL peak fitting support these observations: Given that the experimental and theoretical WL integrated intensities are very similar for Dy_2O_3 and LADTP, it follows that the observed change in WL height must be driven by a change in width, and not differences in peak intensity. Put more precisely, the WL change is not due to the presence of more *d*-states available, but because the *d*-states become closer together for the same intensity and number of *d*-states, hence the width gets narrower and the peak heigh is visibly bigger. This is clear from the fitted peak widths, which show significant changes (ratios of 0.79 experimentally and 0.93 theoretically). The idealized structure used in generating the computational spectrum resulted in FEFF overestimating the peak width by approximately 15%, resulting in broader theoretical WLs in computational spectra compared to experiment. The narrowing of peak width in LADTP is seen to be underestimated by FEFF also due to the application of an idealized structure, resulting in similar heights for the WL peaks. Combining the learnings from experimental observations in literature, and peak fitting of the spectra in this work, it is supported that an increase in coordination number results in narrower *d*-orbital splitting, as observed in the LADTP system.

Post-white-line features - Jeon *et al.*,[43] have suggested that features that occur approximately 60 eV above the WL, such as 'c' and 'd' in **Figure 5.5**, are due to absorber-ligand interactions. Feature 'c' could only be assigned to Dy-Dy interactions if an interatomic distance of at least 3.2 or 3.5 Å is considered. Feature 'd' was attributed to the continuum resonance (CR) caused by O ligands surrounding the Ln^{3+} absorber. The positions of the CR features were explained following the 1D particle-in-a-box phenomenon: As the bond distances between the Dy absorber and its neighbors (either O in the first shell or Dy in the second one) increase, the CR feature shifts towards lower energy.

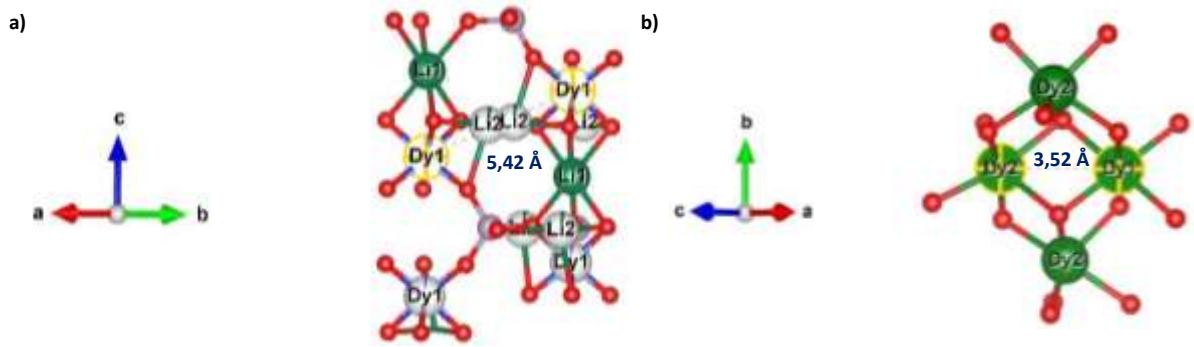


Figure 5.8. Dy-Dy interactions in (a) LADTP with an indirect line of site at 5.42 Å apart and (b) Dy_2O_3 with a direct line of site at 3.52 Å apart. The individual atoms are as follows: oxygen = red, lithium = turquoise, phosphorus = purple, dysprosium in LADTP = blue and dysprosium in Dy_2O_3 = green.

In our results, feature 'c' is small and present in both compounds, but slightly less intense in LADTP than in Dy_2O_3, suggesting that the LADTP is more disordered compared to Dy_2O_3. In LADTP, the Dy^{3+} dopants are assumed to be randomly distributed in the NASICON-type framework's 12*c* sites, with Ti^{4+} and Al^{3+} in neighboring 12*c* octahedra with a Dy-Dy distance of ~5.4 Å from average structure. The presence of excess Li at interstitial 36*f* sites blocks the direct line of sight between the Dy cations, thus likely resulting in weaker interactions between Dy cations (**Figure 5.8 (a)**). The theoretical spectra in **Figure 5.8(a)**, obtained by removing, relative to Dy_2O_3 structure, all Dy-O interactions while keeping the Dy-Dy ones, shows that the peak is still present, supporting the assignment of feature 'c' to metal-metal interactions. It is worth noting that the most important contribution to the DOS (**Figure 5.6(b)**) associated with feature 'c' corresponds to *p*→ *d* transitions. Therefore, feature 'c' is likely not exclusively due to Dy-Dy backscattering interactions but also has a local atomic component. Finally, the presence of feature 'c' in both Dy_2O_3 and LADTP could indicate the presence of Dy in environments similar to the oxide, in the LADTP compound.[48] In Dy_2O_3, the relatively shorter Dy-Dy distance of 3.52 Å would therefore result in feature 'c' appearing at higher energy, relative to that of LADTP (5.42 Å), as observed in this work.

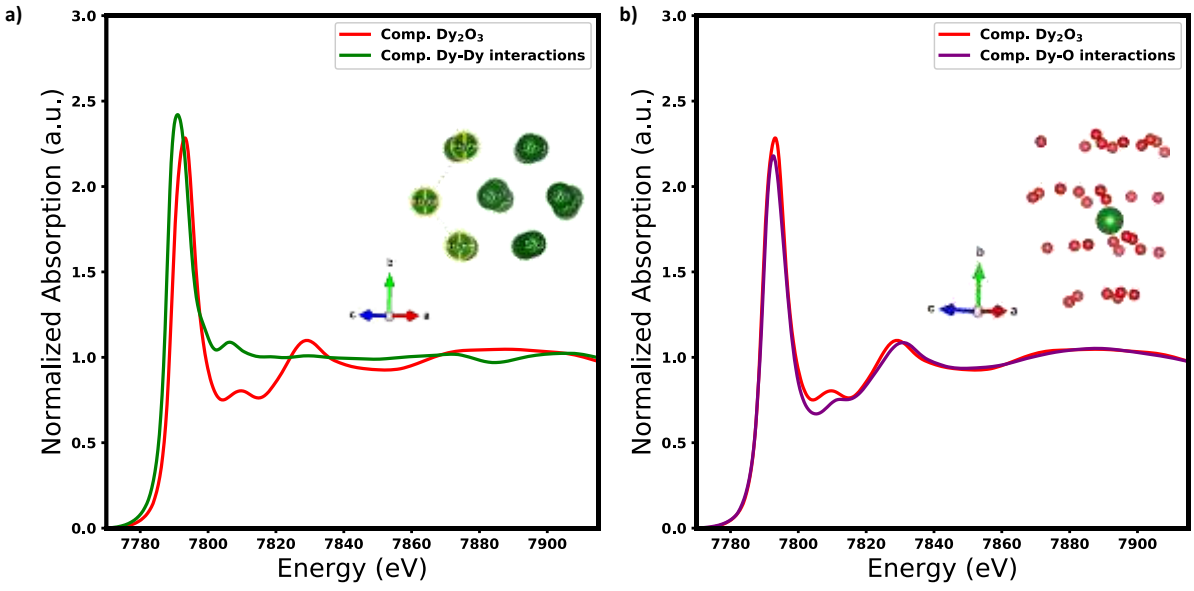


Figure 5.9. Comparison of computational Dy_2O_3 Dy L_3-edge XANES spectra, with that of an *Ia*-3 Dy-only system, showing (a) feature 'c' as Dy-Dy interactions and (b) feature 'd' as Dy-O interactions.

In agreement with the literature assignments, our theoretical results show that feature ‘d’ completely disappears when the O scatterers around the Dy absorber are removed (**Figure 5.9 (a)**) but has almost identical intensity and position when they are included (**Figure 5.9 (b)**). In our LADTP measurements, feature ‘d’ appears 3 eV lower in energy with respect to Dy_2O_3, suggesting a longer Dy-O bond length. The bond distances for Dy_2O_3, $DyPO_4$ (*I*4$_1$/*amd*) and LADTP that were obtained from Rietveld refinement are shown in **Table S5**. Considering Dy in rhombohedral LADTP, the average bond distance is 1.90 Å, significantly shorter than for both the parent oxide and $DyPO_4$ (*I*4$_1$/*amd*) secondary phases. The presence of Dy at the 12*c* site would shift the CR feature ‘d’ to higher energy than both the phosphate and oxide phases. To support this hypothesis, the effect of changing the Dy_2O_3 Dy-O distance from 2.1 to 2.3 Å on the position of feature ‘d’ was investigated and the theoretical results are shown in **Figure 5.10**. The increasing Dy-O distances in the first shell resulted in a shift towards lower energy in feature ‘d’.

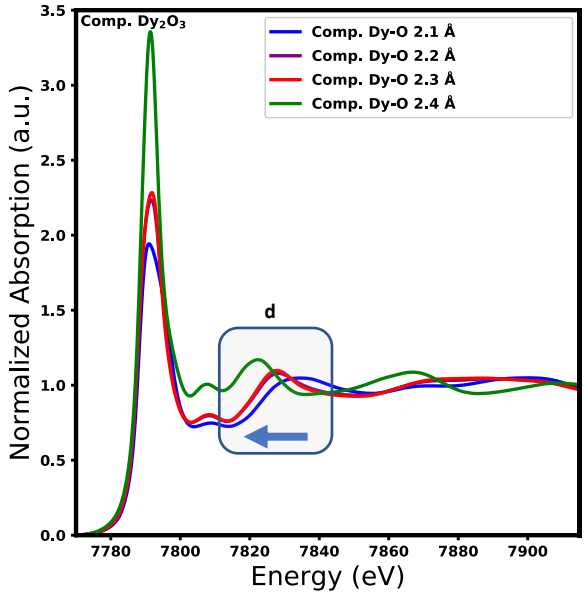


Figure 5.10. Comparison of experimental and computational Dy_2O_3 XANES spectra, showing the effect of Dy-O bond distance on the position of feature ‘d’ at ~7829 eV (marked).

It follows that in the LADTP sample, although Dy is present in the secondary phase ($DyPO_4$, *I*4$_1$/*amd*), the remaining Dy is incorporated into another structure while maintaining the oxide-like environment similar to Dy_2O_3, but with longer Dy-O distance, resulting in the appearance of feature ‘d’ at lower energy, as observed in the experiment.

The formation of Dy_2O_3-like regions apart from $DyPO_4$ ($I4_1/amd$) is supported by the qualitative similarities between the experimental spectra of the LADTP system, and the oxide standard as well as the computational spectrum generated from a Dy_2O_3 (Ia-3), $DyPO_4$ ($I4_1/amd$), $DyPO_4$ ($P2_1/n$) mixture. Furthermore, the peak width of the WL is dominated by the distribution of the multiple transitions making up the d-states shown in the LDOS. In changing the Dy-O bond distance, the distribution of the states also changes (see **Figure S5.5**). Therefore, the longer Dy-O bond length in the oxide-like environment in LADTP results in narrower WL as observed in the experiment, leading to three states that are less separated. The use of a full potential rather than the muffin-tin approximation in determining the XANES and DOS would probably be more suitable in giving a better distribution of the *d*-states.

In summary, the proposed theoretical model for LADTP suggests the presence of Dy in the secondary phase tetragonal ($I4_1/amd$) and monoclinic ($P2_1/n$) environments, as observed from PXRD and PDF, and most importantly, that the remaining Dy could be present as small oxide-like clusters. A reasonable agreement between i) experimental and ii) computational spectra for both compounds was obtained, suggesting a good approximation of the local structure of Dy in LADTP.

5.4. Conclusions

In this work we report a new 12.5% Al, 2.5% Dy co-doped NASICON-type LADTP system, synthesized via the solid-state mechanism. The Rietveld refinement analysis of room-temperature synchrotron XRD results suggested a NASICON-like average structure, indexed to the rhombohedral (space group R-3c) LADTP structure, with Al^{3+} and Dy^{3+} substituted at the 12c site of Ti^{4+}, and excess Li^+ occupied the 36f sites. However, the product also consisted of $DyPO_4$ (space group $I4_1/amd$) and $AlPO_4$ (space group $C222_1$) secondary phases. Raman spectroscopy supported the phase compositions obtained from XRD, showing a majority of the NASICON-type system. The results from Raman spectroscopy did not provide significant insight into the changes in the Ti/Al/Dy octahedra. The crystallographic information obtained from PXRD refinements was used as starting models in the small-box modeling of PDF data and showed a deviation of the local structure from the average structure below 10 Å, showing the best agreement with a monoclinic $P2_1/n$ β-Fe_2SO_4-like local structure. Therefore, the LADTP system is described by the $P2_1/n$ (r < 10 Å) and R-3c (r > 10 Å) models. The qualitative comparison of experimental LADTP to Dy_2O_3 suggested that the LADTP sample may also consist of Dy in oxide-like environments.

Like PDF, computational XAS indicated a deviation of local atomic structure from the rhombohedral average structure. Subsequently, a monoclinic model ($P2_1/n$), analogous to β-$Fe_2(SO_4)_3$ was used in conjunction with the PXRD-obtained $I4_1/amd$ $DyPO_4$ and Dy_2O_3 (Ia-3) models in a 5% $DyPO_4$ ($P2_1/n$): 35% $DyPO_4$ ($I4_1/amd$): 60% Dy_2O_3 (Ia-3) ratio, respectively, to yield the best agreement with experimental LADTP XANES. The post-edge features occurring about 60 eV above the white line were attributed to the Dy-Dy and Dy-O interactions (features 'c' and 'd'), through simulations carried out via FEFF.

In conclusion, this chapter has successfully demonstrated the importance of understanding the LTP-based NASICON-type materials and the effects of doping on the structure from both experimental and theoretical approaches. The combined use of PXRD, Raman spectroscopy, PDF and XAS provides insights ranging from the long-range average to the local atomic and electronic structures perspective that will serve as a tool in informing the design of solid-state electrolytes that are more applicable in an all-solid-state Li-battery. The application of methods such as density functional theory (DFT), as demonstrated by Lang *et al.*,[4] and experimental variable-temperature EIS would further assist in determining the cation migration mechanism and activation energies from first principles, to consolidate the theory vs experiment approaches taken in this work.

5.5. References

1. Bounar, N., Benabbas, A., Bouremmad, F., Ropa, P. and Carru, J.C., 2012. Structure, microstructure and ionic conductivity of the solid solution $LiTi_{2-x}Sn_x(PO_4)_3$. *Physica B: Condensed Matter*, *407*(3), pp.403-407.
2. Aono, H., Sugimoto, E., Sadaoka, Y., Imanaka, N. and Adachi, G.Y., 1990. Ionic conductivity of solid electrolytes based on lithium titanium phosphate. *Journal of the electrochemical society*, *137*(4), pp.1023-1027.
3. Best, A.S., Forsyth, M. and Macfarlane, D.R., 2000. Stoichiometric changes in lithium conducting materials based on $Li_{1+x}Al_xTi_{2-x}(PO_4)_3$: impedance, X-ray and NMR studies. *Solid State Ionics*, *136*, pp.339-344.
4. Lang, B., Ziebarth, B. and Elsässer, C., 2015. Lithium ion conduction in $LiTi_2(PO_4)_3$ and related compounds based on the NASICON structure: a first-principles study. *Chemistry of Materials*, *27*(14), pp.5040-5048.

5. Miyajima, Y., Saito, Y., Matsuoka, M. and Yamamoto, Y., 1996. Ionic conductivity of NASICON-type $Na_{1+x}M_xZr_{2-x}P_3O_{12}$ (M: Yb, Er, Dy). *Solid State Ionics*, *84*(1-2), pp.61-64.
6. Ramar, V., Kumar, S., Sivakkumar, S.R. and Balaya, P., 2018. NASICON-type La^{3+} substituted $LiZr_2(PO_4)_3$ with improved ionic conductivity as solid electrolyte. *Electrochimica Acta*, *271*, pp.120-126.
7. Yaroslavtsev, A.B. and Stenina, I.A., 2006. Complex phosphates with the NASICON structure ($M_x A_2 (PO_4)_3$). *Russian journal of inorganic chemistry*, *51*(1), pp. S97-S116.
8. Martinez-Juarez, A., Rojo, J.M., Iglesias, J.E. and Sanz, J., 1995. Reversible monoclinic-rhombohedral transformation in $LiSn_2(PO_4)_3$ with NASICON-type structure. *Chemistry of Materials*, *7*(10), pp.1857-1862.
9. Anantharamulu, N., Rao, K.K., Rambabu, G., Kumar, B.V., Radha, V. and Vithal, M., 2011. A wide-ranging review on Nasicon type materials. *Journal of materials science*, *46*(9), pp.2821-2837.
10. Kumar, P.P. and Yashonath, S., 2006. Ionic conduction in the solid state. *Journal of Chemical Sciences*, *118*(1), pp.135-154.
11. Xie, H., Goodenough, J.B. and Li, Y., 2011. $Li_{1.2}Zr_{1.9}Ca_{0.1}(PO_4)_3$, a room-temperature Li-ion solid electrolyte. *Journal of Power Sources*, *196*(18), pp.7760-7762.
12. Arbi, K., Hoelzel, M., Kuhn, A., García-Alvarado, F. and Sanz, J., 2013. Structural Factors That Enhance Lithium Mobility in Fast-Ion $Li_{1+x}Ti_{2-x}Al_x(PO_4)_3$ ($0 \leq x \leq 0.4$) Conductors Investigated by Neutron Diffraction in the Temperature Range 100–500 K. *Inorganic chemistry*, *52*(16), pp.9290-9296.
13. Nuernberg, R.B., Basbus, J.F., Lux, K.C., Sainz, M.P., Cuello, G.J., Rodrigues, A.C., Piarristeguy, A.A., Ribes, M. and Pradel, A., 2022. Correlation between Structural Features and Ionic Transport in Lithium-Ion Conducting Glass–Ceramics from the $Li_{1+x}Cr_xGeTi_{1-x}(PO_4)_3$ System. *The Journal of Physical Chemistry C*, *126*(9), pp.4584-4592.
14. Kahlaoui, R., Arbi, K., Sobrados, I., Jimenez, R., Sanz, J. and Ternane, R., 2017. Cation Miscibility and Lithium Mobility in NASICON $Li_{1+x}Ti_{2-x}Sc_x(PO_4)_3$ ($0 \leq x \leq 0.5$) Series: A Combined NMR and Impedance Study. *Inorganic chemistry*, *56*(3), pp.1216-1224.
15. Giarola, M., Sanson, A., Tietz, F., Pristat, S., Dashjav, E., Rettenwander, D., Redhammer, G.J. and Mariotto, G., 2017. Structure and vibrational dynamics of NASICON-type $LiTi_2(PO_4)_3$. *The Journal of Physical Chemistry C*, *121*(7), pp.3697-3706.

16. Gammond, L.V., Auer, H., Mendes Da Silva, R., Zeidler, A., Ortiz-Mosquera, J.F., Nieto-Muñoz, A.M., Rodrigues, A.C.M., d'Anciães Almeida Silva, I., Eckert, H., Benmore, C.J. and Salmon, P.S., 2021. Structure of crystalline and amorphous materials in the NASICON system $Na_{1+x}Al_x Ge_{2-x}(PO_4)_3$. *The Journal of Chemical Physics*, *155*(7), p.074501.
17. Shannon, R.D., 1976. Revised effective ionic radii and systematic studies of interatomic distances in halides and chalcogenides. *Acta crystallographica section A: crystal physics, diffraction, theoretical and general crystallography*, *32*(5), pp.751-767.
18. Coelho, A.A., 2018. TOPAS and TOPAS-Academic: an optimization program integrating computer algebra and crystallographic objects written in C++. *Journal of Applied Crystallography*, *51*(1), pp.210-218.
19. https://www.bnl.gov/nsls2/beamlines/beamline.php?r=6-BM
20. Ravel, B and Newville, M., 2005. ATHENA, ARTEMIS, HEPHAESTUS: data analysis for X-ray absorption spectroscopy using IFEFFIT. Journal of synchrotron radiation, 12(4), pp.537-541.
21. Kas, J.J., Vila, F.D., Pemmaraju, C.D., Tan, T.S. and Rehr, J.J., 2021. Advanced calculations of X-ray spectroscopies with FEFF10 and Corvus. *Journal of Synchrotron Radiation*, *28*(6).
22. Aatiq, A., Ménétrier, M., Croguennec, L., Suard, E. and Delmas, C., 2002. On the structure of $Li_3Ti_2 (PO_4)_3$. *Journal of Materials Chemistry*, *12*(10), pp.2971-2978.
23. Emery, J., Šalkus, T., Abramova, A., Barré, M. and Orliukas, A.F., 2016. NMR investigations in $Li_{1.3}Al_{0.3}Ti_{1.7}(PO_4)_3$ ceramics. Part I: structural aspect. *The Journal of Physical Chemistry C*, *120*(46), pp.26173-26186.
24. Milligan, W.O., Mullica, D.F., Beall, G.W. and Boatner, L.A., 1983. The structures of three lanthanide orthophosphates. *Inorganica Chimica Acta*, *70*, pp.133-136.
25. Arbi, K., Mandal, S., Rojo, J.M. and Sanz, J., 2002. Dependence of Ionic Conductivity on Composition of Fast Ionic Conductors $Li_{1+x}Ti_{2-x}Al_x(PO_4)_3$, $0 \leq x \leq 0.7$. A Parallel NMR and Electric Impedance Study. *Chemistry of materials*, *14*(3), pp.1091-1097.
26. Dinnebier, R.E., Leineweber, A. and Evans, J.S., 2018. *Rietveld refinement: practical powder diffraction pattern analysis using TOPAS*. Walter de Gruyter GmbH & Co KG.
27. Burba, C.M. and Frech, R., 2006. Vibrational spectroscopic study of lithium intercalation into $LiTi_2(PO_4)_3$. *Solid State Ionics*, *177*(17-18), pp.1489-1494.
28. Sherwood, P.M.A. and Sherwood, P.M.A., 1972. *Vibrational spectroscopy of solids* (No. 1). CUP Archive.

29. Prasad, P.N. and Kopelman, R., 1973. External, internal and semi-internal vibrations in molecular solids: spectroscopic criteria for identification. *Chemical Physics Letters*, *21*(3), pp.505-510.
30. Dashjav, E., Ma, Q., Xu, Q., Tsai, C.L., Giarola, M., Mariotto, G. and Tietz, F., 2018. The influence of water on the electrical conductivity of aluminum-substituted lithium titanium phosphates. *Solid State Ionics*, *321*, pp.83-90.
31. Tarte, P., Rulmont, A. and Merckaert-Ansay, C., 1986. Vibrational spectrum of nasicon-like, rhombohedral orthophosphates $M^{I}M^{IV}_2(PO_4)_3$. *Spectrochimica Acta Part A: Molecular Spectroscopy*, *42*(9), pp.1009-1016.
32. Yang, L., Juhás, P., Terban, M.W., Tucker, M.G. and Billinge, S.J., 2020. Structure-mining: screening structure models by automated fitting to the atomic pair distribution function over large numbers of models. *Acta Crystallographica Section A: Foundations and Advances*, *76*(3), pp.395-409.
33. Malavasi, L., 2011. Total scattering investigation of materials for clean energy applications: The importance of the local structure. *Dalton Transactions*, *40*(15), pp.3777-3788.
34. Sanchez, S., Steiner, U. and Hua, X., 2019. Phase evolution during perovskite formation—insight from pair distribution function analysis. *Chemistry of Materials*, *31*(9), pp.3498-3506.
35. Proffen, T.E., Page, K.L., Kolodiazhnyi, T., Cheetham, A.K. and Seshadri, R., 2008. *Local structural origins of the distinct electronic properties of Nb-substituted $SrTiO_3$ and $BaTiO_3$* (No. LA-UR-08-04757; LA-UR-08-4757). Los Alamos National Lab.(LANL), Los Alamos, NM (United States).
36. Xiang, K., Xing, W., Ravnsbæk, D.B., Hong, L., Tang, M., Li, Z., Wiaderek, K.M., Borkiewicz, O.J., Chapman, K.W., Chupas, P.J. and Chiang, Y.M., 2017. Accommodating high transformation strains in battery electrodes via the formation of nanoscale intermediate phases: operando investigation of olivine $NaFePO_4$. *Nano letters*, *17*(3), pp.1696-1702.
37. Aksel, E., Forrester, J.S., Nino, J.C., Page, K., Shoemaker, D.P. and Jones, J.L., 2013. Local atomic structure deviation from average structure of $Na_{0.5}Bi_{0.5}TiO_3$: Combined x-ray and neutron total scattering study. *Physical Review B*, *87*(10), p.104113.
38. Shyam, B., Chapman, K.W., Balasubramanian, M., Klingler, R.J., Srajer, G. and Chupas, P.J., 2012. Structural and mechanistic revelations on an iron conversion

reaction from pair distribution function analysis. *Angewandte Chemie International Edition*, *51*(20), pp.4852-4855.

39. Christensen, C.K., Mamakhel, M.A.H., Balakrishna, A.R., Iversen, B.B., Chiang, Y.M. and Ravnsbæk, D.B., 2019. Order–disorder transition in nano-rutile TiO_2 anodes: a high capacity low-volume change Li-ion battery material. *Nanoscale*, *11*(25), pp.12347-12357.
40. Aono, H., Sugimoto, E., Sadaoka, Y., Imanaka, N. and Adachi, G.Y., 1993. Electrical properties and crystal structure of solid electrolyte based on lithium hafnium phosphate $LiHf_2(PO_4)_3$. *Solid state ionics*, *62*(3-4), pp.309-316.
41. Vitova, T., Denecke, M.A., Göttlicher, J., Jorissen, K., Kas, J.J., Kvashnina, K., Prüßmann, T., Rehr, J.J. and Rothe, J., 2013, April. Actinide and lanthanide speciation with high-energy resolution X-ray techniques. In *Journal of Physics: Conference Series* (Vol. 430, No. 1, p. 012117). IOP Publishing.
42. Boglaienko, D., Andersen, A., Heald, S.M., Varga, T., Mortensen, D.R., Tetef, S., Seidler, G.T., Govind, N. and Levitskaia, T.G., 2022. X-ray absorption spectroscopy of trivalent Eu, Gd, Tb, and Dy chlorides and oxychlorides. *Journal of Alloys and Compounds*, *897*, p.162629.
43. Jeon, Y., Lu, F., Jhans, H., Shaheen, S.A., Croft, M. and Ansari, P.H., 1988. X-ray absorption spectroscopy studies of high-Tc superconductors. *Journal of Applied Physics*, *63*(8), pp.4190-4192.
44. Kuz'micheva, G.M., Ivleva, L.I., Kaurova, I.A., Khramov, E.V., Dunaeva, E.E., Svetogorov, R.D. and Rybakov, V.B., 2020. Local structural features and composition of the $Bi_4Ge_3O_{12}:Dy^{3+}$ crystals: effect of doping concentration. *CrystEngComm*, *22*(34), pp.5666-5677.
45. Asakura, H., Shishido, T., Teramura, K. and Tanaka, T., 2015. Local structure and L_1- and L_3-edge X-ray absorption near edge structure of late lanthanide elements (Ho, Er, Yb) in their complex oxides. *The Journal of Physical Chemistry C*, *119*(15), pp.8070-8077.
46. Asakura, H., Shishido, T., Teramura, K. and Tanaka, T., 2014. Local structure and La L_1 and L_3-edge XANES spectra of lanthanum complex oxides. *Inorganic Chemistry*, *53*(12), pp.6048-6053.
47. Asakura, H., Hosokawa, S., Teramura, K. and Tanaka, T., 2021. Local Structure and L_1-and L_3-Edge X-ray Absorption Near Edge Structures of Middle Lanthanoid

Elements (Eu, Gd, Tb, and Dy) in Their Complex Oxides. *Inorganic Chemistry*, *60*(13), pp.9359-9367.

48. Tiwari, N., Kumar, S., Ghosh, A.K., Chatterjee, S., Jha, S.N. and Bhattacharyya, D., 2017. Structural investigations of (Mn, Dy) co-doped ZnO nanocrystals using X-ray absorption studies. *RSC advances*, *7*(89), pp.56662-56675.

5.7. Supplementary Information

Table S5.1. Crystallographic data for LADTP from Rietveld refinement of synchrotron XRD results (28-ID-1 at NSLS-II, 1.6635 Å).

	LADTP (ICSD 95979)	**AlPO4 (ICSD 98382)**	**DyPO4 (ICSD 35705)**
RBragg	3.25	4.07	3.49
Weight %	94.3(2)	3.5(2)	2.2(7)
Space group	*R*-3*c*	$C222_1$	$I4_1/amd$
a (Å)	8.515(2)	7.07(2)	6.922(9)
b (Å)	8.515(2)	7.285(7)	6.922(9)
c (Å)	20.910(1)	6.93(2)	6.06(1)
Volume (Å3)	1313.2(1)	357(1)	290.3(1)
Phase density (g/cm3)	2.96	2.27	5.89

Whole pattern refinement parameters: Rexp = 14.43%, Rwp = 5.30, Rp = 4.32, GOF = 0.37.

Table S5.2. Structural parameters of LADTP deduced from Rietveld refinement of synchrotron XRD.

Atom	**Wyckoff Position**	**occ**	**x**	**y**	**z**	**B**
Li1	6*b*	1	0	0	0	2.86
Li2	36*f*	0.05	0.062	0.274	0.086	4.09
Ti	12*c*	0.85(6)	0	0	0.142	0.21
Al	12*c*	0.12(5)	0	0	0.143	0.21
Dy	12*c*	0.03(8)	0	0	0.138	0.21
P	18*e*	1	0.289	0	0.25	0.78
O1	36*f*	1	0.182	0.996	0.189	0.96
O2	36*f*	1	0.174	0.484	0.247	0.84

Table S5.3. Raman spectroscopy peak assignment for the NASICON-type rhombohedral LADTP system.

Raman shift (cm^{-1})	**Band assignment**	**Phenomenon**
139.5	Eg (2)	External modes: -PO_4 translations; pseudo-rotations -M^{4+} translations
178.5	A1g (1)	
240.7	Eg (5)	
275.5	Eg (6)	
312.1	A1g (3)	
354.3	Eg (7)	
434.3	A1g (4)	PO_4 symmetric bending (v2)
449.4	A1g (5)	
551.1	Eg (11)	PO_4 antisymmetric bending (v4)
969.8	Eg (14)	PO_4 antisymmetric stretching (v3)
991.3	Eg (15)	
1009.1	Eg (16)	PO_4 symmetric stretching (v1)
1069.3		PO_4 stretching of $DyPO_4$ ($I4_1/amd$) impurity phase [3]
1095.8	A1g (8)	PO_4 antisymmetric stretching (v3)

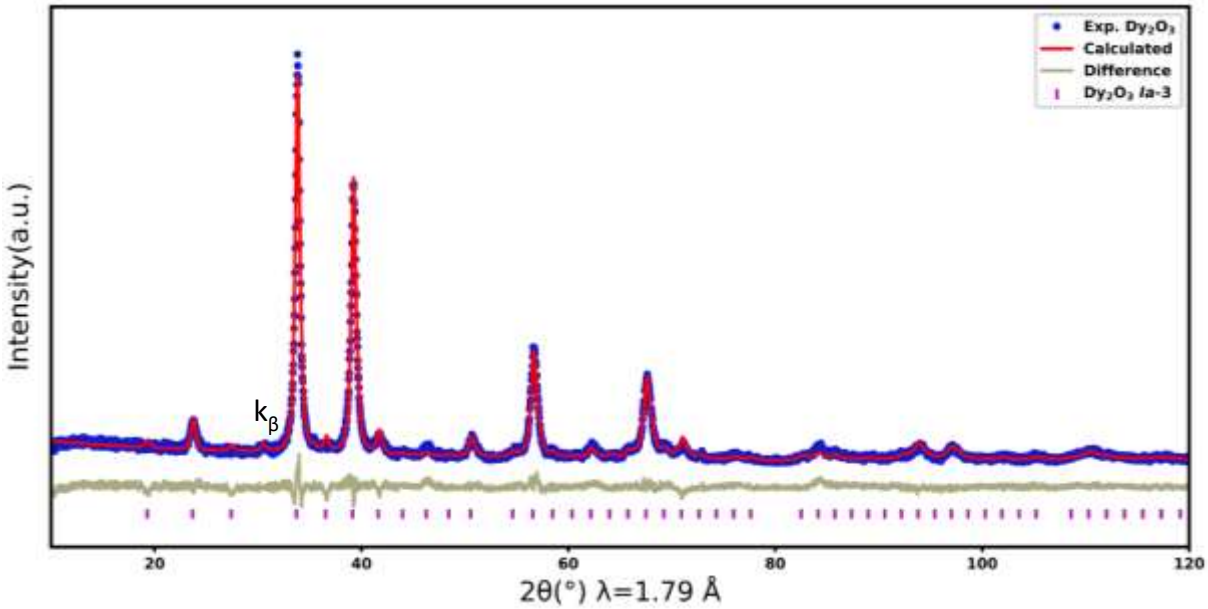


Figure S5.1. Laboratory PXRD pattern of Dy_2O_3 standard, with Rietveld refinement as implemented on Topas ACADEMIC based on the cubic *Ia*-3 structure (ICSD 66736).[1]

Table S5.4. Crystallographic data for Dy_2O_3 from Rietveld refinement from laboratory PXRD results (D2 Phaser, Co Kα) in the range 10 to 120° 2θ.

RBragg	2.45
Weight %	100
Space group	*Ia*-3
a (Å)	10.68 (1)
Volume ($Å^3$)	1218.28
Phase density (g/cm^3)	8.13 (2)

Whole pattern refinement parameters: Rexp = 6.54%, Rwp = 9.19, Rp =7.04, goodness of fit = 1.41

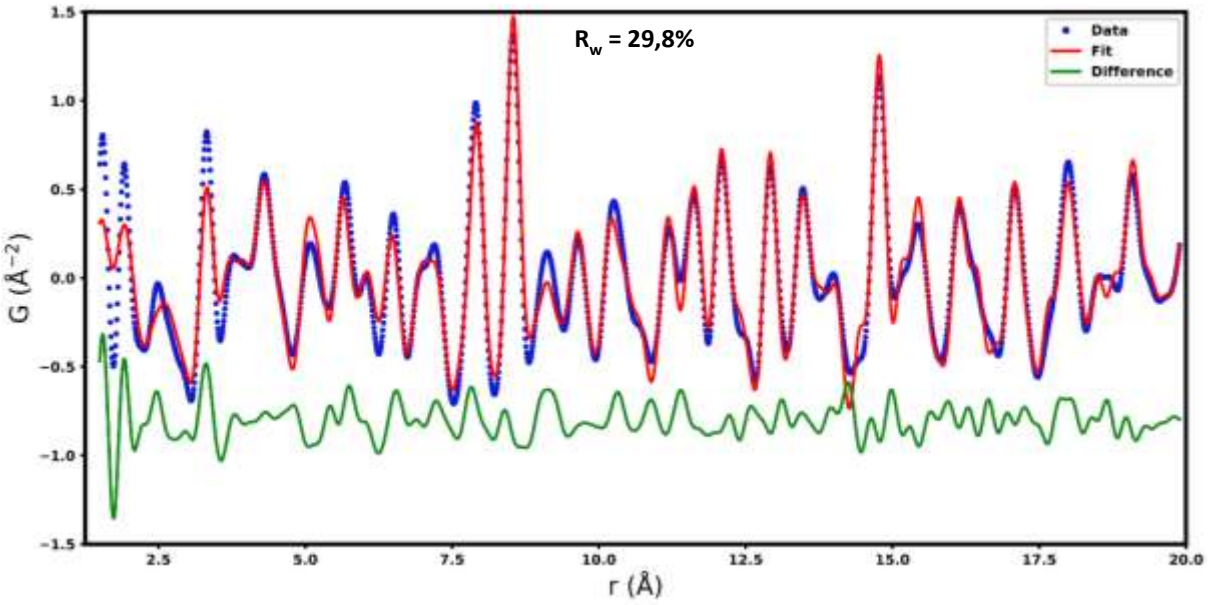


Figure S5.2. Results from structure mining for G(r) for experimental LADTP refined against $LiTi_2(PO_4)_3$ (space group *R*-3*c*) (COD 722215/ ICSD 95979).[2] Experimental data = blue, calculated data = red, difference = black (Rw = 29.8%).

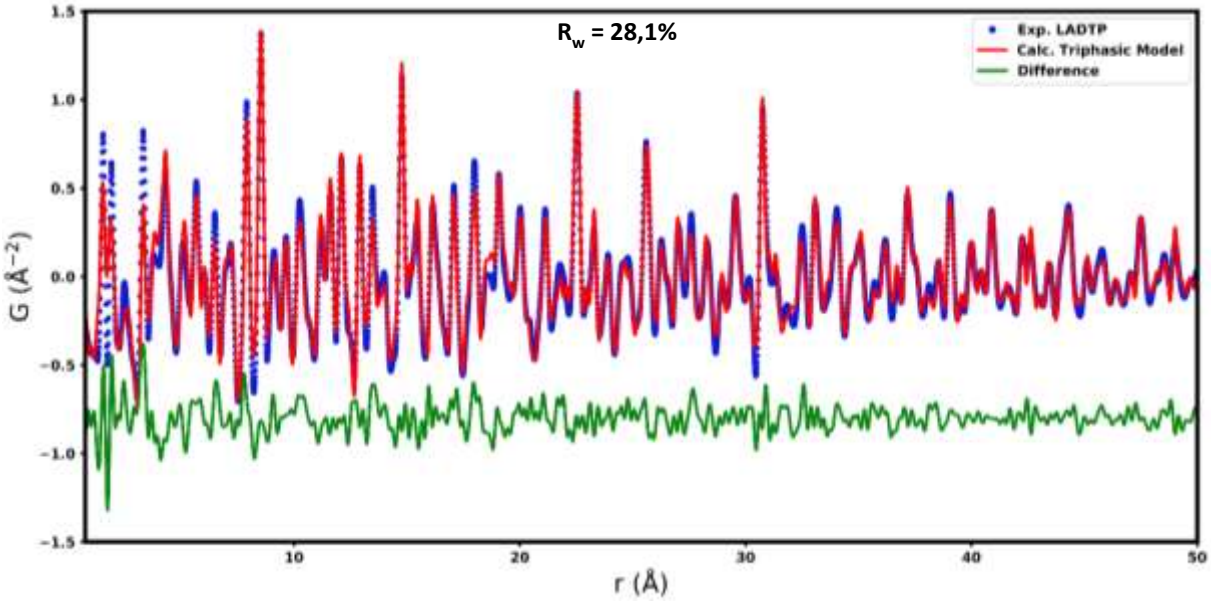


Figure S5.3. The small-box modelling of LADTP using the NASICON-type *R*-3*c*, $AlPO_4$ *C*2221 and $DyPO_4$ $I4_1/amd$ crystalline phases detected from PXRD (Rw = 28.053%).

Table S5.5. The M-O distances in various Dy-bearing compositions obtained via Rietveld refinement of PXRD data, as implemented on TOPAS-Academic.

Composition	**Dy Wyck. symbol**	**Dy-O (Å)**	**Distortion**	**Average Dy-O (Å)**
Dy_2O_3	8*b* 24*d*	2.25 (2) 2.27 (2) 2.29 (6) 2.33 (2)	[6] [2 + 2 +2]	2.29
LADTP	12*c*	1.90 (0) 1.90 (0)	[3 + 3]	1.90
$DyPO_4$	4*a*	2.25 (1) 2.35 (5)	[4 + 4]	2.30

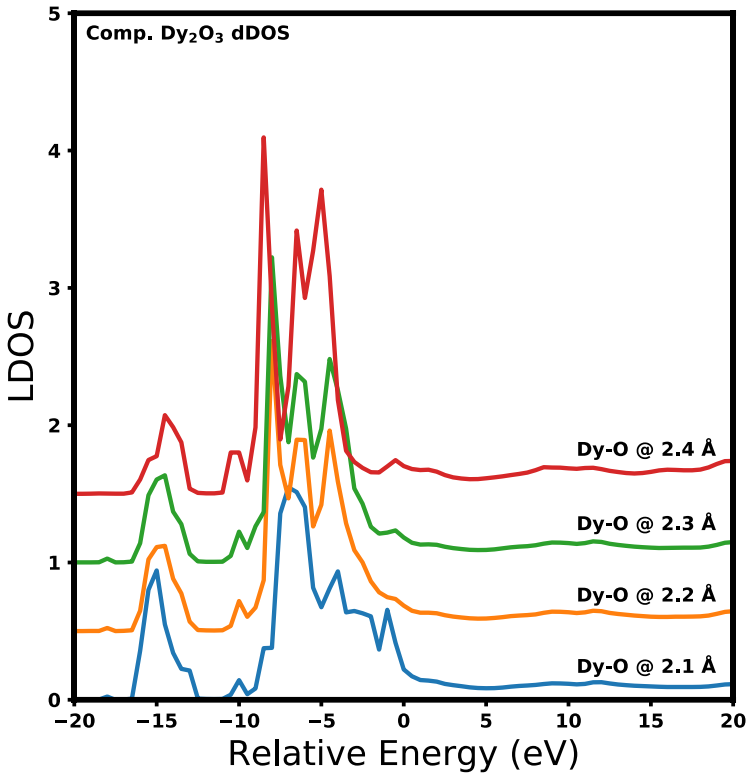


Figure S5.4. Stacked LDOS of Dy_2O_3 in *Ia*-3 space group, showing the effect of increasing Dy-O bond distance in the first shell on the spread of *d*-DOS.

References

1. Antic, B., Oennerud, P., Rodic, D. and Tellgren, R., 1993. The structure characteristics of the diluted magnetic semiconductor $Y_{2-x}Dy_xO_3$. *Powder Diffraction*, *8*(4), pp.216-220.
2. Aatiq, A., Ménétrier, M., Croguennec, L., Suard, E. and Delmas, C., 2002. On the structure of $Li_3Ti_2(PO_4)_3$. *Journal of Materials Chemistry*, *12*(10), pp.2971-2978.
3. Meenambal, R., Poojar, P., Geethanath, S., Anitha, T.S. and Kannan, S., 2019. Lanthanide phosphate ($LnPO_4$) rods as bio-probes: A systematic investigation on structural, optical, magnetic, and biological characteristics. *Journal of Biomedical Materials Research Part B: Applied Biomaterials*, *107*(5), pp.1372-1383.

Chapter 6: General Conclusions & Recommendations

6.1. General Conclusions

The purpose of this work was to improve the room-temperature ionic conductivity of LTP, a NASICON-type rhombohedral solid-state electrolyte material. The literature-reported conductivity of this fast-ion conducting material in the order of 10^{-7} S/cm is too low for its application in all-solid-state batteries for renewable energy storage. The proposed mechanisms for conductivity improvement are: i) the replacement of Ti at the 12*c* site with isovalent cations of larger ionic radii to improve the tunnel size for Li ion migration, and ii) replacement of Ti with +3 cations that would increase the concentration of Li^+ charge carriers since the change in stoichiometry would require excess Li for charge balance. Most studies presented on Li-based NASICON-type solid electrolytes have focused on the effects of doping on the ionic conductivity, with some also explaining the cationic migration of Li^+ through DFT studies. However, there have seldom been studies that seek to provide structure-property correlations through synchrotron-based techniques such as the PDF and XAS.

Throughout this work, the solid-state synthesis method was applied in material synthesis. In **Chapter 3**, Ti^{4+} (0.68 Å) was systematically replaced with Sn^{4+} (ionic radius 0.74 Å) (from 2 to 10 and 50%). The major phase was the rhombohedral NASICON LTP-type structure, with TiP_2O_7 as a persistent secondary phase, established through laboratory-based PXRD with Rietveld analysis. Furthermore, the existence of an isostructural NASICON-type $LiSn_2(PO_4)_3$ phase was observed at 50%. Raman spectroscopy confirmed the formation of the phases observed in PXRD, however, we also noted that the replacement of Ti with Sn resulted in the alteration of the crystallinity of the main phase, with significantly poor crystallinity at 50%. The Ti K-edge XAS data confirmed the oxidation state of Ti4+ across all compositions. The main spectral features of the Sn-doped systems matched the experimental features of undoped LTP. Further analysis through EXAFS showed a better agreement with a perfectly octahedral TiO_6 motif description, instead of the [3+3] TiO_6 bonding described by the average structure. Finally, to correlate the structure of Sn-doped LTP systems to their performance, EIS studies were used to show that the replacement of Ti with Sn improved the room-temperature ionic conductivity only up to a certain point, prior to reaching a plateau. We further investigated the possibility of improving the ionic conductivity by using a lower amount of dopant cations to

minimize the change in the geometric configuration of the MO^6 polyhedra that would possibly negatively affect the Li^+ migration in the structure.

In **Chapter 4**, we presented two new formulations of 10% Al, 5% Sn (LATSP) and 12.5% Al, 2.5% Dy (LADTP) LTP-based systems. The co-doped formulations were compared to 15% Al-doped LTP (LATP) and LTP. Synchrotron-based PXRD showed the successful incorporation of the dopants into LTP, to a limited extent. The replacement of Ti with Al seemingly suppressed the formation of TiP_2O_7, however $AlPO_4$ was present. Similarly, in the co-doped formulations $AlPO_4$ and $DyPO_4$ were present as secondary phases. These were attributed to the limited lattice site substitution. The larger ionic radius of Dy (0.92 Å) resulted in a limited lattice site substitution at the Ti site due to the size differences. Hence the formation of $DyPO_4$. Nonetheless, the dopants were incorporated into LTP, as observed through the changes in the lattice parameters, from PXRD. Raman spectroscopy further confirmed the rhombohedral NASICON-type main phase; however, the technique was limited in providing information on the changes in the framework, particularly around the PO4 tetrahedra, as a result of doping. The qualitative analysis of total scattering data through the PDF revealed the lattice site preference of dopant cations, depending on size. The smaller Al cations were revealed to occupy the adjacent ribbon 12*c* site about 5 Å from Ti, while the larger Sn and Dy cations occupied sites about 6 Å away from Ti at the adjacent ribbon. XAS confirmed that the doping did not cause any notable changes in the configuration of the TiO_6 octahedra. EIS showed an improvement in the ionic conductivity by at least 7 times, attributed to co-doping.

In **Chapter 5**, the LADTP system initially presented in Chapter 4 was explored further, probing the average, local and electronic structure through the Dy dopant perspective from PDF and XAS. The PDF has not been used extensively in the characterization of the local structure of NASICON-type systems. The application of structure mining as a methodology of determining the possible model describing the PDF data showed that the experimental PDF data had >90% similarity index to the *R*-3*c* NASICON-type structure, as expected from PXRD. However, the small-box modelling of LADTP PDF data using the rhombohedral *R*-3*c* model showed only a reasonable agreement with experimental data at relatively higher *r*, even with the secondary phases of $AlPO_4$ and $DyPO_4$ accounted for. Still, the low-r region was not described well by the average structure model. In previous studies reported in literature, doping has been stated to induce local triclinic and monoclinic distortions. As such, a monoclinic $P2_1/n$ model was tested in the region below 10 Å and was found to be the best descriptor of the local

structure, showing deviations from average structure. The LADTP system was further studied using XAS and compared to Dy_2O_3 standard as a reference material. The qualitative analysis of the Dy L_3-edge showed similar spectral signatures across Dy_2O_3 and LADTP, with slight changes in the white line (WL) width and intensities of other spectral features. This suggested that some Dy in LADTP was present in oxide-like environments similar to Dy_2O_3. The narrower WL in LADTP, relative to Dy_2O_3 was attributed to the higher coordination number in LADTP (7) than in the standard (6). It was found in literature that the replacement of Ti with aliovalent cations such as Dy^{3+} resulted in the excess Li^+ added for charge balance, occupying the 36*f* sites adjacent to the dopant, hence the dopant at the 12*c* site would have a coordination number of at least 7; with 6 O atoms and the nearest-neighboring Li^+ at 36*f*. The origin of the observed XAS spectral features were determined from first principles through FEFF calculations. The best reproducibility of the LADTP experimental spectrum was found through the combination of 60% Dy_2O_3, 35% $DyPO_4$ ($I4_1/amd$) secondary phase determined from PXRD and 15% monoclinic ($P2_1/n$) $DyPO_4$ as described by the PDF modelling. These fractions are not indicative of Dy explicitly existing as separate phases with their respective structures, but that the Dy local environment in LADTP can be best described as mostly oxide-like, with some regions similar to the monoclinic description.

In conclusion, this work has demonstrated the application of characterization techniques, PXRD, PDF and XAS, to provide insights into the structure of Li-based NASICON-type electrolytes across various length scales. The small-box modelling of PDF and the theoretical XAS approaches have successfully been applied to establish potential models that describe the local and electronic structure of doped LTP systems, reported for the first time to the author's knowledge. We have also successfully corroborated the importance of co-doping with larger and aliovalent cations in enhancing the room-temperature ionic conductivity for further improvement and application in all solid-state Li-ion batteries.

6.2. Recommendations

The work presented herein has successfully demonstrated the improvement in room-temperature ionic conductivity of NASICON-type Li-based systems through co-doping. The proposed next steps would be as follows:

- Developing and testing **alternative synthesis methods** to improve the phase purity and determine the resulting room-temperature ionic conductivities relative to conventional solid-state synthesis methods presented in this work. The phase purity influences the electrochemical stability window of the solid electrolyte materials, as the practical stability is attributed to kinetic phase stabilization.[1]
- **Studying the local order** around the framework of Sn-doped systems through techniques such as the pair distribution function (PDF) with small-box modelling, along with **Sn** and **P XAS**.
- **Construction of exemplary all-solid-state batteries (ASSBs)** using the proposed materials to study the **performance and degradation mechanisms** of the battery systems using our proposed co-doped LATSP and LADTP electrolytes. Techniques such as **X-ray tomography** can provide such insights.
- **Neutron diffraction** operando experiments to trace the migration mechanism,[2] of Li ions in the co-doped systems (^{7}Li) and pinpointing the location of Dy in LADTP system to be reconciled with PDF and XAS studies.
- **Variable-temperature PXRD** to assess the temperature-dependent polymorphism that has been cited to impact the ionic conductivity of NASICON-type systems and determine the coefficients of thermal expansion to establish compatibility with anode and cathode components.
- **Ti K-edge XAS pre-edge fitting** for all compositions to determine the variations in the degree of hybridization as a result of (co)-doping.
- **Theoretical Ti K-edge XANES using FEFF10** to understand the origin of the pre-edge features for NASICON-type Li-based systems.
- **Combined structure solution using PXRD, PDF and XAS** to find a model that best describes the structures from average, local and electronic perspectives to guide product redesign of improved energy storage systems.

Although these above-mentioned strategies provide more information on improving structure-property technical aspects of the solid-state electrolyte materials, it remains equally important that other key factors such their environmental effects are accounted for. It is therefore imperative that the production and post-consumer environmental effects/sustainability are also investigated.[3]

The implementation of the EPR legislation in South Africa in the Energy Sector requires in-depth analysis through life cycle assessment in battery manufacturing,[4] as well as the infrastructure required to recycle the end-of-life post-consumer solid-state batteries. The placement of large-scale facilities for grid energy contributions of renewable energy needs careful consideration of their location, and the impact of said facilities on the flora, fauna and communities. Successful implementation would require collaboration with communities so as to apply indigenous knowledge systems in the implementation plans of these facilities, the skills development and job creation in the Green Economy, and lastly, the integration of small businesses in the operations of the plants.

6.3. References

1. Benabed, Y., Rioux, M., Rousselot, S., Hautier, G. and Dollé, M., 2021. Assessing the electrochemical stability window of NASICON-type solid electrolytes. *Frontiers in Energy Research*, *9*, p.682008.
2. Shah, A.R., Shutt, R.R., Smith, K., Hack, J., Neville, T.P., Headen, T.F., Brett, D.J., Howard, C.A., Miller, T.S. and Cullen, P.L., 2021. Neutron studies of Na-ion battery materials. *Journal of Physics: Materials*, *4*(4), p.042008.
3. Zhang, J., Ke, X., Gu, Y., Wang, F., Zheng, D., Shen, K. and Yuan, C., 2022. Cradle-to-gate life cycle assessment of all-solid-state lithium-ion batteries for sustainable design and manufacturing. *The International Journal of Life Cycle Assessment*, *27*(2), pp.227-237.
4. Walzberg, J., Carpenter, A. and Heath, G.A., 2021. Role of the social factors in success of solar photovoltaic reuse and recycle programmes. *Nature Energy*, *6*(9), pp.913-924.